AMINO ACID FUNCTIONALIZED FULLERENOLS: SYNTHESIS AND APPLICATIONS IN ENZYME MIMICRY AND ORGANOCATALYSIS

A THESIS SUBMITTED TO
THE GRADUATE SCHOOL OF NATURAL AND APPLIED SCIENCES
OF
MIDDLE EAST TECHNICAL UNIVERSITY

BY

VOLKAN DOLGUN

IN PARTIAL FULFILLMENT OF THE REQUIREMENTS
FOR
THE DEGREE OF DOCTOR OF PHILOSOPHY
IN
CHEMISTRY

MARCH 2025

Approval of the thesis:

AMINO ACID FUNCTIONALIZED FULLERENOLS: SYNTHESIS AND APPLICATIONS IN ENZYME MIMICRY AND ORGANOCATALYSIS

submitted by **VOLKAN DOLGUN** in partial fulfillment of the requirements for the degree of **Doctor of Philosophy** in **Chemistry, Middle East Technical University** by,

Prof. Dr. Naci Emre Altun
Dean, **Graduate School of Natural and Applied Sciences**

Prof. Dr. Ayşen Yılmaz
Head of the Department, **Chemistry**

Assoc. Prof. Dr. Salih Özçubukçu
Supervisor, **Chemistry, METU**

Examining Committee Members:

Prof. Dr. Cihangir Tanyeli
Chemistry, METU

Assoc. Prof. Dr. Salih Özçubukçu
Chemistry, METU

Assoc. Prof. Dr. Serhan Türkyılmaz
Chemistry, METU

Assoc. Prof. Dr. Gülcihan Gülseren
Molecular Biology and Genetics, KFAU

Assoc. Prof. Dr. Onur Alptürk
Chemistry, ITU

Date: 06.03.2025

I hereby declare that all information in this document has been obtained and presented in accordance with academic rules and ethical conduct. I also declare that, as required by these rules and conduct, I have fully cited and referenced all material and results that are not original to this work.

Name Last name: Volkan Dolgun

Signature:

ABSTRACT

AMINO ACID FUNCTIONALIZED FULLERENOLS: SYNTHESIS AND APPLICATIONS IN ENZYME MIMICRY AND ORGANOCATALYSIS

Dolgun, Volkan
Doctor of Philosophy, Chemistry
Supervisor: Assoc. Prof. Dr. Salih Özçubukçu

March 2025, 229 pages

Buckminsterfullerene (C_{60}) and its derivatives, particularly fullerenol, have gained attention due to their versatile applications. Fullerenol is hydrophilic and can be easily functionalized, making it a promising scaffold for catalysis. Amino acid-functionalized fullerenols tend to aggregate and form enzyme-like structures known as ‘fullerenzymes,’ which mimic enzymatic activity and serve as catalysts in organic reactions.

In the first part of this study, arginine functionalized fullerenol (**F**-Arg) was used as a biomimetic catalyst for LarE, the sulfur insertase of lactic acid racemase (Lar) from *Lactobacillus plantarum*. **F**-Arg facilitated the conversion of cysteine and nicotinic acid derivatives in buffer solution, mimicking the enzymatic transformation to dehydroalanine.

In the second part, histidine and serine functionalized fullerenol (**F**-HS) was coordinated with nickel ions and investigated as an esterase-mimic for acetylcholine detection in human serum. The **F**-HS-Ni sensor exhibited high sensitivity and selectivity, demonstrating its potential for biomedical applications.

In the third part, fullerenols and their amino acid derivatives were explored as organocatalysts. They efficiently catalyzed carbon dioxide fixation under mild conditions. Additionally, **F**-Arg served as basic catalysts in the Morita-Baylis-Hillman reaction and chromene synthesis. Fullerenols were also used as Brønsted acid catalysts in the Prins reaction.

These findings highlight the potential of fullerenol-based catalysts in biomimetic and organic transformations.

Keywords: Fullerene, Enzyme mimics, Sulfur insertase, Organocatalysis, Alzheimer’s disease.

ÖZ

AMİNO ASİT İLE FONKSİYONLANDIRILMIŞ FULLERENOLLER: SENTEZİ VE ENZİM TAKLİDİ İLE ORGANOKATALİZ UYGULAMALARI

Dolgun, Volkan
Doktora, Kimya
Tez Yöneticisi: Doç. Dr. Salih Özçubukçu

Mart 2025, 229 sayfa

Buckminsterfulleren (C_{60}) ve türevleri, özellikle fullerenol, sahip olduğu geniş uygulama alanları nedeniyle dikkat çekmektedir. Fullerenol, hidrofilik yapısı ve kolay fonksiyonlandırılması sayesinde katalizör uygulamaları için uygun bir platform olarak görülmektedir. Amino asit ile fonksiyonlandırılmış fullerenoller, kendi kendine düzenlenerek enzim benzeri yapılar oluşturabilir ve 'fullerenzimler' olarak adlandırılan bu yapılar organik tepkimelerde katalizör görevi görebilir.

Bu çalışmanın ilk bölümünde, arjinin ile fonksiyonlandırılmış fullerenol (**F**-Arg), *Lactobacillus plantarum* kaynaklı laktik asit rasemazının (Lar) sülfür insertaz bileşeni LarE'nin biyomimetik bir katalizörü olarak kullanılmıştır. **F**-Arg, sistein ve nikotinik asit türevlerinin tampon çözelti içerisindeki dönüşümünü katalize ederek enzimatik olarak dehidroalanin oluşumunu taklit etmiştir.

İkinci bölümde, histidin ve serin ile fonksiyonlandırılmış fullerenol (**F**-HS) nikel iyonları ile koordine edilerek, insan serumunda asetilkolin tespiti için esteraz benzeri bir enzim modeli olarak incelenmiştir. **F**-HS-Ni sensörü yüksek hassasiyet ve seçicilik göstermiş, biyomedikal uygulamalar için potansiyelini ortaya koymuştur.

Üçüncü bölümde, fullerenoller ve amino asit türevleri organokatalizör olarak incelenmiştir. Ilımlı koşullarda karbon dioksit fiksasyonunda etkin bir katalizör olarak görev yapmıştır. Ayrıca, **F**-Arg, Morita-Baylis-Hillman tepkimesi ve kromen sentezinde bazik katalizör olarak değerlendirilmiştir. Fullerenoller ise Prins tepkimesinde Brønsted asidi katalizörü rolünü üstlenmiştir.

Bu bulgular, fullerenol bazlı katalizörlerin biyomimetik ve organik dönüşümlerdeki potansiyelini ortaya koymaktadır.

Anahtar Kelimeler: Fulleren, Enzim taklitleri, Sülfür insertaz, Organokatalizör, Alzheimer hastalığı.

To my oldest friend Kali Hansfarliwer

ACKNOWLEDGMENTS

During my long PhD journey, I had the privilege of meeting many wonderful people who added immense value to my life. And as this truly long story comes to an end, I would like to extend my deepest thanks to all of them.

First and above all, I would like to express my sincere gratitude and respect to my supervisor, Assoc. Prof. Dr. Salih Özçubukçu. His guidance, patience, understanding, brilliant intellect, and the consistently positive influence of his role model throughout this academic journey have been invaluable to me. Being a member of the Özçubukçu Lab Group for over a decade has been both a great honor and a privilege.

I would like to express my sincere gratitude to my thesis monitoring committee, Assoc. Prof. Dr. Serhan Türkyılmaz and Assoc. Prof. Dr. Gülcihan Gülseren for their valuable time and the insightful guidance they provided throughout this journey. After every monitoring meeting, I found myself filled with fresh ideas and renewed motivation which I consider a great privilege. I am also deeply thankful to my thesis committee members, Prof. Dr. Cihangir Tanyeli, Assoc. Prof. Dr. Onur Alptürk and Assoc. Prof. Dr. Serdal Kaya for dedicating their time and effort to reviewing my work and providing constructive feedback that helped shape this thesis. I am also grateful to Dr. Antoine Marion for his valuable contributions to the theoretical calculations, which supported the interpretation of the experimental results.

On this journey, I would like to thank every past, present, and perhaps even future member of the Özçubukçu Lab Group, with whom I shared most of my time. Among them, I will only mention my "arch enemy," Seçkin Kesici. I also extend my thanks to one of the former lab members, Muzaffer Gökçe. Working alongside my comrades in fate, Enes Uzun, Elif Akar, and Gamze Yılmaz, during holidays, weekends, and even late at night has created memories I will always carry with me. I also want to give a special thanks to my little friend Burak Can Kalemci. Moreover, I express my deepest gratitude to Berat Kocaş, Doruk İşler, and Ulaş Mutlu. I am proud to describe them not as undergraduate students, but as friends. Their support and companionship have truly contributed to the making of this thesis. Most importantly, I offer my sincere thanks and respect to Dr. Aytül Saylam, who has been a mentor to me in every possible way. She supported me through every lost motivation, every doubt, every result whether good or bad, and every challenge in my life. In this story, she not only provided academic guidance but also taught me what it means to be human. I would also like to thank Dr. Güzide Aykent and Yalçın Boztaş for their support along the way.

I would like to thank TUBİTAK (118Z921) and BAP (GAP-103-2021-10634) for financial support.

I would also like to thank Kali Hansfarliwer, who has been by my side since the time I could not even read and who will always be with me. The world we created together and the dreams we realized within it have always been a guiding light for me. Even without words or actions of his own, the mere presence of my oldest friend has always given me strength and helped me stay on my feet.

Lastly, I would like to express my gratitude to my family, whom I am proud to call my own. I am deeply thankful for their unwavering love and support throughout this journey. As I grow older, I find myself appreciating their sacrifices, values, and the depth of their care even more. I am honored by their presence in my life and the goodness they bring into this world.

TABLE OF CONTENTS

CHAPTERS

APPENDICES

LIST OF TABLES

TABLES

LIST OF FIGURES

FIGURES

LIST OF SCHEMES

SCHEMES

LIST OF ABBREVIATIONS

ABBREVIATIONS	
ACA	2-acetamido acrylic acid
Ach	Acetylcholine
AD	Alzheimer’s disease
Dha	Dehydroalanine
DLS	Dynamic light scattering
EDX	Energy-dispersive X-ray spectroscopy
F-AA	Amino acid functionalized fullerenol
FE-SEM	Field emission scanning electron microscopy
FT-IR	Fourier Transform Infrared Spectroscopy
HPLC	High-performance liquid chromatography
LAR	Lactic acid racemase
LC-MS	Liquid chromatography–mass spectrometry
MBH	Morita-Baylis-Hillman
TBAI	Tetrabutylammonium iodide
TCEP	Tris(2-carboxyethyl)phosphine hydrochloride
TEM	Transmission Electron Microscopy
TGA	Thermogravimetric analysis

CHAPTER 1

INTRODUCTION

1.1 Fullerene

In 1985, Harold Walter Kroto, James R. Heath, Sean C. O'Brien, Richard Errett Curl and Robert Floyd Smalley participated in a project focused on exploring how long-chain carbon molecules form in interstellar space and circumstellar shells [1]. In this process, laser irradiation was used to vaporize graphite, leading to the production of a remarkably stable cluster made up of 60 carbon atoms. They suggested that its structure is a polygon with 60 points and 32 faces, consisting of 12 pentagons and 20 hexagons, where 60 carbon atoms are bound together by single and double bonds, resembling a football (Figure 1).

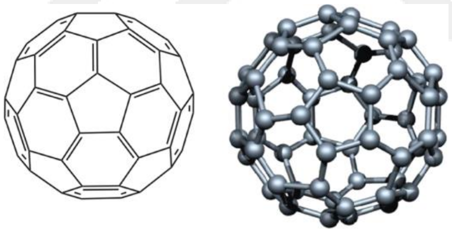

Figure 1. Structure and 3D representation of fullerene C_{60}.

The carbon number of this stable compound, generated following laser irradiation, was determined using time-of-flight mass spectrometry (TOF-MS). The results were improved by increasing the applied helium density. Consequently, a dominant proportion of C_{60} was obtained, along with approximately 5% C_{70} was observed (Figure 2).

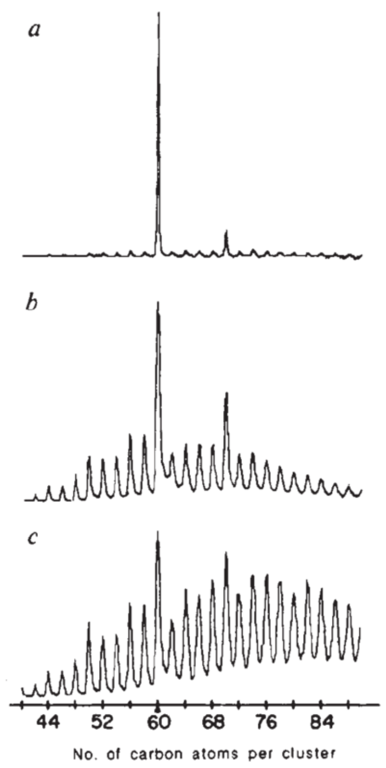

Figure 2. Varying helium pressures influenced cluster formation: (c) low pressure (<10 torr) led to direct graphite ejection, (b) ~760 torr enhanced C_{60} and C_{70} via gas-phase reactions, and (a) optimized conditions promoted thermalization [1].

Independently, in 1986, Haymet demonstrated the possibility of a structure consisting of 12 pentagonal and 20 hexagonal rings, resembling a truncated icosahedral shape, through theoretical calculations [2]. Inspired by the synthesis of corannulene (Figure 3) in 1971 [3], it was suggested that, if such a structure exist, small metal ions can easily be trapped inside, thanks to its diameter (around 7 Å) and demonstrate extraordinary properties with potential applications in various fields, as supported by theoretical calculations. It was also pointed out that, after the completion of the calculations, the large peak in the mass spectrum belonging to 60 carbon atoms, published by Kroto *et al.*, was observed and considered to represent C_{60}, the structure predicted and theoretically calculated by Haymet.

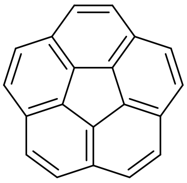

Figure 3. Structure of [5.6.1] corannulene.

Haymet initially proposed the name "footballene" for this molecule. However, Kroto and colleagues ultimately named it "buckminsterfullerene" due to its resemblance to the geodesic domes designed by architect Buckminster Fuller. Other suggestions, including "ballene," "sphrene," "soccerene," and "carbosoccer," were considered but not adopted. The term "fullerene" has since become widely used in scientific literature. In recognition of their groundbreaking discovery, Kroto, Smalley, and Curl were awarded the 1996 Nobel Prize in Chemistry [4].

1.1.1 Physical and Chemical Properties of Fullerene

The discovery of fullerene established it as the third recognized allotrope of carbon, alongside the naturally occurring allotropes diamond and graphite [1]. Later, in 1990, Krätzschmer and Huffman successfully synthesized C_{60} in gram quantities using a carbon arc method, enabling further studies into its unique properties and applications [5].

Structurally, fullerenes are composed of fused pentagonal and hexagonal rings with conjugated bonds, where each carbon atom is sp^2 hybridized and bonded to three neighboring carbon atoms. This hybridization results in a delocalized π-electron system, contributing to the molecule's unique electronic and chemical properties, with bond lengths averaging 0.145 nm for single bonds and 0.141 nm for double bonds [6]. As a result, the delocalized π-electrons provide stability to the spheroid structure through resonance, with 12,500 resonance structures contributing to this stabilization [7].

C_{60} fullerene belongs to the icosahedral symmetry group (I_h), which is characterized by 120 symmetry operations. These operations include rotations and inversions that together define the highly symmetrical structure of the molecule [8]. It also demonstrates unique aromatic characteristics due to its delocalized π-electron system, with Kroto suggesting that it could be 'the first example of a spherical aromatic molecule' following its discovery [1]. Even though it does not fully conform to Hückel's rule for planar aromatic systems [9], the conjugated π-electrons spread over its spherical surface, contributing to its stability. The compound displays localized aromaticity within its six-membered rings, whereas the five-membered rings introduce anti-aromatic behavior. This combination of aromatic and anti-aromatic character results in partial spherical aromaticity, distinguishing fullerene from conventional planar aromatic compounds [10].

In addition to its unique electronic and structural properties, fullerene also exhibits thermal stability up to 250 °C, with a quick sublimation starting around 370 °C and complete combustion occurring once the temperature reaches approximately 550 °C [11].

1.1.2 Functionalization of Fullerene C_{60}

C_{60} is now widely recognized for behaving like an electron-deficient olefin, owing to the unique electronic properties of its π-conjugated system. The reason for this electron-deficiency is the curvature-induced strain and the delocalized π-electrons, which make the carbon atoms on the fullerene surface more electrophilic [12]. Consequently, C_{60} can undergo nucleophilic addition reactions with a variety of nucleophilic reagents.

The most notable among these are active methylene compounds, such as diethyl bromomalonate, which contain acidic hydrogen atoms positioned between electron-withdrawing groups. These compounds exhibit significant reactivity with C_{60}, known as the Bingel reaction [13] (Scheme 1).

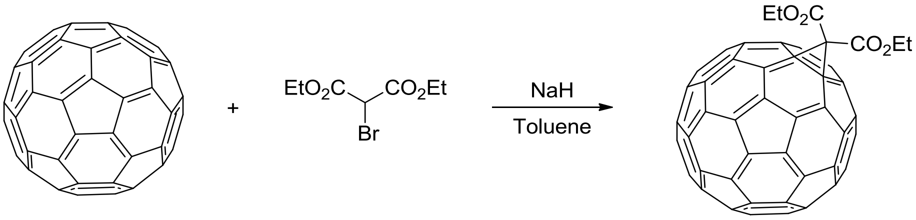

Scheme 1. Bingel Reaction: Cyclopropylation of fullerene [13].

Additionally, other nucleophilic reactions of C_{60} reported in the literature include those with cyanide ions, yielding to cyano-functionalized fullerenes [14]; carbanions produced through silyl ethers, resulting in carbon-carbon bond formation [15], and organometallic reagents [16] such as Grignard reagents [17].

C_{60} can also be reduced to fullerene anions either through electrolysis [18] or by chemical reduction using various metals, including lithium [19], cesium [20], barium [21], and mercury [22]. The resulting anionic species can subsequently act as nucleophiles, making possible further chemical alteration and functionalization [23-25]. Furthermore, C_{60} exhibits a strong tendency to act as dienophiles in Diels-Alder reactions [26] and can undergo 1,3-dipolar cycloaddition with azomethine ylides, a process widely recognized as the Prato reaction [27] (Scheme 2).

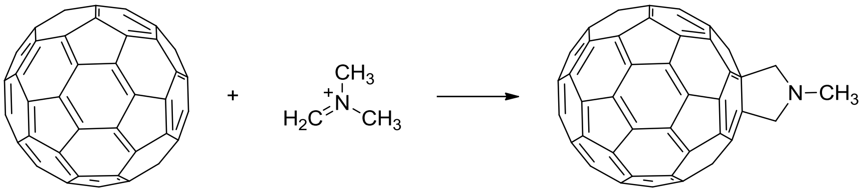

Scheme 2. Prato Reaction: Synthesis of fullerene pyrrolidines [27].

The first reported example of a [2+2] cycloaddition involving fullerenes was published by Hoke in 1992 [28]. In this study, benzyne was reacted with fullerene, and the resulting product was successfully characterized. Subsequently, various photochemical [2+2] cycloaddition reactions were reported, including the study of Wilson *et al.*, which described the reaction of cyclohexenone with fullerene under 308 nm irradiation [29], and the 1996 study by Foote *et al*. reporting the reaction of fullerene with *N*,*N*-diethyl-4-methyl-3-penten-1-yn-1-amine [30] (Scheme 3).

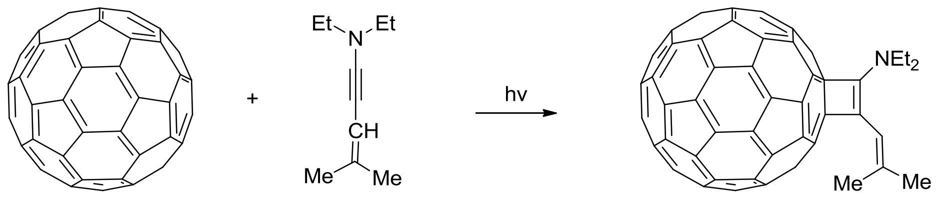

Scheme 3. [2+ 2] Cycloaddition of fullerenes [30].

In 1998, Saunders *et al.* reported the bulk production of the [2+2] dimerization of C_{60} accomplished via solid-state mechanochemical reaction involving KCN as a catalyst, utilizing the high-speed vibration milling (HSVM) technique [31]. This reaction was also demonstrated using potassium salts, including potassium carbonate and potassium acetate, as well as various metals such as lithium, sodium, potassium, magnesium, aluminum, and zinc (Scheme 4).

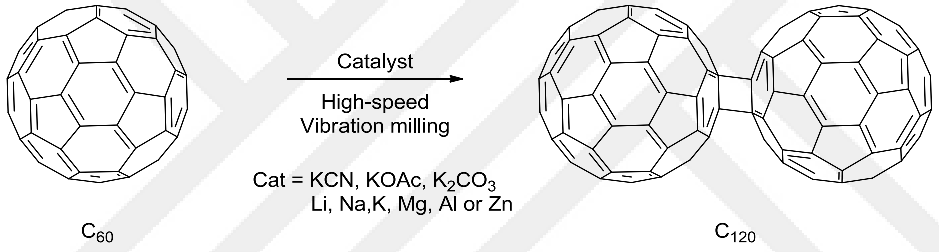

Scheme 4. [2+2] dimerization of C_{60} [31].

1.1.3 Endohedral Fullerenes

Shortly after the discovery of fullerene, Smalley *et al.* used laser vaporization of graphite impregnated with $LaCl_3$ and detected a stable LaC_{60} peak in the gas phase using mass spectrometry [32]. Subsequently, with the advancement of theoretical calculations for endohedral (inside-the-cage) fullerene complexes [33], Smalley *et al.* successfully synthesized La@C_{82} on a macroscopic scale and introduced the nomenclature "@C_n" for such complexes [34]. The isolation and characterization of La@C_{82} were later achieved by Kikuchi *et al.* in 1993, providing further insights into its structure and stability [35]. Subsequently, Y@C_{82} and Sc@C_{82} were synthesized by arc discharge method with other group 3 metals [36, 37], and early studies also reported the synthesis of dimetallic and trimetallic endohedral fullerenes, such as $Sc_2@C_{82}$ and $Sc_3@C_{82}$ [38].

In the following years, significant studies were developed to encapsulate various metal-containing structures into fullerenes composed of different numbers of carbon atoms (Figure 4). Among these are metal nitrides (NCFs) [39], metal carbides (CCFs) [40], metal cyanides (CYCFs) [41], metal oxides (OCFs) [42], metal sulfides (SCFs) [43], metal hydrocarbides (HCCFs) [44] and metal carbonitride cluster fullerenes (CNCFs) [45].

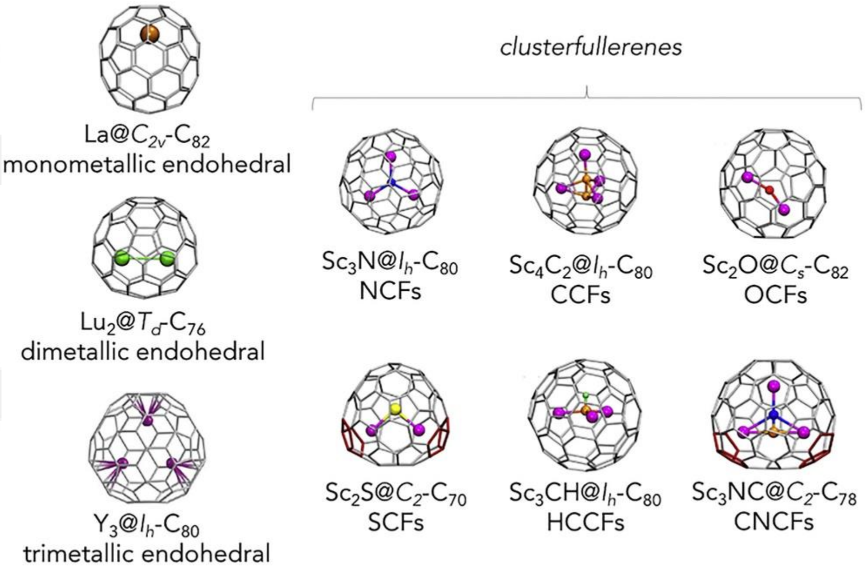

Figure 4. Different types of endohedral fullerenes [46].

Endohedral fullerene studies have predominantly achieved success with fullerenes containing a high number of carbon atoms, with C_{82} being the most frequently used. This preference is largely attributed to the greater internal cavity size of higher-order fullerenes, which facilitates the encapsulation of the compounds. In contrast, successful examples involving C_{60} fullerenes are more limited due to the smaller cavity size, which poses significant challenges for encapsulating larger atoms or complexes.

Among the notable exceptions, $Ne@C_{60}$ and $He@C_{60}$ have been synthesized and isolated using small noble gases, demonstrating the feasibility of encapsulating atoms with minimal steric requirements [47]. However, in the case of metal-encapsulated fullerenes (M@C_{60}), the only successful study to date was reported in 1997 with the synthesis and isolation of Li@C_{60}, where lithium atoms were encapsulated within the C_{60} cage [48].

1.1.4 C_{60} Fullerenol

C_{60} Fullerenes exhibit limited solubility in most organic solvents, with significantly better solubility observed in specific solvents such as hexane, toluene, and carbon disulfide (CS_2) at room temperature [49]. Their hydrophobic nature makes them naturally insoluble in water unless chemically modified [50]. Nonetheless, various approaches have been investigated to disperse unmodified C_{60} in aqueous systems.

Scrivens *et al*. prepared an aqueous dispersion of C_{60} by dissolving it in benzene and sequentially diluting the solution with THF, acetone and water, followed by distillation to remove the organic solvents [51]. Another study by Prilutski *et al*. used sonication a mixture of a C_{60} solution in toluene and water for several hours until all the toluene evaporated. Instead of precipitating during toluene removal, C_{60} formed a stable colloidal dispersion in water [52]. However, both methods involved using organic solvents like benzene or toluene, neither of which are ideal for safety or environmental reasons.

While aqueous dispersions of pristine C_{60} have been achieved, their practical applications remain limited due to poor stability, low solubility, and the reliance on toxic organic solvents during preparation [53]. To overcome these challenges, functionalization of the fullerene cage has developed as an effective strategy to enhance water solubility and broaden its potential applications. Among the various functionalized derivatives, hydroxylated fullerenes, commonly known as fullerenols or fullerols, have garnered significant attention due to their improved solubility and versatile properties.

The first synthesis of fullerenol was reported by Chiang *et al.* in 1992, utilizing a mixture of H_2SO_4 and HNO_3 as oxidizing agents at temperatures ranging between 85 °C and 115 °C. This method resulted in the addition of 18-20 hydroxyl groups per C_{60} molecule [54]. Since this initial work, several synthetic pathways have been developed for fullerenols with varying degrees of hydroxylation, generally represented by the formula $C_{60}(OH)_n$, where $2 \leq n \leq 42$ [55-58].

Fullerenols with a lower degree of hydroxylation, such as $C_{60}(OH)_{10-12}$, exhibit solubility in polar organic solvents, including THF, DMF and DMSO. On the other hand, medium degree hydroxylated fullerenols, such as $C_{60}(OH)_{16}$ and $C_{60}(OH)_{20-24}$, are reported to be water-soluble [59]. The most widely utilized method for synthesizing fullerenol with 24–26 hydroxyl groups is the one described by Li in 1993 [55]. This procedure involves the direct reaction of fullerene with NaOH solution, using quaternary ammonium hydroxides, generally tetrabutylammonium hydroxide (TBAH), as phase-transfer catalysts (Scheme 5).

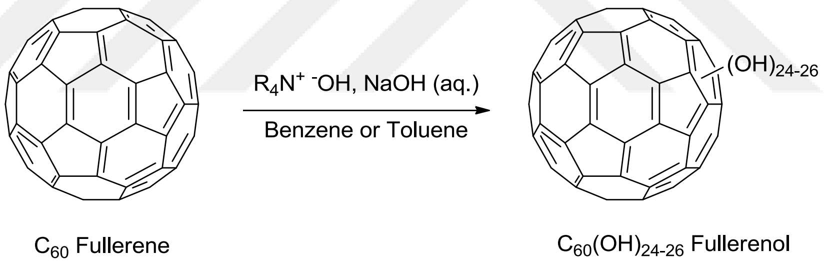

Scheme 5. Synthesis of $C_{60}(OH)_{24-26}$ fullerenol [55].

Density Functional Theory (DFT) studies on $C_{60}(OH)_{24}$ isomers revealed that increased hydroxyl group distribution along the equatorial region of the C_{60} cage lowers the molecular energy, indicating higher stability [F60]. This stabilization results in an egg-shaped structure for $C_{60}(OH)_{24}$ as shown in Figure 5.

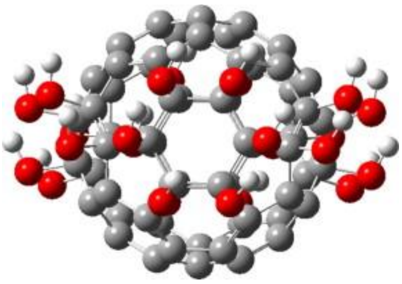

Figure 5. Egg-shaped structure for $C_{60}(OH)_{24}$ [60].

1.1.4.1 Applications of Fullerenol

A significant limitation in fullerenol research is the challenging synthesis process, which produces a mixture of derivatives, predominantly with 18 to 24 hydroxyl groups. This variability in composition poses reproducibility challenges, particularly in applications where precise chemical properties are critical [61]. Despite this, they have emerged as promising candidates for a wide range of applications.

1.1.4.1.1 Antioxidant Properties

In 1995, Chiang *et al.* reported that water-soluble fullerenols, owing to their moderate electron affinity and allylic hydroxyl groups, efficiently scavenge superoxide radical anions ($O_2^{\bullet -}$) produced by xanthine and xanthine oxidase in aqueous solutions, highlighting their potential as water-soluble antioxidants [62]. Highly hydroxylated fullerenols, such as $C_{60}(OH)_{32}$, have also been shown to neutralize cell damage induced by H_2O_2, further emphasizing their antioxidant capabilities [63]. Lai *et al.* also investigated the antioxidant effects of fullerenols *in vivo*, pointing out their ability to scavenge free radicals in ischemia-reperfusion-injured intestines and grafts after small bowel transplantation in dogs [64, 65]. In addition, in 2004, Mirkov *et al.* provided the first evidence of the direct nitric oxide (NO) quenching activity of fullerenols across various environments, confirming their free radical-scavenging properties [66].

These findings support the versatility of fullerenols as powerful antioxidants in biological systems. Their ability to scavenge reactive oxygen species (ROS) and reactive nitrogen species (RNS) identifies them as potential candidates for medical treatments focusing on neurodegenerative diseases, cardiovascular disorders, and even cancer [67].

Although the ROS-scavenging mechanisms of fullerenols are not fully understood, the proposed hydroxyl radical scavenging mechanism suggests that hydroxyl radicals remove a hydrogen atom from the hydroxyl groups of fullerenols, followed by their addition to an sp^2 carbon in the fullerene [68] (Scheme 6).

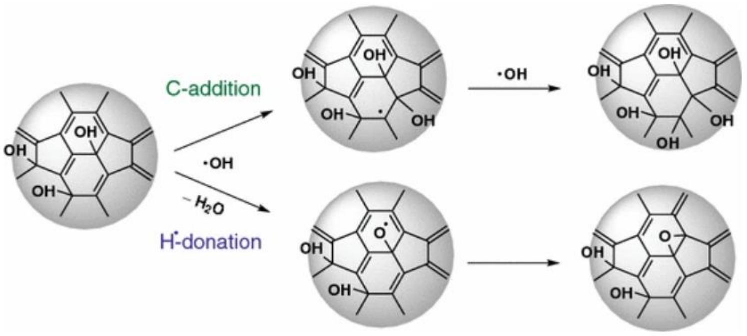

Scheme 6. The proposed hydroxyl radical scavenging mechanism of fullerenol [68].

1.1.4.1.2 Catalytic Applications

Beyond biomedical applications, fullerenols have demonstrated catalytic activities in various chemical reactions. For instance, studies have shown that fullerenols can contribute to the stabilization and activation of ruthenium nanoparticles, significantly enhancing their catalytic activity for the hydrogen evolution reaction (HER) in alkaline environments [69]. In another example, Ouyang *et al*. reported that the addition of $C_{60}(OH)_n$ enabled the adsorption of silver ions and citrate onto its surface [70]. This promoted the transfer of electrons between citrate and silver ions, overcoming the ineffective collisions that otherwise prevent the silver nitrate–

trisodium citrate reaction in solution. Consequently, this process resulted in the formation of metallic silver, 1,3-acetonedicarboxylic acid, and CO_2 (Figure 6).

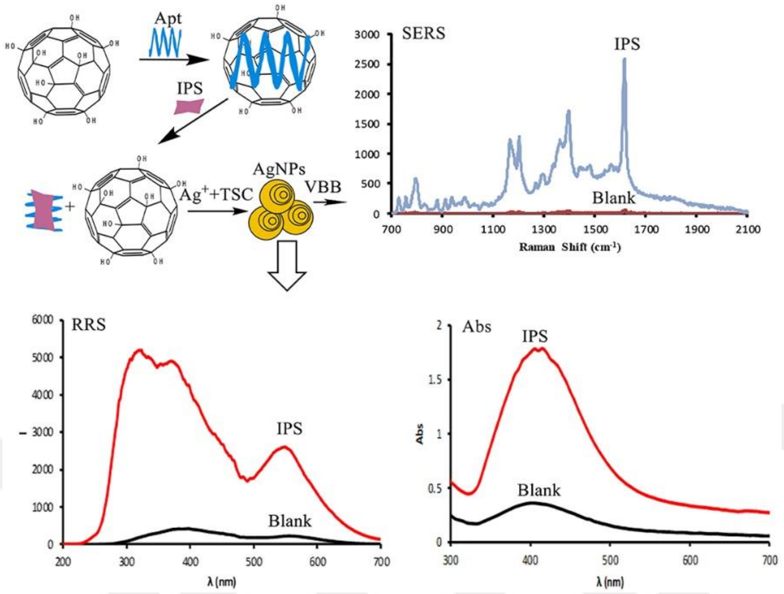

Figure 6. Aptamer-based trimodal platform with $C_{60}(OH)_n$-catalyzed IPS amplification and a trifunctional AgNP probe.

1.1.4.1.3 Conjugations with Biomolecules

Although fullerenols have been utilized in various fields, reports on their chemical conjugation with other molecules remain limited. Enhancing the functional versatility of fullerenols by conjugation is significant for their integration into advanced applications. In a notable study, published in 2009 by Sengupta *et al.*, fullerenols were first activated using *p*-nitrophenyl chloroformate, a reagent commonly employed to catalyze ester and carbamate bond formation. Following activation, doxorubicin, a chemotherapeutic agent, and polyethylene glycol (PEG), a biocompatible polymer widely used to improve solubility in biological systems, were conjugated to the fullerenols (Scheme 7). The resulting fullerenol-doxorubicin-PEG product was developed for potential application in targeted cancer chemotherapy [71]. However, the characterization of the conjugated fullerenol was limited to UV-Vis spectroscopy, and the degree of substitution was not reported in the study.

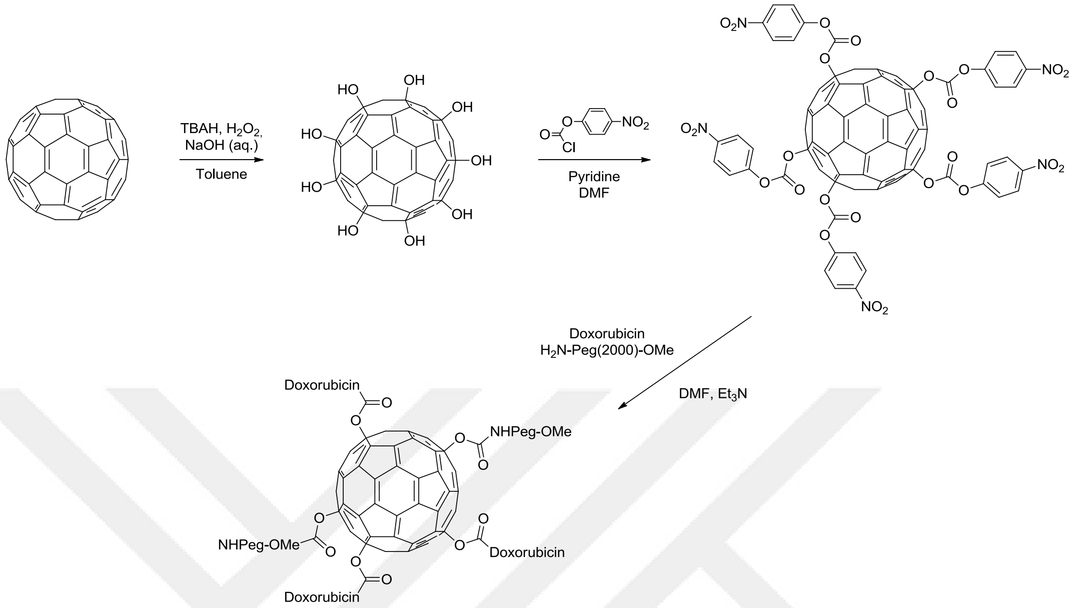

Scheme 7. Schematic representation of the synthetic route to bioconjugate fullerenol [71].

Another example, published in 2021, focused on the conjugation of doxorubicin and folic acid to fullerenol for studying its anticancer activity *in vitro* [72]. In this study, fullerenol was first functionalized with oxalohydrazide to provide active sites for the subsequent conjugation of doxorubicin and folic acid. The final product retained hydroxyl groups on the fullerene which is significant due to the essential role of hydroxyl groups in enhancing the solubility of the and enabling for further functionalization. (Scheme 8). In this publication, the synthesized product was characterized using ^{1}H NMR and IR spectroscopy and the average degree of substitution was reported.

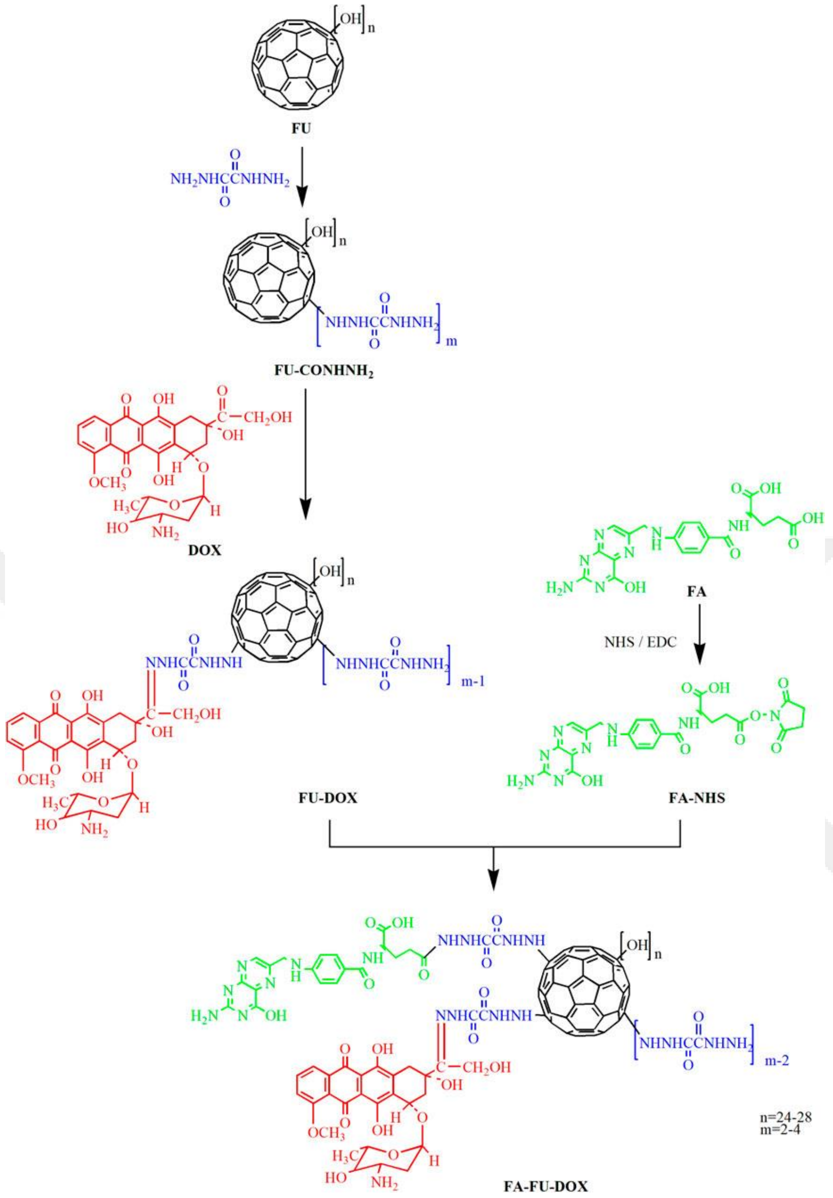

Scheme 8. Schematic representation of the synthetic route to **FA-FU-DOX** [72].

A study published in 2022 noted as the third example of fullerenol conjugation, here with gentamicin which is an aminoglycoside antibiotic, to investigate its cytotoxic and antibacterial properties [73]. In this work, fullerenol was initially activated with 3-(glycidyloxypropyl)trimethoxysilane (GLYMO), forming a structure with an epoxide group at the terminus, making it suitable for nucleophilic reaction. Gentamicin was subsequently conjugated to the activated fullerenol through a nucleophilic reaction with the epoxide, resulting in the formation of the desired conjugated product (Scheme 9). The product was characterized by XPS, TGA, and FTIR, which determined that, on average, 11 GLYMO groups were substituted onto each fullerenol molecule and 0.8 gentamicin molecules covalently bonded per GLYMO group.

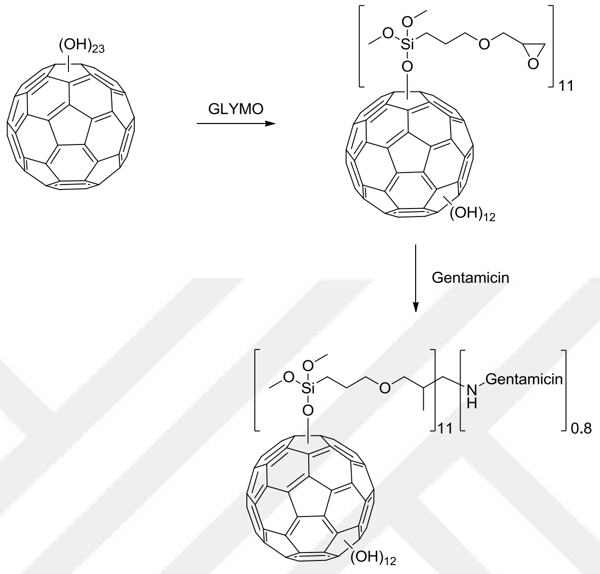

Scheme 9. Schematic representation of the synthetic route to fullerenol gentamicin [73].

1.2 Enzymes

In the simplest definition, enzymes are specialized biological catalysts that significantly accelerate the rates of chemical reactions within living organisms [74]. Even tough, humankind has used enzymes for thousands of years, such as in the fermentation of sugar into alcohol, the hidden mechanism was unknown until the field of enzymology emerged [75]. French scientists Anselme Payen and Jean-François Persoz identified the earliest known enzyme mixture, which was diastase in 1833 [76]. This enzyme also called alpha-amylase, breaks down complex carbohydrates like starch into smaller sugars [77].

Fermentation chemistry was first described by Louis Pasteur in 1858, who proposed that the fermentation process was driven by a "vital force" and took place within living yeast cells [78]. This view conflicted with Liebig's perspective, which argued that enzymes were chemical substances and did not require the concept of vitalism. Finally, Eduard Büchner demonstrated in 1897 that a non-living yeast extract could also produce the same fermentation reaction as living yeast, effectively disproving the concept of vitalism [79].

In 1926, in a revolutionary finding, James B. Sumner, John H. Northrop, and Wendell M. Stanley demonstrated that enzymes are proteins composed of amino acids by successfully crystallizing urease [80]. This groundbreaking work was awarded by the Nobel Prize in Chemistry in 1946.

Emil Fischer introduced the lock-and-key model to explain enzyme-substrate binding in 1894 [81], and the Michaelis–Menten method for studying enzyme kinetics was developed [82]. Over the years, significant progress has been made in enzymology, including the discovery of numerous enzymes and extensive studies to understand their structures, mechanisms, and properties. These ongoing studies have explored many fascinating details of enzymatic function, as shown in Figure 7 [83].

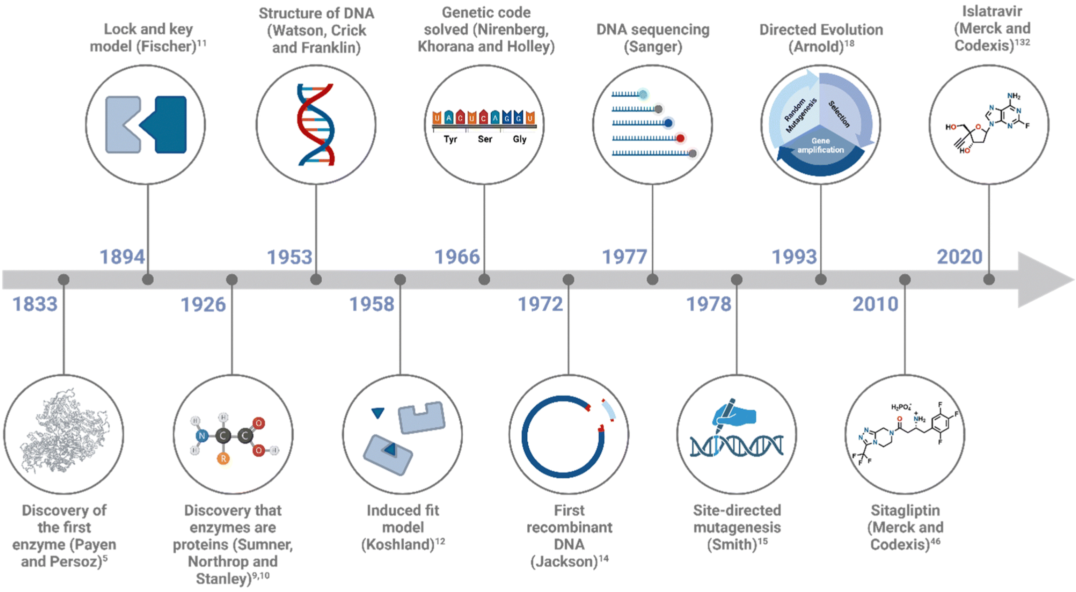

Figure 7. Key milestones in biocatalysis over time [83].

1.2.1 Enzyme Mimics

Enzymes have ability to catalyze chemical reactions with remarkable efficiency and selectivity, generally increasing the reaction rates by 10^{10} to 10^{15} times compared to uncatalyzed processes [84]. However, due to their low thermal stability, poor tolerance to experimental conditions, limited adaptability to non-biological reactions, narrow substrate versatility and the high costs of preparation and purification significantly limit their applications [85]. As a result, there is a strong interest in developing enzyme mimics, and known as artificial enzymes, that retain the desirable properties of natural enzymes.

Enzyme mimics are artificial systems designed to replicate the substrate-binding ability and catalytic efficiency of natural enzymes by simulating their active sites and reaction mechanisms. The studies of enzyme mimics were accelerated after the pioneering work of Ronald Breslow's in late 1960s and 1970s. In his 1969 study, Breslow utilized cyclodextrins which are molecules formed by glucose units and resemble a doughnut (Figure 8) to mimic enzyme binding sites by providing non-polar cavities that stabilized the transition states of reactions, such as ester hydrolysis [86]. Additionally, in 1970, Breslow demonstrated the catalytic activity of a nickel complex of pyrimidine-2,5-dicarboxylic acid for the hydrolysis of *p*-nitrophenyl acetate to mimic metalloenzymes [87].

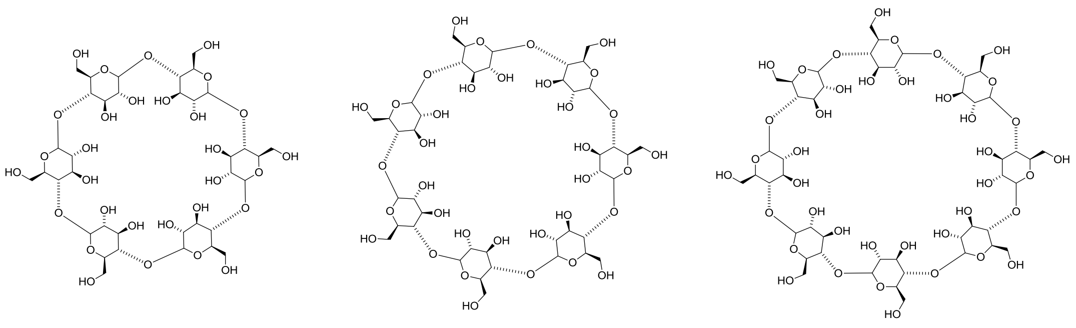

α-Cyclodextrin β-Cyclodextrin γ-Cyclodextrin

Figure 8. Structures of α-cyclodextrin, β-cyclodextrin and γ-cyclodextrin.

Following this groundbreaking study, numerous advancements have been made in the field of enzyme mimics. One of the most significant studies in this context was the development of nanozymes. In 2004, Scrimin *et al.* introduced the term “nanozyme” and demonstrated the use of triazacyclonane-functionalized gold nanoparticles as catalysts for transphosphorylation reactions [88]. In the study, a highly effective catalyst for phosphate ester cleavage was developed through the self-assembly of triazacyclonane functionalized thiols onto nanoscale gold particles. As a result of coordination with Zn^{2+} ions, these functionalized nanoparticles exhibited remarkable catalytic activity (Figure 9). Another notable example of nanozymes emerged in 2007 when Yan *et al.* made a groundbreaking discovery demonstrating the intrinsic peroxidase-like activity of Fe_3O_4 nanoparticles [89].

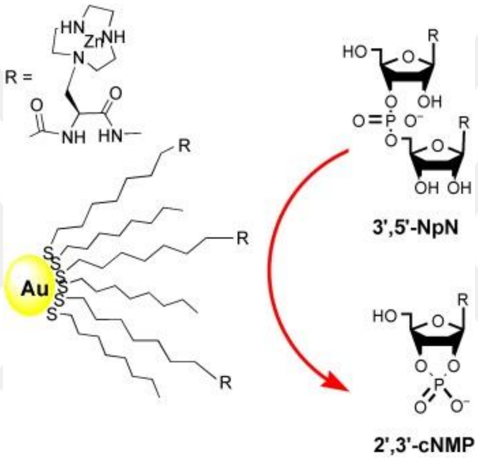

Figure 9. Triazacyclonane-thiol self-assembled gold nanoparticles as Zn(II)-mediated catalysts for phosphate ester cleavage [88].

Over the years, numerous systems have been developed and employed as enzyme mimics like polymeric materials [90], catalytic antibodies [91], and metal coordinated bio-macromolecules or cofactors [92].

1.2.1.1 Peptide Based Enzyme Mimics

The outstanding catalytic efficiency of enzymes can be attributed to their unique three-dimensional structures and the precise arrangement of essential amino acid residues. The requirement to maintain a stable, folded conformation likely explains their relatively large molecular size (>10,000 Da) [93]. Studies have suggested that the earliest protein enzymes might have been short peptides, with amyloid structures providing stable frameworks for their catalytic activity [94]. Considering the versatility of peptides, these findings have inspired the development of peptide-based enzyme mimics. To mimic trypsin and α-chymotrypsin, Atassi and Manshouri developed a 29-amino-acid cyclic peptide catalyst [95]. Even though the desired catalytic activity was not achieved in this study, it was indicated that insufficient conformational stability hindered the interaction between the catalytic center and the substrate, offering valuable insight for future research.

Peptides have been widely explored as enzyme mimics in numerous studies. However, the time-consuming nature of synthesis and the difficulties in arranging active amino acids into exact geometries and conformations have limited the scope of these studies. Peptides with specific amino acids, mostly histidine, aspartic acid, and serine (or cysteine), were synthesized with the aim of achieving self-assembly into precise conformations and mimicking the catalytic activity of the target enzyme [96]. However, it usually requires extensive screening to find the proper combination and sequence of the peptides containing the active site's amino acids. For instance, in 2014, Rufo et. al reported that using a heptapeptide having various histidine amino acid residues showed significant metalloprotease activity. To reach the conclusion, about fourteen peptides were screened and the only one with the Ac-IHIHIQI-NH_2 sequence (Figure 10) showed the significant activity with a k_{cat}/K_m value around 62 $M^{-1}s^{-1}$ [97].

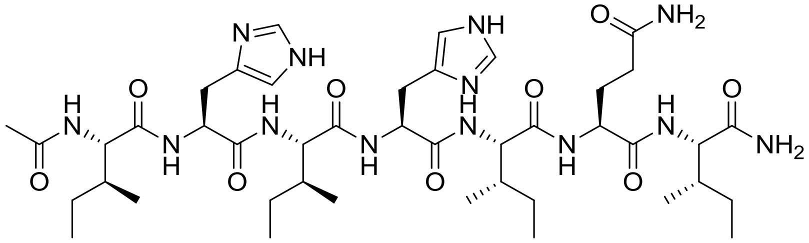

Ac-IHIHIQI-NH_2

Figure 10. Structure of Ac-IHIHIQI-NH_2 sequence [97].

In another study published in 2014, Zhang *et al.* reported three peptides, each composed of 14 amino acids, including glycine, histidine and arginine residues (Figure 11). These peptides demonstrated the ability to self-assemble through beta-sheet interactions facilitated by their N-terminal regions. This self-assembly process was reported to be critical for their catalytic activity, as it mimicked the active site geometry of natural hydrolase enzymes. Among the three peptides, two exhibited notable hydrolase activity, with k_{cat}/K_m values of 0.90 $M^{-1}s^{-1}$ and 0.150 $M^{-1}s^{-1}$, respectively, indicating the capability of self-assembled peptides to act as enzyme mimics [98].

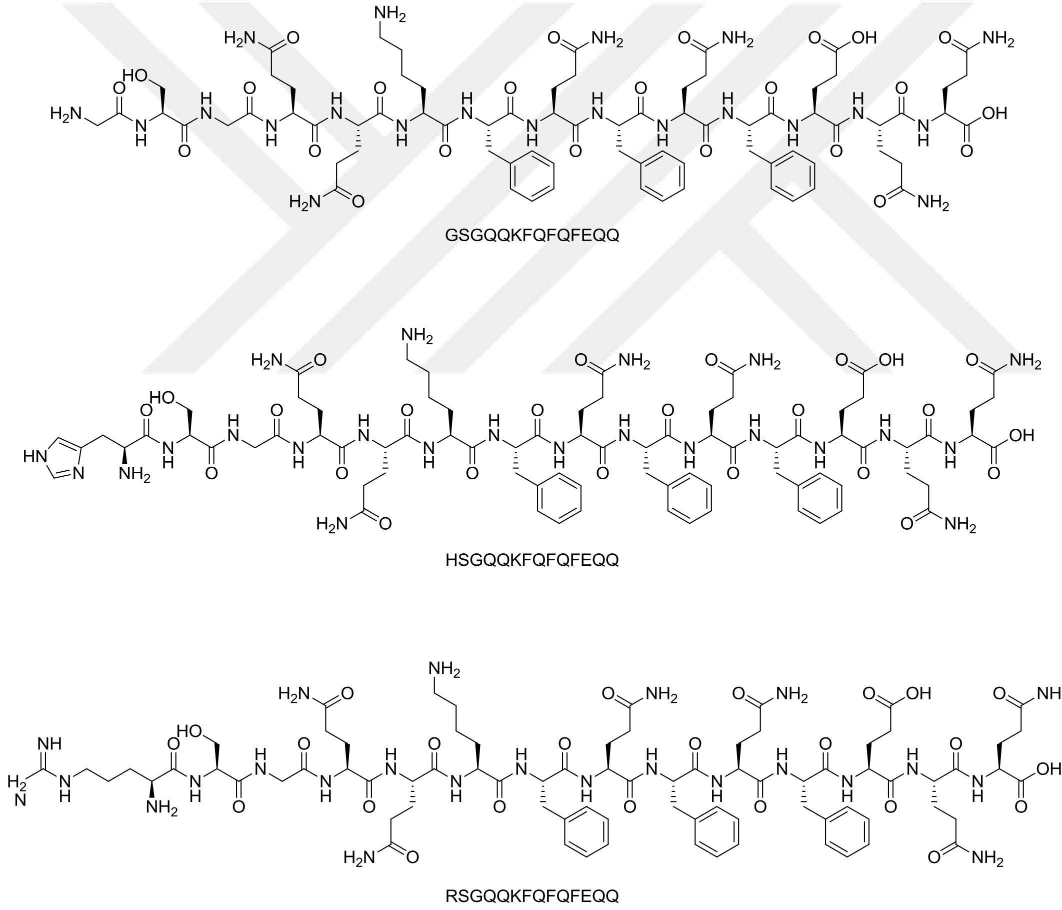

Figure 11. Structure of peptides in the study by Zhang *et al* [98].

Moreover, unnatural amino acids (UAAs) have been used to increase the catalytic activities of enzyme mimics. For example, *p*-nitro-L-phenylalanine (*p*NO_2Phe), an unnatural amino acid, was used in a study by Jackson *et al*. by substituting a tyrosine residue in the active site of an enzyme. This substitution significantly enhanced the enzyme's activity, showing the potential of genetically encoded UAAs to improve enzyme function [99]. However, it is more challenging to synthesize artificial amino acids for the residues of peptides. The reason of the difficulty often arises from the need for stereospecificity, low yields in chemical synthesis, and the requirement for specialized reagents or equipment.

1.2.1.2 Fullerenzyme

In 2021, Özçubukçu *et al.* introduced a novel catalyst design that brought fullerenes into the field of biocatalysis [100]. These catalysts, referred to as fullerene nanocatalysts and “fullerenzymes”, emulate enzymatic active sites through multifunctional self-assembled nanostructures. To illustrate this concept, they demonstrated the remarkable catalytic activity of these nanostructures by mimicking the reactivity of hydrolases, incorporating the essential functional components of the parent enzyme.

In this study, fullerenols conjugated with specific amino acids, such as glycine (F-Gly), serine (F-Ser), and histidine (F-His), as well as ethanolamine (F-EA) and histamine (F-EA), which do not contain a carboxylic acid functional group, were synthesized Additionally, fullerene conjugates functionalized with two different amino acids simultaneously were also prepared. Subsequently, the hydrolase mimicking properties of these conjugates, as well as those of various conjugate mixtures, were investigated. This pioneering work opened a new direction for fullerene research by merging structural design with biological function. An overview of these catalytic systems and their structural compositions is presented in Table 1.

Table 1. Enzymatic activity of fullerene-based nanocatalysts at pH 7.4 [100].

Entry	**Group**	**k_{cat} (s^{-1} x 10^{-2})**	**K_M (mM)**	**k_{cat}/K_M (M^{-1} s^{-1})**
1	F-His	1.77 ± 0.18	0.12 ± 0.13	147.5 ± 13.8
2	F-HA	1.47 ± 0.25	0.15 ± 0.23	98.0 ± 10.8
3	F-Gly	1.03 ± 0.17	0.31 ± 0.31	33.2 ± 5.5
4	F-Ser	0.18 ± 0.04	NA	NA
5	F-EA	0.31 ± 0.06	NA	NA
6	F-HS	4.71 ± 0.26	0.22 ± 0.09	214.1 ± 29.6
7	F-HAS	2.54 ± 0.22	0.10 ± 0.11	254.0 ± 20.5
8	Fullerenol	0.008	NA	NA
9	F-His/F-Ser	3.78 ± 0.37	1.36 ± 0.32	27.8 ± 11.5
10	F-His-F-EA	3.04 ± 0.24	0.81 ± 0.22	37.5 ± 11.9
11	FHA/F-Ser	1.99 ± 0.67	1.55 ± 1.12	12.8 ± 5.6
12	F-HA/F-EA	0.92 ± 0.22	0.35 ± 0.43	26.3 ± 5.2
13	F-His/F-EA/F-Gly	5.45 ± 0.57	1.04 ± 0.33	52.4 ± 1.79
14	F-His/F-Ser/F-Gly	3.39 ± 0.44	0.61 ± 0.29	55.6 ± 1.52
15	F-HA/F-EA/F-Gly	2.68 ± 0.19	0.26 ± 0.11	103.1 ± 16.6
16	F-HA/F-Ser/F-Gly	2.34 ± 0.33	0.55 ± 0.29	42.5 ± 11.5

The proposed catalytic mechanisms of F-Gly and F-HA are shown in Scheme 10. As a result, the combination of three fullerene nanocatalysts, each individually presenting histidine, ethanolamine, and glycine moieties, exhibited the highest catalytic activity among the designed catalysts.

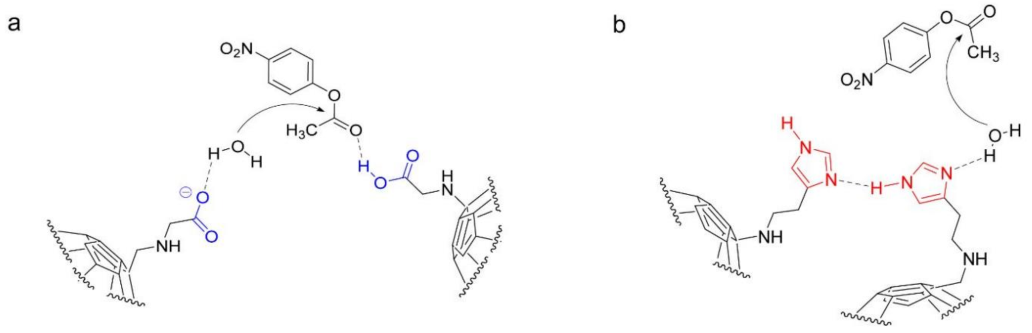

Scheme 10. Proposed catalytic mechanisms of a. F-Gly and b. F-HA [100].

In another study published in 2022, Gülseren *et al.* designed new fullerene-based nanostructures that mimic phosphatase activity without requiring metal cofactors [101]. Histidine and serine were chosen for fullerene functionalization due to their presence in the active sites of numerous enzymes and their frequent use as catalytic residues in artificial enzyme studies. These nanostructures undergo spontaneous self-assembly into nanoclusters, generating numerous randomly distributed active sites. Their catalytic activity in cleaving both phosphomonoesters and phosphodiesters was investigated, revealing that the monoesterase activity of these enzyme mimics was six orders of magnitude higher than their diesterase-like activity (Table 2).

Table 2. Quantitative analysis of enzyme mimic kinetics [101].

	***p*NPP**			**bis-*p*NPP**		
	k_{cat} (min^{-1} x 10^{-2})	**K_M (mM)**	**k_{cat}/K_M (M^{-1} s^{-1})**	**k_{cat} (min^{-1} x 10^{-2})**	**K_M (mM)**	**k_{cat}/K_M (M^{-1} s^{-1})**
F-His/F-Ser	7.13 ± 0.32	0.13 ± 0.05	9.27 ± 1.16	13.52 ± 0.78	1.45 ± 0.21	1.57 ± 0.63
F-His	6.28 ± 0.47	0.21 ± 0.05	5.05 ± 0.82	13.64 ± 0.97	2.16 ± 0.34	1.04 ± 0.47
F-Ser	2.27 ± 0.59	0.43 ± 0.46	0.89 ± 0.21	2.75 ± 0.75	0.51 ± 0.54	0.89 ± 0.23

In addition to their enzyme-mimicking properties, the mineralization capacity of both the F-His/F-Ser mixture and the individual components (F-His and F-Ser) was investigated. These nanocatalysts replicated the biological roles of their natural counterparts by promoting biomineralization and inducing osteogenesis in preosteoblast and mesenchymal stem cells *in vitro*. Among them, the F-His/F-Ser mixture exhibited the highest mineralization capacity, followed by F-His.

Consequently, it was shown that amino acid conjugated fullerene derivatives can serve a much wider range of enzymatic functions, making them valuable both for advancing next-generation catalyst design and for exploring the influence of specific chemical groups on enzymatic activity in fundamental research.

1.3 Lactic Acid Racemase

Lactic acid, also known as 2-hydroxypropionic acid, plays a crucial role in the energy metabolism of many microorganisms. It was first identified in 1780 by Swedish-German pharmaceutical chemist Carl Wilhelm Scheele with isolating from sour milk in the form of an impure, brownish syrup [102]. It is the simplest hydroxycarboxylic acid containing an asymmetrical carbon atom (Figure 12).

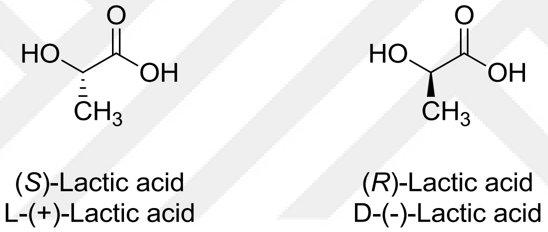

Figure 12. Structure of lactic acid.

Lactic acid is widely used in biotechnology, particularly in the food, pharmaceutical, and polymer industries. In food, it acts as a preservative, pH regulator, and flavoring agent [103]. In pharmaceuticals, it is utilized in dermatological drugs and osteoporosis treatments [104]. Additionally, it serves as a key monomer in polylactic acid (PLA), a biodegradable polymer used in medical implants [105].

Although some organisms can metabolize both enantiomers of this α-hydroxy acid (i.e., L- and D-lactic acid), others require a specific enzyme, known as lactic acid racemase (Lar), to interconvert the two isomers [106]. To date, only two α-hydroxy acid racemases have been identified, with Lar being the second member. Unlike many racemases that require pyridoxal phosphate (PLP) or metal ions, Lar operates through a cofactor-independent mechanism [107]. Its role is essential for microbial metabolic flexibility, enabling the interconversion of L- and D-enantiomers, which are crucial for energy metabolism, stress adaptation, and cell wall biosynthesis [108]. Understanding its catalytic mechanism and structural properties is key to elucidating its biochemical function and potential biotechnological applications.

The D-lactate formation pathway in certain bacteria, such as *Lactobacillus plantarum*, was identified and reported many years ago [109], but the exact mechanism of Lar was unclear due to its high tendency to oxidation [110]. In 2014, Desguin *et al.* successfully synthesized Lar in *Lactobacillus plantarum* and identified nine proteins involved in its biosynthesis, designated as LarA, B, C, D, E, (MN), O, Q, and R [111]. Among these, the active racemase LarA was crystallized, providing structural insights into its function as indicated in Figure 13. Further analysis revealed that LarA is a nickel-dependent enzyme that requires binding with a nickel-pincer nucleotide (NPN) cofactor to exhibit catalytic activity.

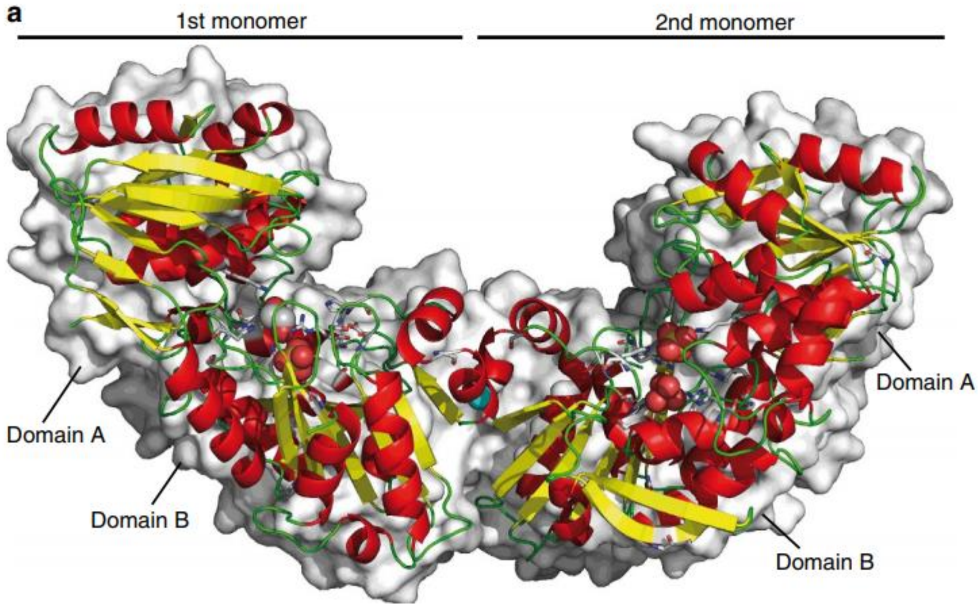

Figure 13. 3D structure of LarA [111].

As shown in Scheme 11, the biosynthesis of this cofactor is sequentially carried out by three proteins: LarB, LarE, and LarC. The process begins with nicotinic acid adenine dinucleotide (NaAD), which undergoes LarB-catalyzed carboxylation, introducing a carboxyl group at the pyridinium ring (P2CMN) while releasing AMP. This reaction produces a biscarboxylic acid intermediate, which then undergoes LarE-dependent sulfur insertion. Acting as a sacrificial sulfur insertase, LarE donates sulfur atoms from its own Cys176 residue, leading to its conversion into dehydroalanine and subsequent inactivation. The sulfur inserted intermediate subsequently binds Ni^{2+}, a process facilitated by LarC, forming the mature nickel-pincer cofactor. With its structure finalized, this unique organometallic cofactor is incorporated into LarA, where it provides the active catalytic center for lactic acid racemization. This biosynthetic pathway is distinct from conventional enzyme maturation processes, as it relies on self-sacrificial sulfur insertion to establish the functional cofactor [112].

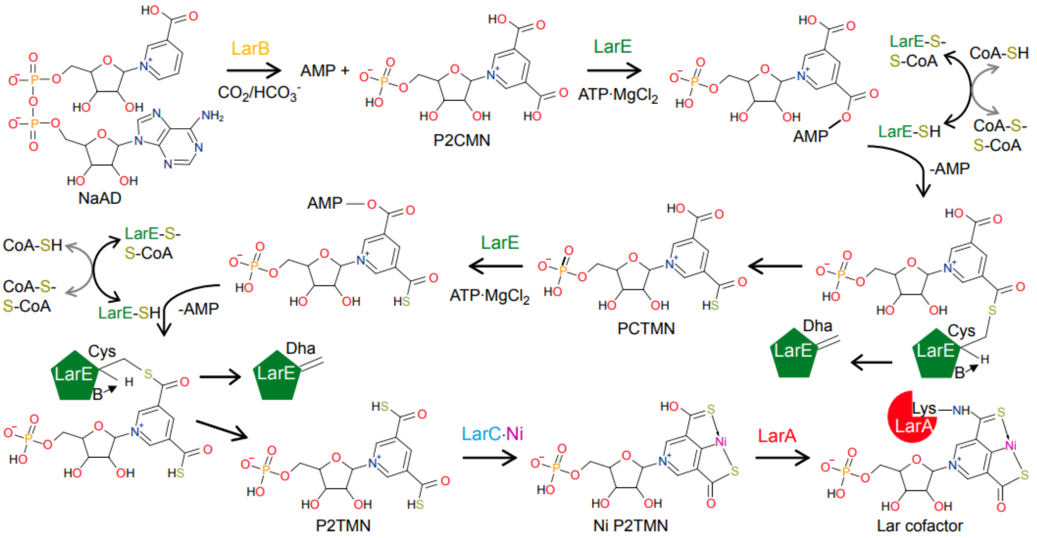

Scheme 11. Enzymatic biosynthesis of LarA cofactor [112].

In 2015, Hausinger and Hu identified the mechanism of lactic acid racemization in LarA, demonstrating that the process is catalyzed by a nickel-pincer cofactor, which enables the interconversion between D- and L-lactate [113]. The nickel center plays a crucial role in stabilizing the reaction intermediate, facilitating the proton transfer required for enantiomeric conversion. This process leads to stereochemical inversion and occurs efficiently without the need for additional cofactors, highlighting LarA's role as a specialized racemase (Scheme 12).

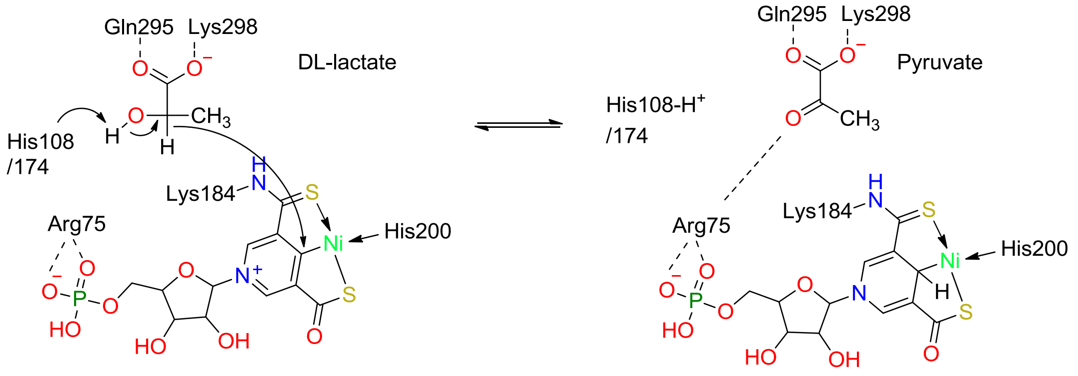

Scheme 12. Proposed catalytic mechanism of LarA [113].

1.3.1 LarE

In 2017, Fellner *et al.* reported that the biosynthesis of the nickel-pincer cofactor involves a sulfurization step catalyzed by LarE, the only known ATP-dependent sacrificial sulfur insertase [114]. During this process, LarE donates its sole cysteine residue, converting it into dehydroalanine, which permanently inactivates the enzyme. Thus, rather than functioning as a true enzyme, LarE acts as a reactant in the synthesis, making its mechanism fundamentally distinct from other known enzymatic processes. Understanding and fully characterizing this unusual self-sacrificial mechanism is crucial for the broader field of biochemistry, as enzymatic cysteine desulfurization is a rare process. Gaining insight into how LarE catalyzes this reaction would introduce a new model for biochemical transformations.

The crystal structure of LarE, resolved by Fellner in 2017, provided critical insights into its unique function and quaternary structure. Structural analysis revealed that LarE assembles into a hexameric complex, with each subunit contributing to the overall stability and catalytic function of the enzyme. Figure 14 illustrates this hexameric arrangement, highlighting the organization of active sites within the complex.

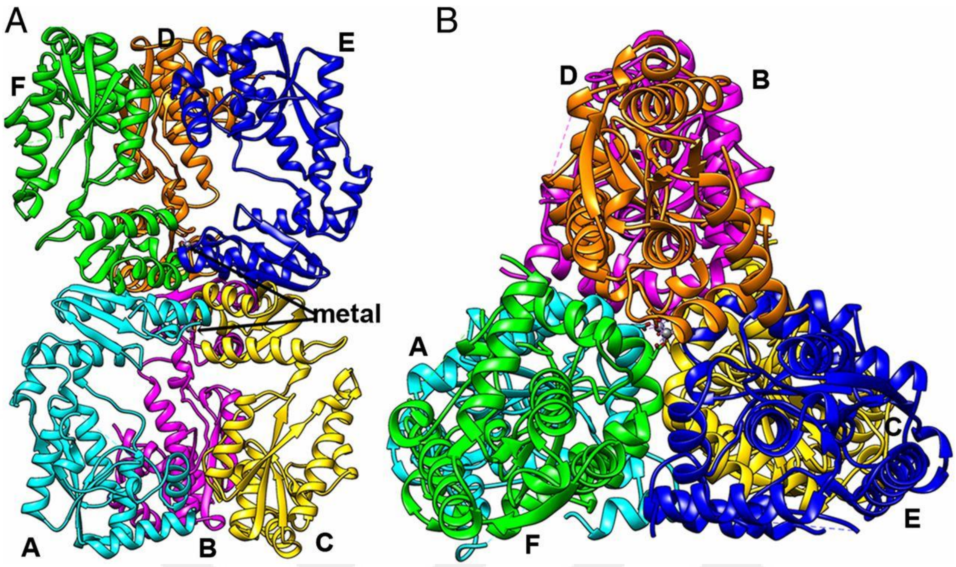

Figure 14. Quaternary structure and metal binding of LarE [114].

Before this study, no theoretical work had been reported on the system. Figure 15 illustrates the active site of LarE, which was co-crystallized with adenosine monophosphate (AMP). During catalysis, the natural substrate (P2CMN) binds to LarE, undergoes reaction, and releases PPi as a leaving group, forming a new substrate. The Cys176 residue of LarE attaches to the phosphoester moiety of the substrate, effectively becoming a new substrate itself. Arg181 and Glu200 function as base catalysts, abstracting the α-hydrogen of Cys176, which is already covalently bound to the substrate.

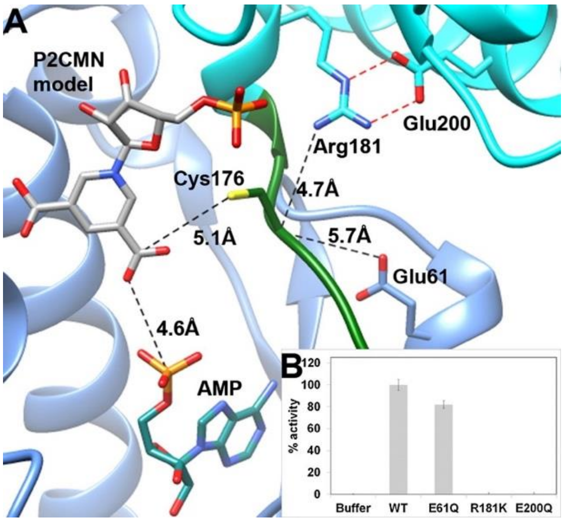

Figure 15. Structural model of P2CMN-bound LarE [11].

Following deprotonation, LarE undergoes irreversible conversion into dehydroalanine, rendering it inactive. This reaction occurs sequentially on both carboxylate groups of nicotinic acid, ultimately generating an intermediate essential for cofactor biosynthesis in lactic acid racemization. The proposed mechanism is depicted in Scheme 13.

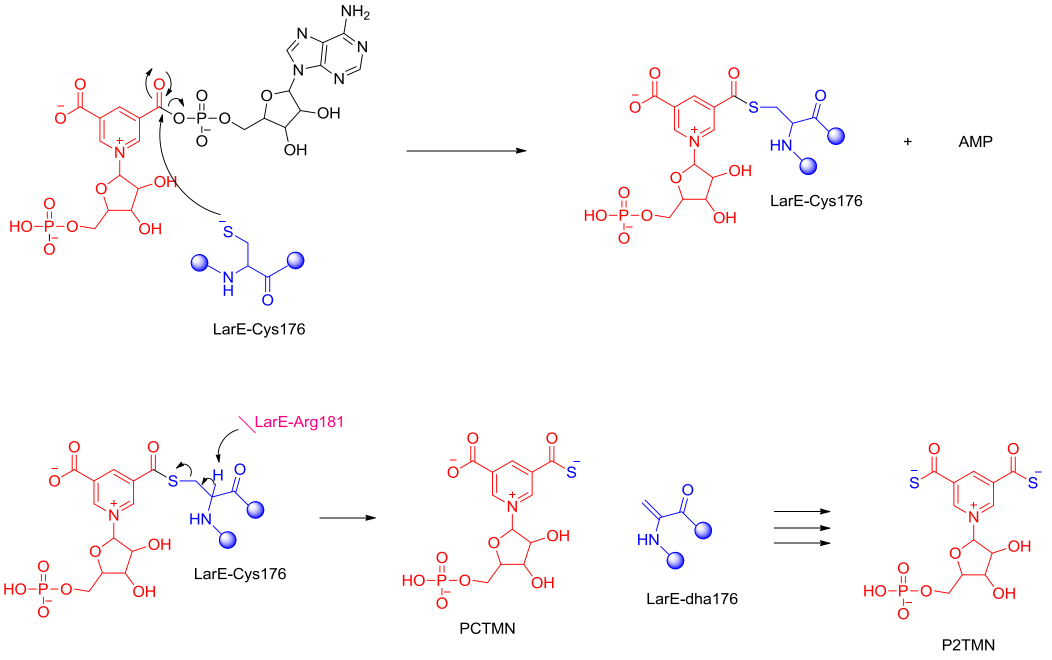

Scheme 13. Proposed mechanism of formation of dehydroalanine [114].

1.4 Alzheimer’s Disease

Alzheimer’s disease (AD) is the most frequently diagnosed neurodegenerative disorder, affecting millions worldwide [115]. It leads to progressive cognitive decline, memory loss, and the deterioration of essential neurological functions [116]. Despite extensive research, its exact causes remain unclear, with multiple pathological mechanisms contributing to its development [117]. These include; β-amyloid plaque accumulation, Tau protein hyperphosphorylation, oxidative stress and neuroinflammation, cholinergic dysfunction and acetylcholine depletion [118]. Among these, the loss of cholinergic neurons and the resulting decline in acetylcholine (ACh) levels are closely associated with cognitive impairment in AD patients [119]. Since ACh plays a fundamental role in memory and learning, its depletion is considered one of the key factors behind the cognitive decline observed in AD [120]. ACh consists of a quaternary ammonium group and an ester linkage, which are essential for its biological activity (Figure 16).

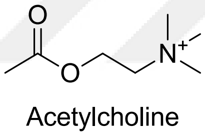

Figure 16. Structure of acetylcholine.

As a result, the ability to accurately detect ACh levels is critical for both understanding disease progression and developing potential diagnostic tools.

1.4.1 Acetylcholine Detection

Several analytical techniques have been developed for acetylcholine (ACh) detection, including high-performance liquid chromatography (HPLC), electrochemical biosensors, and spectrophotometric assays. Among these, electrochemical sensors have gained significant attention due to their low cost, fast response time, and operational simplicity in field applications [121]. Electrochemical sensing technology works by detecting specific physical, chemical, or biological interactions and converting them into readable signals, making it a highly sensitive approach for neurotransmitter quantification.

Most electrochemical ACh sensors depend on enzymatic processes, particularly acetylcholinesterase (AChE)-based biosensors. While these systems provide high specificity, their practical application is limited by critical drawbacks, including enzyme instability, selectivity issues, and high cost [122]. Due to these limitations, the demand for non-enzymatic sensing technologies has been growing. In recent years, several alternative nanomaterials have been investigated as catalysts for electrochemical ACh detection, eliminating the reliance on enzymatic processes. Notably, various transition metal-based nanomaterials, including NiO nanostructures, Fe_2O_3 nanoparticles, MnO_2 functionalized metal-organic frameworks and $CuCo_2O_4$ nanostructures have demonstrated potential in non-enzymatic ACh sensing [123,124,125]. These materials exhibit catalytic properties that facilitate the electrochemical oxidation of ACh at electrode surfaces, improving detection sensitivity while maintaining stability.

Additionally, Menamparambath *et al.* reported a copper cobaltite/MWCNT composite-based non-enzymatic sensor with an impressive limit of detection (LOD) of 0.8 nM [126]. Another study utilized NiAl layered double hydroxides with a flower-like morphology, decorated with carbon dots, demonstrating strong long-term stability and selectivity for ACh detection [127].

1.5 Fullerenol Applications as Organocatalysts

Organocatalysis has gained significant attention in recent years as a sustainable and metal-free alternative in catalytic reactions. Despite their potential, the use of fullerenol as an organocatalyst remains relatively unexplored in the literature, making it an intriguing alternative to conventional catalysts. There is only one report about the application of fullerenol as hydrogen bond donor catalysis in CO_2 fixation.

1.5.1 CO_2 Fixation

Currently, the increase in atmospheric CO_2 concentration is widely recognized as one of the primary factors for global warming [128]. Consequently, the utilization of CO_2 as a recyclable and environmentally sustainable C_1 source has captured significant attention in the scientific community [129,130,131]. This process, known as CO_2 fixation, involves the transformation of inorganic CO_2 into organic compounds by living organisms or chemical methods. This approach not only aims to reduce greenhouse gas emissions but also promotes the development of green chemistry solutions [132]. One of the best promising methods for this process is the synthesis of cyclic carbonate derivatives through the reaction of CO_2 with epoxide derivatives (Scheme 14).

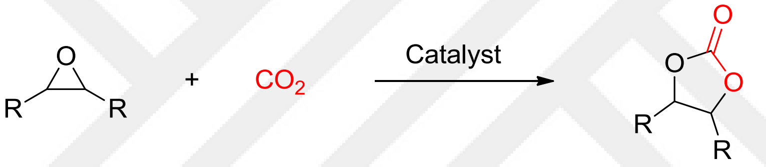

Scheme 14. Cyclic carbonate synthesis with CO_2 fixation.

In addition to the synthesis of organic hydrocarbon products from inorganic CO_2, this process offers another significant advantage of producing cyclic carbonates as a source of economically valuable and industrially relevant chemicals. These chemicals are extensively used as electrolytes in energy storage systems, especially lithium-ion batteries, an innovation that earned the 2019 Nobel Prize in Chemistry [133], as well as in aprotic polar solvents for various chemical processes [134]. Additionally, they act as significant precursors for the synthesis of polycarbonate derivatives and other advanced chemical materials [135]. Industrial processes generally involve 1,2-diols and phosgene as the carbon source (C1) for the synthesis of cyclic carbonates [136]. Nevertheless, the high toxicity of phosgene and the generation of byproducts such as hydrochloric acid and waste solvents result in crucial environmental concerns [137]. Consequently, the direct conversion of epoxides and CO_2 under mild conditions has gained attention as a sustainable and environmentally friendly approach.

1.5.1.1 Catalysts for CO_2 Fixation

CO_2 is known for its significant thermodynamic and kinetic stability, which poses challenges for its activation [138]. Nevertheless, the electron-deficient nature of the carbonyl carbons in CO_2 provides a strong affinity for nucleophiles and electron-donating reagents. Additionally, CO_2 can be regarded as an "anhydrous carbonic acid" that reacts readily with basic compounds [139]. For instance, organometallic compounds like Grignard reagents can easily undergo reactions with CO_2, even under low-temperature conditions [140]. Nevertheless, the cycloaddition of CO_2 to epoxides requires an efficient catalyst. The primary difficulty in proposing an effective catalytic system for the cycloaddition of CO_2 to epoxides under mild conditions involves designing multifunctional catalysts [141]. These catalysts should simultaneously contain active sites that can activate the epoxide and nucleophilic groups capable of either opening the ring of the activated epoxide or interacting with CO_2 to initiate the catalytic cycle (Scheme 15).

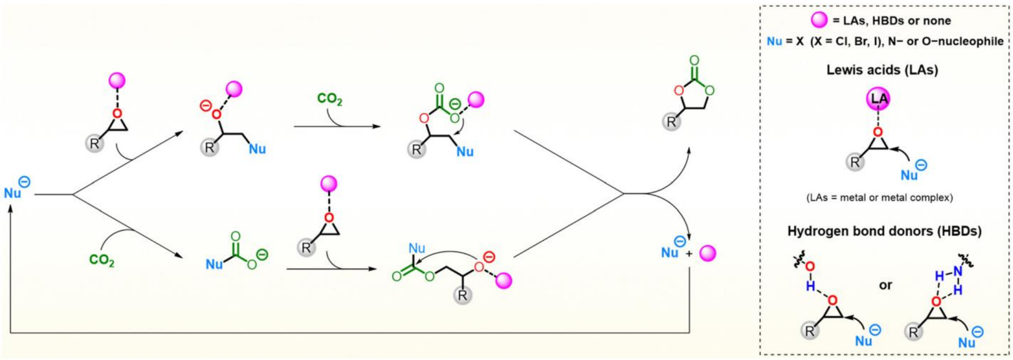

Scheme 15. General mechanistic pathways of the cycloaddition of CO_2 to epoxides [141].

In recent decades, numerous catalysts have been developed and reported, including metal complex systems with using halide sources as co-catalysts. Metal complexes incorporating elements such as Al [142], Co [143], Fe [144], Zn [145], and Ni [146], which have shown strong catalytic performance under mild conditions (Figure 17). Although the synthesis of these complexes is both expensive and experimentally challenging.

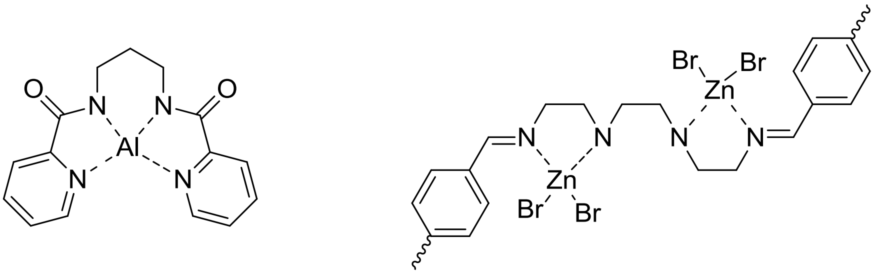

Al-PPPA **Te-TETA-Zn**

Figure 17. Metal complex catalysts for CO_2 fixation [142, 145].

To overcome these limitations, halogen-free catalytic systems have been explored. Amine- and carboxylate-based catalysts have emerged as promising alternatives, facilitating epoxide activation and subsequent carbonate formation. One example is in a study published by Shi *et al.*, where phenol and an organic base, such as DMAP, were utilized as co-catalysts under elevated temperature and pressure conditions, achieving a cyclic carbonate yield of approximately 91% [147] (Scheme 16).

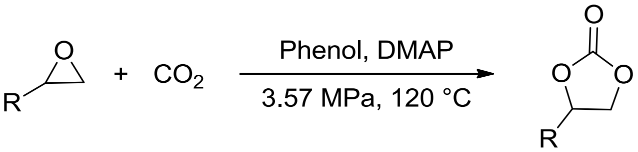

Scheme 16. Cyclic carbonate synthesis using phenol and DMAP [147].

Another notable example of halogen-free catalysis in the literature is provided by the study published by Yue *et al* [148]. In this work, ionic liquids containing carboxylate anions and quaternary ammonium cations were used as the catalytic system (Figure 18). In the study, it was pointed out that, more than 90% conversion was achieved at a reaction temperature of 100 °C and a pressure of 0.5 MPa.

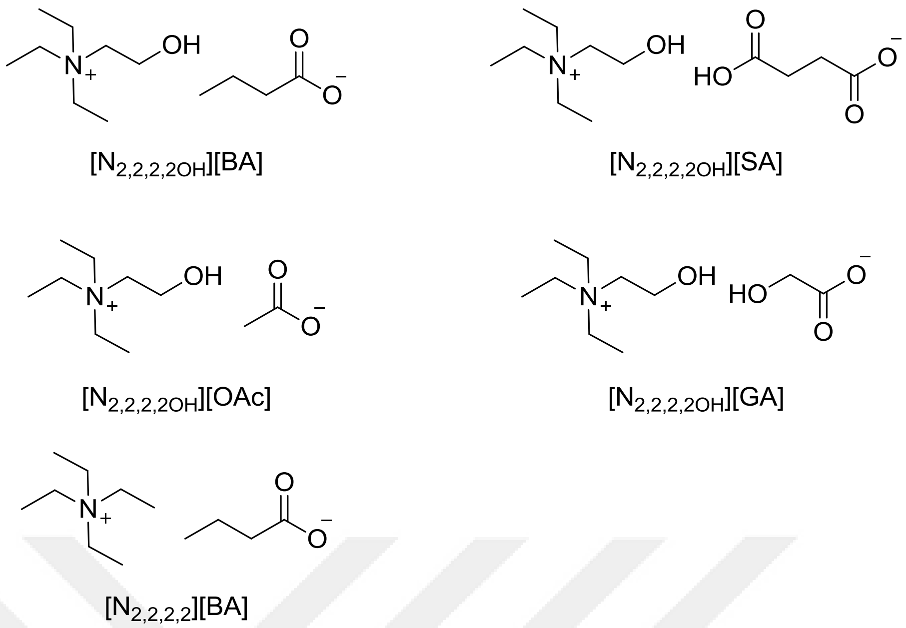

Figure 18. Ionic liquids catalysts for CO_2 fixation [148].

The literature contains a wide variety of catalysts with properties and functionalities similar to those described. However, two specific examples hold particular significance, as they have provided key inspiration and a starting point for the development in this part of the thesis. One of them is the study published by Zhang *et al.* in 2014 [149]. The catalytic potential of several amino acids as co-catalysts was systematically investigated in combination with an alkali metal salt, potassium iodide (KI), in the study. The research aimed to understand the specific effects and contributions of these amino acids to the catalytic process. Glycine, aspartic acid, threonine, histidine and tryptophan were selected, and the most potent catalytic effect was achieved with tryptophan (Scheme 17). The reactions were carried out at 120 °C and 2 MPa, and under tryptophan catalysis, various epoxide derivatives demonstrated approximately 90% conversion, particularly over extended reaction times.

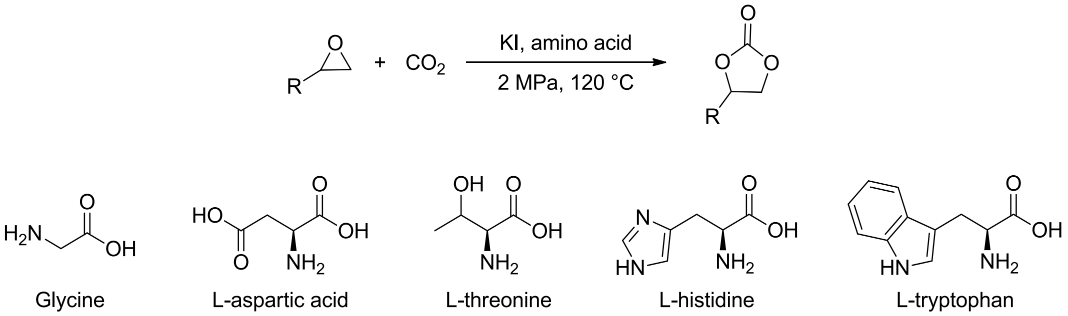

Scheme 17. Amino acid catalyzed cyclic carbonate synthesis [149].

The second study is another article published in 2014, this time by Song *et al* [150]. In the study, C_{60} fullerenol was selected as the catalyst and KI was used as the co-catalyst for the cycloaddition reaction and the reaction conditions are at 120 °C and 2 MPa (Scheme 18). The proposed mechanism is shown in Scheme 18. Under these conditions, the combination of KI and fullerenol as catalysts achieved a 95% conversion when propylene oxide was used as the starting material. However, the conversion dropped significantly to 3.2% when KI was used as the sole catalyst and further decreased to 0.3% when fullerenol was used independently. Moreover, when the pressure was reduced to 0.5 MPa, the conversion was observed to decline to 56%.

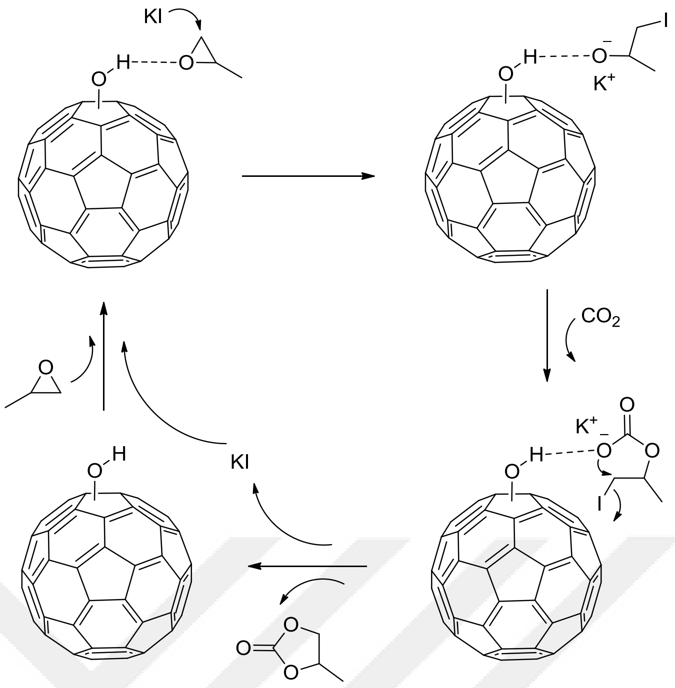

Scheme 18. Proposed mechanism of fullerenol catalyzed cyclic carbonate synthesis [150].

While numerous catalysts have been developed and reported in the literature, their ability to achieve high conversion rates was generally observed under demanding conditions, such as elevated pressures and high temperatures. There are only a limited number of examples that operate effectively at relatively low temperatures and atmospheric pressure. One of them is the study by Mattson in 2014, reactions were utilized using a balloon of CO_2 at 1 bar and silanediol as catalyst [151] (Scheme 19).

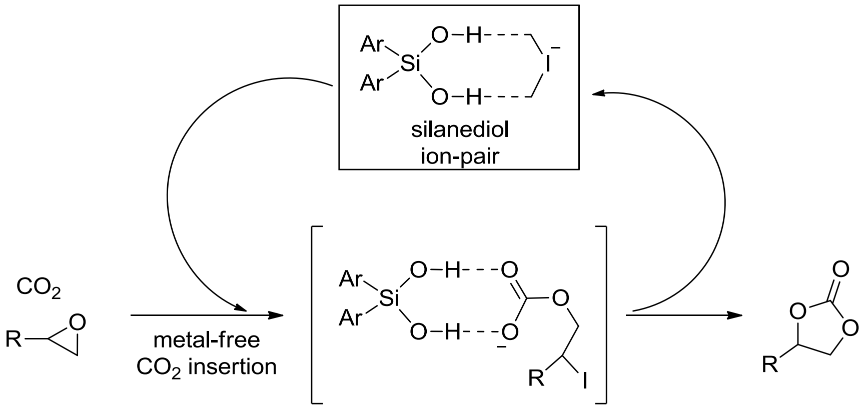

Scheme 19. Proposed mechanism of silanediol catalyzed CO_2 fixation [151].

1.6 The Morita-Baylis-Hillman (MBH) Reaction

The Morita-Baylis-Hillman (MBH) reaction is a multifunctional organic reaction involving the condensation of an α,β-unsaturated alkene with an aldehyde under catalytic conditions. This reaction typically employs nucleophilic catalysts such as tertiary amines or phosphines, which facilitate the formation of highly functionalized molecules (Scheme 20). First introduced to the literature in 1968 by Morita using phosphine as catalysts [152], the reaction was independently introduced by Baylis and Hillman in 1972 [153], who described an alternative pathway utilizing tertiary amine catalysts.

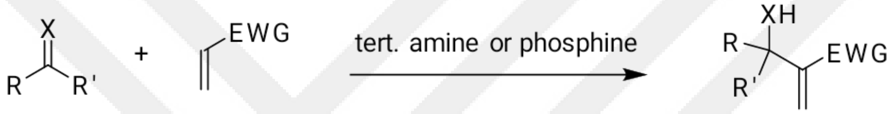

R = aryl, alkyl, heteroaryl, etc. R' = H, CO_2R^*. alkyl, etc.
X = O, NCO_2R^*, NSO_2Ar, etc
EWG = COR^*, CHO, CN, CO_2R^*, $PO(OEt)_2$, SO_2Ph, SO_3Ph, SOPh, etc.

Scheme 20. General synthetic route of the MBH reaction.

The key mechanistic step in the MBH reaction involves a nucleophilic attack at the β-position of the α,β-unsaturated alkene via a Michael addition, leading to the formation of an enolate intermediate. This enolate subsequently undergoes an aldol addition with the aldehyde substrate. Finally, a proton transfer occurs, resulting in the formation of a double bond between the α- and β-carbons, accompanied by the elimination of the nucleophile initially bound to the β-position (Scheme 21).

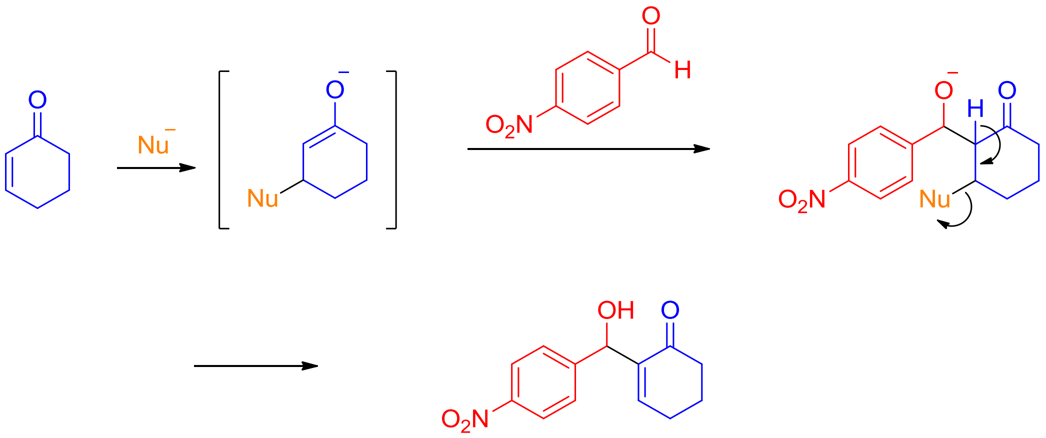

Scheme 21. Proposed mechanism of MBH reaction.

1.6.1 MBH catalysts

Although the MBH reaction features atom economy and the ability to generate multiple functional groups, it remained ignored until Drewes and Emslie referenced the Baylis-Hillman reaction in their 1982 article on total synthesis of integerrinecic acid [154]. The products generated from the MBH reaction have been widely utilized in synthetic organic chemistry. Their unique structural features and multifunctional nature make them invaluable substrates for the construction of complex natural products [155 ,156, 157], biologically active heterocycles [158, 159], and pharmaceutically relevant compounds [160, 161, 162].

Tertiary amines are extensively employed as catalysts in the MBH reaction because of their capacity for nucleophilic activation of the α,β-unsaturated compounds [163]. Among them, DABCO [164] is the most widely used due to its efficiency in catalyzing the reaction (Scheme 22). Still, other tertiary amines, including 1,8-diazabicyclo[5.4.0]undec-7-ene (DBU) [165], imidazole [166], triethylamine (Et_3 N) [167], hexamethylenetetramine (HMT) [168], and 4-dimethylaminopyridine (DMAP) [169], have also been successfully applied as catalysts.

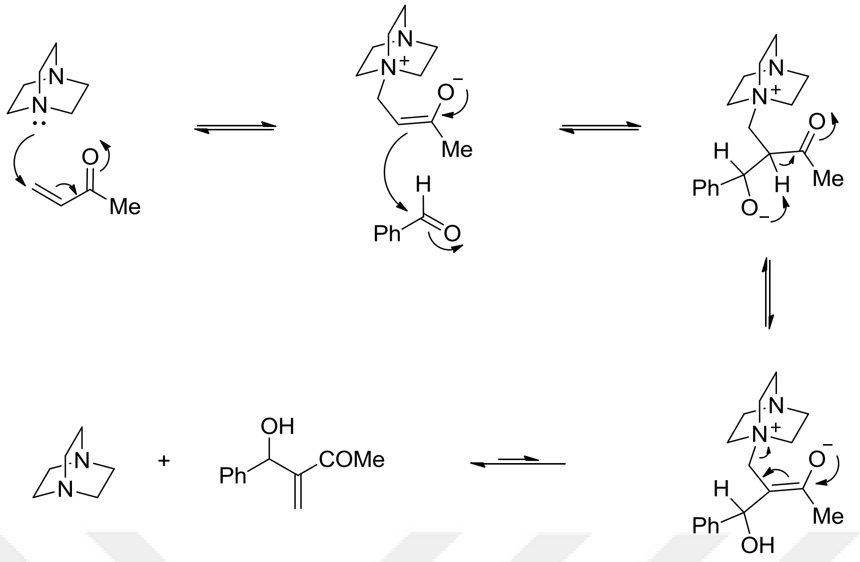

Scheme 22. Proposed mechanism of DABCO catalyzed MBH reaction [164].

Furthermore, the reaction rate of MBH reaction was significantly enhanced while Lewis acids and tertiary amines were utilized together as co-catalysts [170]. In a study that reported by Caputo *et al.* in 2000, the single use of titanium tetrachloride ($TiCl_4$) as a catalyst, without the addition of a base, and employing DCM as the solvent, enabled the synthesis of several MBH products with yields exceeding 50% [171]. In a 2009 publication by Sunoj and Patel [172], a comprehensive study was carried out to investigate the product distribution in the $TiCl_4$ -promoted MBH reaction under different reaction conditions (Scheme 23).

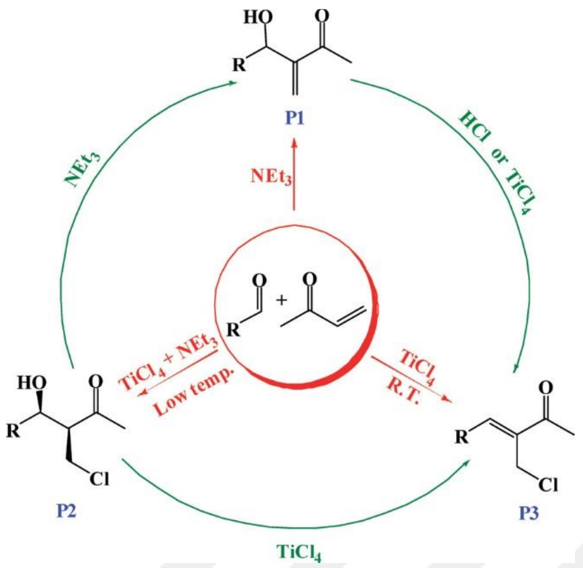

Scheme 23. Synthetic route of $TiCl_4$ -promoted MBH reaction [172].

Additionally, the detailed reaction mechanism involving $TiCl_4$ was investigated by highlighting the role of $TiCl_4$ as a Lewis acid catalyst and characterizing all the intermediates by using density functional theory (DFT) methods (Scheme 24).

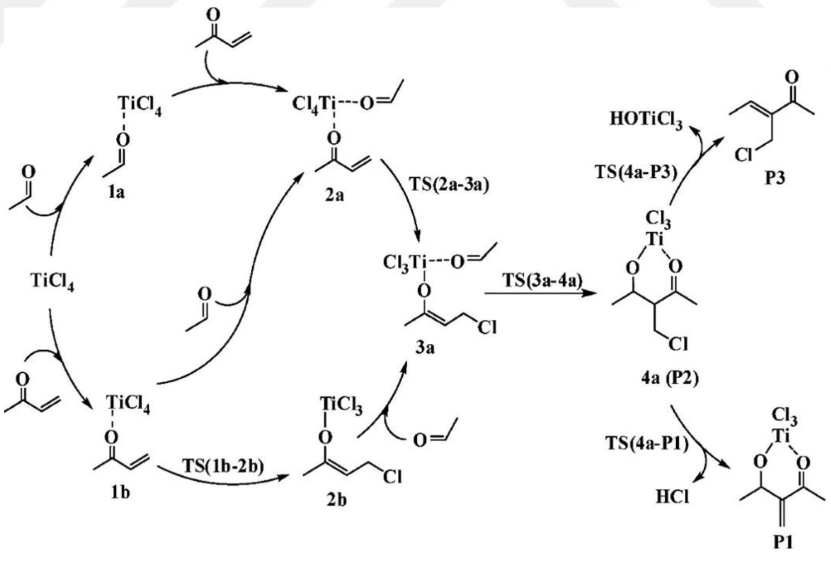

Scheme 24. Mechanism of $TiCl_4$ -promoted MBH reaction [172].

1.6.1.1 Enzyme-Catalyzed MBH Reactions

In addition to conventional organocatalysts, certain enzymes containing nucleophilic amino acid residues have been explored as biocatalysts for MBH reactions due to their high specificity and efficiency under mild conditions. A notable study, published by Joshi *et al.* in 2016, which inspired this part of the thesis, investigated the catalytic potential of certain proteins in MBH reaction between *p*-nitrobenzaldehyde as an electrophile and 2-cyclohexen-1-one, as an activated alkene [173].

The study examined several proteins, including RNase A, α-chymotrypsinogen, lysozyme, α-chymotrypsin, myoglobin, trypsin, and ubiquitin. These proteins were specifically chosen for their structural features, particularly the presence of histidine and arginine residues in their active sites (Table 3).

Table 3. Proteins facilitating His-Arg pair in the MBH reaction [173].

Entry	**Catalyst**	**His and Arg pair**
1	RNase A	1 (H119, R10)
2	α-Chymotrypsinogen	1 (H40, R145)
3	Lysozyme	1 (H15, R14)
4	α-Chymotrypsin	2 (H91, R93; H65, R217)
5	Myoglobin	2 (H24, R118; H113, R31)
6	Trypsin	0
7	Ubiquitin	0

Histidine, which contains nucleophilic imidazole side chain, was considered to participate in the nucleophilic activation of the alkene and promote the reaction. Arginine, on the other hand, was considered to have the potential to assist the proton shift process during the transition state. The study focused on examining how these enzymes work on MBH reaction and pointed out their different efficiencies and how the side chains affect the reaction yields and obtain the best conversions using lysosome and myoglobin. Another noteworthy thing was that the reactions were carried out in PBS buffer and at room temperature (Scheme 25). This choice of reaction medium and temperature was significant because it provided a biologically relevant environment.

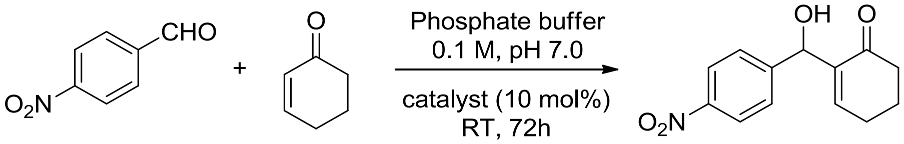

Scheme 25. Biocatalysis in MBH reaction [173]

1.7 2-Amino Chromene Derivative Synthesis

2-Amino-4H-chromenes are a class of heterocyclic compounds structurally related to chromenes. They are formed by fusing the 5,6-positions of a 4H-pyran ring with a benzene or naphthalene ring. (Figure 19). The fundamental structural framework of these compounds represents a typical characteristic of polyphenols which are widely found in tea, vegetables and fruits, mostly in grapes [174, 175].

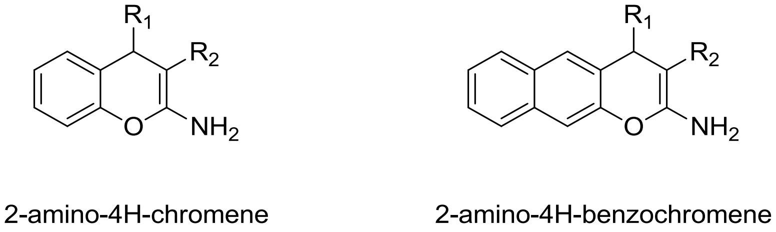

Figure 19. Structure of 2-amino-4H-chromene and 2-amino-4H-benzochromene.

These derivatives have attracted significant research interest due to their diverse applications, including their use as laser dyes [176], fluorescence markers [177] and photochromic materials [178]. Among them, 2-amino-3-cyano-4H-chromene derivatives have been the focus of significant research because of their existence in a wide range of biologically active natural products and their potential in pharmaceutical applications. For instance, some derivatives (Figure 20) have been investigated for their as anticancer agent, insulin-regulated aminopeptidase (IRAP) inhibitor and antibacterial agent [179, 180, 181].

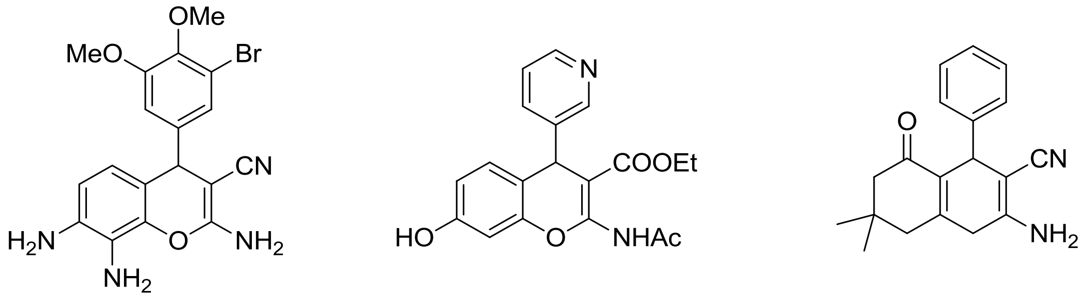

Anticancer Agent	IRAP Inhibitor	Antibacterial Agent

Figure 20. Biologically active chromenes [179, 180, 181].

1.7.1 Synthesis of Chromene Derivatives and Catalysts

The simplest and most widely employed method for the synthesis of 2-amino-3-cyano-4H-chromenes involves the one-pot, three-component reaction of malononitrile, aryl aldehydes, and phenol or 2-naphthol derivatives in the presence of either homogeneous or heterogeneous catalysts at elevated temperatures (Scheme 26).

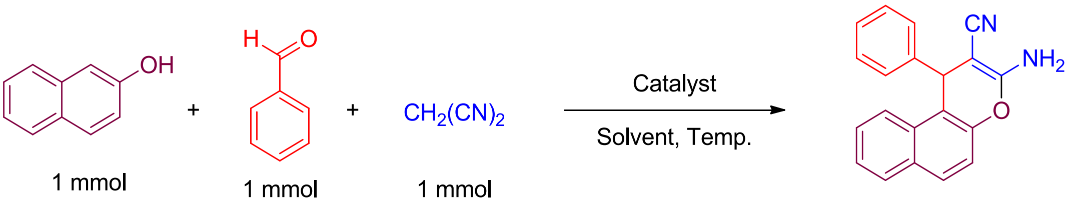

Scheme 26. Synthesis of 2-amino-3-cyano-4H-chromenes.

Due to the widespread applications of these derivatives, numerous catalytic systems have been developed over the past two decades. Some of the most notable catalysts include: Metal-based catalysts, such as Co_3O_4 and Eu-doped Co_3O_4, under microwave-assisted conditions [182].

- Heterogeneous bismuth-based catalysts, including Bi_2O_3, $BiVO_4$, and Bi_2WO_6 nanoparticles [183].
- Basic catalysts, such as K_2CO_3 [184, 185], Na_2CO_3 [186], DMAP [187, 188], and potassium phthalimide [189].

Furthermore, a key study that inspired this part of the thesis was reported by Heydari *et al.* in 2014 [190]. As a catalyst, non-toxic, eco-friendly and the most basic amino acid arginine was used. By synthesizing arginine-immobilized magnetic nanoparticles, Fe_3O_4 @L-arginine, as a catalyst, up to 95% yields have been achieved (Table 4).

Table 4. Effect of conditions on the chromene derivative synthesis yield [190].

Entry	**Catalyst**	**(mg)**	**Solvent**	**Time (h)**	**Temp (°C)**	**Yield (%)**
1	-	-	-	12	100	0
2	L-Arginine	10	-	12	100	40
3	L-Arginine	20	-	12	100	70
4	L-Arginine	20	EtOH	12	80	62
5	L-Arginine	20	H_2O	12	100	50
6	L-Arginine	20	MeOH	12	80	45
7	Fe_3O_4	20	-	12	100	50
8	Fe_3O_4	40	-	12	100	60
9	Fe_3O_4@L-arginine	20	-	12	rt	20
10	Fe_3O_4@L-arginine	20	-	12	50	65
11	Fe_3O_4@L-arginine	40	-	12	50	85
12	Fe_3O_4@L-	40	-	12	80	90
13	Fe_3O_4@L-arginine	40	-	12	100	95

Also in the report, it was highlighted that with an external magnet, the catalyst could be isolated from the reaction mixture and reused four times without losing its activity. The proposed reaction mechanism for this synthesis is shown in Scheme 27, outlining the catalytic role of arginine in each step of the transformation.

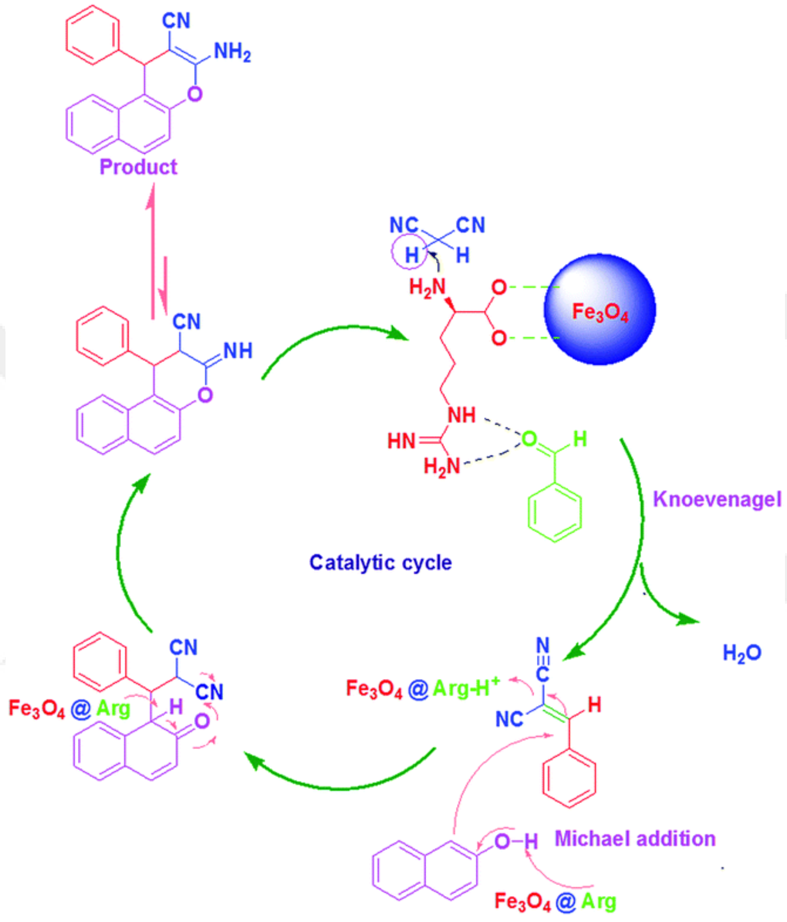

Scheme 27. Proposed mechanism of arginine catalyzed 2-amino-3-cyano-4H-chromene synthesis [190].

1.8 Prins Cyclization

The Prins reaction [191] exhibits a strong correlation with the Kriewitz reaction [192], which is a reaction in that α-pinene reacts with formaldehyde via a thermal ene rearrangement to yield an unsaturated alcohol. On the other hand, when an alkene reacts with an aldehyde in the presence of an acid catalyst, the process is specifically referred to as the Prins reaction (Scheme 28).

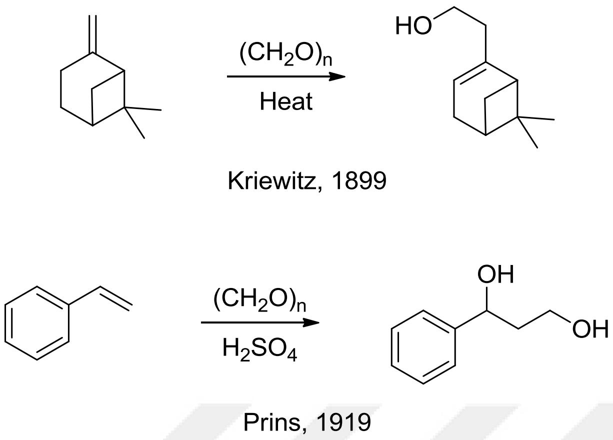

Scheme 28. Kriewitz reaction [192] and Prins reaction [191].

Prins cyclization is a variation of the Prins reaction that involves an acid-catalyzed reaction between a homoallylic alcohol and an aldehyde, resulting in the formation of tetrahydropyran and dihydropyran rings which are characteristic structures commonly found in a wide range of natural products [193–197] (Scheme 29).

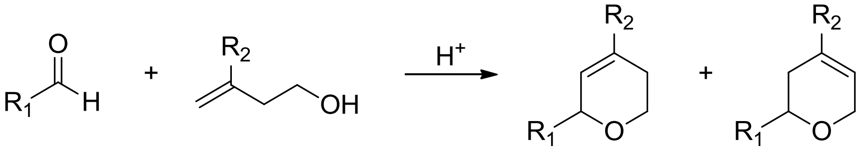

Scheme 29. General synthetic route of Prins cyclization.

1.8.1 Catalysts for Prins Cyclization

Prins cyclization typically takes place under strong acid catalysis, with Brønsted acids such as sulfuric acid [198], trifluoroacetic acid (TFA) [199], and p-toluenesulfonic acid [200] widely used to promote the reaction. These acidic conditions facilitate the formation of the oxocarbenium ion intermediate, which undergoes cyclization to yield the desired dihydropyran products. The proposed reaction mechanism illustrating this process is shown below (Scheme 30).

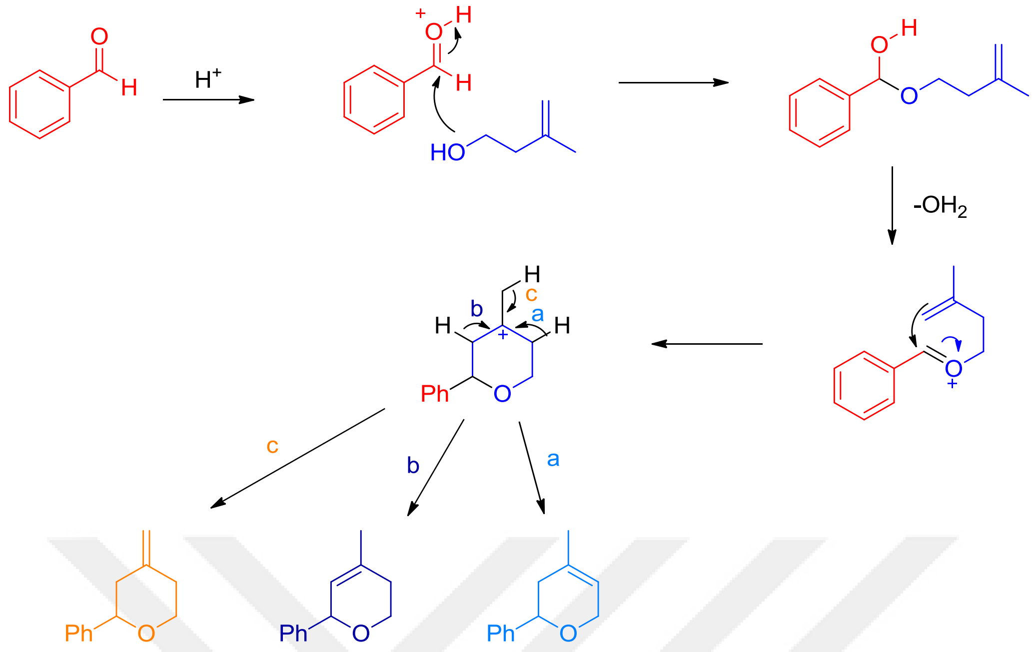

Scheme 30. Proposed mechanism of Prins cyclization.

In addition to strong Brønsted acids, Lewis acids have also been extensively utilized in Prins cyclization. Notably, reactions conducted in the presence of ferric chloride ($FeCl_3$) or ferric bromide ($FeBr_3$) lead to the formation of chlorinated or brominated dihydropyran derivatives respectively [201, 202]. Similarly, iodine catalyzed Prins cyclization leads to iodinated dihydropyran derivatives [203] (Figure 21). This halogen incorporation broadens the scope of Prins cyclization, allowing access to halopyran compounds that serve as valuable intermediates for further functionalization.

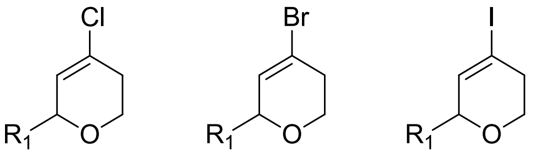

Figure 21. Halopyran derivatives.

A notable extension of the Prins reaction is the one-pot, three-component Prins−Friedel−Crafts reaction, which enabled the synthesis of 4-aryltetrahydropyran derivatives. One such example was reported by Saikia *et al.* in 2009 [204], where an aldehyde reacted with a homoallylic alcohol and an arene in the presence of boron trifluoride etherate ($BF_3{\cdot}OEt_2$) as a catalyst (Scheme 31).

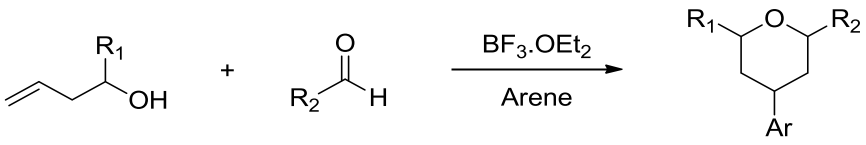

Scheme 31. Prins−Friedel−Crafts reaction [204].

Another example involves post-treatment modifications following the completion of the Prins reaction. When TFA was used as the catalyst, subsequent addition of a saturated aqueous Na_2CO_3 solution followed by solid NaOH led to the selective formation of cis-2-phenyltetrahydro-2H-pyran-4-ol as the sole product [205] (Scheme 32).

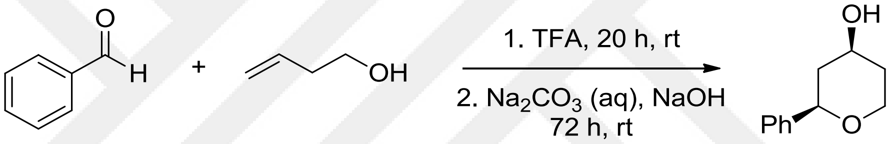

Scheme 32. cis-2-phenyltetrahydro-2H-pyran-4-ol synthesis [205].

1.9 Aim of the Study

1.9.1 LarE

The primary objective of this study was to develop a non-enzymatic model to mimic the sacrificial sulfur insertion mechanism of LarE, specifically focusing on the formation of dehydroalanine (Dha). In the biosynthesis of the nickel-pincer cofactor, LarE donates its Cys176 residue, converting it into Dha, thereby inactivating itself. To replicate this transformation without an enzyme, p-nitrophenyl nicotinate was selected as a nicotinic acid derivative, serving as a substrate analog. Various cysteine derivatives were tested in place of Cys176, investigating their ability to undergo a similar transformation under biologically relevant conditions. A crucial aspect of this study was the incorporation of fullerene-based enzyme mimics to replace Arg181 in

LarE, which plays a key role in proton abstraction during the reaction. Arginine-functionalized fullerenes were chosen due to their exceptional structural versatility, catalytic activity, and ability to mimic biological functions. Inspired by recent advances in fullerene-based biocatalyst mimics, this approach allowed for the design of a modular and highly efficient system that emulates enzymatic reactivity. The reactions were conducted in phosphate-buffered saline (PBS) at pH 7.4, ensuring biologically relevant conditions. By constructing this fullerene-assisted enzyme mimicry model, this study aimed to gain mechanistic insights into the role of key functional groups in sulfur insertion, while demonstrating the potential of fullerenes as biomimetic catalysts in cofactor biosynthesis. The proposed mechanism of the study is shown below (Scheme 33).

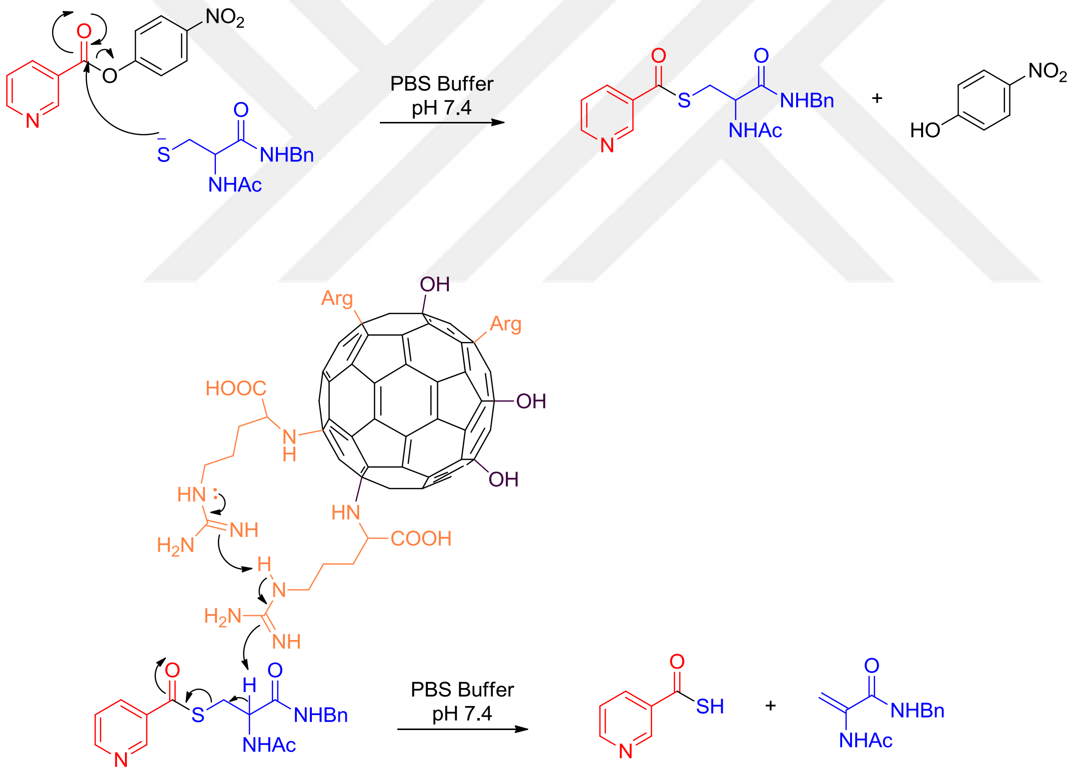

Scheme 33. Proposed reaction mechanism for the LarE mimic study.

1.9.2 Acetylcholine Detection

Fullerenes and their derivatives have demonstrated remarkable potential as enzyme mimics due to their unique electronic properties and tunable surface functionalization. In the previous part, amino acid-functionalized fullerenols were explored as biomimetic catalysts, mimicking the sulfur insertase activity of lactic acid racemase (LarE). Inspired by this approach, this study expands the application of fullerenzymes to the field of biosensing, particularly for the non-enzymatic electrochemical detection of acetylcholine (ACh). The findings presented in this section are based on our previously published work [206], with key results included here for completeness.

To address the limitations of traditional acetylcholinesterase (AChE)-based biosensors, a fullerenzyme-based electrochemical sensor was developed for the sensitive and selective quantification of ACh in human serum samples. Fullerenols, due to their high surface area, excellent electron transfer properties, and stability, have been employed as key components in acetylcholine biosensors to enhance detection sensitivity and performance.

The sensor is based on the coordination of nickel with fullerenol-histidine-serine (**F**-HS-Ni), where **F**-HS serves as the functional scaffold, enabling enzyme-inspired catalysis (Scheme 34, 35). Similar to its role in LarE mimicry, functionalized fullerenol in this system facilitates biomimetic catalysis, eliminating the need for biological enzymes. Nickel incorporation further enhances the catalytic efficiency, while the structured electrode surface ensures high electroactivity and stability.

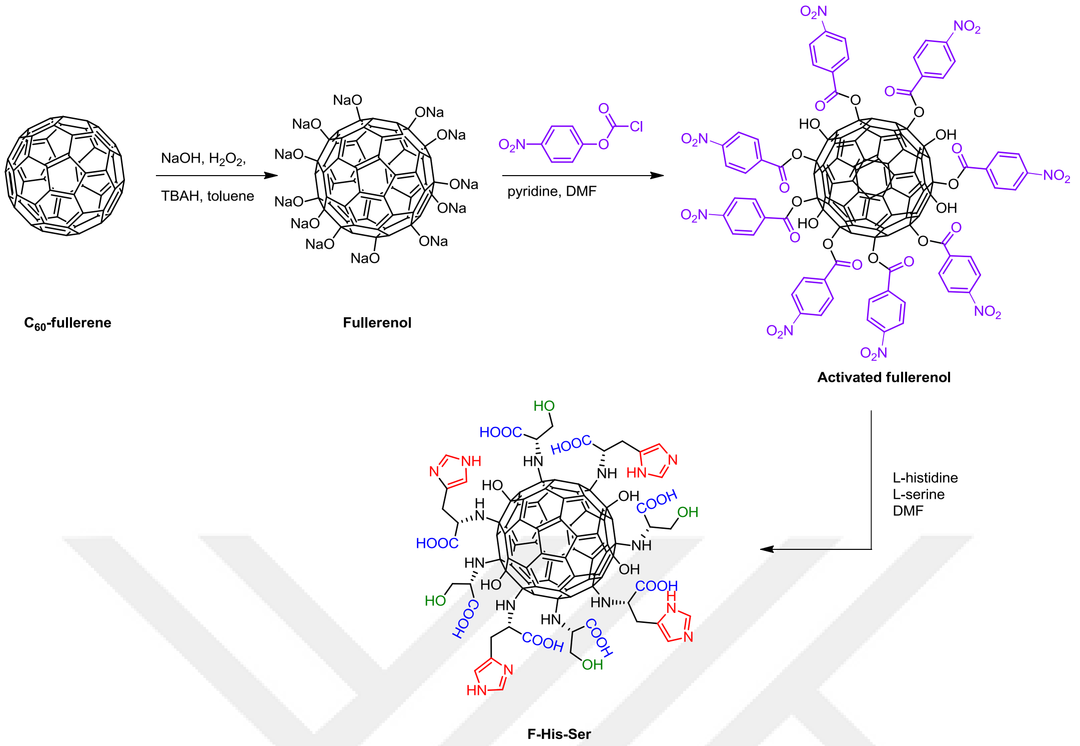

Scheme 34. Synthetic route of **F**-HS.

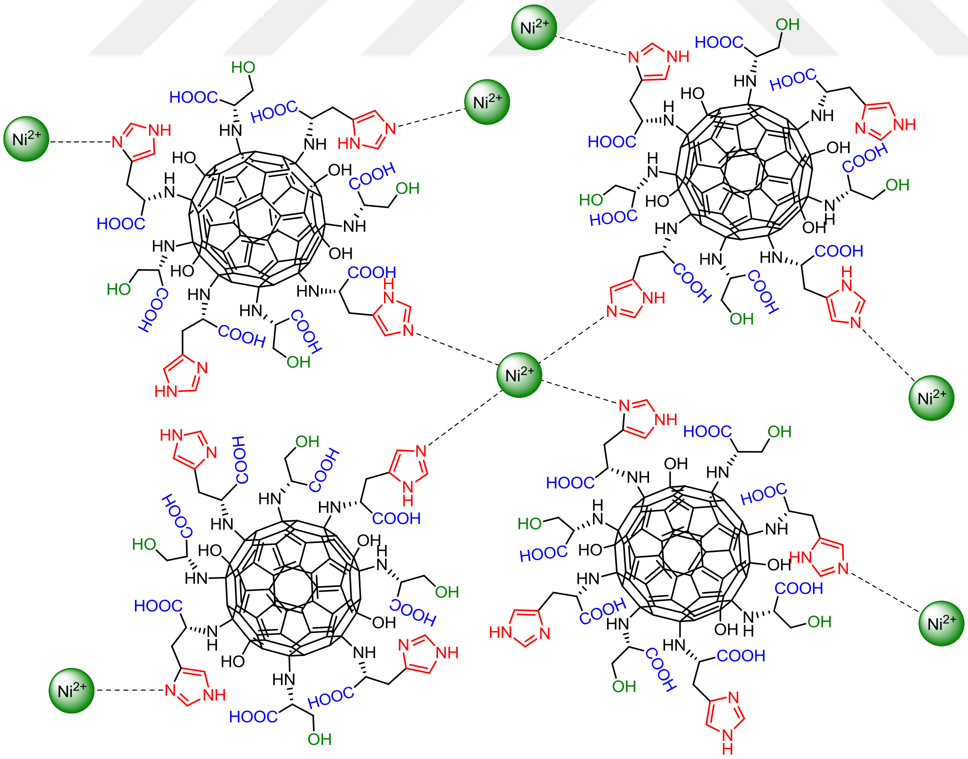

Scheme 35. Nickel coordination of **F**-HS.

The developed sensor demonstrated high sensitivity, a broad linear range, and long-term stability, making it a promising alternative for ACh quantification in biomedical applications. This study highlights the versatility of fullerenzymes, showcasing their potential not only in enzyme mimicry but also in the development of reliable, cost-effective, and stable electrochemical biosensors for real-world applications.

1.9.3 Fullerenol Applications as Organocatalysts

In this part of the thesis, fullerenol and amino acid-conjugated fullerenols have emerged as promising organocatalysts due to their unique electronic properties, high stability, and ability to participate in various reaction mechanisms.

Fullerenol and its amino acid derivatives were employed as organocatalysts in four distinct transformations: CO_2 fixation, Morita-Baylis-Hillman (MBH) reaction, 2-amino chromene synthesis, and Prins cyclization. These reactions were well-established in organic chemistry, typically catalyzed by amines, Lewis acids, or other known catalysts. However, this study explored the feasibility of fullerenol-based catalysts as a novel approach, providing insights into their catalytic activity, reaction scope, and efficiency compared to conventional catalytic systems.

1.9.3.1 CO_2 Fixation

This part of the thesis explored the development of novel catalysts for CO_2 fixation under relatively mild conditions. Specifically, reactions were carried out at atmospheric pressure, a parameter rarely reported in the literature. Fullerenols conjugated with various amino acids were employed as catalysts, while different iodine sources were utilized as co-catalysts. The efficiency of these catalytic systems in converting epoxides into cyclic carbonates was systematically investigated.

As outlined in the proposed reaction mechanism (Scheme 36), the hydroxyl groups and carboxylates of amino acids conjugated to fullerene promote the activation of the epoxide, making it susceptible to nucleophilic attack by iodine. Simultaneously, the side chains of the amino acids bind to carbon dioxide, interact with the epoxide in its activated, open-ring state, and terminate the cyclization process. This study explored the potential of fullerenol-based catalysts as an effective, sustainable, and metal-free strategy for CO_2 fixation, conducted under atmospheric pressure and relatively low temperatures.

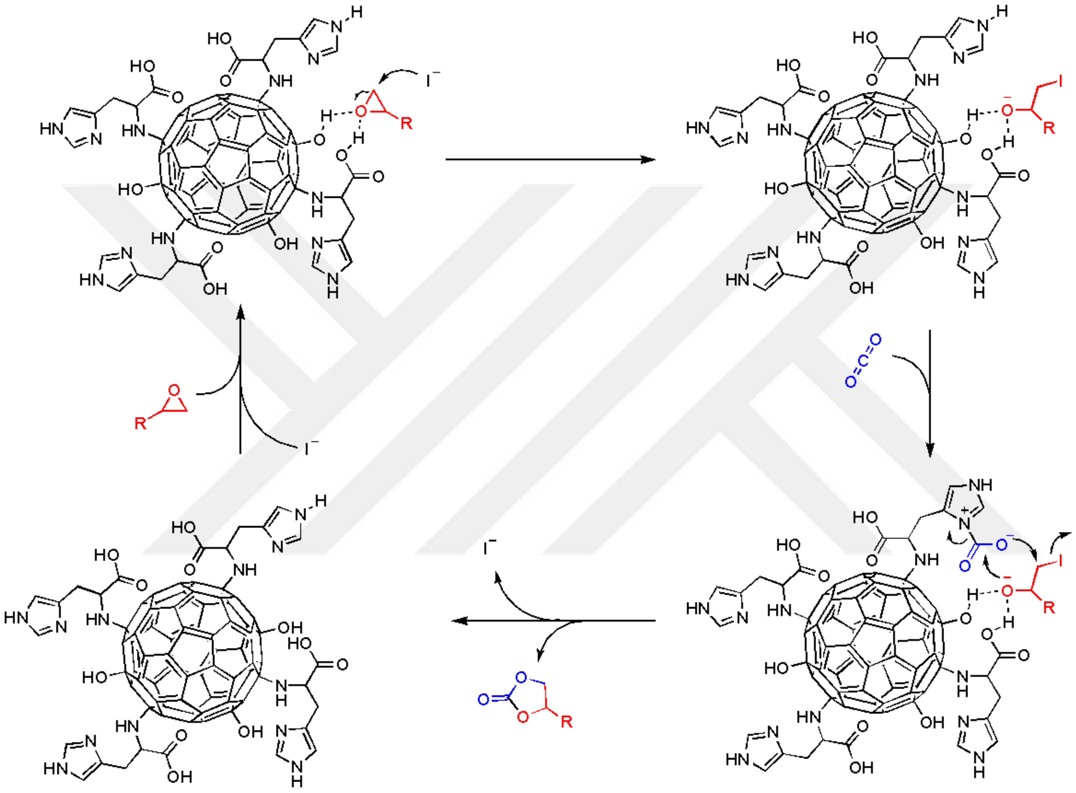

Scheme 36. Proposed CO_2 fixation mechanism catalyzed by **F**-His in this study.

1.9.3.2 MBH Reaction

The catalytic efficiency of enzymes in the Morita-Baylis-Hillman (MBH) reaction has been attributed to the presence of nucleophilic amino acid residues, particularly histidine and arginine, in their active sites. Inspired by this enzymatic mechanism, this study explores the potential of fullerene derivatives functionalized with histidine and arginine as organocatalysts for the MBH reaction.

Fullerenes are well-known for their unique electronic and structural properties, making them promising candidates for catalytic applications. By conjugating fullerenes with histidine and arginine, we aimed to mimic the enzymatic environment, leveraging the nucleophilic nature of histidine for substrate activation and the proton-transfer capability of arginine to facilitate the reaction pathway.

To support this hypothesis, a detailed mechanistic proposal has been developed (Scheme 37), illustrating the key steps involved in the catalysis. The efficiency of these fullerene-based catalysts was evaluated under various reaction conditions, and the results were compared to enzyme-catalyzed MBH reactions reported in the literature. Through this approach, we sought to bridge the gap between biomimetic catalysis and fullerene chemistry, offering a novel strategy for the development of efficient, metal-free organic catalysts.

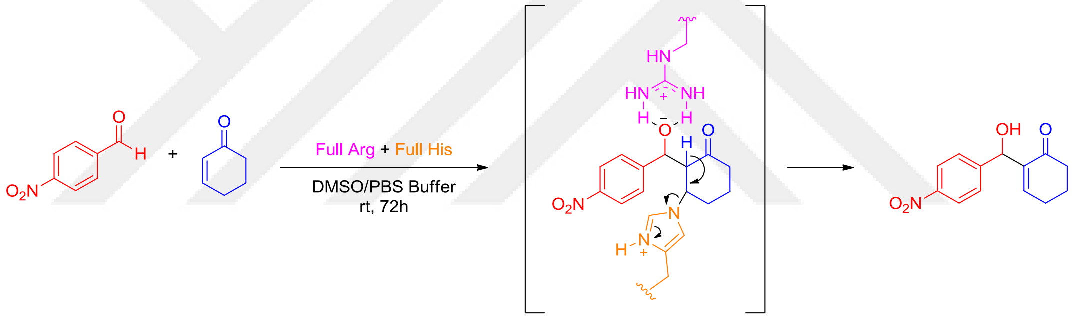

Scheme 37. Proposed MBH reaction mechanism catalyzed by **F**-Arg and **F**-His in this study.

1.9.3.3 2-Amino Chromene Derivative Synthesis

In this part of the thesis, fullerenol arginine, which had shown its remarkable base-catalyst behavior in previous works, was employed as a catalyst for the multi component synthesis of 2- amino- 3- cyano- 4H- chromene.

Based on the proposed reaction mechanism (Scheme 38), **F**-Arg acts as a base catalyst by abstracting the acidic hydrogen from malononitrile, thereby facilitating the initiation of the Knoevenagel reaction. The catalyst further promotes the formation of the naphtholate anion, which undergoes a rapid reaction with the dicyanoolefin intermediate. This step is followed by cyclization and rearrangement, ultimately leading to the formation of the corresponding chromene.

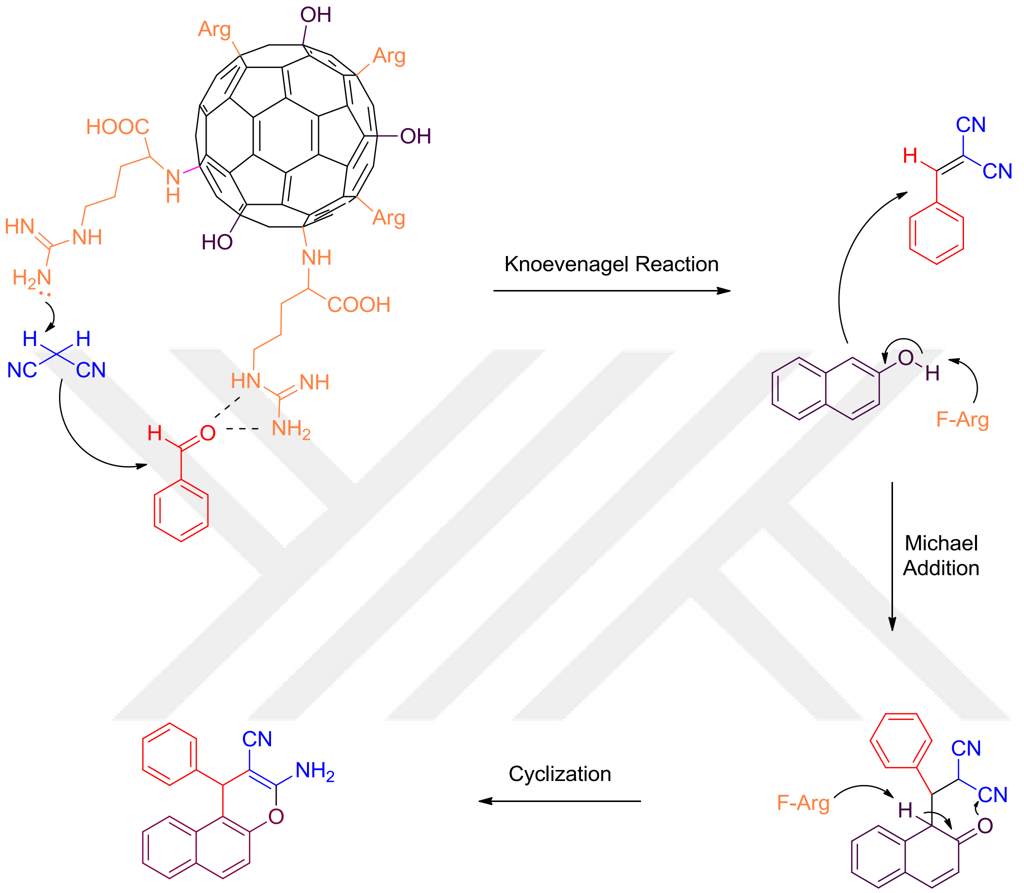

Scheme 38. Proposed 2-amino chromene synthesis mechanism catalyzed by **F**-Arg in this study.

1.9.3.4 Prins Cyclization

The pK_a of fullerenol has been reported to be approximately 3.5 [207] making it a promising candidate for use as an acid catalyst in Prins cyclization. In this part of the thesis, fullerenol was used as an acid catalyst for Prins cyclization reaction between benzaldehyde and homoallylic alcohol to investigate its efficiency (Scheme 39). The reaction was carried out under neat conditions and in the presence of solvents to compare the reactivity.

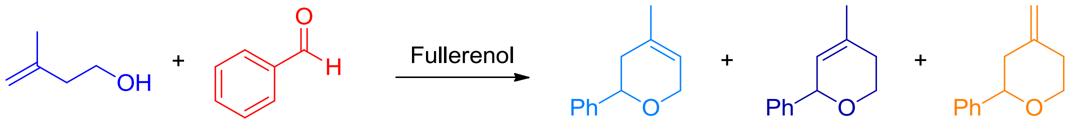

Scheme 39. Synthetic pathway of Prins cyclization in this study.

Additionally, fullerenol-catalyzed Prins cyclization was extended to a Prins−Friedel−Crafts reaction, incorporating an arene as a nucleophile. Moreover, a subsequent addition step was explored, in which the reaction was followed by saturated Na_2CO_3 solution and NaOH addition, a reaction known to influence product selectivity. To further investigate the catalytic role of the acidic nature of fullerenol, a comparison was made using formic acid, which has a pK_a value close to that of fullerenol.

Through this systematic investigation, this part of the thesis aimed to evaluate the potential of fullerenol as an acid catalyst in Prins cyclization and its expanded applications.

CHAPTER 2

RESULTS AND DISCUSSION

2.1 LarE Mimic

In this part of the thesis, arginine functionalized fullerenol (**F**-Arg) was selected as a catalyst to model the non-enzymatic formation of dehydroalanine (Dha), inspired by the sulfur insertion mechanism of the LarE enzyme. Mimicking the role of Cys176 and Arg181 in LarE, the study aimed to replicate key steps of the reaction under biologically relevant conditions. Through this model, the catalytic influence of **F**-Arg was evaluated independently in a controlled, enzyme-free environment. Catalytic performance, substrate preference, and mechanistic behavior were systematically examined to evaluate the effectiveness of this biomimetic approach.

2.1.1 Synthesis of Fullerene Arginine (F-Arg)

2.1.1.1 Synthesis of Fullerenol

For the synthesis of **F**-Arg, the literature method was followed [71]. C_{60}-Fullerene was first converted to fullerenol. After subsequent activation with *p*-nitrophenyl chloroformate, it was functionalized with arginine amino acid (Scheme 40).

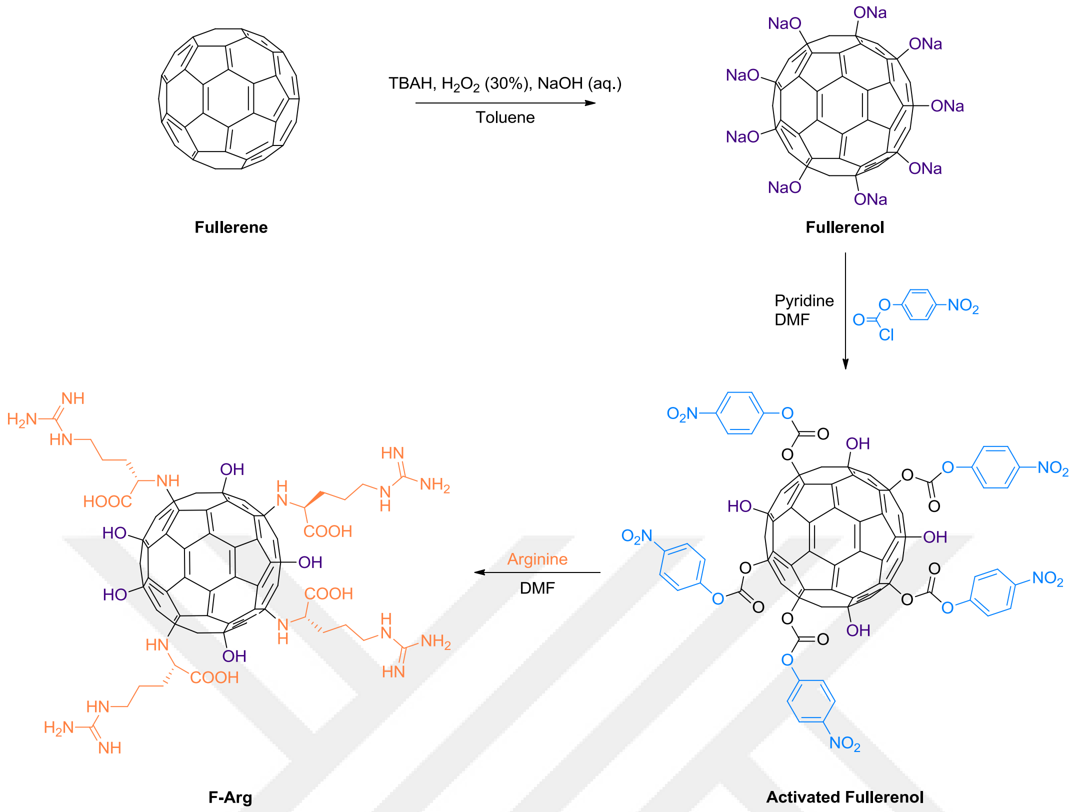

Scheme 40. Schematic representation of the synthetic route to **F**-Arg.

Synthesis of fullerenol took place under basic conditions, which were established using a 1.0 g/mL aqueous NaOH solution. However, due to the poor solubility of C_{60} in water and protic solvents, it remained in a highly aggregated state, preventing the hydrophilic peroxide (-OOH) groups generated by hydrogen peroxide (H_2O_2) from accessing its reactive sites effectively. To enable the hydroxylation reaction, C_{60} was dissolved in toluene and a phase-transfer catalyst, tetrabutylammonium hydroxide (TBAH) was employed. TBAH promoted the transfer of hydrogen peroxide from the aqueous phase to the organic phase, facilitating interaction with C_{60} molecules dissolved in toluene. The reaction mixture was stirred continuously for five days, after which toluene was removed. The resulting solid was then washed with ethanol to eliminate residual TBAH and other impurities, yielding fullerenol as a brown solid.

The first indication of successful functionalization was the increased solubility of the obtained product in water, followed by further characterization using FT-IR spectroscopy (Figure C.1). The FT-IR spectrum of fullerenol exhibits a broad peak around 3200 cm^{-1}, corresponding to hydroxyl groups on the fullerenol core, confirming the successful functionalization of fullerene C_{60}. Additionally, peaks at 1574 cm^{-1} and 1394 cm^{-1} were assigned to C=C and C–O bond vibrations, respectively.

The number of hydroxyl groups substituted on the fullerenol core was estimated to be between 24 and 26 based on previous studies and TGA measurements (Figure 22). An empirical formula was applied to determine the hydroxylation degree:

$$Number\ of\ hydroxyl\ groups = \left(\frac{720}{y}\right) x \left(\frac{x}{m}\right)$$

where:

- 720 is the molecular weight of C_{60} fullerene
- y corresponds to the percentage of mass loss above 570 °C resulting from the decomposition of fullerene
- x is the percentage of weight loss between 150–570 °C
- m is the molecular weight of each attached group (17 for hydroxyl groups).

Weight loss below 150 °C was excluded as it corresponds to the removal of solvents and adsorbed water. By substituting the experimental values into the formula, the number of hydroxyl groups was determined to be 26, consistent with the expected range.

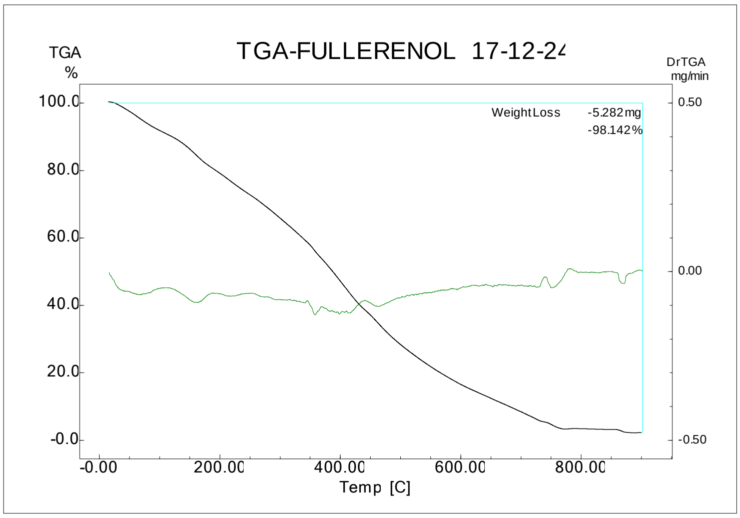

Figure 22. TGA thermogram of fullerenol.

2.1.1.2 Synthesis of Activated Fullerenol

Following the synthesis and characterization of fullerenol, an activated form was prepared using *p*-nitrophenyl chloroformate to functionalize the hydroxyl groups on the fullerenol core. Pyridine was employed as a base to deprotonate these hydroxyl groups, enhancing their reactivity toward 4-nitrophenyl chloroformate. Additionally, 4-dimethylaminopyridine (DMAP), a common catalyst in esterification reactions, was used to facilitate the process. The choice of p-nitrophenyl chloroformate was due to its strong leaving group ability, which facilitated the nucleophilic attack on the fullerenol core. As a result, this derivatized product is referred to as the activated form of fullerenol.

The activated fullerenol was characterized using FTIR (Figure C.2) and ^{1}H NMR spectroscopy (Figure A.1). The ^{1}H NMR spectrum of activated fullerenol exhibits doublets at 6.9 ppm and 8.2 ppm, corresponding to the p-nitrophenyl group, confirming the formation of the activated derivative. Additionally, peaks at 8.8 ppm, 8.3 ppm, and 7.8 ppm indicate the presence of pyridine residues from the synthesis process. The activated fullerenol was used in the subsequent step without further purification, as the residual pyridine was considered beneficial for the functionalization of amino acids.

Furthermore, the FT-IR spectrum of activated fullerenol displays characteristic peaks around 1715 cm^{-1}, 1539 cm^{-1}, and 1393 cm^{-1}, which correspond to the ester carbonyl group (C=O) and the asymmetrical and symmetrical stretching vibrations of nitro groups (NO_2), respectively, further supporting successful activation.

2.1.1.3 Synthesis of F-Arg

After characterization, the activated fullerenol was reacted with arginine without using any additional catalyst. The reaction proceeded under mild conditions, as the activated fullerenol was sufficiently reactive to facilitate functionalization. The product was then characterized via ^1H NMR spectroscopy, confirming the successful conjugation of arginine onto the fullerene core (Figure A.2).

2.1.1.3.1 Determination of the Degree of Arginine Substitution on Fullerenol

The degree of arginine substitution was determined by ^1H NMR using an internal standard. For this measurement, 14 mg of **F**-Arg was dissolved in D_2O, and 10 μL of DMF (9.4 mg, 0.129 mmol) was introduced as an internal standard. The aldehydic hydrogen peak of DMF and the α-proton of arginine were used as reference signals. The spectrum revealed that for every 1 mole of DMF, 0.37 moles of arginine were present (Figure 23). This calculation indicated that 14 mg of fullerenol-arginine conjugate contained 0.0477 mmol (8.2 mg) of arginine.

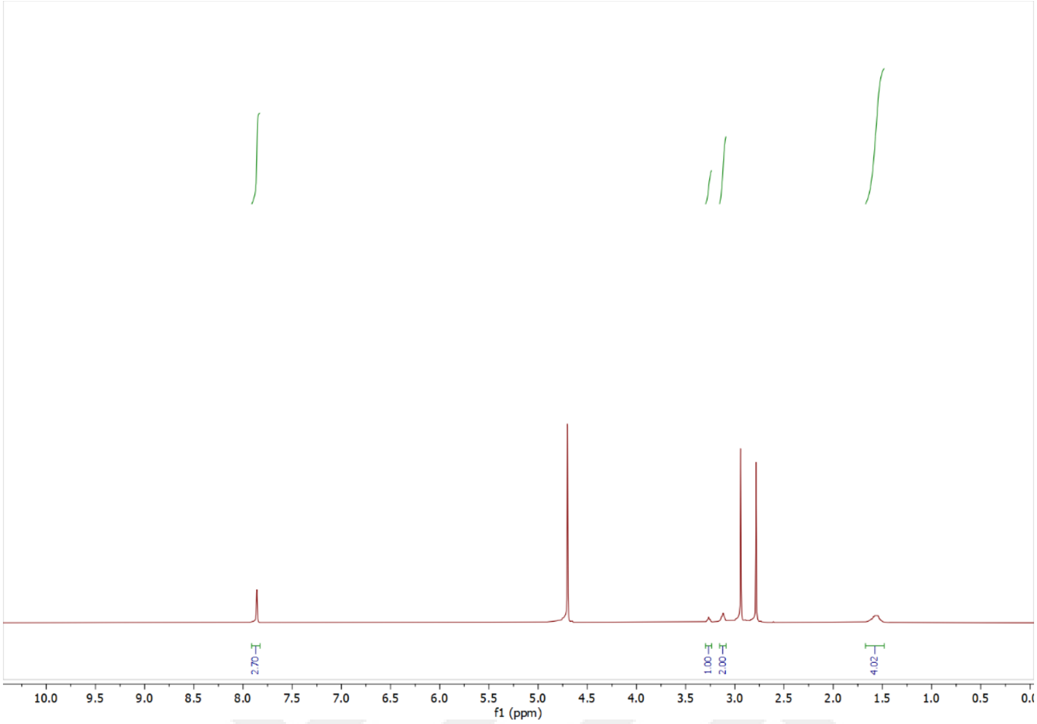

Figure 23. ^{1}H NMR spectrum of **F**-Arg in D_2O with DMF as an internal standard.

The molecular weight of fullerenol arginine was calculated in $g\ mol^{-1}$ using the formula below;

$$720 + 173x + 17(26 - x)\ g/mol$$

where:

- 720 represents the molecular weight of the C_{60} fullerene core,
- 173 corresponds to the molecular weight of L-arginine,
- x corresponds to the degree of arginine substitution,
- 17 represents the molecular weight of the hydroxyl (OH) group,
- 26 hydroxyl groups are initially present in fullerenol before functionalization.

Since the functionalization process involved the substitution of hydroxyl groups with arginine molecules, this factor was considered in the calculation. By calculating the molecular weight ratio between **F**-Arg and arginine, the degree of substitution (x) was determined as follows:

$$\frac{173x\ [g\ mol^{-1}]}{720 + 173x + 17(26 - x)\ [g\ mol^{-1}]} = \frac{8.2\ [mg]}{14\ [mg]}$$

Solving for x yielded 8.33, indicating that approximately 8 arginine units were substituted into the fullerenol core in **F**-Arg.

2.1.2 Synthesis of Substrates

As a first approach, to mimic the LarE mechanism and facilitate the formation of dehydroalanine derivatives, *p*-nitrophenyl nicotinate (**1**) and *N*-acetyl-L-cysteine *N'*-methylamide (**2a**) were designed as substrates (Scheme 41). The reaction progress and dehydroalanine formation were monitored using HPLC. Additionally, nicotinate diester was considered as a potential substrate, and its synthesis was tried for this purpose.

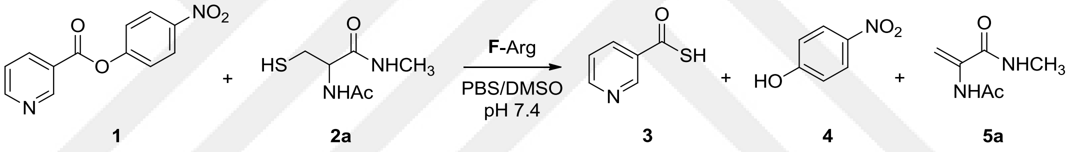

Scheme 41. Enzyme mimic reaction with compound **2a**.

2.1.2.1 Synthesis of *p*-Nitrophenyl Nicotinate

The synthesis of the substrates began with the preparation of *p*-nitrophenyl nicotinate (**1**), which was obtained by coupling niacin with *p*-nitrophenol using 1-ethyl-3-(3-dimethylaminopropyl)carbodiimide (EDCI) as the coupling agent and DMAP as the catalyst [208]. This reaction facilitated the formation of the ester bond between niacin and *p*-nitrophenol, yielding the product **1** in good efficiency (Scheme 42).

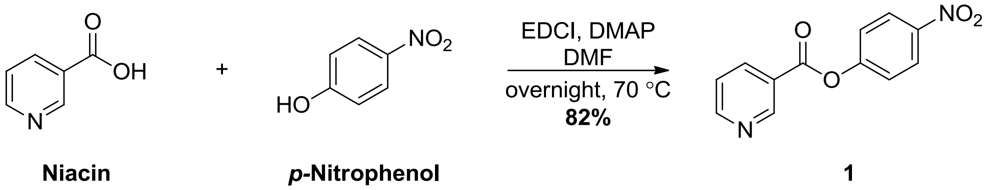

Scheme 42. Synthesis of **1** from niacin and *p*-nitrophenol.

2.1.2.2 Synthesis of *N*-Acetyl-L-cysteine-*N′*-methylamide (2a)

The first cysteine derivative designed for this study was *N*-Acetyl-L-cysteine *N'*-methylamide (**2a**), which was synthesized starting from L-cysteine using literature methods [209]. The synthesis began with the conversion of L-cysteine to its methyl ester hydrochloride salt (**Cys-OMe**), achieved by reacting L-cysteine with methanol and thionyl chloride to protect the carboxylic acid residue. This intermediate was then treated with acetic anhydride (Ac_2O) to acetylate both the amine and thiol groups, forming a diacetylated product (**Cys-Diac)**. In the final step, the acetyl group on the thiol was selectively hydrolyzed by reacting the intermediate with methylamine in methanol overnight, generating the free thiol group. Simultaneously, the methyl ester group was converted to a methyl amide through an amide formation reaction, yielding the desired compound **2a** as the final product (Scheme 43).

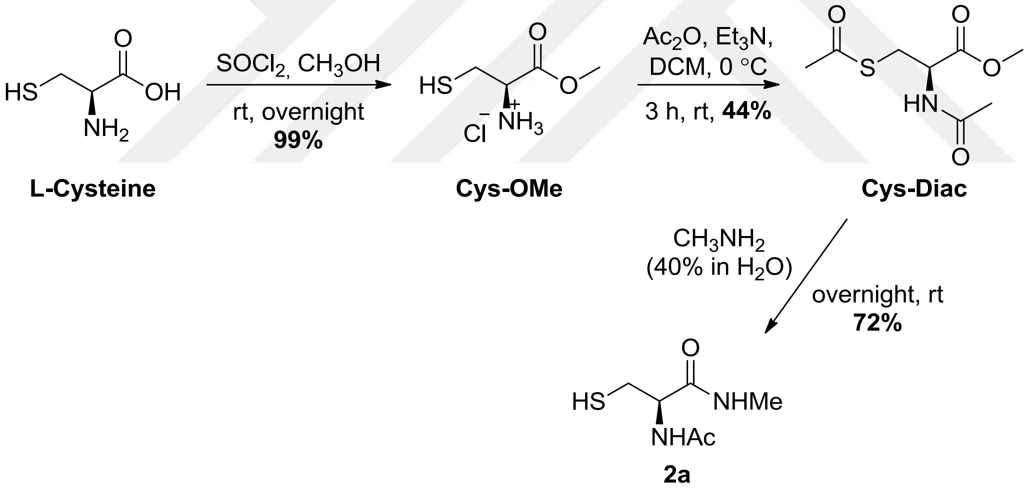

Scheme 43. Schematic representation of the synthetic route to **2a**.

2.1.2.3 Synthesis of Dehydroalanine Derivative 5a

To establish a reference and precisely determine the retention time of the expected dehydroalanine derivative in HPLC, attempts were made to synthesize this compound separately using various synthetic approaches.

The first approach focused on obtaining a dehydroalanine derivative by dehydrating a serine derivative, facilitating the removal of a hydroxyl group to form the desired unsaturated amino acid. For this purpose, *N*-acetyl-L-serine *N'*-methylamide (**6**) was synthesized using L-serine ethyl ester as the starting material (Scheme 44). The synthesis followed the similar methodology previously established for compound **2a**. At the end of the reaction, a mixture of the desired product and *N*-methylacetamide was obtained. Since purification was not achieved, the mixture was used directly in the subsequent reaction without further purification.

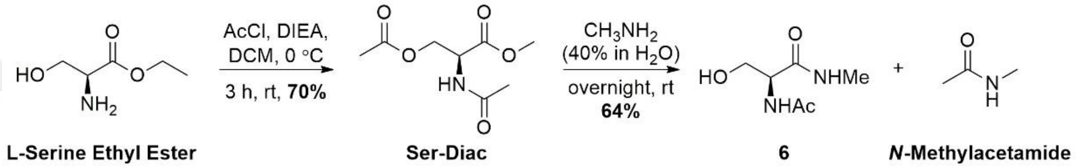

Scheme 44. Schematic representation of the synthetic route to **6**.

Following the synthesis of compound **6**, compound **5a** was tried to be synthesized using two different approaches. The first strategy involved converting the hydroxyl group into a better leaving group through mesylation, followed by its elimination using the non-nucleophilic base DBU [210]. The second strategy involved using EDC and CuCl, as described in the literature [211]. However, neither approach successfully yielded the desired product, **5a** (Scheme 45).

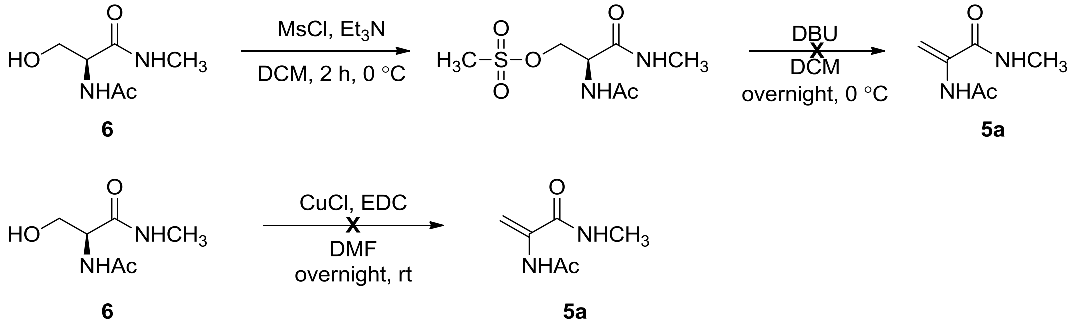

Scheme 45. Schematic representation of the synthetic route to **5a** (first approach).

The second approach involved a coupling reaction between 2-acetamido acrylic acid (**ACA**) and methylamine. First, **ACA** was synthesized using pyruvic acid and acetamide as starting materials (Scheme). After its successful synthesis, various coupling agents, including EDCI, PyBOP, DCC, and HOBt, were tested to facilitate the formation of compound **5a**. Additionally, different methylamine sources were explored, including methylamine solution in water, methylamine hydrochloride salt, and pure methylamine in gaseous form. However, none of these attempts yielded the desired product (Scheme 46).

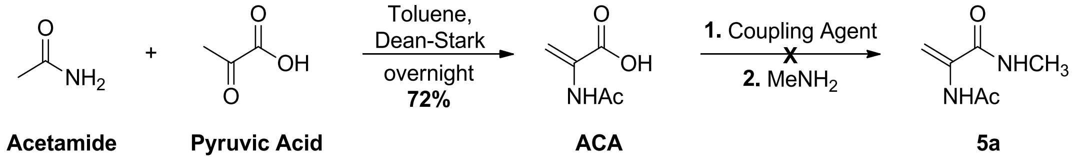

Scheme 46. Schematic representation of the synthetic route to **5a** (second approach).

Following these results, it was decided to proceed with enzyme mimic reaction without synthesizing the compound **5a** as a reference. This expected product which will be formed in the enzyme mimic reaction would be identified by LC-MS analysis.

Following the synthesis of substrates and **F**-Arg, the study proceeded to the mimicry reaction of the LarE mechanism, which is the primary objective of this part of the thesis.

2.1.3 Enzymatic Mimic Study with Compound 2a as a Cysteine Derivative

For the initial enzymatic mimic study, a 12 mM stock solution of compound **1** was prepared in DMSO. A 0.2 mM stock solution of **F**-Arg was prepared in phosphate buffer (10 mM, 150 mM KCl, pH 7.4). Additionally, a stock solution containing 4.0 mM of compound **2a** was prepared in a PBS mixture. The retention times of these compounds were then determined using HPLC (C18 column, gradient elution from 1% to 90% MeCN/H_2O over 20 minutes), ensuring proper separation and identification before proceeding with kinetic measurements (Figure B.1, Figure B.2).

The reaction was proposed to proceed as initially, compound **1** and compound **2a** rapidly react to form a thioester intermediate. Subsequently, **F**-Arg acts as a base, abstracting the α-proton of the thioester, leading to the formation of the dehydroalanine derivative (**5a**) and compound **3** (Scheme 47).

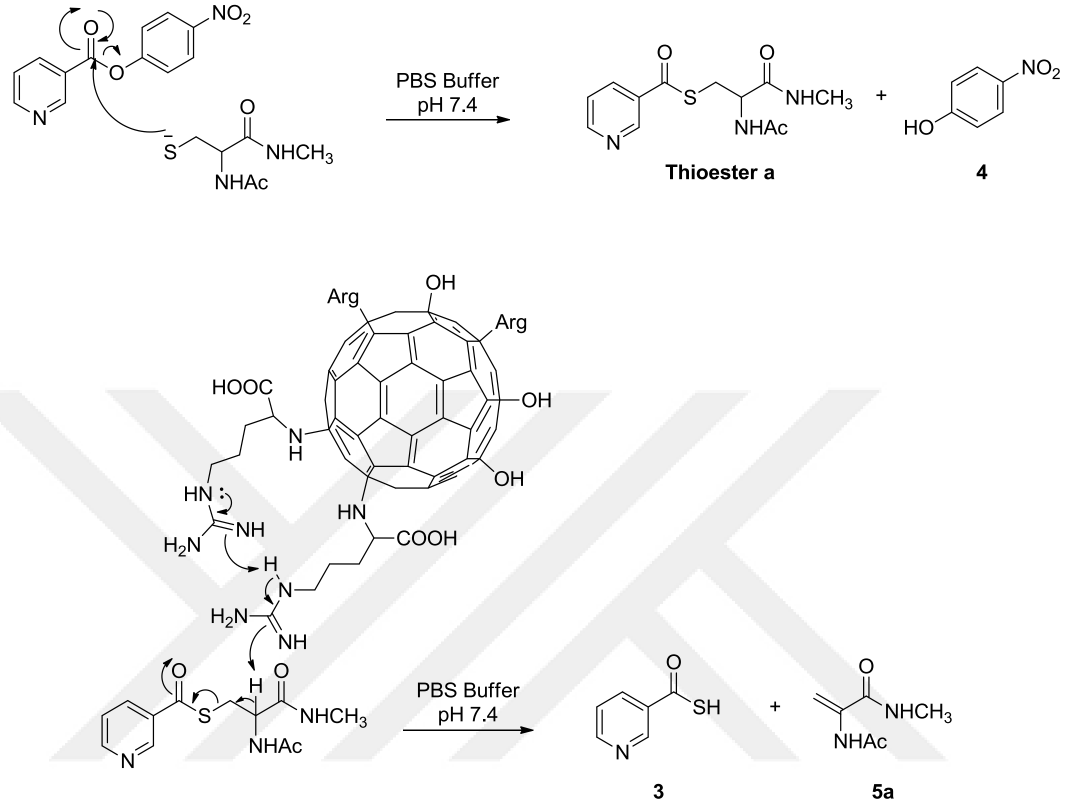

Scheme 47. Proposed mechanism of the study.

After confirming the retention times and assigning peaks in HPLC, kinetic measurements were then carried out to evaluate the reaction under these conditions. TCEP was first added to the compound **2a** solution prepared from the stock to break the disulfide bond which was partially formed during isolation. Then, appropriate volumes of compound **1** and **F**-Arg solutions were taken, mixed, and diluted to the predetermined concentrations before being added to the cysteine derivative (compound **2a**) solution. The final concentrations were adjusted as follows: compound **1**: 0.6 mM, compound **2a**: 0.5 mM, and **F**-Arg: 0.005 mM (1 mol%).

The reaction was carried out at room temperature, and after 10 seconds, a sample was taken from the reaction mixture and quenched by acidification with a 1% TFA solution. This process was repeated at 70, 130, 190, 250, 310, 460, 610, 910, 1210, and 1810 seconds. Each terminated reaction was then analyzed using HPLC. However, even after 1810 seconds, no peak corresponding to compound **5a** was observed (Figure 24, Figure 25). As shown in Figure B.2, the peak at 10.15 minutes corresponds to compound **4**, while the peak at 13.78 minutes corresponds to compound **1**. Additionally, a peak at 8.99 minutes, which increased in intensity as the reaction progressed, was considered to correspond to the **thioester a** intermediate.

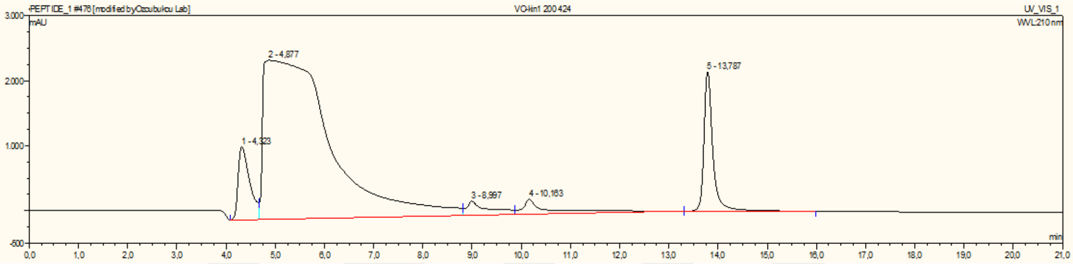

Figure 24. HPLC chromatogram of the enzymatic reaction with compound **2a** (t = 190 seconds) at 210 nm (C18, 20 min, gradient).

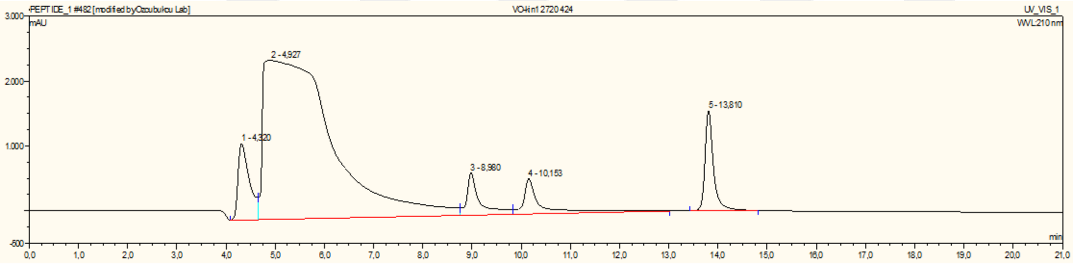

Figure 25. HPLC chromatogram of the enzymatic reaction with compound **2a** (t = 1810 seconds) at 210 nm (C18, 20 min, gradient).

Following this initial unsuccessful attempt, the **F**-Arg concentration was gradually increased from 1 mol% to 2, 5, 8, and finally 10 mol%. However, in none of these reactions was a compound **5a** peak observed after thioester formation. Subsequently, the reaction time was extended to 1 hour, 2 hours, and 3 hours with 10 mol% **F**-Arg. However, even though thioester formation was complete, no dehydroalanine formation was observed (Figure 26).

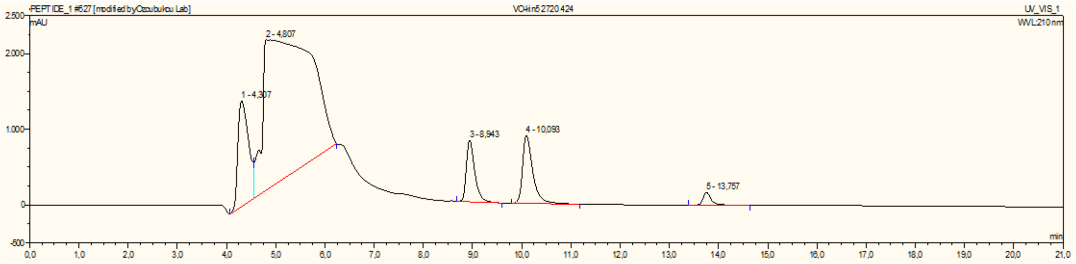

Figure 26. HPLC chromatogram of the enzymatic reaction with compound **2a** with 10 mol% **F**-Arg (t = 1810 seconds) at 210 nm (C18, 20 min, gradient).

Based on these results, it was concluded that **F**-Arg did not exhibit sufficient catalytic activity with this cysteine derivative (Scheme 48). Therefore, it was decided to synthesize and evaluate different cysteine derivatives to continue the study.

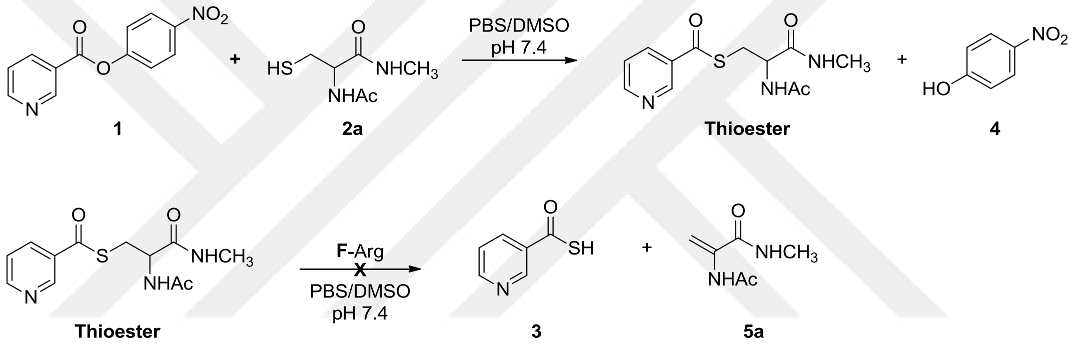

Scheme 48. Unsuccessful dehydroalanine formation.

2.1.4 Fluorescent-Labeled Cysteine Derivative: Synthesis and Evaluation

Due to the time-consuming nature of HPLC measurements and the extended duration required for testing new conditions, alternative methods were explored to enable UV-based analysis for the experiments. The first approach involved converting the cysteine derivative UV-active, considering that the expected dehydroalanine derivative formed during the reaction would exhibit absorption at a different wavelength. This would allow the concentration increase of the product over time to be monitored using UV spectroscopy. For this purpose, a cysteine derivative functionalized at the N-terminus with fluorescein isothiocyanate (FITC), possessing fluorescent properties, was synthesized (Scheme 49).

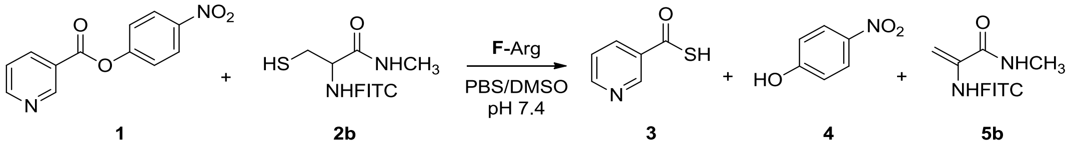

Scheme 49. Enzyme mimic reaction with compound **2b**.

FITC functionalized cysteine derivative (**2b**) was synthesized starting from L-cystine (**Cys$_2$**) using literature methods. The synthesis began with the conversion of **Cys$_2$** to its methyl ester (**Cys$_2$-OMe**), achieved by reacting with methanol in the presence of $SOCl_2$ at 0 °C. In the second step, **Cys$_2$-OMe** was treated with di-tert-butyl dicarbonate (Boc_2O) and triethylamine in a mixture of THF and water to protect the amine groups, yielding Boc-protected cystine methyl ester (**Boc-Cys$_2$-OMe**) [212]. Next, **Boc-Cys$_2$-OMe** was reacted with methylamine in an aqueous solution at 0 °C. This step selectively converted the methyl ester to a methylamide, forming Boc-protected cystine methylamide (**Boc-Cys$_2$-NHCH$_3$**). In the subsequent step, the Boc-protecting groups were removed by treating **Boc-Cys$_2$-NHCH$_3$** with TFA in DCM at room temperature for 2 hours, yielding the free amine derivative (**Cys$_2$-NHCH$_3$)** with a high yield of 95%. Finally, **Cys$_2$-NHCH$_3$** was functionalized with fluorescein isothiocyanate (FITC) by reacting it with FITC in the presence of triethylamine in DMF overnight at room temperature. This step produced the final product, **FITC-Cys$_2$-NHCH$_3$** (**2b**), as the fluorescently labeled cystine derivative (Scheme 50). However, the final compound was obtained with impurities, as complete purification was not achieved.

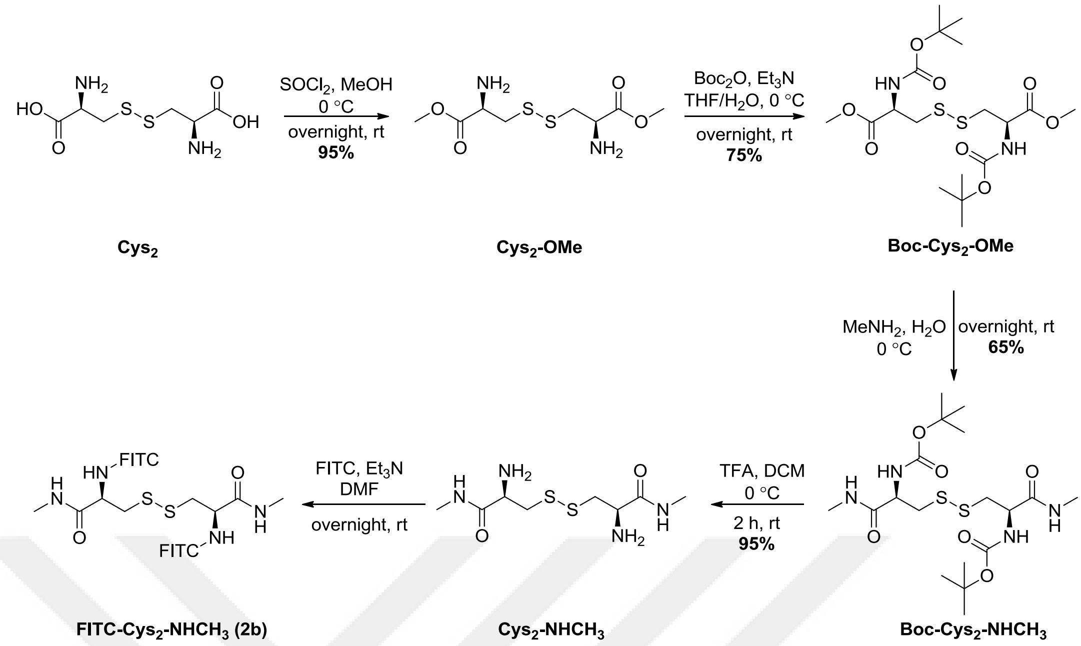

Scheme 50. Schematic representation of the synthetic route to **2b**.

After completing the syntheses, kinetic measurement trials were initiated. The reaction conditions were kept identical to those used in the previous substrate experiments. The disulfide bond of compound **2b** was reduced using TCEP, and the reactions were set up and monitored by UV spectroscopy. However, due to both the insufficient purity of compound **2b** and spectral overlaps in the UV analysis, the expected results could not be obtained. Considering the prolonged synthesis process, the inability to achieve sufficient purification, and the unavoidable UV interferences, no further studies were conducted with this cysteine derivative.

2.1.5 Thiohydantoin Derivative of Cysteine: Synthesis and Evaluation

The second approach involved using the thiohydantoin derivative of cysteine as a substrate in a LarE mimic reaction (Scheme 51). According to the literature, the maximum absorption wavelength (λ_{max}) of 3-phenyl-2-thiohydantoin of cysteine was reported to be 280 nm, whereas the λ_{max} for 3-phenyl-2-thiohydantoins was 320 nm [213]. This difference in absorption maxima suggested that the reaction could be effectively monitored using UV spectroscopy.

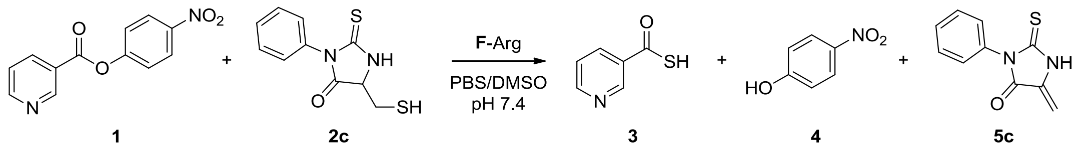

Scheme 51. Enzyme mimic reaction with compound **2c**.

The thiohydantoin derivative of cysteine utilized in this study (**2c**) was synthesized starting from **Cys$_2$** and phenyl isothiocyanate (PhSCN). The synthesis began with the reaction of **Cys$_2$** with PhSCN in the presence of potassium hydroxide in a water-ethanol mixture at room temperature for 2 days. This step allowed the formation of a thiohydantoin derivative, where the amino group of cystine reacted with the isothiocyanate group of phenyl isothiocyanate. Following this, the reaction mixture was treated with concentrated hydrochloric acid for 2 hours to remove unreacted cystine and any side products, although the overall yield of this step was 5%, indicating challenges in efficiency.

To further process this intermediate, TCEP (tris(2-carboxyethyl)phosphine hydrochloride) was employed as a reducing agent to break the disulfide bond of the cystine derivative. The final product **2c** is a thiohydantoin derivative of dehydroalanine with a free thiol group, making it suitable for further applications and analytical studies (Scheme 52).

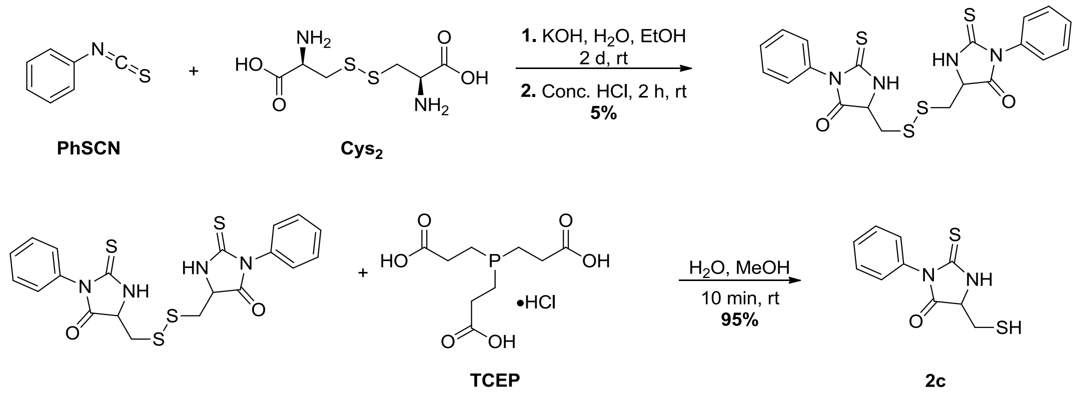

Scheme 52. Schematic representation of the synthetic route to **2c**.

The thiohydantoin derivative of dehydroalanine (**5c**) was synthesized starting from L-serine and PhSCN in the presence of sodium hydroxide in a water-pyridine mixture at 40 °C for 1 hour [214]. This step facilitated the formation of a thiohydantoin derivative of serine. Following this, the pH of the reaction mixture was adjusted to 2 using concentrated HCl at room temperature, and the product compound **5c** was obtained after overnight incubation at 4 °C with a 61% yield (Scheme 53).

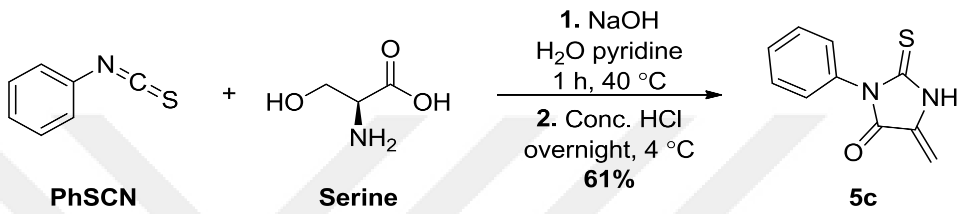

Scheme 53. Synthesis of **5c** from PhSCN and serine.

Following the successful synthesis of compounds **2c** and **5c**, their individual UV spectroscopy measurements were conducted. As considered, λ_{max} for compound **2c** was determined to be 280 nm, while compound **5c** exhibited a λ_{max} of 320 nm (Figure 27). Given that the by-product *p*-nitrophenol has a known λ_{max} of 410 nm, no interference was expected in the UV measurements. Therefore, the increase observed at 320 nm was considered suitable for kinetic calculations.

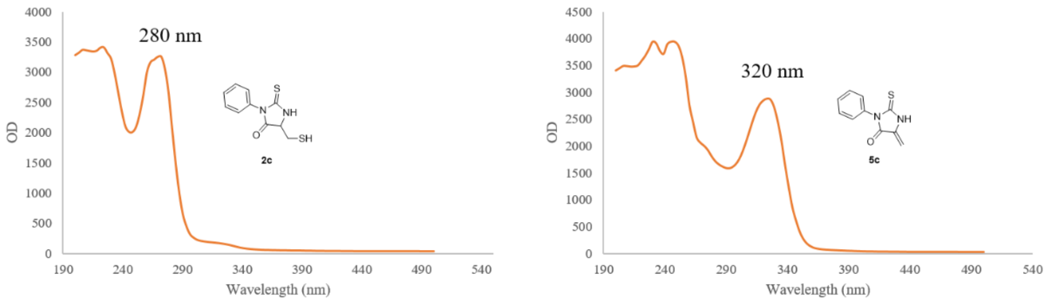

Figure 27. UV chromatograms of compounds **2c** and **5c.**

Subsequently, the experiment was conducted under the same conditions, and UV measurements were taken at certain intervals. However, no increase was observed at 320 nm, which was expected for the formation of compound **5c**. Additionally, no increase was detected at 410 nm, which would have indicated the formation of *p*-nitrophenol at that time interval. These findings suggested that, for an unknown reason, the initial reaction, the thioester formation of the reaction between **2c** and **1**, did not proceed when substrate **2c** was used (Scheme 54).

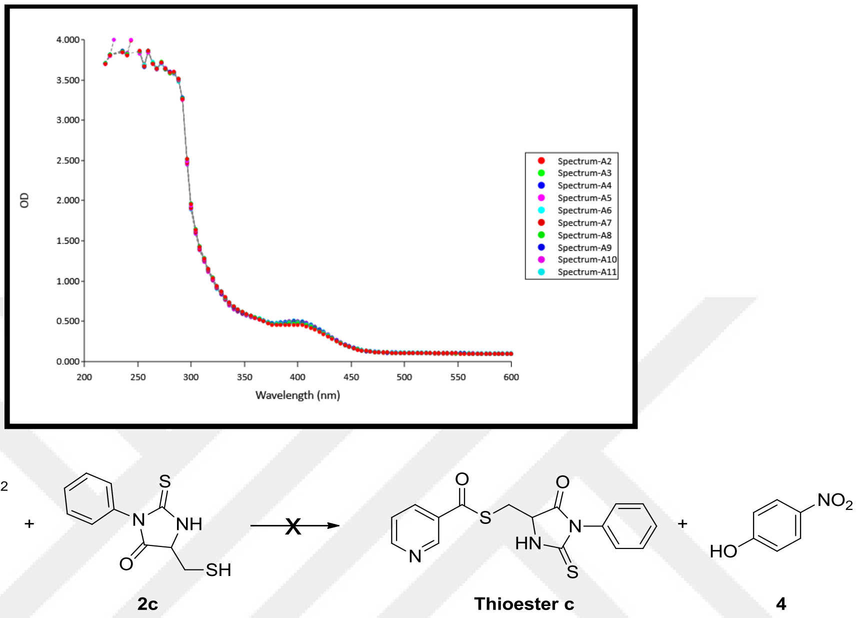

Scheme 54. Unsuccessful **thioester c** formation.

Following this result, a strategic decision was made to modify the experimental approach. The extremely low yield and challenging synthesis of compound **2c**, along with the inability to form **thioester c**, indicated the requirement for an alternative strategy. Consequently, it was decided to synthesize a different cysteine derivative as a substrate and monitor the reaction progress using HPLC to obtain more reliable kinetic data.

2.1.6 Benzylamide Derivative of Cysteine: Synthesis and Evaluation

Considering the aromatic nature of the non-hydroxylated region of fullerenol derivatives, it was hypothesized that using a benzyl cysteine derivative as the substrate, which would result from π-π interaction with **F**-Arg (Scheme 55), could potentially overcome the issues encountered in the previous experiments.

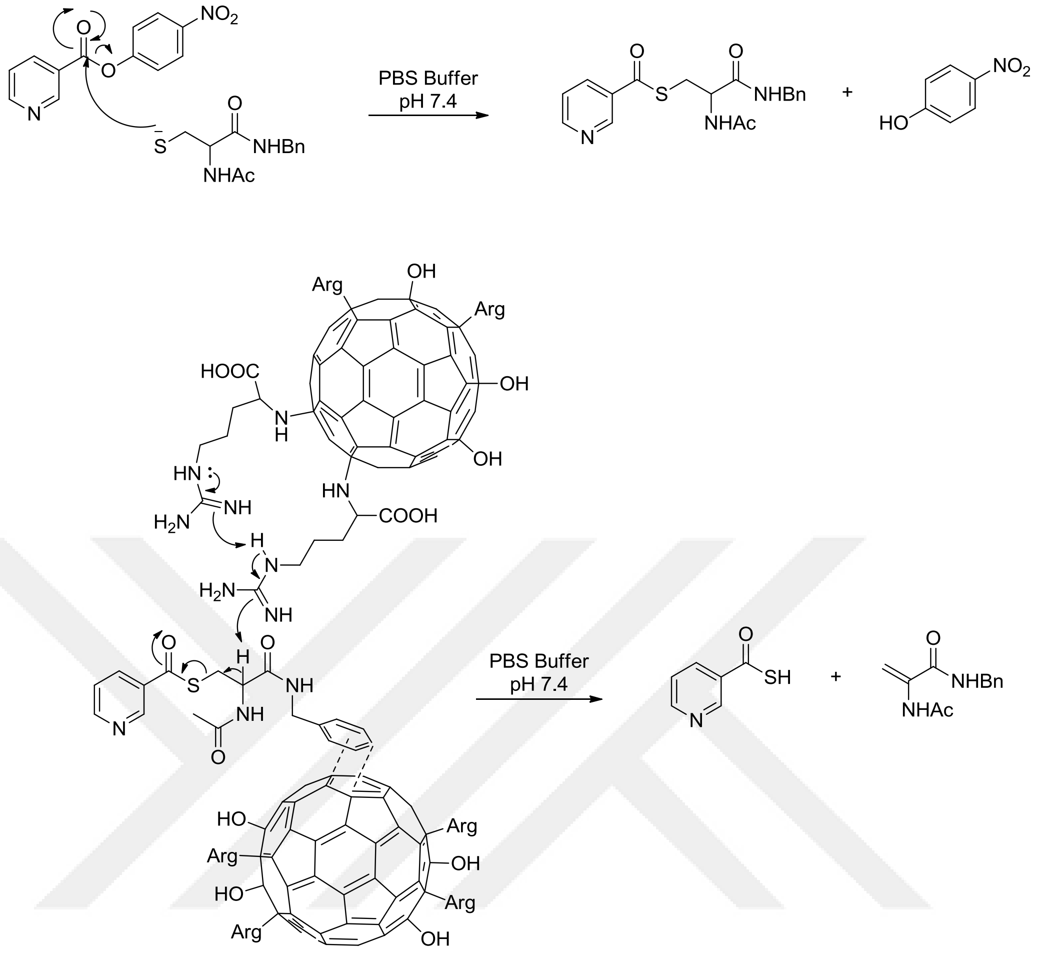

Scheme 55. Proposed reaction mechanism and π-π interaction between compound **2d** and **F**-Arg.

This approach was expected to enhance molecular interactions between the substrate and enzyme mimic. Therefore, it would provide a more favorable environment for the reaction to proceed efficiently (Scheme 56).

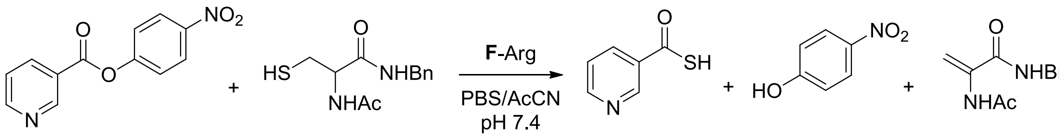

1 **2d** **3** **4** **5d**

Scheme 56. Enzyme mimic reaction with compound **2d**.

As the substrate, *N*-Acetyl-L-cysteine-*N'*-benzylamide (**2d**) was chosen for further investigation. The synthesis of compound **2d** was initially attempted using the same method employed for compound **2a**, where **Cys-Diac** underwent an amide formation reaction with benzyl amine. However, the reaction resulted in an extremely low yield (11%), indicating significant inefficiencies in the process (Scheme 57).

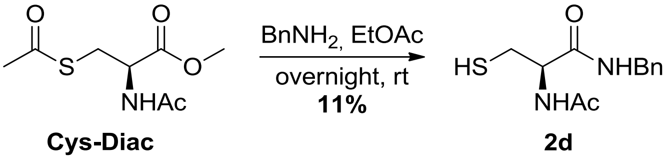

Scheme 57. Synthesis of **2d** from **Cys-Diac**.

To improve the efficiency, compound **2d** was synthesized using an alternative literature-based method, starting from N-Acetyl-L-cysteine (**NAC**), following a multi-step procedure to protect, modify, and deprotect the molecule.

The synthesis began with the protection of the thiol group in **NAC** using trityl chloride (Trt-Cl) [215], yielding **Trt-NAC** with a good yield of 82%. In this step, the highly reactive thiol group of **NAC** was effectively protected with the trityl group, ensuring that no undesired side reactions would occur during subsequent steps. Next, the protected compound **Trt-NAC** was subjected to an amide bond formation reaction with benzylamine ($BnNH_2$) [216]. The reaction began with the activation of the carboxyl group of **Trt-NAC** using isobutyl chloroformate (IBCF) and N-methylmorpholine (NMM). Following activation, benzylamine was added to the reaction mixture and this process successfully yielded *N*-Acetyl-*S*-trityl-L-cysteine benzyl amide (**Trt-NAC-NHBn**) with a yield of 80%. Finally, the trityl protecting group was deprotected using TFA in the presence of triisopropylsilane (TIPS) as a scavenger [217]. After the reaction, the target compound **2d** was obtained. This final step restored the free thiol group while leaving the benzylamide moiety preserved (Scheme 58).

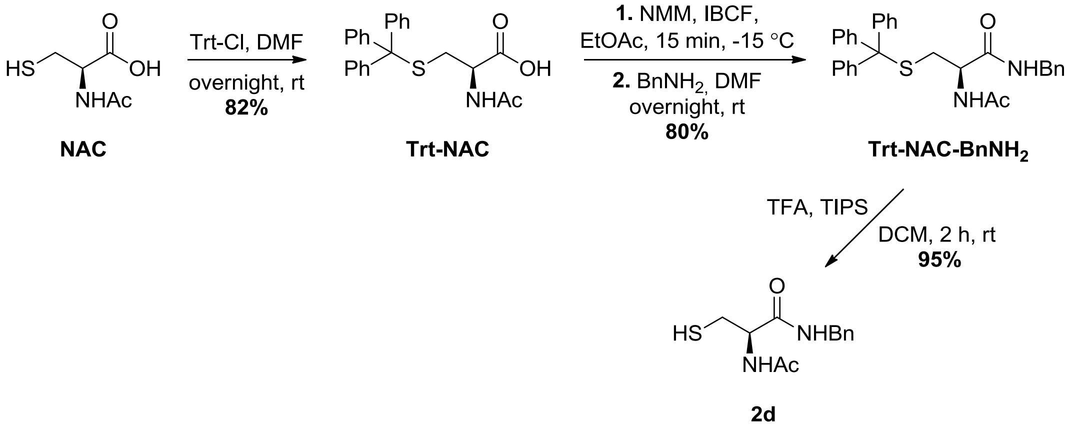

Scheme 58. Schematic representation of the synthetic route to **2d**.

To accurately determine the retention time of compound **5d** in HPLC and use it as a reference, this compound was independently synthesized.

The first reaction was the synthesis of **ACA** following the same procedure as described before. Next, **ACA** underwent an amide bond formation reaction with benzylamine. The carboxyl group of **ACA** was first activated using DCC and *N*-hydroxysuccinimide (HOSu). This activation step facilitated the formation of a reactive succinimide ester intermediate, which was subsequently reacted with benzylamine overnight at room temperature. The reaction successfully yielded the final product, compound **5d**, with a yield of 65% (Scheme 59).

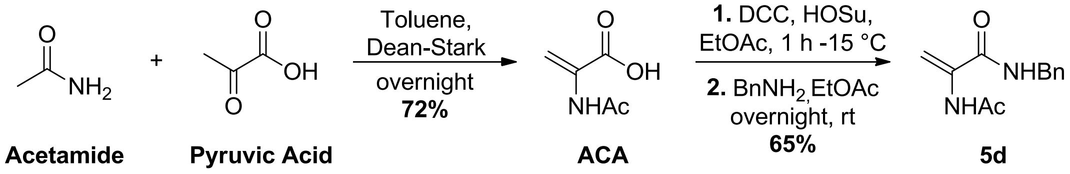

Scheme 59. Schematic representation of the synthetic route to **5d**.

2.1.7 Enzymatic Mimic Study with Compound 2d as a Cysteine Derivative

In these measurements, acetonitrile (MeCN) was used instead of DMSO, which had been used as a co-solvent in previous experiments. This substitution was made because DMSO resulted in a large band in the HPLC chromatogram and had the potential to cause various interferences and peak overlaps.

2.1.7.1 HPLC Calibration of Dehydroalanine Derivative Compound 5d

Compound **5d** was dissolved in acetonitrile at six known concentrations. Subsequently, HPLC analysis was performed. This analysis served two purposes: to determine the retention time of compound **5d** in HPLC and to establish a correlation between HPLC peak areas and known concentrations, allowing for the quantification of this dehydroalanine derivative in kinetic measurements (Table 5). After analyzing compound **5d** at these six concentrations, a calibration curve was generated, and the resulting equation (Figure 28) was established for use in subsequent calculations.

Table 5. Calibration curve of **5d**.

Entry	Concentration (mM)	Peak Area (mAU.min)
1	0.12	53.6675
2	0.25	101.4794
3	0.5	271.1415
4	0.7	327.358
5	1.0	502.9939
6	1.3	664.2216

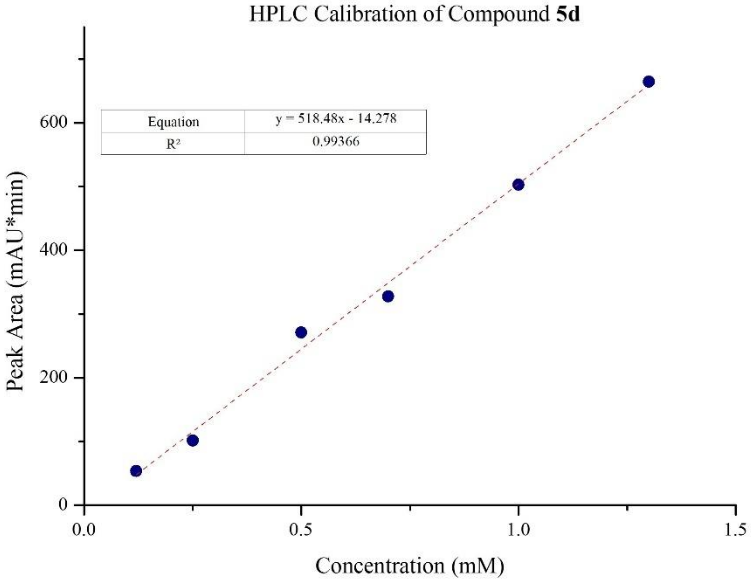

Figure 28. Calibration curve graph of **5d**.

2.1.7.2 Optimization of the Enzymatic Mimic Study

For kinetic measurements, a 12 mM stock solution of compound **1** was prepared in MeCN, while a 0.2 mM stock solution of **F**-Arg was prepared in phosphate buffer (100 mM, 60 mM KCl, pH 7.4). Additionally, a 4.0 mM stock solution of compound **2d** was prepared in a PBS and MeCN mixture. Before starting the kinetic studies, HPLC analysis was conducted (PS-C18 column, gradient elution from 1% to 90% MeCN/H_2O over 30 minutes) to confirm the retention times of the compounds and ensure proper separation (Figure B.3, Figure B.4, Figure B.5). The established calibration curve was then applied for quantification in subsequent kinetic evaluations.

Next, the initial reactions were carried out as described in previous trials (compound **1**: 0.6 mM, compound **2d**: 0.5 mM, and **F**-Arg: 0.005 mM (1 mol%). The reaction was monitored by HPLC at regular intervals over 30 minutes. While a gradual increase in thioester concentration was observed over time, the formation of the dehydroalanine derivative (compound **5d**) which has a retention time of 19.0 min, was not detected (Figure 29). This suggests that the conversion of thioester to compound **5d** occurs at a slower rate than initially anticipated.

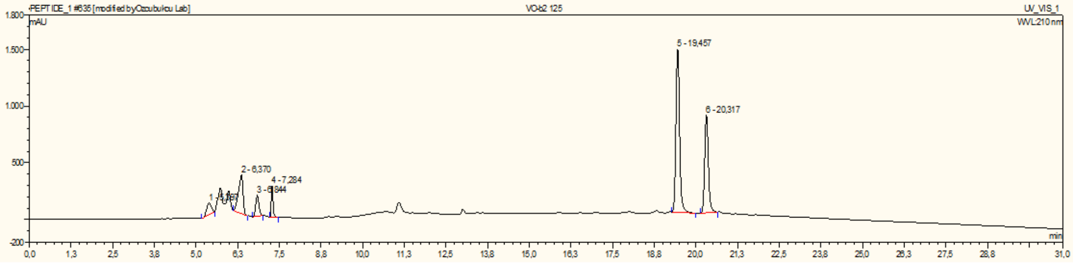

Figure 29. HPLC chromatogram of thioester formation with no detectable dehydroalanine (compound **5d**).

Therefore, thioester formation was first carried out without the addition of **F**-Arg. For this, the reaction mixture was stirred at room temperature for 1 hour in a test tube. Subsequently, 2 mol% **F**-Arg was added, and the reaction mixture was divided into four equal portions. The first portion was kept stirring at room temperature, while the others were stirred at 35 °C, 45 °C, and 55 °C, respectively.

After preparing these reaction sets, samples were taken every five minutes for one hour from each reaction and acidified to quench the reaction progress. The samples were then analyzed by HPLC. In the reaction conducted at room temperature, no dehydroalanine formation was observed even after one hour. In contrast, decomposition was detected in the reactions at 45 °C and 55 °C (Figure 30), while in the reaction carried out at 35 °C, a dehydroalanine peak was observed in all samples taken after the 45th minute (Figure 31).

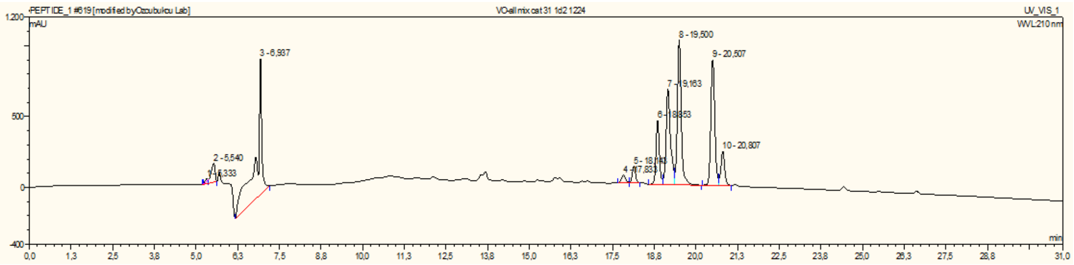

Figure 30. HPLC chromatogram of decompositions in the reaction at 55 °C.

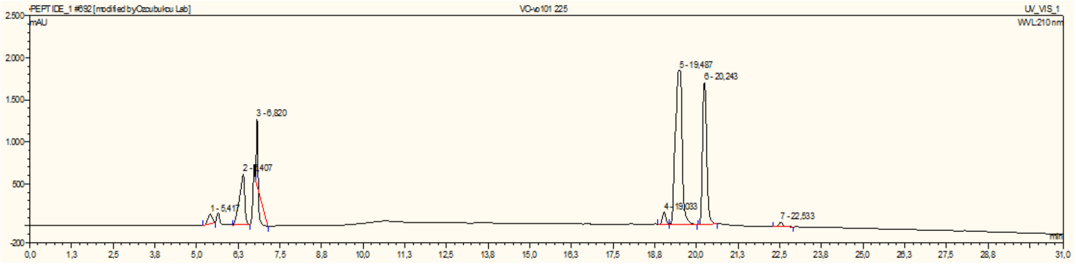

Figure 31. HPLC chromatogram of dehydroalanine formation in the reaction at 35 °C.

As a result, the reaction was successfully optimized under these conditions, and kinetic measurements were set to begin starting from the 45th minute.

2.1.7.3 LC-MS Analysis of the Reaction and Dehydroalanine Formation

To further confirm the formation of dehydroalanine, LC-MS analysis was performed both before catalyst addition as a control experiment and under optimized reaction conditions with the catalyst at 35 °C, starting from the 45th minute.

In the absence of the catalyst, LC-MS analysis of the reaction mixture revealed no detectable peak corresponding to dehydroalanine derivative compound **5d**. The LC chromatogram recorded under these conditions (Figure 32) displayed two peaks at 22.65 min and 23.48 min, corresponding to the starting material compound **2d** and the intermediate thioester d, respectively. The mass spectra of these peaks (Figures 33 and Figure 34) confirmed their expected molecular ion peaks. The peak at 22.65 min exhibited an observed mass of m/z 253.0949 in positive ion mode, in agreement with the theoretical value of m/z 253.0966 for $[M+H]^+$. Similarly, the peak at 23.48 min showed an observed mass of m/z 358.1163, in agreement with the theoretical m/z 358.1181 for $[M+H]^+$ of **thioester d**.

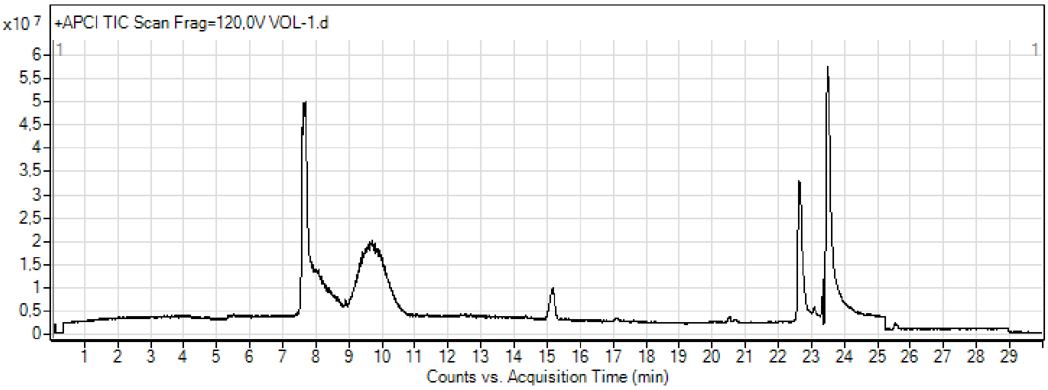

Figure 32. LC chromatogram of the reaction without the catalyst.

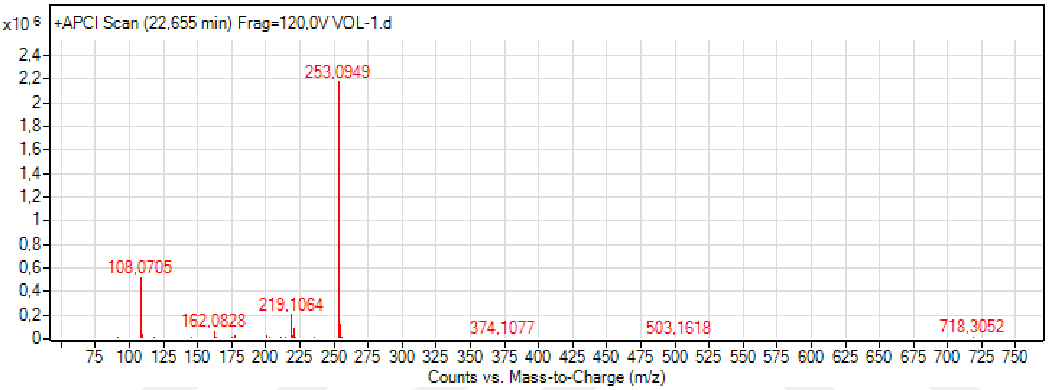

Figure 33. Mass spectrum of compound **2d** (peak 1 at 22.65 min).

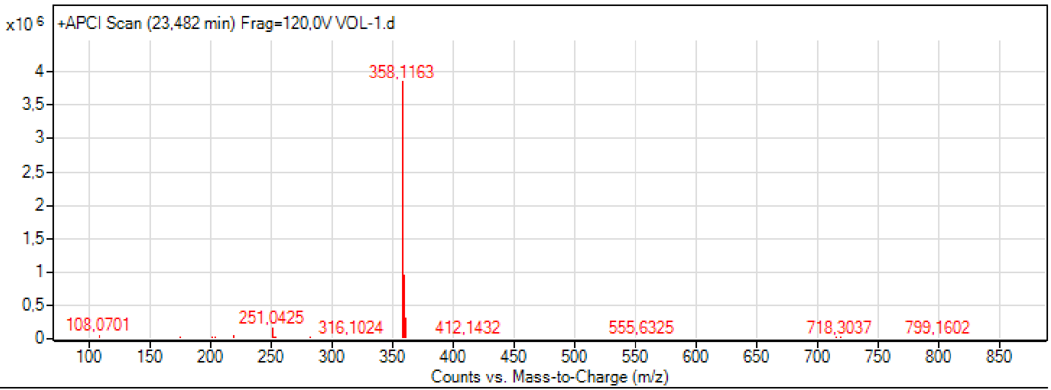

Figure 34. Mass spectrum of **thioester d** (peak 2 at 23.48 min).

A separate reaction involving **F**-Arg was conducted under optimized conditions, and LC-MS analysis revealed an extra peak compared to the catalyst-free experiment. While the peaks corresponding to compound **2d** and **thioester d** were still present, an additional peak at 22.61 min was detected (Figure 35). The mass spectrum of this peak exhibited an observed mass of m/z 219.1070 (Figure 36), in agreement with the expected m/z 219.1089 for $[M+H]^+$ of compound **5d**, confirming its formation under these conditions.

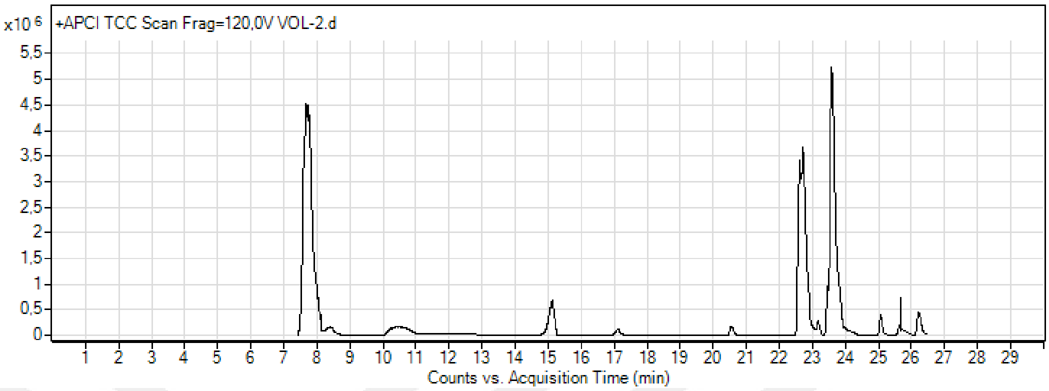

Figure 35. LC chromatogram of the reaction with **F**-Arg.

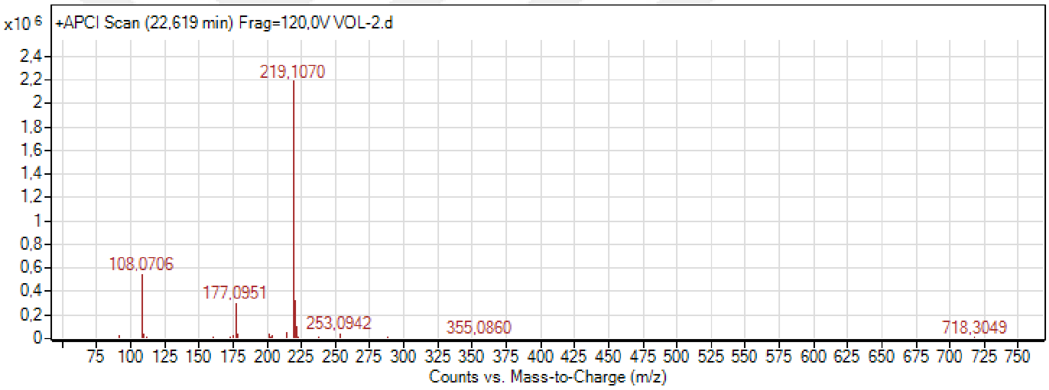

Figure 36. Mass spectrum of compound **5d** (peak at 22.61 min).

2.1.7.4 Kinetic Measurements

After successfully completing the optimization for kinetic measurements, the first set of experiments was prepared. In this set, 0.6 mM compound **1** and 0.5 mM compound **2d** were mixed and stirred at room temperature for 1 hour to allow thioester formation to reach completion. The reaction mixture was then heated to 35 °C, and 0.01 mM (2 mol%) **F**-Arg was added. Samples were collected at 45, 75, 110, 150, 200, 300, 420, and 1440 minutes, and the reactions were quenched by acidification before being analyzed by HPLC to monitor reaction progress (Figure 37).

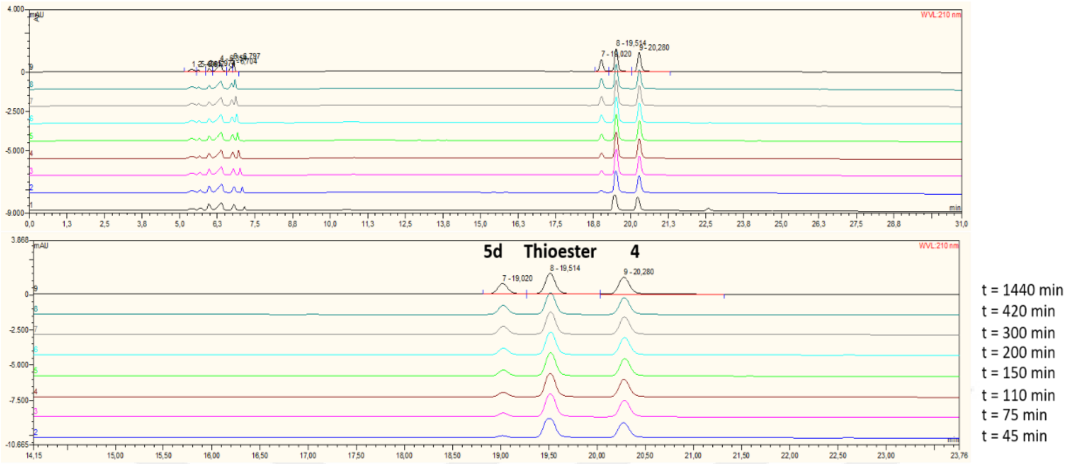

Figure 37. HPLC chromatograms of the time-dependent progress of the reaction at 35 °C monitored at 210 nm.

As observed in the graph (Figure 38) and chromatograms, the concentration of compound **5d** increased over time. However, despite the presence of thioester in the reaction mixture, the reaction progress began to slow after the 5th hour (300 min) and eventually reached a plateau around the 7th hour (420 min).

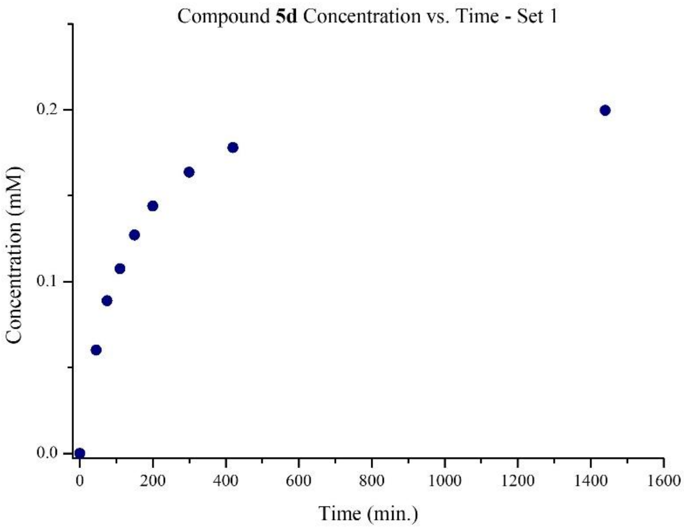

Figure 38. Kinetic measurements of Set 1.

Since the reaction progressed linearly up to 200 minutes before the slope started decreasing and eventually reached a plateau, only the first 200 minutes were considered for kinetic analysis. For consistency, the same approach was applied to the other sets, and only data up to 200 minutes were evaluated (Figure 39).

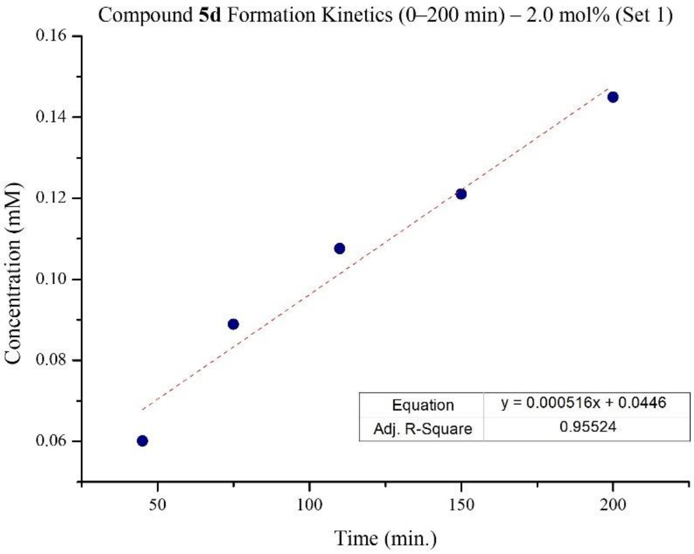

Figure 39. Kinetic measurements of Set 1 (0-200 min).

Next, to investigate the effect of catalyst concentration on the reaction rate, the reaction was conducted using a constant concentration of compound **1** and compound **2d** while varying the **F**-Arg concentration to 1, 1.3, and 2.7 mol% (Figure 40). As expected, increasing the catalyst concentration led to a corresponding increase in reaction rate, supporting the catalytic role of **F**-Arg in the conversion.

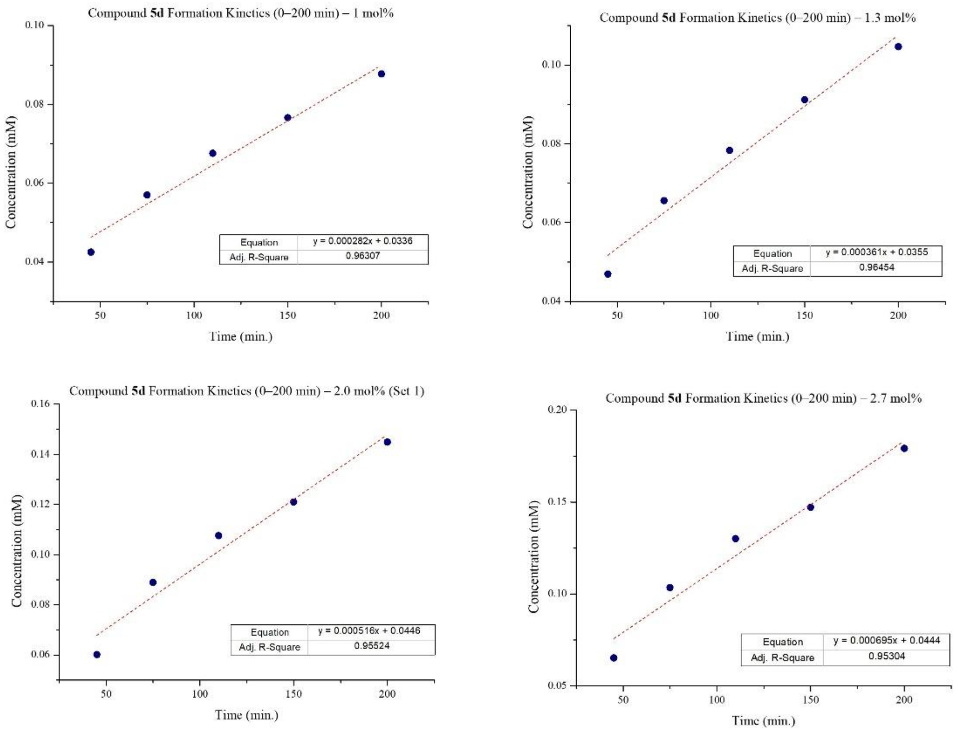

Figure 40. Kinetic measurements of different **F**-Arg concentrations.

Following the initial measurements, the reactions were conducted again to confirm the previous results and to evaluate the consistency of the linear increase at different time points. This time, a new set of experiments was conducted by selecting four time points (30, 50, 70, and 90 minutes), using the same **F**-Arg concentration as in the first series. As a result, four additional graphs were obtained (Figure 41). As expected, the calculated slopes were in strong agreement with the initial measurements. These findings provided further support for the reproducibility and reliability of the kinetic behavior observed in this experimental framework.

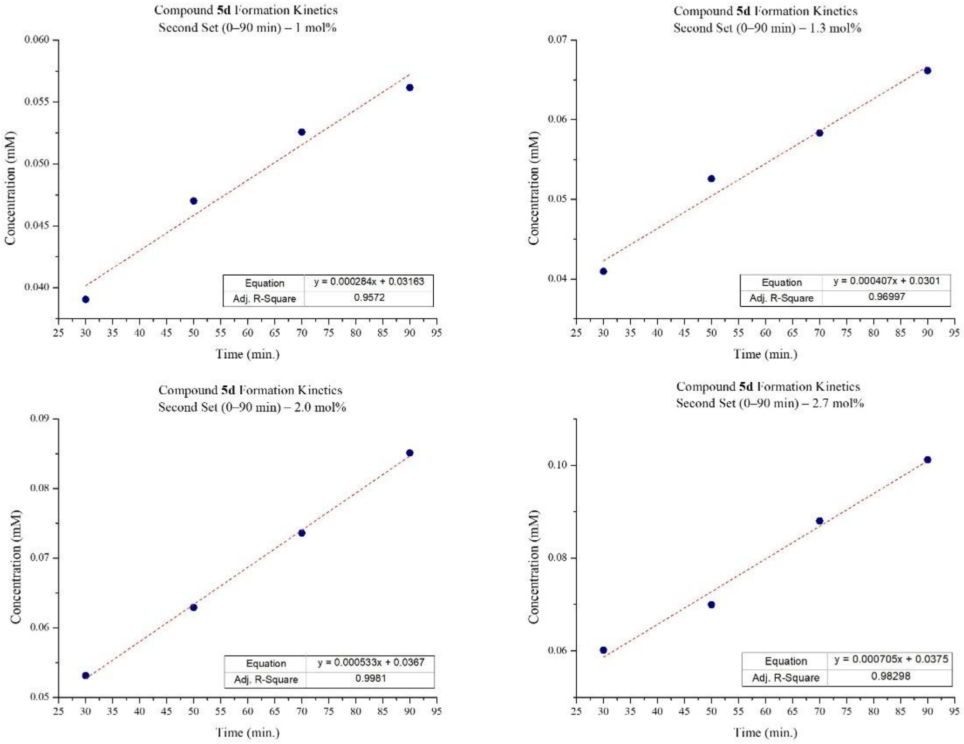

Figure 41. Second set of kinetic measurements of different **F**-Arg concentrations.

To evaluate the effect of catalyst concentration on the reaction rate, the average value of the slopes obtained from both the initial and second sets of measurements was calculated for each **F**-Arg concentration. These average values were then plotted against the corresponding catalyst concentrations to investigate the dependence of the reaction rate on **F**-Arg concentration. As shown in Figure 42, the resulting trend line displayed a clear linear relationship, suggesting that the reaction follows first-order behavior with respect to the catalyst under the tested conditions. This plot was also used to calculate the turnover number (k_{cat}) from the slope of the line. This provided a quantitative evaluation of how efficiently **F**-Arg catalyzed the reaction.

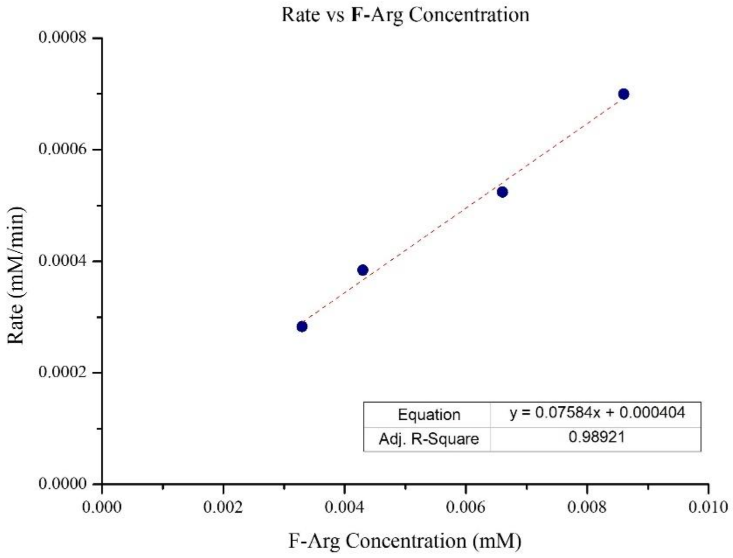

Figure 42. Rate vs **F**-Arg concentration graph.

The observed linear correlation between reaction rate and catalyst concentration further confirmed that **F**-Arg was directly responsible for the rate increasing in direct proportion to its concentration. Based on the slope of the trend line (0.0758 mM/min per mM **F**-Arg), k_{cat} was determined as 0.0758 min^{-1}. The linearity of the plot, supported by an R^2 value of 0.989, suggested a strong correlation between catalyst concentration and reaction rate. The calculated value illustrated the catalytic potential of **F**-Arg in this transformation.

After determining k_{cat}, the next step was to evaluate the effect of substrate concentration on reaction kinetics and determine the Michaelis constant (K_m). For this purpose, the concentration of **F**-Arg was kept constant, while the concentrations of compound **1** and compound **2d** were systematically varied. This approach enabled the investigation of how substrate concentration influences the reaction rate, providing further insights into the kinetic behavior of the system.

The variations in substrate concentration were designed based on a reference set containing 0.6 mM compound **1**, 0.5 mM compound **2d**, and 1.3 mol% **F**-Arg. In the additional experimental sets, compound **1** and compound **2d** concentrations were systematically adjusted as follows:

- Set 5: 0.4 mM compound **1**, 0.33 mM compound **2d**
- Set 6: 0.9 mM compound **1**, 0.75 mM compound **2d**
- Set 7: 1.2 mM compound **1**, 1.0 mM compound **2d**
- Set 8: 1.5 mM compound **1**, 1.25 mM compound **2d**

By varying these concentrations while keeping **F**-Arg constant, the effect of substrate availability on reaction kinetics was evaluated (Figure 43).

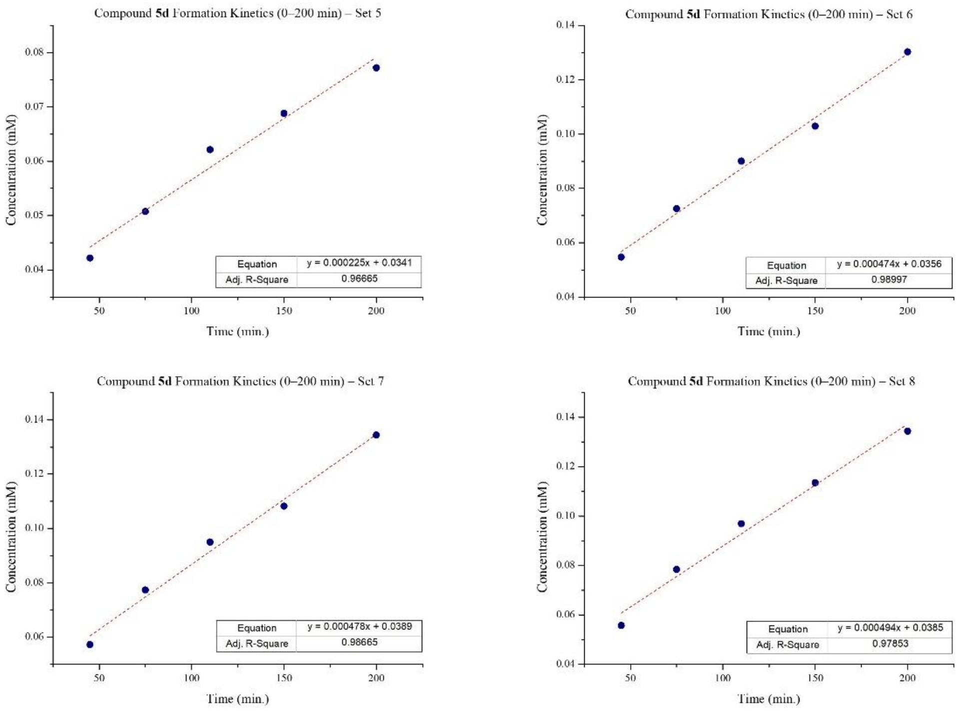

Figure 43. Kinetic measurements of different substrate concentrations.

The reaction rate was determined for each condition and plotted against substrate concentration to evaluate the dependence of the rate on substrate availability. In these experiments, the concentration of Compound **2d** was taken into account (Figure 44). This allowed a clearer observation of how substrate concentrations influenced catalytic behavior.

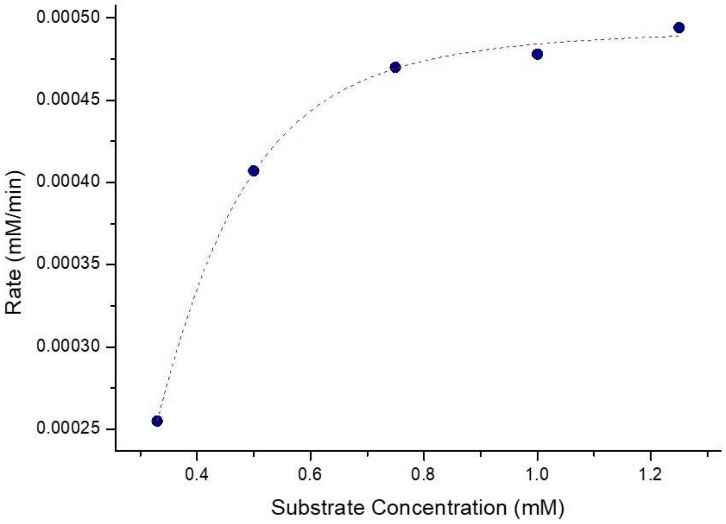

Figure 44. Rate vs substrate concentrations graph.

To determine K_m, the reaction rate data was analyzed to identify the substrate concentration at which the reaction rate reached half of V_{max}. This approach follows the classical Michaelis-Menten model, where K_m represents the substrate concentration required to achieve half-maximal velocity. Based on the experimental data, K_m was estimated as 0.33 mM.

To evaluate the catalytic efficiency of the system, k_{cat}/K_m ratio was determined. This parameter demonstrated how efficiently the catalyst worked when substrate concentration was low. Based on the experimental data, k_{cat}/K_m was calculated as 0.2297 mM^{-1} min^{-1}, indicating the catalyst's efficiency in converting substrate to product. However, since LarE acts more like a reactant than a conventional enzyme in LarA synthesis, a direct comparison of these values with the literature was not possible.

The experimental data indicated that substrate saturation was reached quickly, which limited the number of data points available for accurately determining K_m. While this did not affect the overall evaluation of the kinetic behavior, additional measurements at lower substrate concentrations could improve the precision of K_m. However, due to the clear saturation trend was observed, no further experiments were performed within the scope of this study.

Following these determinations, the reaction was carried out under the same conditions but without **F**-Arg and no formation of dehydroalanine was observed. Additionally, when pristine arginine was used in the ratios applied in this study, product formation did not occur. However, when pristine arginine was used in a stoichiometric amount with the substrates, dehydroalanine was observed. This result indicated that pristine arginine was only effective in equimolar quantities, whereas **F**-Arg exhibited a distinct catalytic role, driving the reaction in a manner that mimicked enzymatic efficiency.

Although the results presented here suggest a promising catalytic role for **F**-Arg in mimicking the enzymatic activity of LarE, it is important to note that these findings are based on preliminary kinetic measurements. The experiments were conducted in single and duplicate runs under controlled conditions, providing an initial but limited view of the catalytic properties of the biomimetic framework. To further evaluate the reproducibility and consistency of these results, additional repetitions could be conducted. These could involve varied degrees of arginine substitution, as well as other amino acid-functionalized fullerenols. These future studies would not only validate the current findings but also provide a deeper understanding of how structural variations influence catalytic performance.

2.2 Acetylcholine Detection

In this part of the thesis, the synthesis, characterization, and electrochemical evaluation of histidine and serine functionalized fullerenol (**F-**HS) for acetylcholine detection, a biomarker in Alzheimer's disease diagnosis were described. The structural and morphological properties of the synthesized conjugates were analyzed using NMR spectroscopy, SEM, TEM, and DLS, while their acetylcholine binding and detection capabilities were evaluated through electrochemical measurements.

While the synthesis and characterization were carried out as part of this study, the electrochemical measurements were performed by Dr. Söylemez from Necmettin Erbakan University. The findings from these analyses provided valuable information into the structural stability and functional behavior of the enzyme mimics, which were discussed in detail below. This study has been previously published in [206], and the key results are presented here for completeness, along with additional discussions relevant to this thesis.

2.2.1 Synthesis and Characterization of F-HS

The synthesis of **F**-HS was carried out using the same method as F-Arg synthesis. However, unlike in **F**-Arg synthesis, where only a single amino acid was used, histidine and serine were added together to the reaction mixture to ensure the functionalization of a single fullerene core with two different amino acids (Scheme 60). Once the reaction was complete, the purification steps were performed in the same way as in the **F**-Arg synthesis.

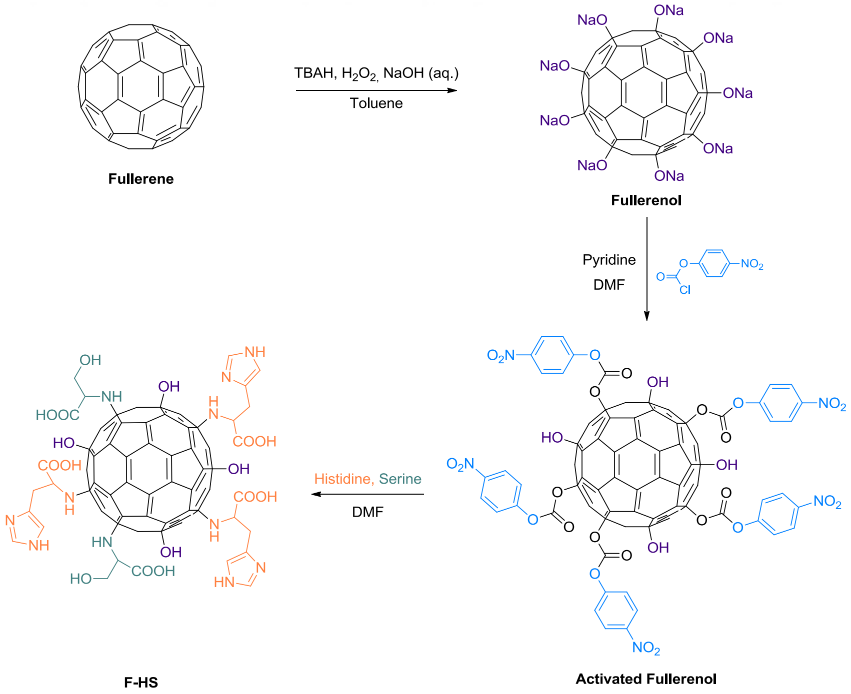

Scheme 60. Schematic representation of the synthetic route to **F**-HS.

The degree of histidine and serine substitution was determined using ^{1}H NMR spectroscopy by incorporating an internal standard, following the same method used for arginine substitution analysis. Following NMR analysis, it was determined that the amounts of integrated serine and histidine on fullerenol were approximately equal. Using the calculation equation, the number of histidine units per **F**-HS molecule was found to be around six (x = 6.23), while the number of serine units was also six.

2.2.2 The Stability Test of F-HS at pH 13

To determine the optimal pH conditions for both the overall experimental procedure and the efficient detection of acetylcholine, electrode optimization was performed by Dr. Söylemez in NaOH solutions with varying pH values, corresponding to concentrations ranging from 0.05 M to 0.2 M. Among these, the electrochemical response at pH 13 (0.1 M NaOH) was found to be the highest, fastest, and most stable compared to other conditions. Therefore, the stability test for **F**-HS was conducted at pH 13.

The stability of **F**-HS under these conditions was investigated using ^{1}H NMR spectroscopy, where the sample was monitored at pH 13 for 24 hours (Figure 45). No significant decomposition was observed, and the structure remained intact even after 72 hours (Figure 46), confirming the stability of the conjugate in highly basic conditions.

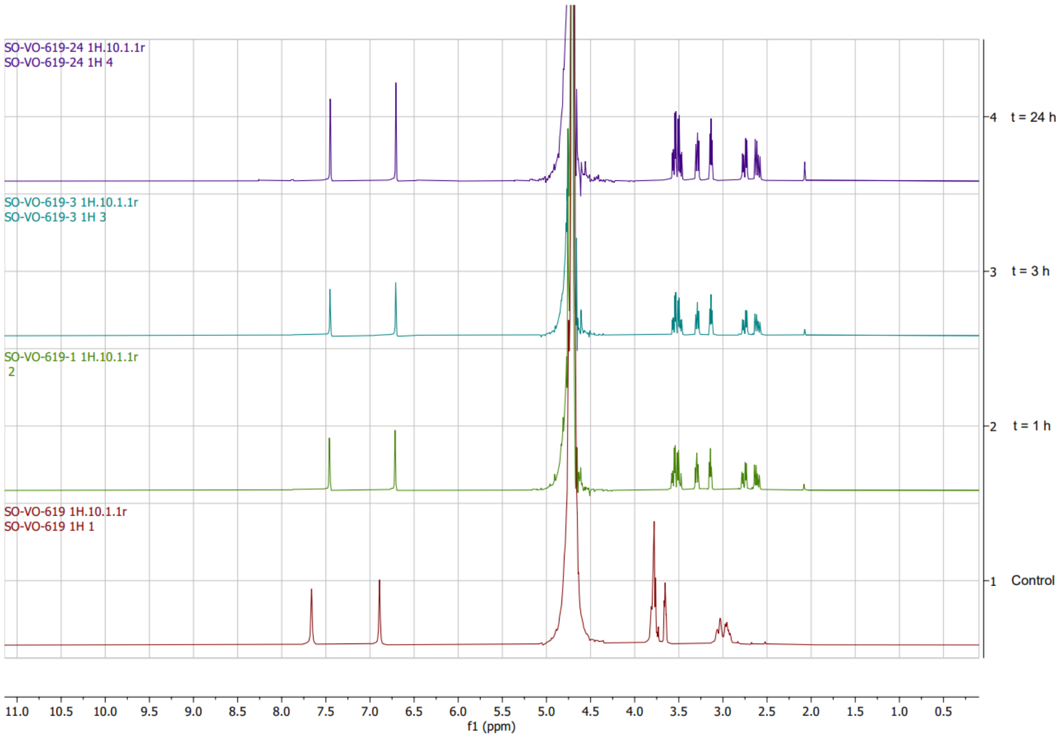

Figure 45. Stability analysis of **F**-HS under basic conditions (pH 13) by ^{1}H NMR spectroscopy in D_2O.

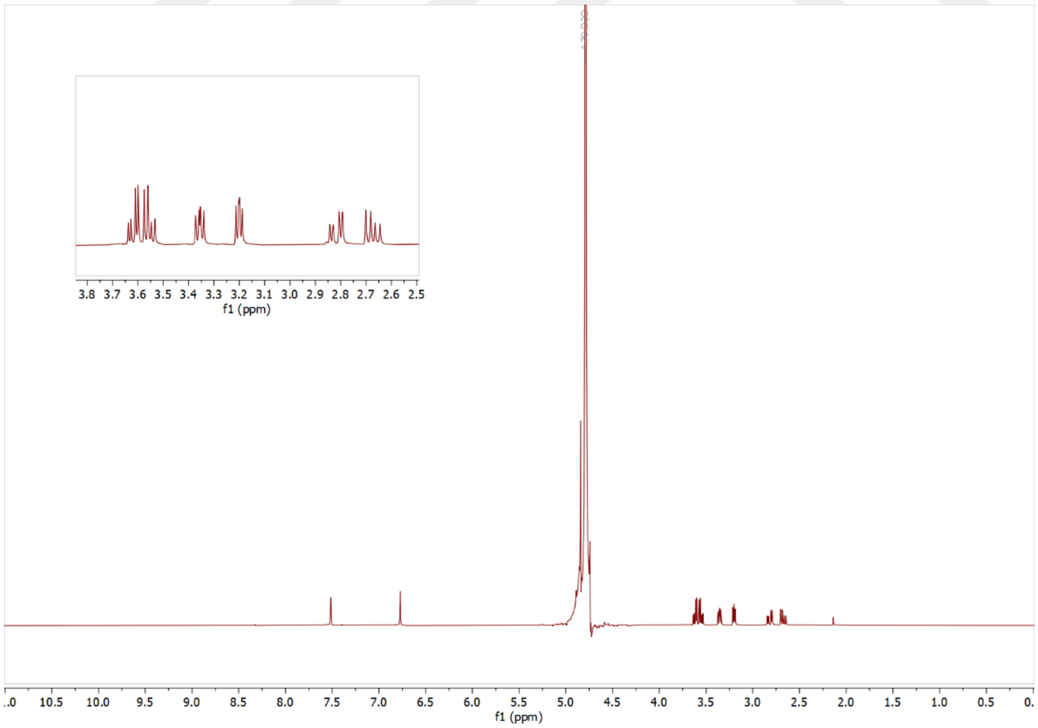

Figure 46. ^{1}H NMR spectrum of **F**-HS at pH 13 for 72 h in D_2O.

2.2.3 Morphological Analysis of F-HS and F-HS-Ni

In this study, nickel ions were coordinated with the nitrogen of the imidazole ring in the histidine moiety. The morphologies of **F**-HS and **F**-HS-Ni were analyzed using field emission scanning electron microscopy (FE-SEM), which confirmed their spherical structures (Figure 47). Upon the addition of nickel ions to the **F**-HS solution, coordination led to the formation of larger particles and increased aggregation compared to pristine **F**-HS, as observed in FE-SEM images and confirmed by dynamic light scattering (DLS) measurements (Figure 48).

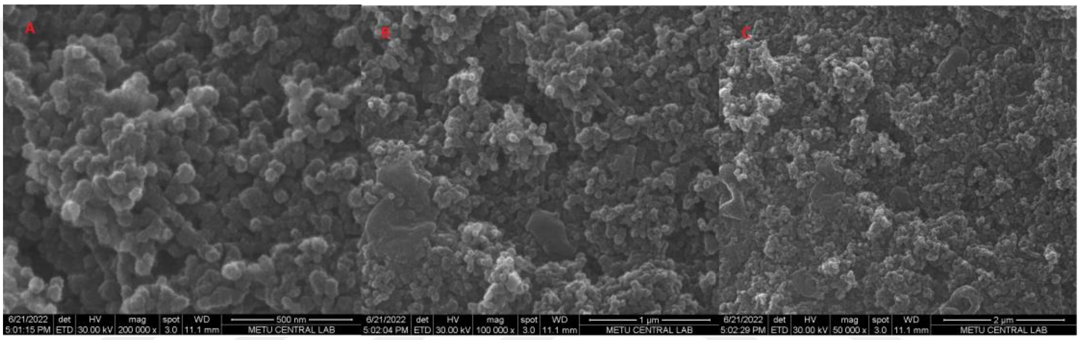

Figure 47. FE-SEM images of **F**-HS at different magnifications: (A) 500 nm, (B) 1 µm, and (C) 2 µm.

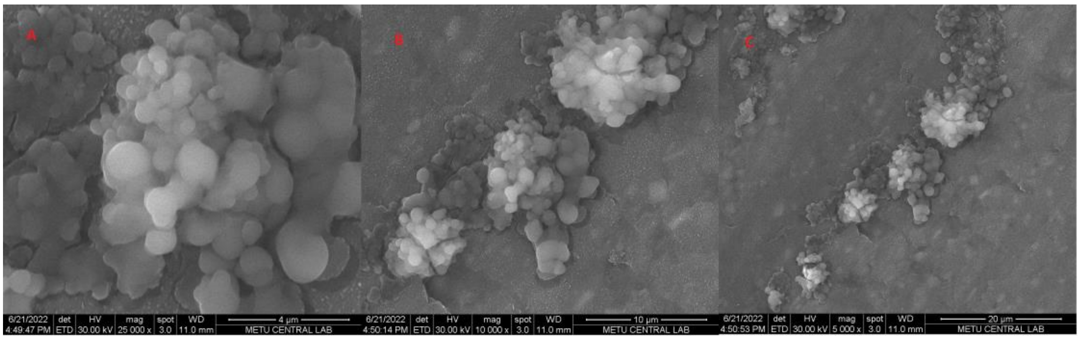

Figure 48. FE-SEM images of **F**-HS-Ni at different magnifications: (A) 4 µm, (B) 10 µm, and (C) 20 µm.

The presence of nickel ions was further supported by energy-dispersive X-ray spectroscopy (EDX) analysis (Figure 49). The size distributions of **F**-HS and nickel-coordinated **F**-HS were measured using DLS at 24 °C, with solutions sonicated for 30 minutes to break up aggregates. The results showed that the average particle size increased from 16 nm to 173 nm after nickel coordination (Table 6). The significant increase in particle size indicates that nickel ions interacted with the imidazole rings of histidine, leading to aggregation. This aggregation was most likely driven by metal-ligand coordination and electrostatic interactions. Similar behavior had been reported in metal-coordinated nanomaterials, where transition metals promoted self-assembly and clustering as crosslinking agents.

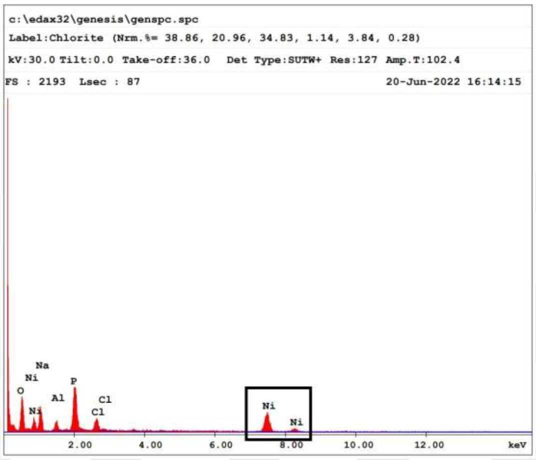

Figure 49. EDX result of the coordination of **F**-HS with a nickel ion.

Table 6. DLS size distribution of **F**-HS and **F**-HS-Ni.

Compound	Size (d.nm)	Number%
F-HS	16.08	100
F-HS-Ni	173.6	93.5

TEM images also revealed structural differences between the samples, further confirming the aggregation behavior (Figure 50, Figure 51). The clustering observed in **F**-HS-Ni indicated that nickel coordination had a strong effect on the material's dispersion. This aggregation could affect its electrochemical properties by increasing the active surface area for acetylcholine detection, potentially enhancing sensor performance.

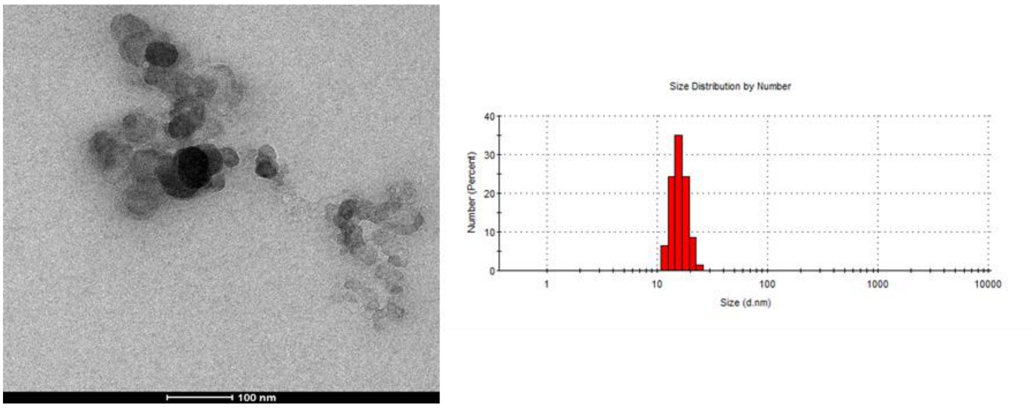

Figure 50. TEM image and corresponding DLS readout of **F**-HS.

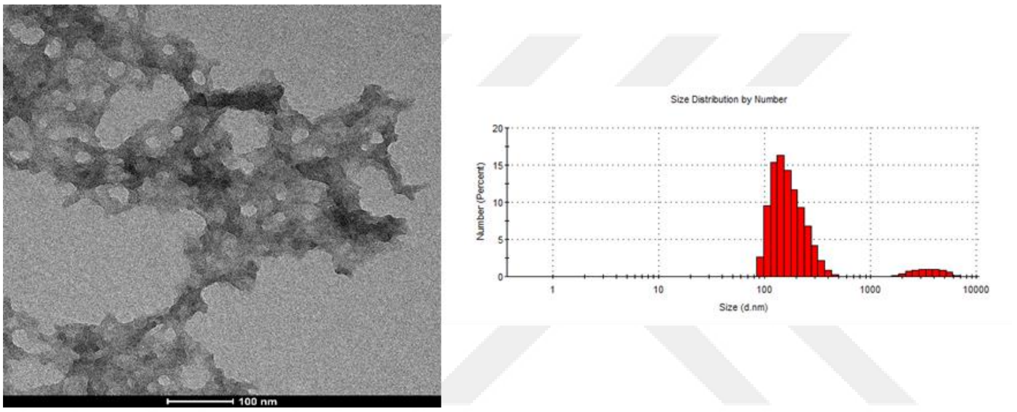

Figure 51. TEM image and corresponding DLS readout of **F**-HS-Ni.

2.2.4 FTIR Analysis of F-HS and F-HS-Ni

FTIR analysis was performed to compare **F**-HS and **F**-HS-Ni. The broad peak at 3470 cm^{-1} in the FTIR spectrum corresponded to the OH groups of fullerenol and serine. The aromatic C-H stretching of histidine appeared at 3010 cm^{-1}, while the C=O stretching of the carboxyl groups in histidine and serine was observed around 1720 cm^{-1}. The peaks at 2840 and 2940 cm^{-1} were assigned to the C–H stretching of the aliphatic regions of fullerene after conjugation with histidine and serine. The C–O stretching of histidine, serine, and fullerenol was detected at 1330 cm^{-1}. N–H stretching of the amine groups in histidine appeared in the 3380–3420 cm^{-1} range (Figure 52). After coordination with nickel ions, this N–H stretching became more distinct, suggesting a direct interaction between nickel and the imidazole ring of histidine. These spectral changes aligned with typical metal-ligand interactions and provided strong confirmation of successful nickel binding to the histidine moiety.

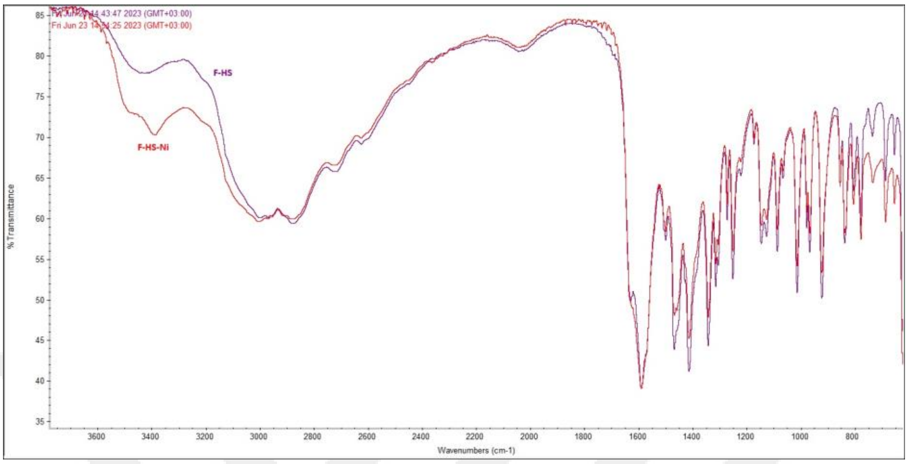

Figure 52. FTIR Analysis of **F**-HS and **F**-HS-Ni (Purple line: **F**-HS, red line: **F**-HS-Ni).

2.2.5 Electrochemical Performance and Sensor Application of F-HS-Ni

In this part of the thesis, the synthesis and characterization of **F**-HS were carried out, and its structural and morphological properties were thoroughly analyzed using NMR, SEM, TEM, DLS, and FTIR. Following these steps, the electrochemical measurements and sensor evaluations were conducted by Dr. Söylemez to evaluate the electrocatalytic performance of the synthesized material.

Electrochemical studies demonstrated that the **F**-HS-Ni/GE non-enzymatic sensor introduced a novel electrode-building approach. It achieved a linear detection range of 20 to 6000 μM for acetylcholine (ACh). The detection limit was as low as 8.01 μM. In human serum samples, the **F**-HS-Ni/GE sensor exhibited a fast response time of 10 seconds while maintaining good stability and reproducibility. Furthermore, the sensor enabled the sensitive and selective analysis of ACh in human serum samples with high accuracy, highlighting its potential for biomedical applications, particularly in Alzheimer’s disease diagnostics.

Beyond its strong sensing performance, **F**-HS-Ni demonstrates potential as a reliable enzyme-mimicking electrocatalyst. Its stability and selectivity made it a promising candidate for further development in biosensing technologies, particularly for real-world diagnostic applications.

2.3 Fullerenol Applications as Organocatalysts

As a starting point for evaluating catalytic activity, CO_2 fixation was chosen to evaluate whether the **F**-AA catalysts could promote the reaction through hydrogen bonding or nucleophilic activation under mild conditions. The potential of fullerenol and its amino acid derivatives as organocatalysts was explored in this part of the thesis by evaluating their catalytic potential in four distinct reactions: CO_2 fixation, Morita-Baylis-Hillman (MBH) reaction, 2-amino chromene derivative synthesis, and Prins cyclization. While these transformations are typically catalyzed by amines, Lewis acids, or other conventional catalysts, the use of fullerenol as an organocatalyst remains relatively underexplored. Due to its rich electronic structure, multiple reactive functional groups, and stability, fullerenol presents a promising alternative in organocatalysis.

2.3.1 CO_2 Fixation

The fixation of carbon dioxide (CO_2) into valuable products has gained significant attention as a sustainable approach for carbon utilization. In this part of the thesis, fullerenol-amino acid derivatives (**F**-AA) were evaluated as catalysts for the conversion of CO_2 and epoxides into cyclic carbonate derivatives under mild conditions. The catalytic efficiency of different **F**-AA derivatives was examined, along with the effects of reaction parameters such as temperature, catalyst type, co-catalyst selection, and substrate diversity. The results were compared with literature examples to highlight the advantages and limitations of this approach.

2.3.1.1 Catalytic Activity of Fullerenol and F-AA Derivatives

To evaluate the catalytic efficiency of the synthesized catalysts, initial reactions were conducted using fullerenol and **F**-AA derivatives. Styrene oxide (**SO**) was selected as the epoxide substrate due to its extensively studied reactivity in CO_2 fixation reactions, while tetrabutylammonium iodide (TBAI) was used as the iodide source and co-catalyst to enhance reaction efficiency (Scheme 61). In order to compare the different effects, basic amino acids (arginine and histidine), acidic amino acids (glutamic acid and aspartic acid), and a simple amino acid (glycine) were selected for functionalization with fullerenol. For their synthesis, the same method as the synthesis of **F**-Arg was followed, and the degree of amino acid substitutions was determined using the same approach.

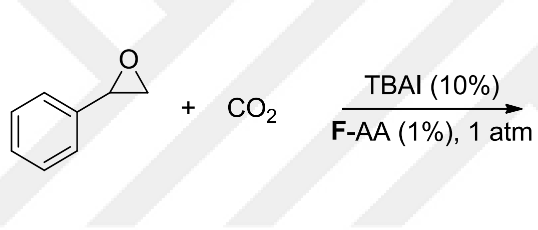

SO

SC

AA: Arginine, histidine, glycine
glutamic acid, aspartic acid

Scheme 61. Schematic representation of the synthetic route to the cyclic carbonate.

The extant of conversations was determined using ^{1}H NMR spectroscopy, by comparing the integration of product peaks with those of the starting materials. The analysis was performed by analyzing a sample collected from the reaction mixture at the completion of the reaction using ^{1}H NMR spectroscopy. As shown in Figure 52, the, ^{1}H NMR spectrum of the reaction carried out with **F**-His as the catalyst at 50 °C for 24 hours. The peaks at 2.73, 3.07, and 3.79 ppm corresponded to the starting material, **SO**, while the peaks at 4.27, 4.74, and 5.62 ppm were assigned to the cyclic carbonate product, compound **SC**. Due to peak overlap between the aromatic hydrogen signals of the compound **SO** and the product **SC**, these signals were not considered for conversion calculations. The unassigned peaks in the spectrum originate from TBAI, which was present in the reaction mixture. As a result, the conversion rate for this reaction was determined to be 61% (Figure 53).

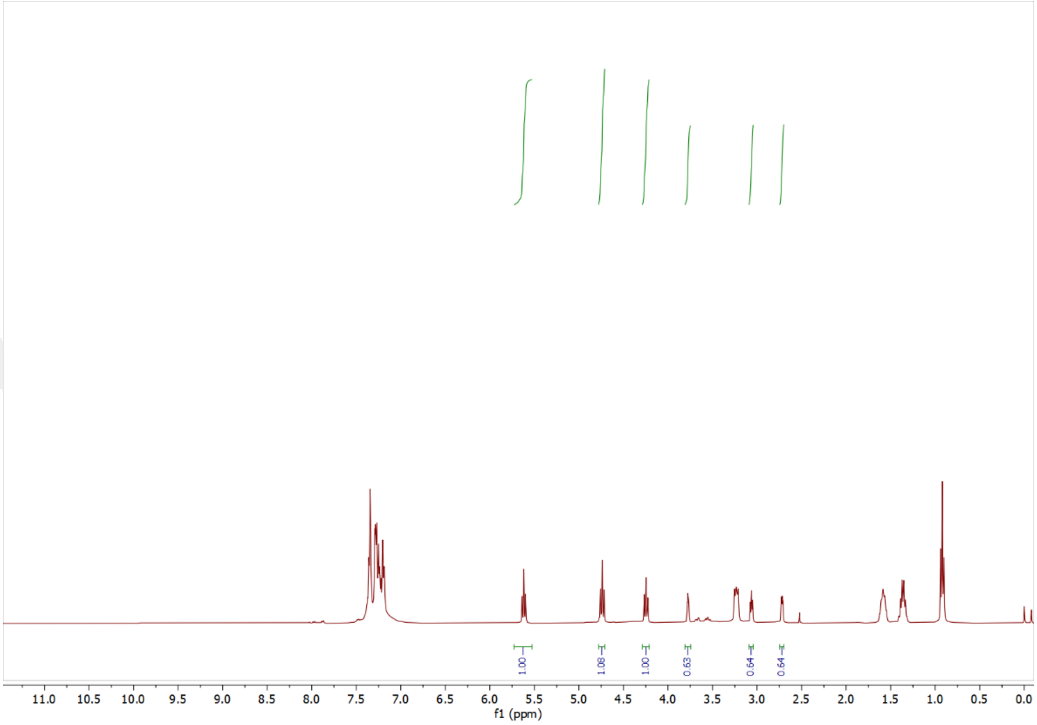

Figure 53. ^{1}H NMR spectrum of **F**-His catalyzed CO_2 fixation reaction at 50 °C in $CDCl_3$.

As shown in Table 7, fullerenol was initially used as the catalyst to determine the optimal reaction time at room temperature. However, even after 24 hours, the conversion remained insufficient (approximately 25%), leading to an evaluation of the reaction at an elevated temperature (50 °C) for the same duration. Notably, at room temperature, **F**-His exhibited an even lower conversion than fullerenol, suggesting that histidine functionalization alone did not enhance catalytic activity under these conditions. As indicated in the table, reactions conducted with **F**-AA catalysts resulted in an overall increase in conversion, approximately 20% higher than that of fullerenol. However, no significant differences were observed among the various amino acid derivatives. Additionally, when free amino acids (L-His, L-Glu, and L-Arg) were used as catalysts, the conversions remained remarkably low, highlighting the importance of functionalizing fullerenol with amino acids to enhance catalytic activity.

Table 7. Effect of catalyst type, reaction time, and temperature on the conversion efficiency in CO_2 fixation.

Catalyst (1 mol%)	Time (h)	Temperature (°C)	Conversion (%)
Fullerenol	2	RT	9
Fullerenol	5	RT	14
Fullerenol	8	RT	19
Fullerenol	24	RT	26
F-His	24	RT	23
Fullerenol	24	50	51
F-His	24	50	61
F-Gly	24	50	63
F-Asp	24	50	60
F-Arg	24	50	56
F-Glu	24	50	63
L-Histidine	24	50	10
L-Glutamic Acid	24	50	11
L-Arginine	24	50	10

The initial results demonstrated that **F**-AA derivatives could act as highly efficient catalysts for cyclic carbonate synthesis. These reactions were conducted under solvent-free (neat) conditions. To further investigate the effect of solvent on catalytic performance, the reaction was carried out using **F**-His as the catalyst under the same conditions (50 °C, 24 h) in the presence of DMF, a solvent capable of dissolving **F**-His. When the reaction was performed in 0.5 mL of DMF, the conversion decreased to 18%, and a further reduction to 12% was observed when 1.0 mL of DMF was used. This decline in conversion suggests that dilution of the reaction mixture in the presence of a solvent negatively affected the efficiency of the catalytic process.

2.3.1.2 Effects of Different Iodide Sources on Catalytic Performance

To further optimize the reaction conditions, different iodide sources were evaluated as co-catalysts. The initial reactions were conducted with TBAI and further analyses were performed using KI (potassium iodide) and BaI_2 (barium iodide) to compare their effects on catalytic performance. These iodide sources were selected based on their structural differences and common usage in similar catalytic systems, aiming to explore how co-catalyst identity affected the overall efficiency.

Table 8. Effect of iodide source on the conversion efficiency in CO_2 fixation.

Iodide Source (10 mol%)	Catalyst (1 mol%)	Time (h)	Temperature (°C)	Conversion (%)
TBAI	Fullerenol	24	50	51
KI	Fullerenol	24	50	32
BaI_2	Fullerenol	24	50	33
TBAI	**F**-His	24	50	61
BaI_2	**F**-His	24	50	41
KI	**F**-His	24	50	42
TBAI	**F**-Arg	24	50	56
BaI_2	**F**-Arg	24	50	40
KI	**F**-Arg	24	50	42
TBAI	**F**-Asp	24	50	60
BaI_2	**F**-Asp	24	50	39
KI	**F**-Asp	24	50	41

As shown in Table 8, when KI or BaI_2 was used as the iodide source, a decrease in conversion was observed (approximately 40%). This outcome was expected due to the reaction was performed under neat conditions, where solubility of the co-catalyst could influence the efficiency. Unlike the metal iodide salts, TBAI exhibited partial solubility in styrene oxide, leading to a more homogeneous reaction environment. This improved interaction likely contributed to the enhanced catalytic performance observed in the reaction

2.3.1.3 GC-MS Analysis

Additionally, conversion rates were monitored using GC-MS to ensure both accuracy and consistency in the analysis. To quantify the product yields, a calibration curve of compound **SC** was established by plotting signal intensity against known concentrations (Figure 54). This calibration provided a reliable reference point for evaluating the results. The GC-MS measurements served as an independent method for confirming the consistency of the product yields.

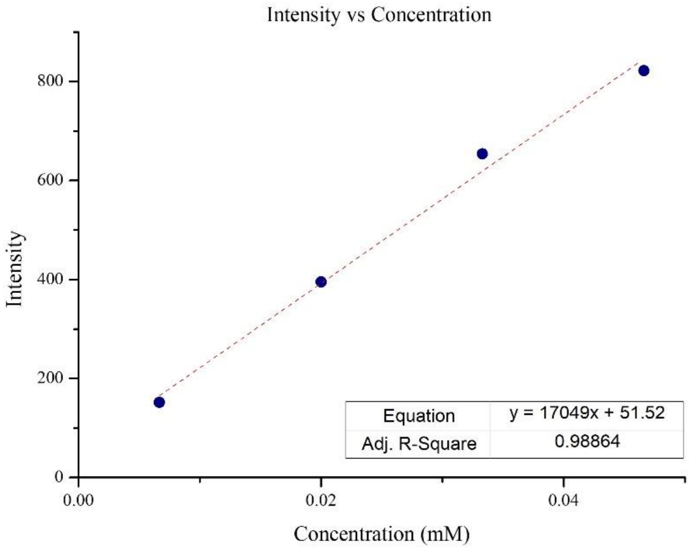

Figure 54. Calibration curve of the product **SC**.

In this set of experiments, the reactions were carried out at 75 °C. As shown in Table 9, compared to fullerenol, the use of **F**-AA catalysts resulted in approximately a 20% increase in conversion. However, no significant difference was observed among the different amino acid derivatives, similar to the previous result.

Table 9. Conversion efficiency in CO_2 fixation as determined by GC-MS.

Catalyst (1 mol%)	Time (h)	Temperature (°C)	Conversion (%)
Fullerenol	24	75	72
F-Arg	24	75	81
F-His	24	75	86
F-Asp	24	75	88
F-Glu	24	75	81

Finally, the reaction was performed using cyclohexene oxide and propylene oxide. However, under **F**-His catalysis at 50 °C, the conversions remained low, reaching only 11% and 6%, respectively. Due to these poor yields, no further experiments were conducted with these epoxides.

2.3.2 Morita-Baylis-Hillman (MBH) Reaction

As previously discussed, MBH reaction was chosen as a model transformation to investigate whether nucleophilic amino acid, histidine and arginine functionalized fullerenols could mimic the cooperative behavior observed in enzymatic active sites. In this context, histidine was proposed to serve as the nucleophile, while arginine would facilitate proton transfer, enabling the reaction to proceed efficiently under mild and metal-free conditions. The catalytic efficiency of fullerenol-amino acid derivatives (**F**-AA) in MBH reactions was investigated to explore their potential as enzyme-mimicking organocatalysts. Traditional MBH reactions primarily rely on nucleophilic tertiary amines and phosphines; however, the use of biomimetic catalysts, such as **F**-Arg and **F**-His, offers an alternative approach. In this part of the thesis, the catalytic performance of these fullerene-based catalysts was evaluated in the reaction between *p*-nitrobenzaldehyde (**M1a**) and 2-cyclohexen-1-one (**M2**) (Scheme 62), and the conversion rates were analyzed using ^{1}H NMR spectroscopy.

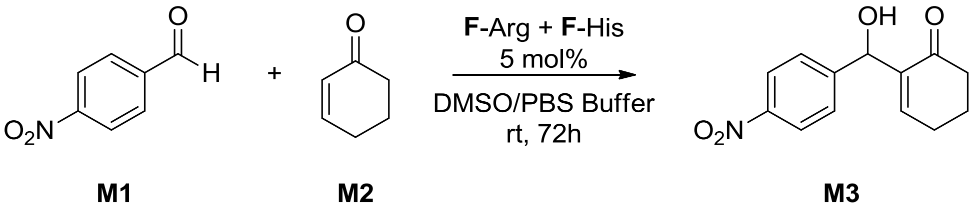

Scheme 62. MBH reaction as performed in this study.

The reaction took place in a solvent mixture with a 9:1 ratio of DMSO to PBS buffer. The starting materials were dissolved in DMSO, while the catalyst, dissolved in pH 7.4 PBS buffer, was added to the reaction mixture at a concentration of 5 mol%. After the reaction time of 72 hours, the organic compounds in the reaction mixture were extracted using EtOAc.

For a systematic comparison, control experiments were conducted under three different conditions: without a catalyst to investigate the background reaction, with free amino acids (L-His and L-Arg) to evaluate their baseline catalytic activity, and with fullerenol-amino acid derivatives (**F**-Arg and **F**-His) to examine the effect of covalent functionalization. Additionally, reactions were performed separately using **F**-Arg and **F**-His alone to determine their individual catalytic efficiencies.

2.3.2.1 Background Reaction and Free Amino Acid Catalysis

To evaluate the catalytic contribution of **F**-AA derivatives, the reaction was initially performed without any catalyst. As expected, no product formation was detected under these conditions, confirming that the reaction requires an active catalyst (Figure 55).

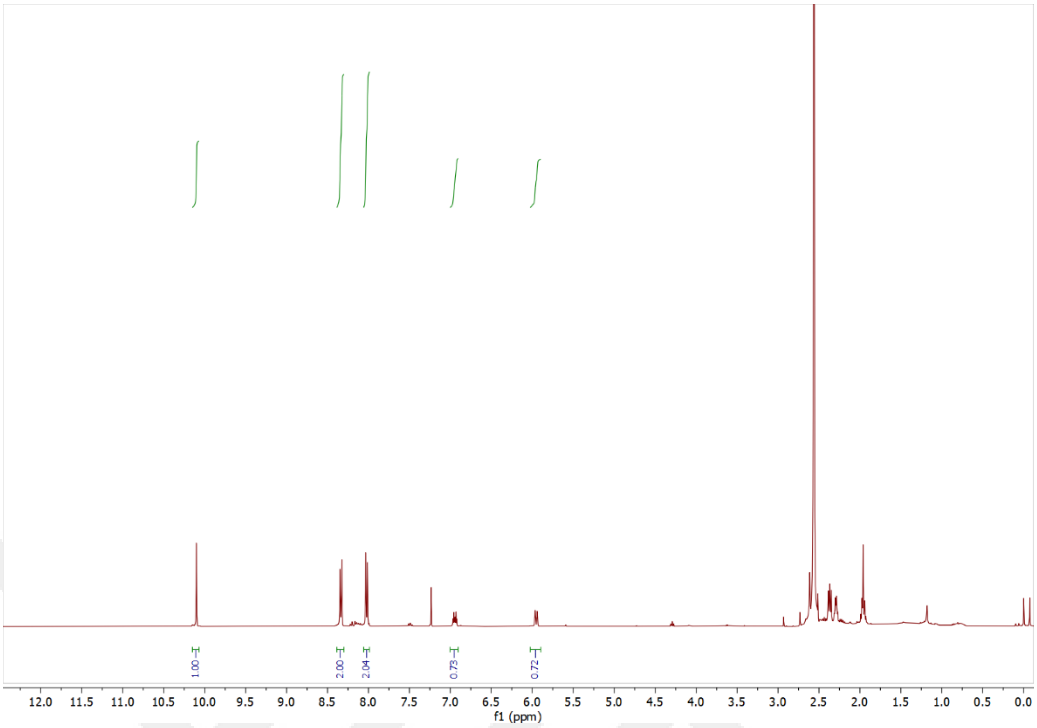

Figure 55. ^{1}H NMR Spectrum of MBH Reaction without catalyst in $CDCl_3$.

As shown in Figure 55, the NMR spectrum of the product obtained after work-up indicates the aldehyde and aromatic hydrogen peaks characteristic of compound **M1**, along with the α and β hydrogen signals of compound **M2** at 6.95 ppm and 5.95 ppm, respectively. However, the expected β-hydrogen peak of compound **M3** (Figure 56), which was reported in the literature [173] to appear at 6.76 ppm, is absent, indicating that the formation of the desired product did not occur. The assigned peaks were sufficient to characterize the starting materials; therefore, the other peaks observed in the spectroscopy were not assigned here.

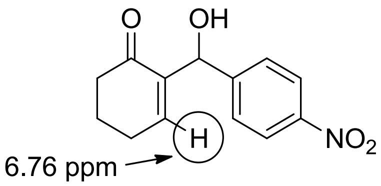

M3

Figure 56. α-hydrogen peak at 6.76 ppm in compound **M3a**.

Subsequently, pristine L-His and L-Arg were used as catalysts. The reaction yielded negligible conversion (Figure 57), indicating that free amino acids alone were not sufficiently reactive for MBH catalysis. This finding was consistent with previous studies suggesting that amino acid-based catalysis required structural stabilization to effectively participate in the reaction.

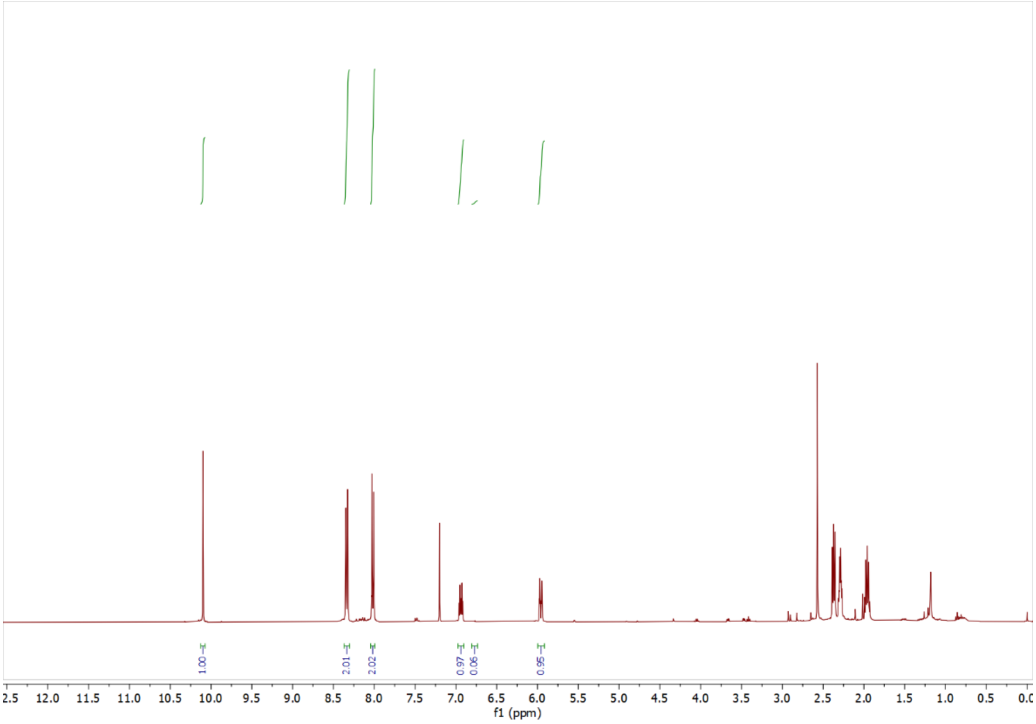

Figure 57. ^{1}H NMR Spectrum of MBH Reaction with L-Histidine and L-Arginine in $CDCl_3$.

As shown in Figure 56, when pristine L-His and L-Arg were used as catalysts, a small triplet peak at 6.76 ppm, corresponding to compound **M3**, was observed. However, the conversion was only 5%.

2.3.2.2 Catalytic Activity of F-Arg and F-His

F-Arg and **F**-His were synthesized using the same approach through the functionalization of fullerenol. When **F**-Arg and **F**-His were used as catalysts, a significant increase in conversion was observed, as indicated by ^{1}H NMR spectral analysis (Figure 58).

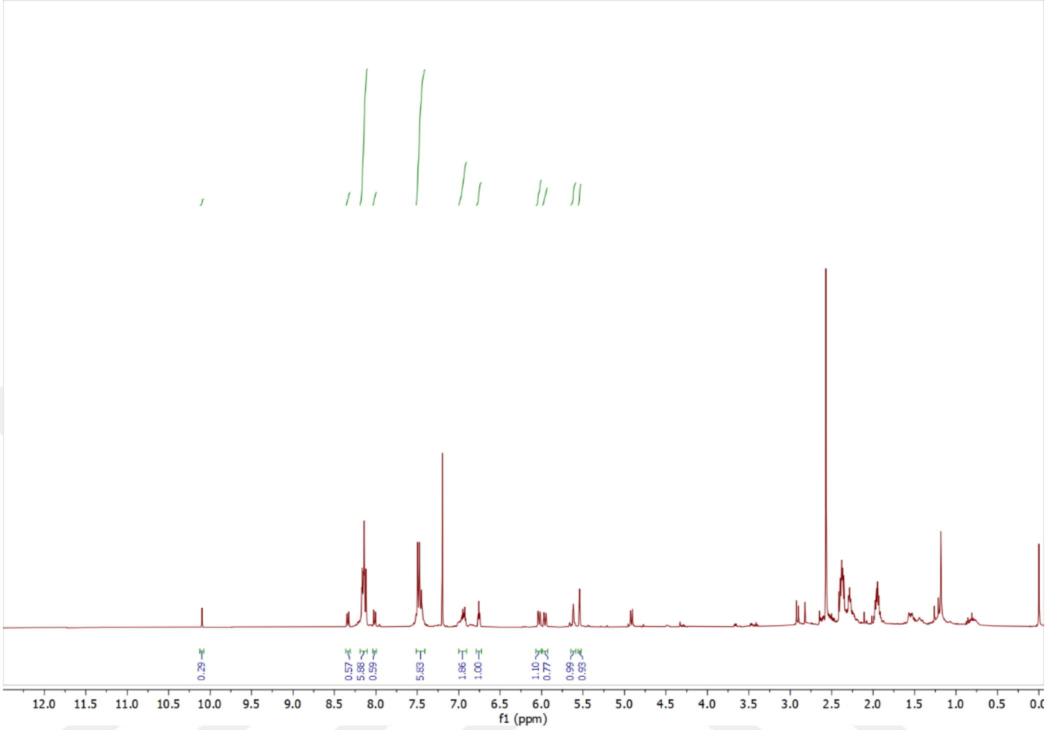

Figure 58. ^{1}H NMR spectrum of MBH reaction catalyzed by **F**-Arg and **F**-His in $CDCl_3$.

According to Figure 57, a triplet peak at 6.65 ppm and a singlet peak at 5.54 ppm were observed, both of which correspond well to the expected signals of the desired product, compound **M3**, in agreement with the NMR data reported in the literature [173]. However, the aromatic region contained peaks with unexpectedly high integration values, as well as additional peaks that clearly did not belong to either the starting materials or compound **M3**. This observation strongly suggested that, along with the formation of the desired product, various by-products were also generated during the reaction.

For this reason, the starting materials were separated using column chromatography. Various approaches were explored to isolate all the formed by-products individually; however, despite applying multiple column chromatography processes with different systems, the separation of the products was not successful, as shown in Figure 59.

Consequently, the characterization of the by-products was carried out using NMR spectroscopy analysis.

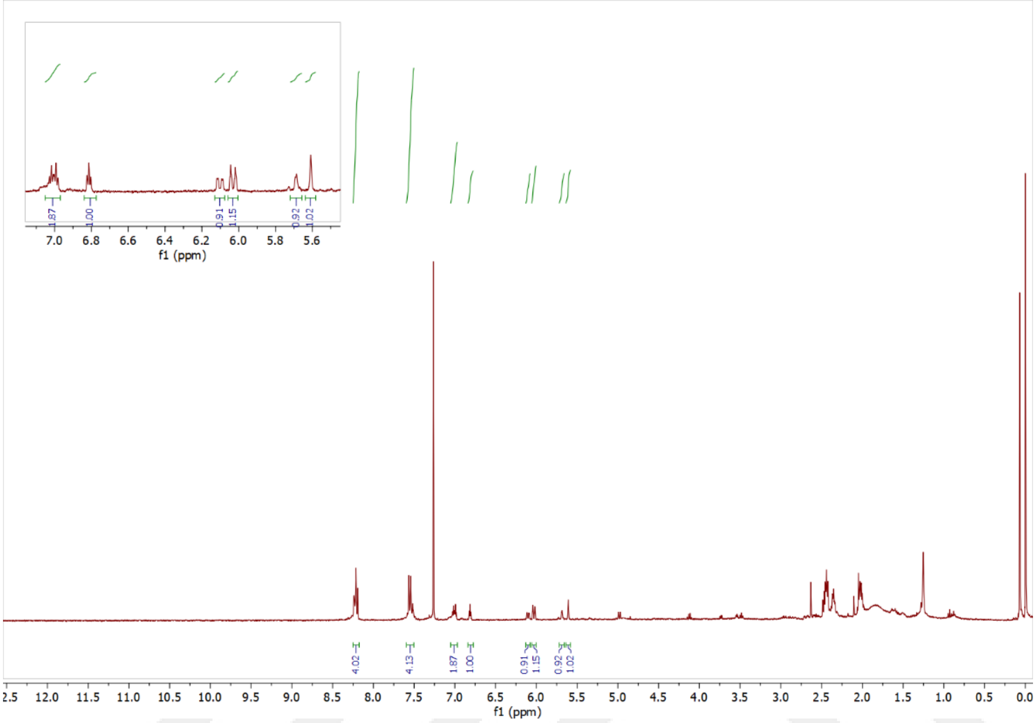

Figure 59. ^{1}H NMR spectrum of MBH reaction catalyzed by **F**-Arg and **F**-His after column chromatography in $CDCl_3$.

After analyzing the NMR spectrum, the formation of a cross-aldol product between 2-cyclohexen-1-one and *p*-nitrobenzaldehyde was considered, as such by-products are commonly encountered in Morita-Baylis-Hillman (MBH) reactions reported in the literature. Through analysis of Figure 59, the singlet peak at 5.69 ppm and the doublet of doublets at 6.10 ppm provided strong evidence for the presence of this cross-aldol product. The formation of similar aldol products has been previously documented, with reported NMR shifts appearing as a singlet at 5.7 ppm and a doublet at 6.2 ppm [218]. Furthermore, the high integration values observed at 7.55 ppm, 8.22 ppm, and 6.95 ppm further supported the existence of this by-product **1**.

The NMR spectrum also indicated the presence of peaks at 5.95 ppm and 6.95 ppm, which correspond to the starting material, compound **M2**. However, since all starting materials had been successfully separated after column chromatography, these peaks were attributed to the unexpected behavior of **F**-Arg as a base in PBS buffer, leading to the formation of a by-product via base-induced Michael addition between two 2-cyclohexen-1-one molecules. Although no exact match for this product has been reported in the literature, the absence of **M2** in this mixture strongly suggested that these peaks belonged to by-product **2**. Based on these findings, the proposed mechanism for the by-product formation is illustrated in Scheme 63.

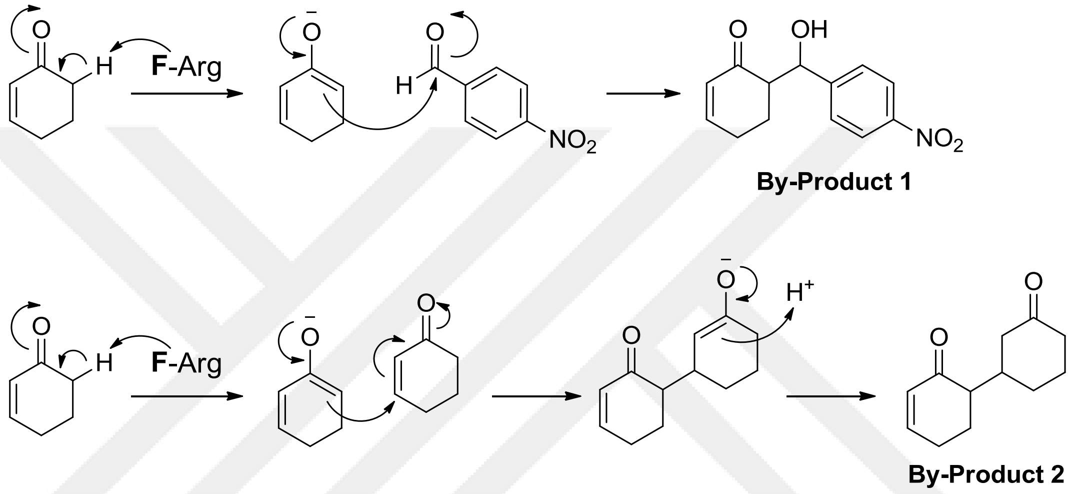

Scheme 63. Proposed mechanism of the by-products.

Next, the reaction was carried out with the catalyst ratio reduced from 5% to 2.5%. However, a significant decrease in product formation was observed. In the following reaction, the catalyst loading was increased to 10%. This time, the integration values in the aromatic region were notably higher compared to other by-products (Figure 60). NMR analysis suggested that a reaction had occurred between the cross-aldol product (**By-product 1**) and *p*-nitrobenzaldehyde, potentially leading to the formation of an acetal (**By-product 3**) (Scheme 64), which is consistent with literature findings [219].

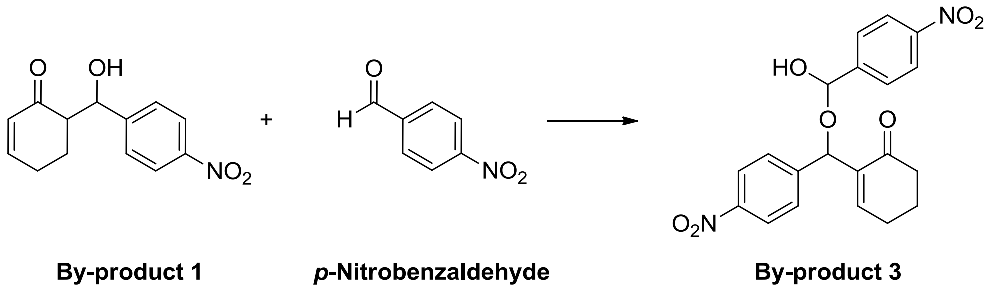

Scheme 64. Formation of **by-product 3**.

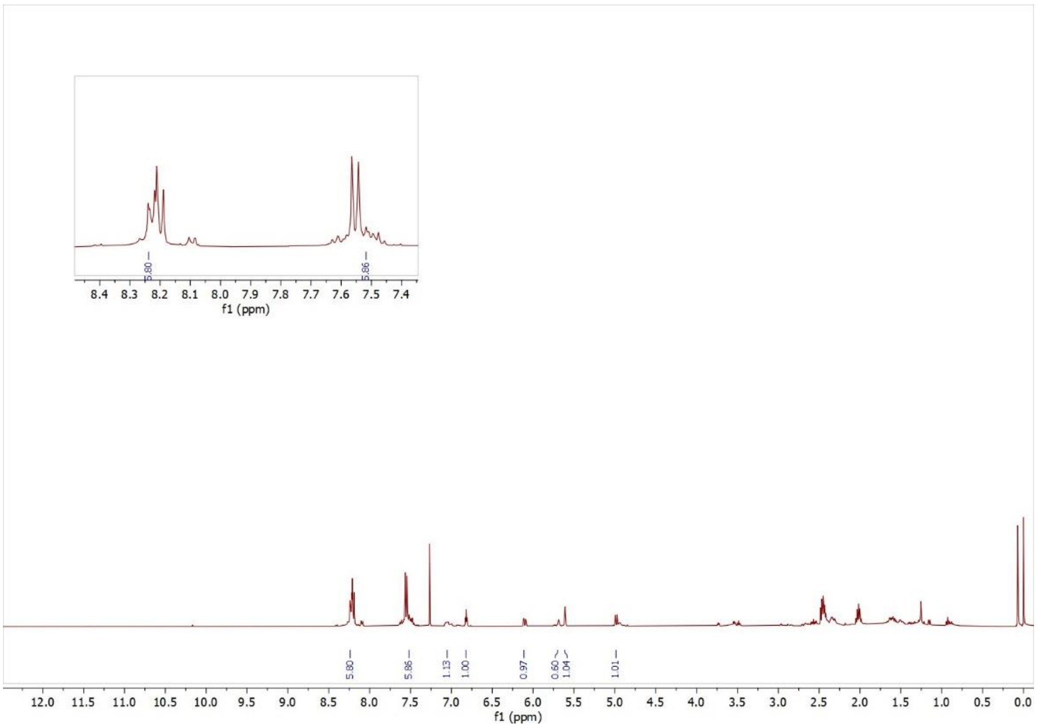

Figure 60. ^{1}H NMR Spectrum of MBH reaction catalyzed by 10 mol% catalyst in $CDCl_3$.

Finally, the reaction was carried out using **F**-Arg and **F**-His catalysts individually. In both cases, by-product peaks were observed in the NMR spectra (Figure A.28 and Figure A.29). However, a significant decrease in yield was recorded compared to when they were used together. These results confirmed that, as expected, the highest catalytic activity was achieved when **F**-Arg and **F**-His were combined. When comparing the triplet peaks at 6.73 ppm of the aldehyde hydrogen in the starting material **M1** and the product **M3**, a higher conversion was observed with **F**-Arg when the two catalysts were compared individually.

2.3.3 2-Amino-3-cyano-4H-chromene Synthesis

After demonstrating strong base-catalytic activity in earlier reactions, **F**-Arg was chosen as the catalyst for the synthesis of 2-amino-3-cyano-4H-chromene derivatives. As previously discussed, the proposed mechanism involves **F**-Arg initiating the reaction by abstracting a proton from malononitrile, facilitating a stepwise transformation that proceeds through Knoevenagel condensation, Michael addition, and cyclization. This setup aimed to evaluate whether **F**-Arg could drive this multicomponent reaction efficiently under mild, metal-free conditions.

In this part of the thesis, the catalytic performance of **F**-Arg in the 2-amino-3-cyano-4H-chromene synthesis was evaluated and comparative experiments were conducted using pristine L-arginine, **F**-Arg, and a catalyst-free reaction. The reactions were performed at different temperatures (room temperature, 50 °C, 70 °C, and 100 °C) to evaluate the influence of thermal conditions on the reaction efficiency. Additionally, the effect of solvent choice and the amount of arginine substitution on the fullerene core were studied.

F-Arg was synthesized following the same approach by functionalizing fullerenol. The degree of arginine substitution for this reaction was determined to be 8.34. This ensured that enough arginine residues were available to contribute meaningfully to the catalytic cycle.

For the reaction, 1 mmol of β-naphthol (**C1**), benzaldehyde (**C2**), and malononitrile (**C3**) were added to a test tube. **F**-Arg was then introduced at a concentration of 0.4 mol%, and the mixture was stirred at the designated temperatures for 20 hours (Scheme 65). Upon completion of the reaction, H_2O and DCM were added to the mixture, allowing for the separation of **F**-Arg and organic compounds via extraction.

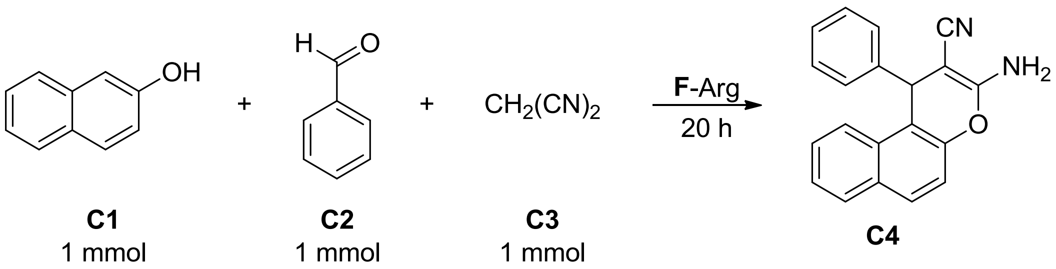

Scheme 65. 2-Amino -3-cyano-4H-chromene synthesis as performed in this study.

However, in reactions yielding high product amounts at elevated temperatures, the absence of a solvent resulted in the near-complete integration of the product with the test tube, forming a solid mass that was nearly impossible to isolate. Consequently, in such cases, additional analyses were performed on samples taken directly from the reaction.

2.3.3.1 Comparison of Catalytic Activity at Different Temperatures

To more effectively analyze the influence of arginine quantity on reaction yield, L-arginine was added in the same molar amount as the arginine content on **F**-Arg (8.34 × 0.4 mol%) in reactions conducted with L-arginine. As a result, 6 mg (0.04 mmol) of arginine was used in these reactions.

The first approach to determine the conversion rates was to use ^{1}H NMR spectroscopy by comparing the integration of the aldehydic hydrogen of benzaldehyde with the stereogenic hydrogen at the C2 position of the chromene scaffold, which is expected to be observed as a singlet at 5.30 ppm (Figure 61) [190]. These peaks were selected because no overlapping signals from other compounds were expected in this region, ensuring accurate integration without interference.

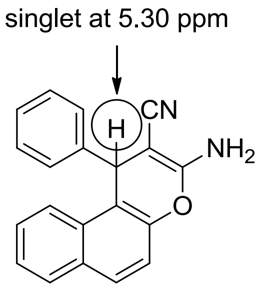

C4

Figure 61. Singlet at 5.30 ppm for the C2 hydrogen in compound **C4**

However, in many reactions, solid masses were obtained as the final product, preventing the application of a standard work-up procedure. Consequently, yields were determined by taking known amounts of these solidified products (approximately 10–15 mg), which were then dissolved in DMSO-d_6. A known volume (8 μL) of DMF was added as an internal standard. The conversion was determined by comparing the singlet peak of the product at 5.30 ppm with the singlet of the *N*-methyl protons of DMF in the ^{1}H NMR spectrum (Figure 62).

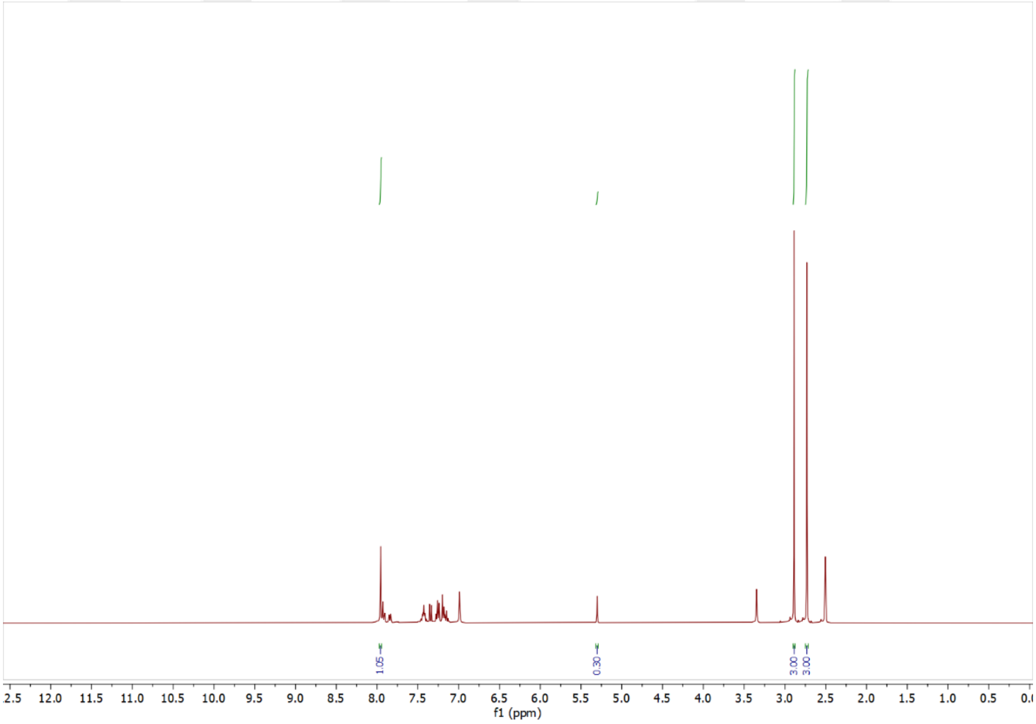

Figure 62. ^{1}H NMR spectrum of the reaction in DMSO-d_6 with DMF as internal standard.

The reaction shown in Figure 62 was carried out using 0.4 mmol **F**-Arg at 100 °C, yielding 280 mg of crude solid at completion. A 10 mg sample was taken from this solid, dissolved in DMSO-d_6, and 8 µL (0.103 mmol) of DMF was added as an internal standard. As seen in Figure 61, the ratio of the product to DMF was determined to be 0.30. Based on this, the sample contained 0.031 mmol (9.24 mg) of the product. Using this calculation, the total reaction mixture was determined to contain 235 mg (0.79 mmol) of the product.

To ensure accuracy, two additional known-mass samples were taken from the crude solid and analyzed by ^{1}H NMR. Although slight variations were observed between them, the results remained within an acceptable range. The average of the calculations from these three samples indicated that the reaction proceeded with a 79% yield.

The primary objective of this study was not to obtain an exact yield. Instead, the focus was on evaluating the catalytic activity of **F**-Arg in comparison to L-arginine and catalyst-free reactions. A consistent comparison was made by applying the same method to all reaction analyses. This consistency allowed for a clearer understanding of how each catalytic condition influenced the outcome.

Following this, the reactions were conducted at varying temperatures, including room temperature, 70 °C, and 100 °C. As shown in Table 10, reaction yields increased with rising temperature. Additionally, in the absence of a catalyst, no significant conversion was detected. However, the expected difference between **F**-Arg and L-arginine was not observed. As described, these yields were calculated using the same method, with additional sample analyses confirming accuracy and consistency.

Table 10. Effect of catalyst type, temperature, and reaction conditions on the yield of the chromene synthesis reaction.

Catalyst	**Percentage**	**Solvent**	**Time (h)**	**Temperature (°C)**	**Yield (%)**
F-Arg	0.4%	Neat	20	100	79
L-Arginine	3.4%, (6 mg)	Neat	20	100	69
No catalyst		Neat	20	100	6
F-Arg	0.4%	Neat	20	70	77
L-Arginine	3.4%, (6 mg)	Neat	20	70	68
No catalyst		Neat	20	70	0
F-Arg	0.4%	Neat	20	RT	9
L-Arginine	3.4%, (6 mg)	Neat	20	RT	7
No catalyst		Neat	20	RT	0

2.3.3.2 Effect of Solvent on Reaction Efficiency

Following the initial results, the effect of solvent on reaction yield was investigated. Acetone was selected as an aprotic solvent, while ethanol was chosen as a protic solvent. Considering the boiling points of the solvents, the reactions were carried out at 50 °C with controlled heating. As shown in Table 11, no conversion was observed when acetone was used. In contrast, an acceptable yield was obtained in 0.5 mL of ethanol. However, significant yield reduction was observed upon further dilution.

The results demonstrated how solvent properties influence reaction efficiency. The failure of the reaction in acetone suggested that an aprotic solvent could not effectively stabilize the intermediates. In contrast, the moderate yield in ethanol suggested that its protic nature could facilitate the reaction, likely through hydrogen bonding or intermediate stabilization. Despite these effects, the expected difference between **F**-Arg and pristine arginine remained undetected.

Table 11. Effect of solvent type and concentration on the yield of the chromene synthesis reaction.

Catalyst	Percentage	Solvent	Time (h)	Temperature (°C)	Yield (%)
F-Arg	0.4%	EtOH (0.5 mL)	20	50	47
L-Arginine	3.4%, (6 mg)	EtOH (0.5 mL)	20	50	41
F-Arg		EtOH (2 mL)	20	50	8
L-Arginine	0.4%	EtOH (2 mL)	20	50	7
F-Arg	3.4%, (6 mg)	Acetone (0.5 mL)	20	50	0
L-Arginine		Acetone (0.5 mL)	20	50	0

2.3.3.3 Effect of Degree of Arginine Substitution on Fullerenol

Finally, the effect of arginine functionalization on fullerenol was investigated. For this purpose, two different **F**-Arg derivatives were synthesized with arginine substitution degrees of 5.35 and 10.5. These values were achieved after numerous optimizations, as the degree of substitution was consistently found to be around 8 in separate syntheses.

For the 5.35 substitution, the same amount of arginine was added to the reaction mixture, but instead of the standard 48-hour reaction time, the process was stopped after 10 hours. In contrast, for the 10.5 substitution, after 48 hours, an additional 10-fold excess of arginine was introduced into the reaction mixture, and the reaction was allowed to proceed for an additional day. These variations, along with a control experiment using 1 mg of pristine arginine (0.6 mol%), were summarized in Table 12 to compare how the amount of pristine arginine and the degree of substitution affected the overall yield.

Table 12. Effect of degree of arginine substitution on the yield of the chromene synthesis reaction.

Catalyst	Percentage	Solvent	Time (h)	Temperature (°C)	Yield (%)
F-Arg (5.35)	0.4%	Neat	20	70	78
L-Arginine	2.3%, (4 mg)	Neat	20	70	53
F-Arg (10.5)	0.4%	Neat	20	70	82
L-Arginine	4.0%, (7 mg)	Neat	20	70	77
F-Arg (8.34)	0.4%	Neat	20	70	77
L-Arginine	3.4%, (6 mg)	Neat	20	70	68
L-Arginine	0.6%, (1 mg)	Neat	20	70	32

As shown in Table 12, the reactions were carried out by adjusting the amount of pristine arginine according to the degree of substitution in **F**-Arg. Finally, a reaction was conducted using 1 mg (0.6 mol%) of arginine to resemble the 0.4 mol% **F**-Arg conditions. The results showed that variations in the degree of substitution of **F**-Arg did not significantly affect the reaction yield. However, the yield was directly influenced by the amount of pristine arginine used in the reaction. These results indicate that the catalytic behavior of **F**-Arg is considered as a property of the entire aggregated system, not simply the result of individual **F**-Arg units.

2.3.4 Prins Cyclization

As the final transformation explored in this study, Prins cyclization was chosen to evaluate whether the natural acidity of fullerenol (pK_a ~ 3.5) could be effectively utilized to act as an effective acid catalyst in this reaction. The study aimed to evaluate the potential of fullerenol under both neat conditions and in the presence of solvents. It also allowed for a direct comparison with other acid catalysts, offering insight into the reactivity and versatility of fullerenol in different environments.

In this part of the thesis, the catalytic performance of fullerenol in Prins cyclization was evaluated in the reaction between an aryl aldehyde and a homoallylic alcohol. The reaction was carried out under various conditions and alternative approaches to compare reactivity and selectivity. Additionally, the catalytic activity of fullerenol was investigated by comparing it with TFA, the catalyst reported in the literature, and formic acid, which has a pK_a value similar to fullerenol. This comparison was conducted in the synthesis of cis-2-phenyltetrahydro-2H-pyran-4-ol via Prins cyclization.

2.3.4.1 Protonation of Fullerenol for Catalytic Activity

Fullerenol was synthesized under basic conditions using NaOH, without an acidic work-up during the isolation process. As a result, its hydroxyl groups remained in their sodium salt form after synthesis. To activate fullerenol for its catalytic role in Prins cyclization, protonation was required, which was achieved using an ion-exchange resin. Amberlyst 15 was selected for this purpose. Fullerenol was first dissolved in water, and Amberlyst 15 was added to the solution. The mixture was stirred, then filtered, and the filtrate was lyophilized to yield the protonated fullerenol catalyst, which was subsequently used in the reaction (Scheme 66).

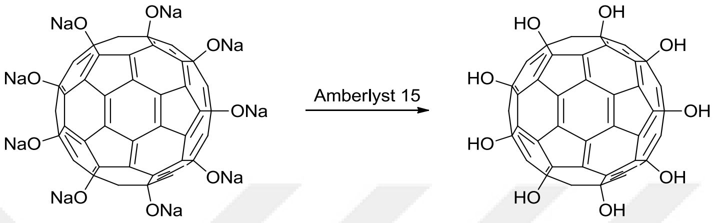

Scheme 66. Protonation of fullerenol with Amberlyst 15.

2.3.4.2 First Experiments and Observations

The initial experiments were conducted using *p*-tolualdehyde, isoprenol, and 2 mol% fullerenol at 40 °C (Scheme 67).

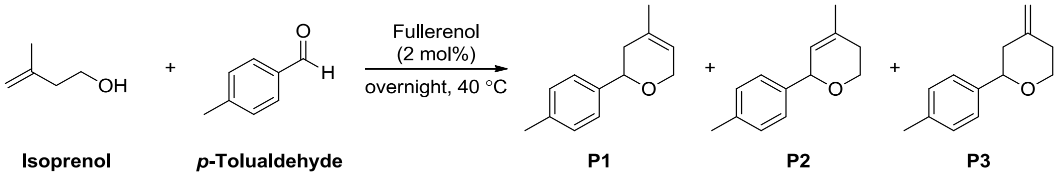

Scheme 67. The Prins cyclization reaction as performed in this study.

Upon completion, the reaction products were analyzed by ^{1}H NMR spectroscopy. However, as shown in Figure 63, the spectrum exhibited an excessive number of peaks, making it unfeasible to fully characterize all three products and determine their relative ratios. Notably, the absence of the aldehyde peak confirmed the complete conversion of *p*-tolualdehyde. Despite the spectral complexity, two key signals at 4.42 ppm as a doublet of doublets and 5.44 ppm as a singlet aligned with literature data [195] and provide strong evidence for the formation of compound **P1**.

Nevertheless, the presence of multiple components made characterization and chromatographic separation highly challenging.

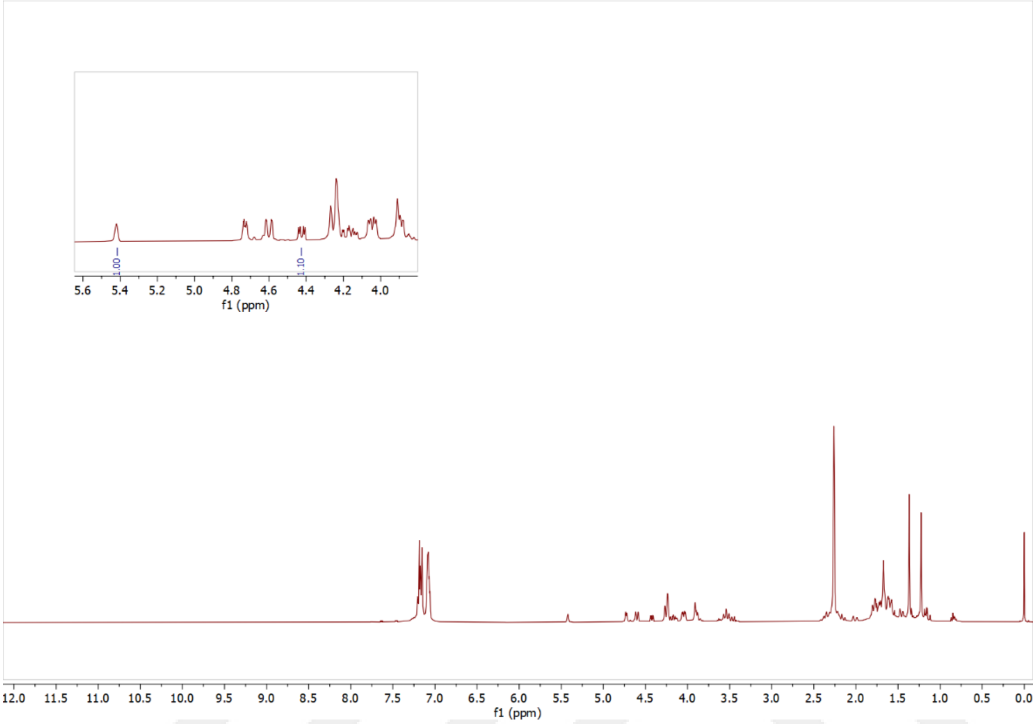

Figure 63. ^{1}H NMR spectrum of the Prins cyclization reaction mixture catalyzed by fullerenol in $CDCl_3$.

Although the products could not be fully characterized in the initial reaction, the results indicated that fullerenol could be a promising catalyst for Prins cyclization. To further support this, the reaction was carried out under the same conditions but without any catalyst. As shown in Figure 64, the ^{1}H NMR spectrum of the reaction mixture exhibited a singlet at 9.70 ppm for the aldehyde proton, doublets at 7.28 and 7.73 ppm corresponding to the aromatic protons, a singlet at 2.37 ppm for the methyl protons, and singlets at 4.72 and 4.80 ppm assigned to the terminal alkene protons of isoprenol. These peaks correspond only to the starting materials, confirming that a catalyst is essential for the reaction to proceed.

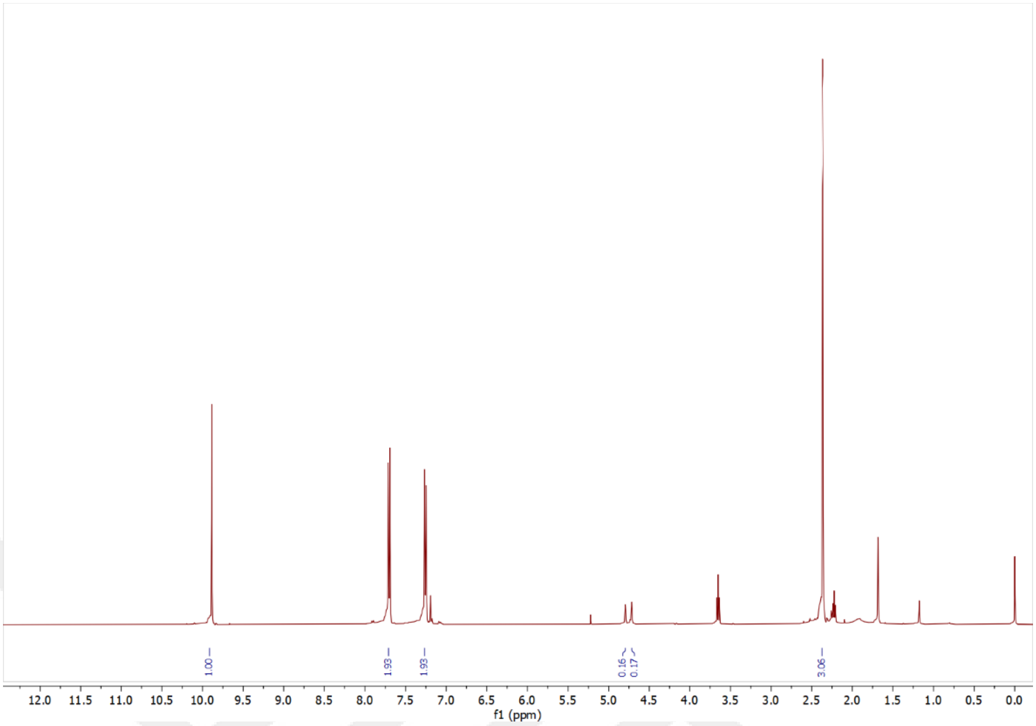

Figure 64. ^{1}H NMR spectrum of the uncatalyzed Prins cyclization reaction mixture in $CDCl_3$.

2.3.4.3 Prins-Friedel-Crafts Reaction

Following these initial results, a different strategy was employed to obtain a single product. Inspired by the Prins–Friedel–Crafts reaction reported in the literature using boron trifluoride etherate ($BF_3 \cdot OEt_2$) as a catalyst [204], the reaction was carried out with fullerenol, aiming to achieve selective product formation. In this reaction, benzaldehyde and 3-buten-1-ol were used as reactants, with benzene serving both as a solvent and as a reactant for the Friedel–Crafts reaction, reacting with the intermediate formed in the Prins cyclization step (Scheme 68). Fullerenol was tested as a catalyst at 2 mol%, 5 mol%, and 10 mol%. However, in all cases, the desired product was not obtained.

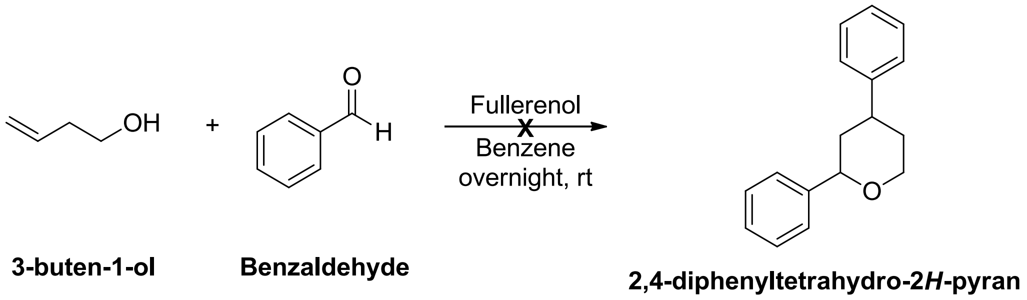

Scheme 68. Prins-Friedel-Craft reaction as performed in this study.

2.3.4.4 cis-2-Phenyltetrahydro-2H-pyran-4-ol Synthesis with Prins Cyclization

The characterization of the **P1**, **P2**, and **P3** products obtained in the first strategy could not be achieved. Additionally, the Prins-Friedel-Crafts reaction did not yield successful results. Therefore, an alternative strategy was developed to obtain a single product.

In the literature, the known Prins reaction catalyzed by TFA lead to the synthesis of cis-2-phenyltetrahydro-2H-pyran-4-ol as the sole product upon the addition of NaOH [205]. In this approach, a 10-fold excess of TFA was used, and the initial reaction was carried out without a solvent. In this study, the reaction was carried out in a THF solution with 20 mol% fullerenol, as a solvent was required due to the solid nature of fullerenol. However, the reaction mixture was kept as concentrated as possible (Scheme 69). For comparison, the reaction was also conducted with TFA in THF as the solvent and further examined with formic acid, which has a pK_a similar to that of fullerenol.

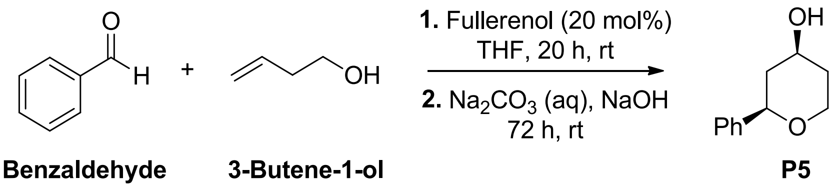

Scheme 69. cis-2-phenyltetrahydro-2H-pyran-4-ol synthesis as performed in this study.

Therefore, three separate reactions were set up simultaneously using fullerenol, TFA, and formic acid as catalysts. The initial yields were determined by comparing the aldehyde peak of benzaldehyde with that of the product in ^{1}H NMR spectroscopy (Figure 65, Figure 66, Figure 67).

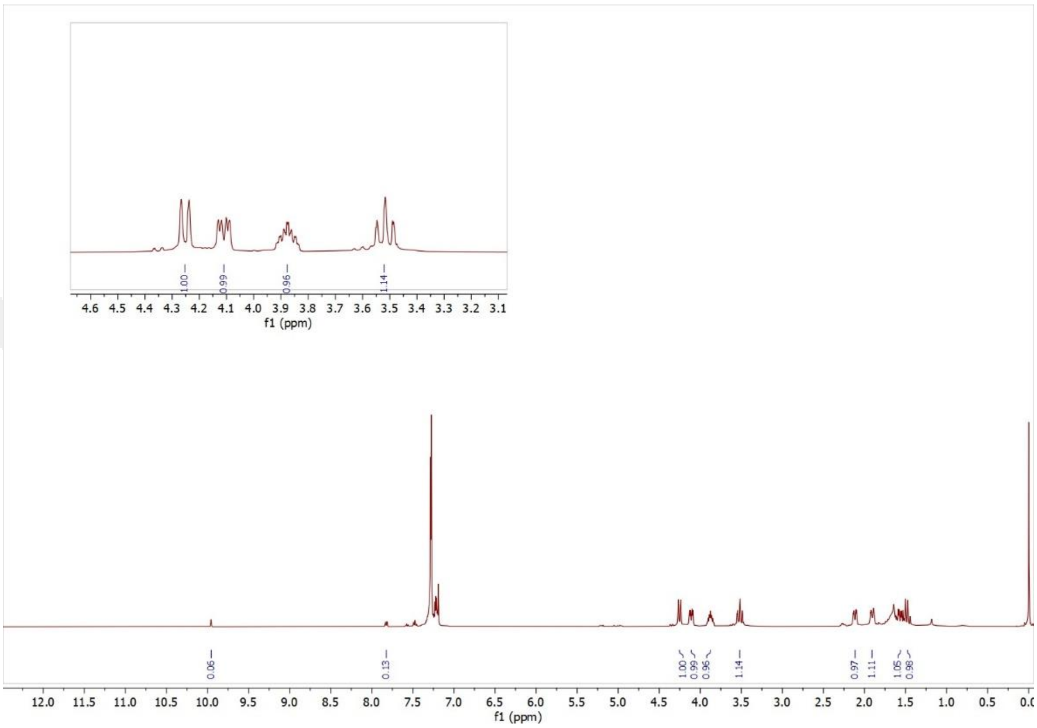

Figure 65. ^{1}H NMR spectrum of **P5** obtained using TFA as the catalyst in $CDCl_3$.

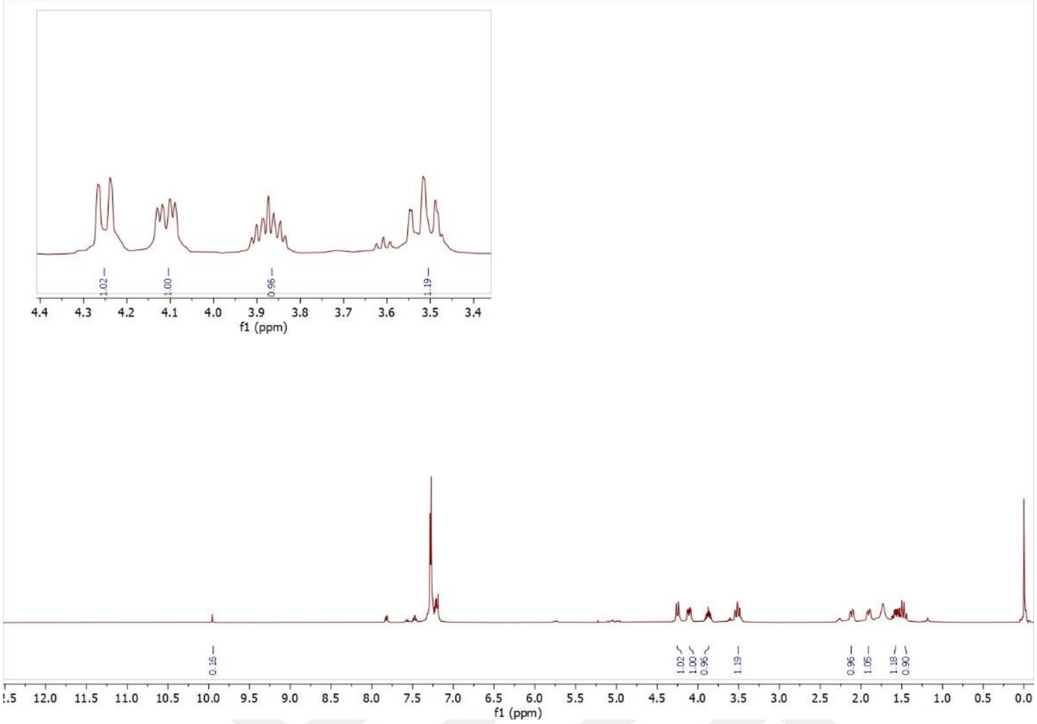

Figure 66. ^{1}H NMR spectrum of **P5** obtained using fullerenol as the catalyst in $CDCl_3$.

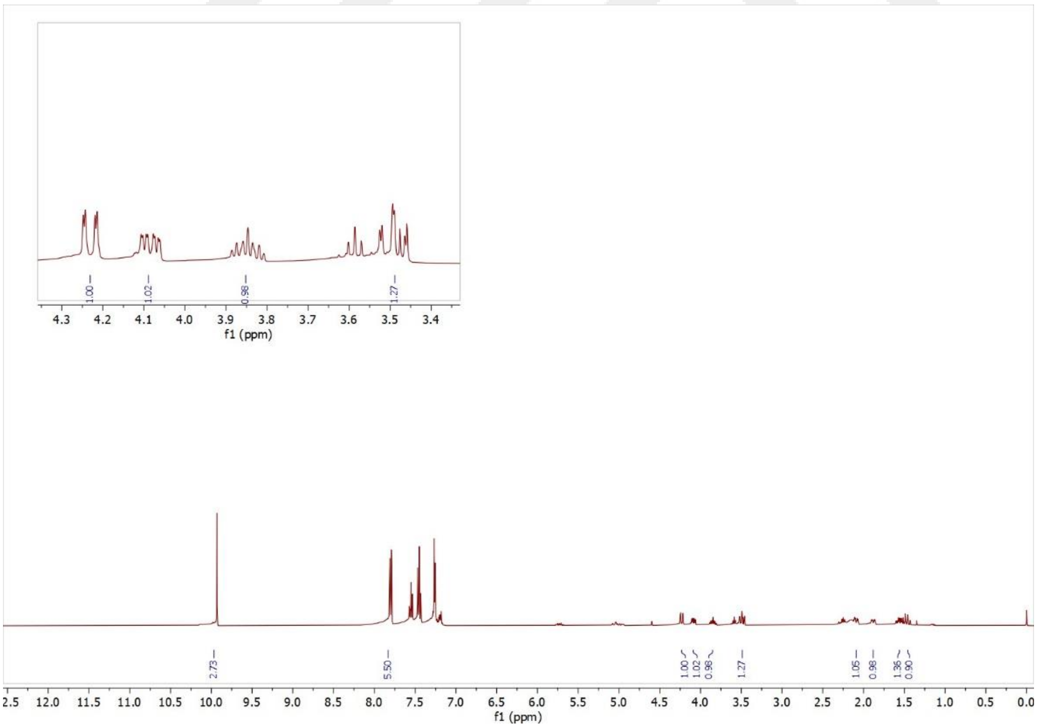

Figure 67. ^{1}H NMR spectrum of **P5** obtained using formic acid as the catalyst in $CDCl_3$.

As shown in Figures 64, 65 and 66, the reaction catalyzed by TFA resulted in a 94% yield, while the yield with fullerenol was determined to be 86%. A slightly lower yield with fullerenol was expected, as Prins cyclization is known to proceed more efficiently with strong acids. However, when compared to the 27% yield obtained with formic acid, it was considered that fullerenol's catalytic activity in this reaction is not only due to its acidity but also related to the structural properties of fullerene. With its conjugated π-system, electron-accepting nature, and potential for non-covalent interactions, fullerenol stabilizes the reaction through transition state stabilization or π-π interactions with benzaldehyde. These features suggest that fullerenol plays a role beyond simple acid catalysis.

The obtained product, compound **P5**, was purified by column chromatography and analyzed by ^{1}H NMR spectroscopy to determine whether it adopted a cis or trans configuration (Figure 68). The configuration was assigned based on *J* coupling constants, providing insight into the spatial arrangement of the protons.

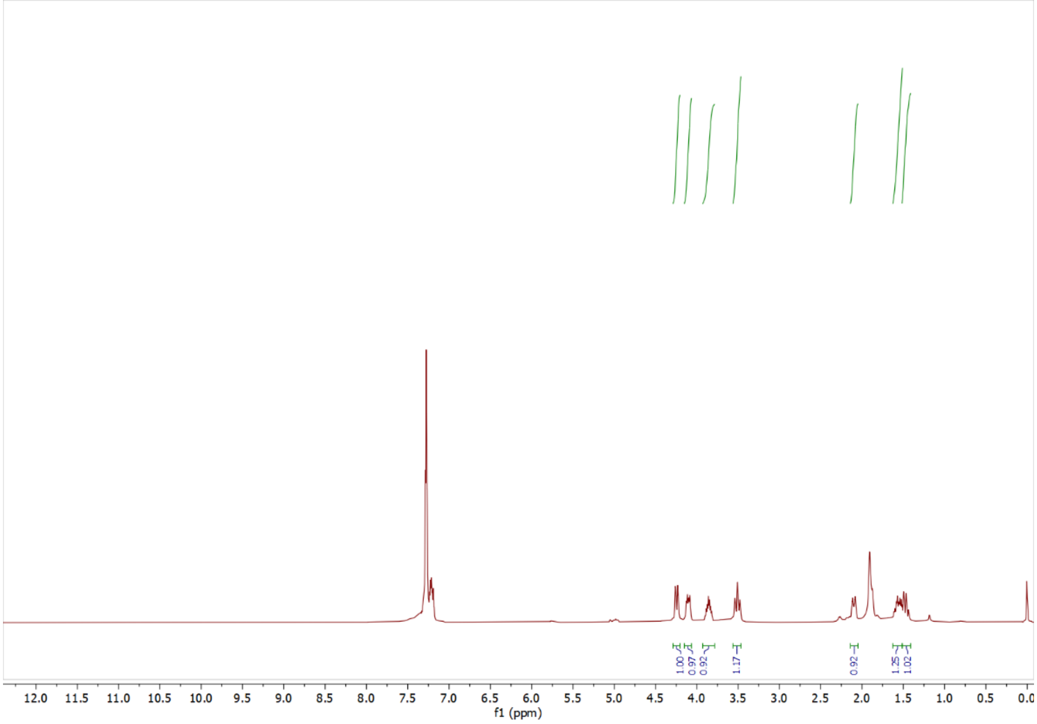

Figure 68. ^{1}H NMR spectrum of **P5** after column chromatography in $CDCl_3$.

The stereochemistry of compound **P5** was determined using ^{1}H NMR spectroscopy by analyzing the vicinal coupling constants (*J*) (Figure 69).

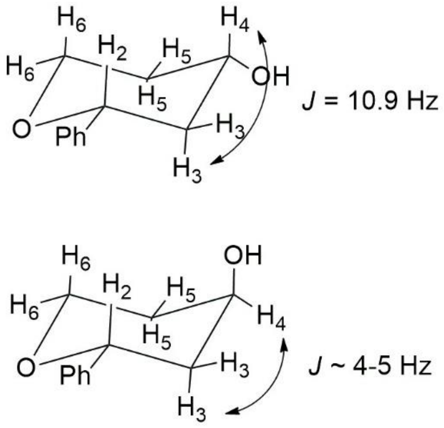

Figure 69. Vicinal coupling constants (*J*) for the cis (top) and trans (bottom) isomers of compound **P5**.

The benzylic proton (H2) appeared at 4.25 ppm as a doublet of doublets (dd, *J* = 11.5, 2.1 Hz)**,** indicating two distinct coupling interactions. The large 11.5 Hz coupling constant corresponds to an axial-axial (trans-diaxial) interaction with H3(ax), while the smaller 2.1 Hz coupling constant suggests an axial-equatorial interaction with H-3(eq).

Furthermore, H-4, located at 3.88 ppm as triplet of triplets (tt, *J* = 10.9, 4.5 Hz) displayed a coupling pattern consistent with both axial-axial and axial-equatorial interactions, supporting the preference for a chair conformation. The coupling constants of H5 (2.11 ppm, ddt, *J* = 12.6, 4.4, 2.1 Hz) and H6 (1.91 ppm, ddt, *J* = 12.5, 4.6, 2.0 Hz) further confirmed that the product adopted a configuration where the benzyl group occupied the equatorial position.

These observations are in agreement with the literature data for the cis configuration, where the bulky benzyl substituent preferentially adopts an equatorial position to minimize steric hindrance. The comparison between the ^{1}H NMR data obtained at 400 MHz and those reported in the literature at 600 MHz further confirm the stereochemical assignment [205].

CHAPTER 3

EXPERIMENTAL

3.1 Materials and Methods

Fullerene was sourced from Nanografi Nanotechnology, while commercial amino acids were obtained from Chem-Impex International Inc. The initial reagents were purchased from Acros Organics, TCI, and Merck. Solvents including DCM, DMF, ethanol, diethyl ether, and methanol were procured from Merck. For column chromatography and extraction, solvents such as ethyl acetate, hexane, and dichloromethane were distilled and subsequently dried over calcium chloride. Dry DMF was used directly from an MBraun MBSPS5 solvent drying system. The progress of reactions was monitored via thin-layer chromatography (TLC) using Merck Silica Gel 60 F254 plates, visualized under UV light at wavelengths of 245 nm and 366 nm. Column chromatography was conducted on Merck Silica Gel 60 (particle size: 0.063-0.20 mm, 230-400 mesh ASTM).

Deuterated solvents were obtained from Merck. Structural characterization of the synthesized compounds was carried out using NMR spectroscopy. The compounds were dissolved in deuterated solvents and analyzed on a Bruker Avance III Ultrashield 400 MHz NMR spectrometer. Chemical shifts are expressed in parts per million (ppm), with tetramethylsilane (TMS) as the internal reference. Spin multiplicities are denoted as follows: s (singlet), d (doublet), dd (doublet of doublets), t (triplet), m (multiplet), and coupling constants (*J*) are provided in Hertz (Hz). The NMR spectra of the compounds are included in Appendix A. All spectra were processed using the MestReNova software.

HPLC analysis was performed using a Dionex Ultimate 3000 Series system equipped with a UV-VIS absorbance diode-array detector with adjustable wavelengths. Analytical HPLC was carried out with RP-C18 columns (Thermo Scientific, ODC

Hypersil 5 µm C18 120 Å LC Column 150 x 4.6 mm and Phenomenex, Luna Omega 5 µm PS-C18 100 Å LC Column 250 x 4.6 mm). The mobile phase employed a gradient elution, with A: water containing 0.1% TFA, and B: acetonitrile (ACN) containing 0.08% TFA. The flow rate was set to 0.500 mL/min for all analytical runs. The gradient conditions were adjusted for each compound based on its specific properties.

LC-MS analyses were conducted using an Agilent 6546 LC/Q-TOF system with gradient solvents, A: water containing 0.1% formic acid, and B: acetonitrile (ACN) containing 0.1% formic acid, at Bilkent University UNAM. UV-VIS spectroscopy was carried out with a BioTek Epoch2 Microplate Reader using Hellma Precision quartz Suprasil cells (10 mm). FT-IR measurements were performed with a Thermo Scientific Nicolet iS10 instrument. Sonication was carried out using a KUDOS HP Series 53 kHz high-frequency ultrasonic cleaner.

3.1.1 Synthesis of Fullerenol

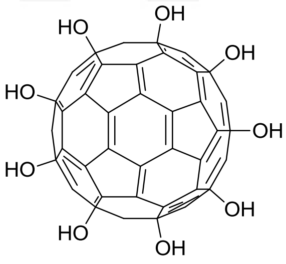

Fullerenol

Based on literature [71], C_{60} (80 mg, 0.11 mmol) was dissolved in 50 mL of toluene. A NaOH solution (2 mL, 1 g/mL) was then introduced, and the mixture was stirred at room temperature. Subsequently, six drops of a 50% H_2O_2 solution were added along with 20 mg of TBAH as a phase transfer catalyst. The reaction mixture was stirred continuously for five days. After this period, the toluene layer was removed, and ethanol was added to the aqueous phase, leading to the precipitation of the product as a dark brown solid. The precipitate was collected via centrifugation (4500 rpm, 5 min) and subjected to five washing cycles with ethanol. The final product was characterized based on its enhanced solubility in water.

3.1.2 Synthesis of Activated Fullerenol

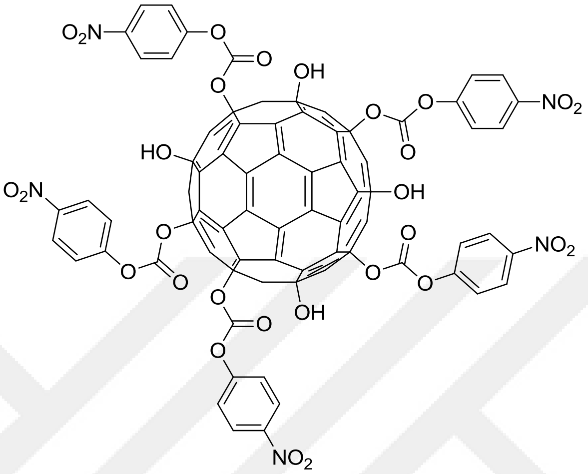

Activated Fullerenol

Based on literature [71], a suspension of fullerenol (60 mg) in DMF was prepared and subjected to sonication for one hour. Following this, *p*-nitrophenyl chloroformate (400 mg), anhydrous pyridine (2 mL), and a catalytic amount of DMAP were introduced at 0 °C. The reaction mixture was stirred under a nitrogen atmosphere for 48 hours, with additional one-hour sonication applied twice a day. Upon completion of the reaction, the addition of diethyl ether induced the precipitation of a brown-colored solid. The precipitate was purified by washing with diethyl ether, DCM, and isopropyl alcohol using centrifugation (4500 rpm, 5 min) to eliminate impurities. The final product exhibited enhanced solubility in DMF and was further characterized by ^{1}H NMR spectroscopy, displaying aromatic doublets at 6.9 and 8.2 ppm.

3.1.3 Synthesis of F-Arg

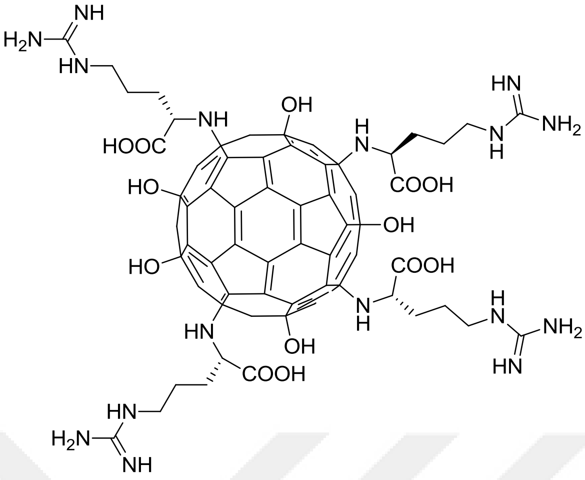

F-Arg

Based on literature [E1], a suspension of activated fullerenol (15 mg) in DMF was prepared and sonicated for 45 minutes before the addition of L-arginine (12 mg). The resulting brown mixture was stirred at room temperature under a nitrogen atmosphere for 48 hours, with additional one-hour sonication applied twice a day. Upon completion, precipitation was induced by the addition of diethyl ether. The solid product was collected and washed four times with 5–6 drops of methanol in DCM, using centrifugation (4500 rpm, 5 min) to remove impurities and any unreacted or unbound L-arginine remaining in the reaction mixture.

^{1}H NMR (400 MHz, D_2O) δ 3.32 (t, J = 6.0 Hz, 1H), 3.11 (t, J = 6.6 Hz, 2H), 1.70 – 1.43 (m, 4H).

3.1.4 Synthesis of *p*-Nitrophenyl Nicotinate (1)

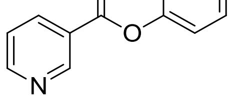

1

Based on literature [208], nicotinic acid (500 mg, 4 mmol) was dissolved in 15 mL of DMF, followed by the addition of *p*-nitrophenol (670 mg, 4.8 mmol), DMAP (50 mg, 0.4 mmol), and EDCI (620 mg, 4 mmol). The reaction mixture was heated to 70 °C and stirred overnight. After cooling to room temperature, the mixture was poured into an ice-water solution, leading to the precipitation of a yellow solid. The precipitate was collected by filtration, yielding 800 mg (3.3 mmol) of product, corresponding to an 82% yield.

^{1}H NMR (400 MHz, $CDCl_3$) δ 9.34 (s, 1H), 8.88 – 8.80 (m, 1H), 8.42 (dt, *J* = 7.9, 1.9 Hz, 1H), 8.28 (d, *J* = 9.0, 2H), 7.48 (dd, *J* = 8.0, 4.9 Hz, 1H), 7.38 (d, *J* = 9.0, 2H).

^{13}C NMR (100 MHz, $CDCl_3$) δ 162.7, 155.0, 154.1, 151.0, 145.6, 138.0, 125.3, 124.8, 123.7, 122.4.

3.1.5 Synthesis of L-Cysteine Methyl Ester Hydrochloride Salt (Cys-OMe)

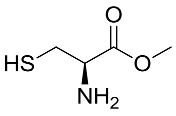

Cys-OMe

L-cysteine (600 mg, 5 mmol) was dissolved in 10 mL of methanol, and thionyl chloride ($SOCl_2$, 750 µL, 10 mmol) was added dropwise at 0 °C. Once the addition was complete, the ice bath was removed, and the reaction mixture was stirred overnight at room temperature. Following this, the solvent was evaporated, yielding a glassy solid. This solid was subsequently dissolved in 5 mL of methanol, and the resulting solution was added to 30 mL of cold ether, leading to the precipitation of the product as a white solid (850 mg, 5 mmol, 95% yield).

^{1}H NMR (400 MHz, D_2O) δ 4.32 (dd, *J* = 5.4, 4.1 Hz, 1H), 3.75 (s, 3H), 3.08 – 2.99 (m, 2H).

3.1.6 Synthesis of *N,S*-diacetyl-L-cysteine Methyl Ester (Cys-Diac)

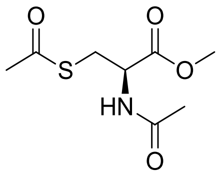

Cys-Diac

Based on literature [209], **Cys-OMe** (500 mg, 2.9 mmol) was dissolved in 15 mL of DCM. To this solution, triethylamine (600 µL, 4 mmol), acetic anhydride (1.3 mL, 13 mmol), and DMAP (20 mg, 0.2 mmol) were sequentially added at 0 °C. The reaction mixture was then stirred at room temperature for 4 hours. After completion, 20 mL of water was added, and the mixture was extracted three times with 15 mL of DCM. The combined organic layers were dried over anhydrous Na_2SO_4, and the solvent was removed under reduced pressure, yielding 280 mg (1.3 mmol) of a white solid with a 44% yield.

^{1}H-NMR (400 MHz, DMSO-d_6) δ 8.45 (d, J = 8.0 Hz, 1H), 4.38 (td, J = 8.1, 5.3 Hz, 1H), 3.64 (s, 3H), 3.31 (dd, J = 13.7, 5.3 Hz, 1H), 3.03 (dd, J = 13.7, 8.4 Hz, 1H), 2.34 (s, 3H), 1.84 (s, 3H).

3.1.7 Synthesis of *N*-Acetyl-L-cysteine *N'*-methylamide (2a)

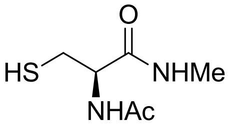

2a

Cys-Diac (200 mg, 0.9 mmol) was combined with methylamine (670 µL, 7.6 mmol, 40% in H_2O) at 0 °C. The reaction mixture was then stirred at room temperature for 6 hours, after which the solvent was evaporated, yielding a yellow oil. The crude product was recrystallized from methanol, resulting in a white solid (115 mg, 0.65 mmol, 72% yield).

^{1}H NMR (400 MHz, DMSO-d_6) δ 8.19 (d, *J* = 8.3 Hz, 1H), 7.98 (q, *J* = 4.6 Hz, 1H), 4.46 (td, *J* = 8.6, 5.3 Hz, 1H), 3.05 (dd, *J* = 13.5, 5.3 Hz, 1H), 2.81 (dd, *J* = 13.3, 8.8 Hz, 1H), 2.58 (d, *J* = 4.5 Hz, 3H), 1.87 (s, 3H).

3.1.8 Synthesis of *N,O*-diacetyl-L-serine Ethyl Ester (Ser-Diac)

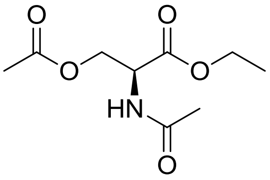

Ser-Diac

Based on literature [209], **Ser-OEt** (620 mg, 4.0 mmol) was dissolved in DCM (10 mL) at 0 °C. Acetyl chloride (300 µL, 4.4 mmol) and *N,N*-Diisopropylethylamine (DIEA, 1.8 mL, 10.2 mmol) were added sequentially, and the reaction mixture was stirred at 0 °C for 3 hours. After completion, water (20 mL) was added, and the mixture was extracted with DCM (15 mL) three times. The combined organic layers were dried over anhydrous Na_2SO_4, and the solvent was evaporated under reduced pressure, yielding the product as a white solid (570 mg, 2.8 mmol, 70% yield).

^{1}H NMR (400 MHz, DMSO-d_6) δ 8.40 (d, *J* = 7.9 Hz, 1H), 4.37 (td, *J* = 8.1, 5.3 Hz, 1H), 4.10 (q, *J* = 7.1 Hz, 2H), 3.32 – 3.26 (m, 1H), 3.05 (dd, *J* = 13.7, 8.2 Hz, 1H), 2.33 (s, 3H), 1.84 (s, 3H), 1.19 (t, *J* = 7.5 Hz, 3H).

3.1.9 Synthesis of *N*-acetyl-L-serine *N'*-methylamide (6)

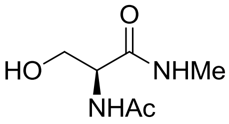

6

Ser-Diac (670 mg, 3.3 mmol) was cooled to 0 °C, and methylamine (10 mL, 40% in H_2O) was added. The reaction mixture was stirred overnight at room temperature, after which the solvent was evaporated, yielding a white solid. ^{1}H NMR analysis revealed the presence of a 1:1 mixture of compound **5** and *N*-methylacetamide as side product. Purification was not achieved, and based on NMR data, the yield was determined to be 64%.

^{1}H NMR (400 MHz, DMSO-d_6) δ 8.18 (d, J = 8.3 Hz, 1H), 7.97 (q, J = 4.7 Hz, 1H), 4.46 (td, J = 8.6, 5.2 Hz, 1H), 3.09 – 2.99 (m, 1H), 2.81 (dd, J = 13.4, 8.9 Hz, 1H), 2.58 (d, J = 4.6 Hz, 3H), 1.85 (s, 3H).

3.1.10 Synthesis of 2-acetamido-N-methylacrylamide (5a) (First Approach)

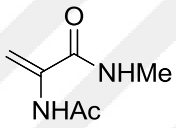

5a

Based on literature [210], compound **5** (100 mg, 0.6 mmol) was dissolved in DCM, and trimethylamine (100 µL, 0.7 mmol) and methanesulfonyl chloride (MsCl, 55 µL, 0.7 mmol) were added at 0 °C. The mesylation process was monitored by TLC. Once mesylation was complete, 1,8-diazabicyclo[5.4.0]undec-7-ene (DBU, 110 µL, 0.72 mmol) was added, and the reaction mixture was stirred overnight at 0 °C. The mixture was then diluted with ethyl acetate, and the organic layer was washed with 10% citric acid. The aqueous layer was extracted three times with ethyl acetate. The combined organic layers were dried over Na_2SO_4, filtered, and the solvent was evaporated under reduced pressure. However, no alkene formation was observed.

3.1.11 Synthesis of 2-acetamido-N-methylacrylamide (5a) (Second Approach)

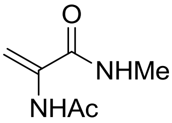

5a

Based on literature [211], compound **5** (100 mg, 0.6 mmol) was dissolved in DMF, followed by the addition of copper(I) chloride (CuCl, 30 mg, 0.3 mmol) and EDC (50 mg, 0.25 mmol). The reaction mixture was stirred overnight at room temperature, but no alkene formation was observed.

3.1.12 Synthesis of 2-Acetamidoacrylic Acid (ACA)

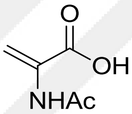

ACA

A mixture of pyruvic acid (2.0 mL, 28 mmol) and acetamide (740 mg, 13 mmol) was added to a flask with 60 mL of toluene. The flask was equipped with a Dean-Stark apparatus, and the reaction mixture was refluxed overnight. The resulting precipitate was collected by filtration and washed several times with hexane and cold methanol. This yielded 1.2 g (9.4 mmol) of 2-acetamidoacrylic acid (ACA) as a white solid, with a 72% yield.

^{1}H NMR (400 MHz, DMSO-d_6) δ 13.2 (bs, 1H), 9.11 (s, 1H), 6.22 (s, 1H), 5.65 (s, 1H), 2.01 (s, 3H).

3.1.13 Enzymatic Mimic Reaction with Compound 2a

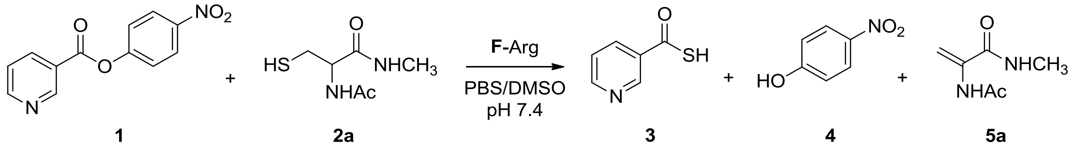

From a stock solution containing 4.0 mM of the cysteine derivative compound **2a**, 0.25 mL was taken and mixed with 0.25 mL of a TCEP solution (prepared by dissolving 10 mg of TCEP in 2.0 mL of PBS). The resulting mixture was then diluted to a final volume of 1.0 mL.

Separately, another solution was prepared by mixing 0.1 mL of compound **1** from a 12 mM stock solution in DMSO with 0.05 mL of **F**-Arg solution from a 0.2 mM stock solution. This mixture was then diluted to a total volume of 1.0 mL with PBS.

The two prepared solutions were combined to obtain final concentrations of 0.5 mM of **2a**, 0.6 mM of **1**, and 0.005 mM of **F**-Arg. The reaction mixture was stirred at room temperature, and at specific time intervals, as described in the Results and Discussion section, a 100 μL sample was taken and acidified with 10 μL of 1% TFA solution to terminate the reaction. The samples were then analyzed using HPLC.

Reactions were also performed using different molar ratios following the same procedure.

3.1.14 Synthesis of L-Cystine Dimethyl Ester Hydrochloride Salt (Cys$_2$-OMe)

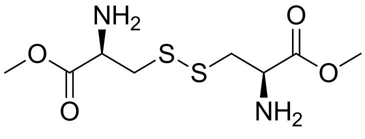

Cys$_2$-OMe

L-Cystine (5.0 g, 20.8 mmol) was dissolved in 100 mL of methanol and cooled to -78 °C. Thionyl chloride (5.0 mL, 69 mmol) was then added dropwise at the same temperature. After the addition was complete, the reaction mixture was gradually warmed to room temperature and refluxed overnight. The solvent was subsequently evaporated, yielding a yellowish solid. The crude product was dissolved in methanol (15 mL) and precipitated by the addition of cold ether (75 mL), resulting in the pure product **Cys$_2$-OMe** as a white solid (7.0 g, 95% yield).

^{1}H NMR (400 MHz, DMSO-d_6) δ 8.98 (s, 3H), 4.34 (t, J = 5.8 Hz, 1H), 3.75 (s, 3H), 3.39 (d, J = 14.7 Hz, 1H), 3.35 – 3.26 (m, 1H).

3.1.15 Synthesis of Boc-Protected L-Cystine Dimethyl Ester (Boc-Cys$_2$-OMe)

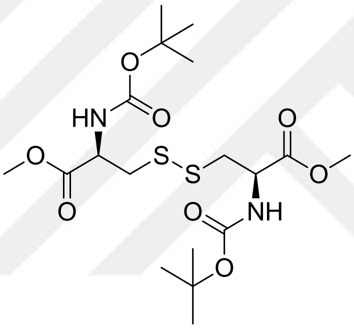

Boc-Cys$_2$-OMe

Based on literature [212], **Cys$_2$-OMe** (250 mg, 0.73 mmol) was dissolved in a mixture of distilled water and THF (10 mL). Trimethylamine (610 µL, 4.4 mmol) and Boc anhydride (350 µL, 1.52 mmol) were then added at 0 °C. The reaction mixture was gradually warmed to room temperature and stirred overnight. THF was removed under reduced pressure, and the aqueous solution was extracted three times with ethyl acetate. The combined organic layers were dried over anhydrous Na_2SO_4, and the solvent was evaporated, yielding the product **Boc-Cys$_2$-OMe** as a white solid (255 mg, 0.55 mmol, 75% yield).

3.1.16 Synthesis of Boc-Protected L-Cystine Methylamide (Boc-Cys$_2$-NHCH$_3$)

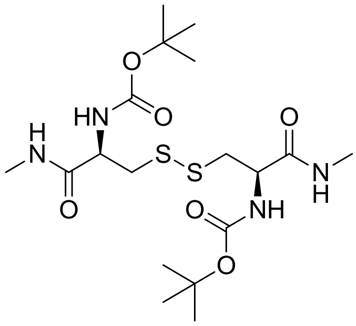

Boc-Cys$_2$-NHCH$_3$

Boc-Cys$_2$-OMe (450 mg, 0.97 mmol) was dissolved in 10 mL of methanol, and methylamine solution (20 mL, in water) was added at 0 °C. The reaction mixture was stirred overnight at room temperature. Water and excess methylamine were then removed under reduced pressure, yielding the crude product as a yellowish oily solid. The crude material was dissolved in 10 mL of methanol, and the solvent was evaporated under reduced pressure. The final product, **Boc-Cys$_2$-NHCH$_3$**, was obtained as a white solid (290 mg, 0.63 mmol, 65% yield).

^{1}H NMR (400 MHz, DMSO-d_6) δ 7.95 – 7.85 (m, 2H), 7.03 (d, J = 8.5 Hz, 2H), 4.14 (td, J = 9.1, 4.6 Hz, 2H), 3.05 (dt, J = 13.4, 7.0 Hz, 2H), 2.80 (dd, J = 13.3, 9.8 Hz, 2H), 2.58 (d, J = 4.6 Hz, 6H), 1.38 (s, 18H).

3.1.17 Synthesis of L-Cystine Methylamide (Cys$_2$-NHCH$_3$)

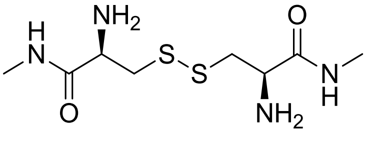

Cys$_2$-NHCH$_3$

Boc-Cys$_2$-NHCH$_3$ (200 mg, 0.43 mmol) was dissolved in 2 mL of DCM and cooled to 0 °C. 5 mL of TFA was then added at the same temperature, and the reaction mixture was stirred for 2 hours. The solvent was removed under reduced pressure, and the remaining residue was lyophilized overnight, yielding the crude product as a yellowish solid. The solid was dissolved in methanol (5 mL), and the solution was added to cold ether (20 mL), resulting in the precipitation of pure **Cys$_2$-NHCH$_3$** as a white solid (110 mg, 100% yield).

^{1}H NMR (400 MHz, DMSO-d_6) δ 8.55 (d, J = 4.9 Hz, 1H), 8.28 (s, 3H), 4.01 – 3.95 (m, 1H), 3.21 (dd, J = 14.4, 5.2 Hz, 1H), 2.98 (dd, J = 14.3, 8.1 Hz, 1H), 2.69 (d, J = 4.6 Hz, 3H).

3.1.18 Synthesis of *N*-FITC-L-Cystine Methylamide (FITC-Cys$_2$-NHCH$_3$, 2b)

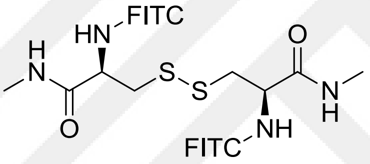

FITC-Cys$_2$-NHCH$_3$ (2b)

Cys$_2$-NHCH$_3$ (50 mg, 0.19 mmol) was dissolved in 10 mL of anhydrous DMF. Fluorescein isothiocyanate (FITC, 155 mg, 0.4 mmol) in 4 mL of anhydrous DMF and triethylamine (56 µL, 0.4 mmol) were then added at room temperature. The reaction mixture was stirred overnight. The solvent was removed under reduced pressure, yielding the crude product as an orange solid. Purification was not achieved, and the crude product was used directly for further analysis.

3.1.19 Enzyme Mimic Reaction with Compound 2b

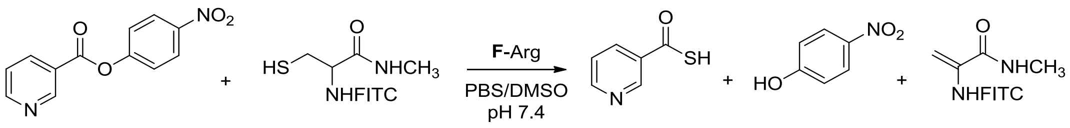

1 **2b** **3** **4** **5b**

The enzyme mimic reaction with compound **2b** was performed following the procedure described in Section **3.1.13.**

3.1.20 Synthesis of Thiohydantoin Derivative of Cysteine (2c)

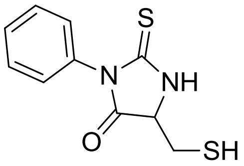

2c

Based on literature [213], L-cystine (1.0 g, 4.2 mmol) and KOH (540 mg, 9.7 mmol) were dissolved in 3.0 mL of water. A solution of phenyl isothiocyanate (PhSCN) (1.2 mL, 9.7 mmol) in 20 mL of ethanol was then added dropwise to the reaction mixture, which was stirred at room temperature for 2 days. After completion, the solvent was evaporated to a small volume, yielding an oily crude product. To dissolve the obtained oil, 20 mL of a 1:1 mixture of glacial acetic acid and concentrated HCl was added, and the solution was allowed to stand overnight at 4 °C. The precipitate was collected by centrifugation. The first purification was carried out using column chromatography (silica gel, DCM:EtOAc 4:1), yielding 200 mg of a yellowish-white crude product. Analysis revealed that the mixture contained both the half-cyclized and fully cyclized products. The crude product was then dissolved in 10 mL of methanol, and a solution of TCEP (75 mg) in 5 mL of water was added. The reaction mixture was stirred at room temperature for 1 hour before the solvent was removed under reduced pressure. The residue was purified by column chromatography (silica gel, DCM:Hexane:EtOAc 8:1:1), resulting 50 mg of pure compound **2c** with a 5% yield.

^{1}H NMR (400 MHz, $CDCl_3$) δ 7.89 (s, 1H), 7.49 – 7.40 (m, 3H), 7.26 (dd, J = 7.1, 1.8 Hz, 2H), 4.45 (t, J = 4.6 Hz, 1H), 3.06 (ddd, J = 14.5, 7.7, 3.7 Hz, 1H), 2.96 (ddd, J = 14.8, 10.3, 5.4 Hz, 1H).

3.1.21 Synthesis of Thiohydantoin Derivative of Dehydroalanine (5c)

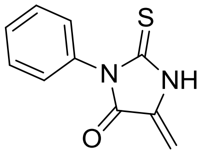

5c

Based on literature [214], L-serine (500 mg, 4.8 mmol) was dissolved in 15 mL of a 1:1 mixture of pyridine and water. The pH of the solution was adjusted to 10 with a 1 M NaOH solution. The reaction mixture was then heated to 40 °C, and PhSCN (600 µL, 5.0 mmol) was added dropwise. Upon addition, the solution turned pale yellow. The mixture was stirred at this temperature for 1 hour. After completion, the reaction mixture was extracted six times with toluene (10 mL per extraction). The aqueous phase was then combined with 50 mL of water and acidified to pH 2 using concentrated HCl. The solution was allowed to stand overnight at 4 °C, subsequently, the precipitate was collected, yielding 600 mg of pure compound **5c** with a 61% yield.

^{1}H-NMR (400 MHz, DMSO-d_6) δ 12.53 (bs, 1H), 7.54 – 7.44 (m, 3H), 7.38 – 7.32 (m, 2H), 5.36 (d, J = 1.9 Hz, 1H), 5.17 (d, J = 1.9 Hz, 1H).

3.1.22 Enzyme Mimic Reaction with Compound 2c

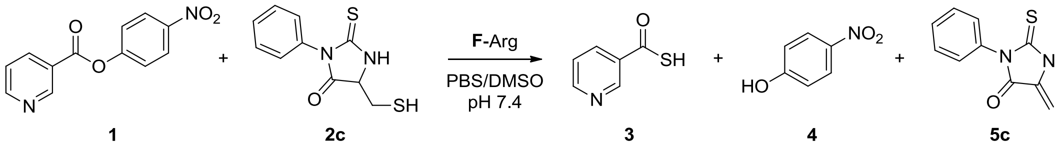

The enzyme mimic reaction with compound **2c** was performed following the procedure described in Section **3.1.13.** The analysis was carried out using UV-Vis spectroscopy. UV-Vis analysis was performed by withdrawing 200 µL aliquots of the reaction mixture at selected time intervals. Each sample was diluted to 1 mL using phosphate buffer (pH 7.4) and transferred into a quartz cuvette for spectral analysis. Absorbance was recorded between 200–600 nm, focusing particularly on 320 nm (indicative of compound 5c) and 410 nm (associated with p-nitrophenol formation).

3.1.23 Synthesis of *N*-Acetyl-L-cysteine-*N'*-benzylamide (2d) (First Approach)

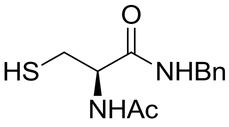

2d

Cys-Diac (200 mg, 0.9 mmol) was dissolved in 10 mL of EtOAc, followed by the addition of benzylamine (350 μL, 3.2 mmol). The reaction mixture was stirred overnight at room temperature. Upon completion, the solvent was evaporated under reduced pressure, yielding a yellow oily crude product. Purification via column chromatography (silica gel, EtOAc:Hexane, 3:1) afforded compound **2d** as a white solid (25 mg, 11% yield).

^{1}H NMR (400 MHz, DMSO-d_6) δ 8.52 (t, J = 6.0 Hz, 1H), 8.13 (d, J = 8.1 Hz, 1H), 7.33 – 7.29 (m, 2H), 7.28 – 7.21 (m, 3H), 4.39 (td, J = 7.8, 5.5 Hz, 1H), 4.29 (d, J = 6.0 Hz, 2H), 2.80 (ddd, J = 13.3, 8.8, 5.6 Hz, 1H), 2.69 (dt, J = 13.4, 7.8 Hz, 1H), 1.89 (s, 3H).

3.1.24 Synthesis of *N*-Acetyl-*S*-trityl-L-cysteine (Trt-NAC)

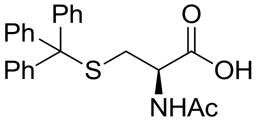

Trt-NAC

Based on literature [215], *N*-Acetyl-L-cysteine (**NAC**) (500 mg, 3.1 mmol) was dissolved in 10 mL of DMF, and triphenylmethyl chloride (Trt-Cl) (1.3 g, 4.6 mmol) was added to the solution. The reaction mixture was stirred overnight at room temperature. After completion, the solvent was evaporated under reduced pressure, and the residue was treated with EtOAc and water. The mixture was extracted, the organic layer was dried over anhydrous Na_2SO_4, and the solvent was evaporated. The crude product was purified by column chromatography (silica gel, EtOAc:MeOH, 4:1), yielding 1.0 g of compound **Trt-NAC** as a white solid (82%).

^{1}H NMR (400 MHz, $CDCl_3$) δ 7.38 – 7.30 (m, 6H), 7.24 – 7.19 (m, 6H), 7.18 – 7.12 (m, 3H), 5.93 (d, J = 7.4 Hz, 1H), 4.39 (td, J = 6.6, 4.6 Hz, 1H), 2.69 (dd, J = 12.7, 6.2 Hz, 1H), 2.61 (dd, J = 12.7, 4.6 Hz, 1H), 1.88 (s, 3H).

3.1.25 Synthesis of *N*-Acetyl-*S*-trityl-L-cysteine-*N'*-benzylamide (Trt-NAC-NHBn)

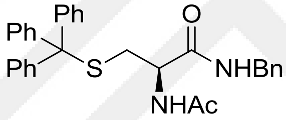

Trt-NAC-NHBn

Based on literature [216], **Trt-NAC** (290 mg, 0.71 mmol) and N-methylmorpholine (NMM) (80 µL, 0.73 mmol) were dissolved in 5 mL of EtOAc and cooled to -15 °C. To this solution, isobutyl chloroformate (IBCF) (95 µL, 0.73 mmol) was added, and the reaction mixture was stirred at this temperature for 15 minutes. Benzylamine (80 µL, 0.71 mmol) was then added, and the reaction mixture was allowed to warm to room temperature. The reaction mixture was subsequently stirred at room temperature for 3 hours. After completion, the mixture was filtered, and the solvent was evaporated under reduced pressure, yielding an oily crude product. Purification by column chromatography (silica gel, EtOAc:Hexane, 4:1) resulted in 280 mg of compound **Trt-NAC-NHBn** as a white solid (80%).

^{1}H NMR (400 MHz, $CDCl_3$) *δ* 7.37 – 7.32 (m, 5H), 7.25 – 7.17 (m, 11H), 7.16 – 7.11 (m, 4H), 6.28 (d, *J* = 6.0 Hz, 1H), 5.85 (t, *J* = 10.6 Hz, 1H), 4.38 – 4.19 (m, 3H), 2.68 (ddd, *J* = 11.6, 6.9, 4.7 Hz, 1H), 2.47 (ddd, *J* = 13.0, 6.0, 2.4 Hz, 1H).

^{13}C NMR (100 MHz, $CDCl_3$) *δ* 170.0, 144.4, 137.6, 129.6, 128.6, 128.1, 127.7, 127.5, 126.9, 67.2, 52.3, 43.6, 33.5, 23.1.

3.1.26 Synthesis of *N*-Acetyl-L-cysteine-*N'*-benzylamide (2d)

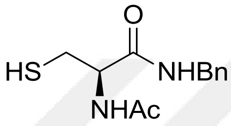

2d

Based on literature [217], **Trt-NAC-NHBn** (150 mg, 0.3 mmol) was dissolved in 1 mL of DCM. To this solution, TFA (1 mL) was added, followed by the dropwise addition of TIPS (185 µL, 0.9 mmol) at room temperature. The reaction mixture was stirred at room temperature for 1 hour, then evaporated with toluene three times. The residue was treated with 5 mL of hexane and stirred for an additional hour. The resulting precipitate was collected by centrifugation, affording 75 mg of compound **2d** with a 100% yield.

^{1}H NMR (400 MHz, DMSO-*d*$_6$) *δ* 8.52 (t, *J* = 6.0 Hz, 1H), 8.13 (d, *J* = 8.1 Hz, 1H), 7.33 – 7.29 (m, 2H), 7.28 – 7.21 (m, 3H), 4.39 (td, *J* = 7.8, 5.5 Hz, 1H), 4.29 (d, *J* = 6.0 Hz, 2H), 2.80 (ddd, *J* = 13.3, 8.8, 5.6 Hz, 1H), 2.69 (dt, *J* = 13.4, 7.8 Hz, 1H), 1.89 (s, 3H).

^{13}C NMR (100 MHz, DMSO-*d*$_6$) δ 169.9, 169.4, 139.2, 129.0, 128.3, 128.2, 127.0, 126.7, 126.2, 55.1, 26.1, 22.5.

3.1.27 Synthesis of 5d

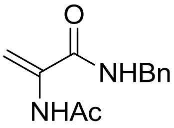

5d

ACA (130 mg, 1.0 mmol) was dissolved in 10 mL of EtOAc and cooled to -15 °C. HOSu (140 mg, 1.2 mmol) and DCC (250 mg, 1.2 mmol) were then added at this temperature, and the reaction mixture was stirred for 1 hour. The mixture was subsequently warmed to room temperature, followed by the addition of benzylamine (200 μL, 1.8 mmol). Stirring was continued overnight at room temperature. Upon completion, the reaction mixture was filtered, and the solvent from the filtrate was evaporated under reduced pressure. The crude product was purified via column chromatography (silica gel, EtOAc:Hexane 2:1), affording compound **5d** as a white solid (140 mg, 65% yield).

^{1}H NMR (400 MHz, DMSO-*d*$_6$) *δ* 9.11 (s, 1H), 8.88 (t, *J* = 6.2 Hz, 1H), 7.29 (m, 5H), 6.03 (s, 1H), 5.43 (s, 1H), 4.36 (d, *J* = 6.1 Hz, 2H), 2.00 (s, 3H).

^{13}C NMR (100 MHz, CDCl$_3$) δ 169.1, 163.9, 137.4, 134.2, 128.9, 128.6, 127.9, 127.8, 100.9, 44.2, 24.7.

3.1.28 Optimized Enzyme Mimic Reaction with Compound 2d

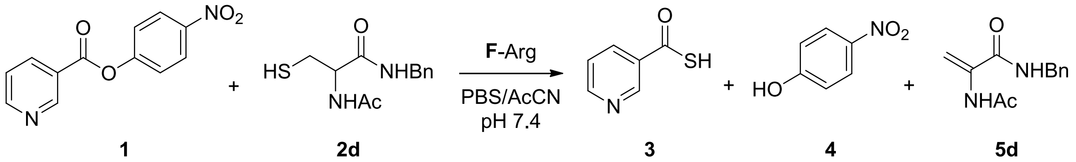

From a stock solution containing 4.0 mM of the cysteine derivative compound **2d**, 0.5 mL was taken and mixed with 0.5 mL of a TCEP solution (prepared by dissolving 20 mg of TCEP in 2.0 mL of PBS). The resulting mixture was then diluted to a final volume of 2.0 mL with PBS. To this solution, 0.2 mL of compound 1 from a 12 mM stock solution in acetonitrile (MeCN) was added, and the total volume was adjusted to 3.9 mL using MeCN and PBS. The reaction mixture was stirred at room temperature for 1 hour to allow the formation of **thioester d**.

After 1 hour, the temperature was increased to 35 °C, and 0.1 mL of an **F**-Arg solution (0.2 mM in PBS) was added. The reaction mixture was stirred at this temperature. At specific time intervals, as described in the Results and Discussion section, a 250 µL sample was taken and acidified with 30 µL of 1% TFA solution to terminate the reaction. The samples were then analyzed using HPLC.

Reactions were also performed using different molar ratios following the same procedure.

3.1.29 Synthesis of F-HS

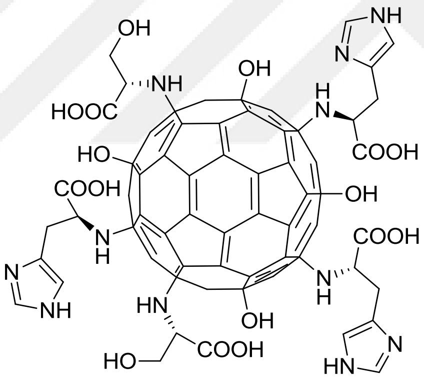

F-HS

For the synthesis of **F**-HS, the same method as **F**-Arg synthesis was applied. Histidine and serine were introduced sequentially into the reaction mixture in equimolar amounts. The degree of substitution was determined using the same approach and calculated to be equal for histidine and serine, with a substitution degree of 6 for each.

3.1.30 Synthesis of F-His

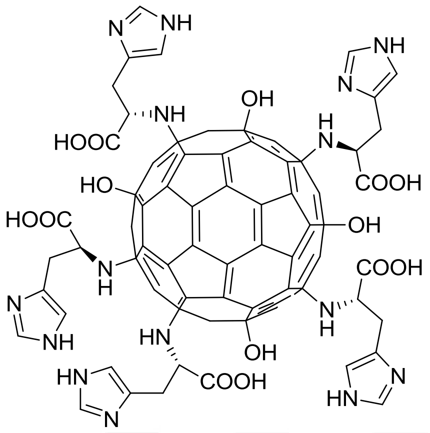

F-His

For the synthesis of **F**-His, the same method as **F**-Arg synthesis was applied. The degree of substitution was determined as 7.

^{1}H NMR (400 MHz, D_2O) δ 7.68 (s, 1H), 6.92 (s, 1H), 3.83 (dd, *J* = 7.9, 4.9 Hz, 1H), 3.08 (dd, *J* = 15.5, 4.9 Hz, 1H), 2.98 (dd, *J* = 15.5, 7.9 Hz, 1H).

3.1.31 Synthesis of F-Gly

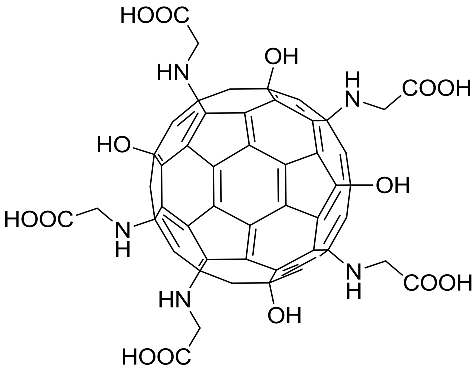

F-Gly

For the synthesis of **F**-Gly, the same method as **F**-Arg synthesis was applied. The degree of substitution was determined as 7.

^{1}H NMR (400 MHz, D_2O) δ 3.42 (s).

3.1.32 Synthesis of F-Asp

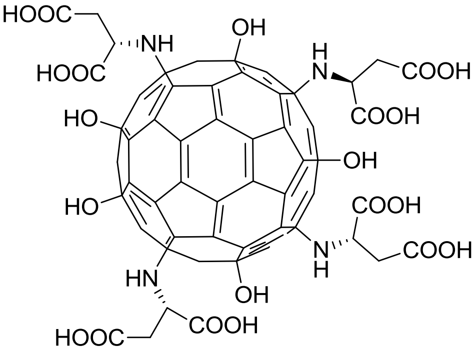

F-Asp

For the synthesis of **F**-Asp, the same method as **F**-Arg synthesis was applied. The degree of substitution was determined as 8.

^{1}H NMR (400 MHz, D_2O) δ 3.90 (dd, J = 6.7, 4.7 Hz, 1H), 2.83 (t, J = 5.7 Hz, 2H).

3.1.33 Synthesis of F-Glu

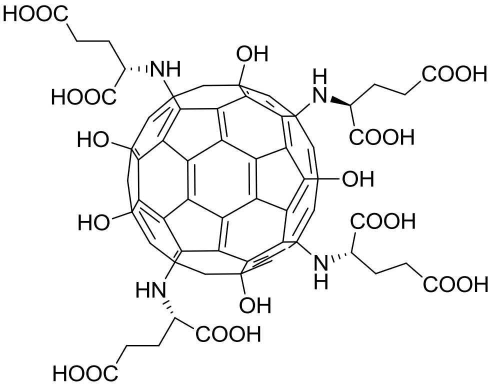

F-Glu

For the synthesis of **F**-Glu, the same method as **F**-Arg synthesis was applied. The degree of substitution was determined as 8.

^{1}H NMR (400 MHz, D_2O) δ 3.66 (t, J = 6.3 Hz, 1H), 2.45 – 2.34 (m, 2H), 2.06 – 1.93 (m, 2H).

3.1.34 Representative CO_2 Fixation Procedure

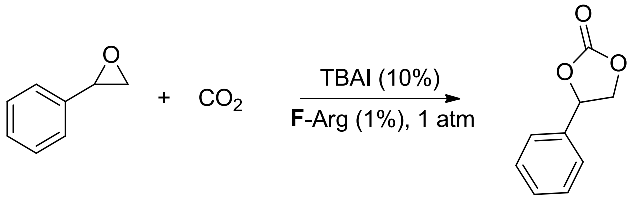

SO **SC**

A mixture of styrene oxide (200 µL, 1.8 mmol), TBAI (65 mg, 0.18 mmol, 10 mol%), and **F**-Arg (200 mg, 0.009 mmol, 0.5 mol%) was stirred in a septum-sealed reaction tube under atmospheric pressure. A CO_2-filled balloon (connected to a syringe) was prepared, and the syringe was inserted through the septum to introduce CO_2 into the system. The reaction mixture was stirred at 50 °C for 24 hours. After completion, an aliquot was taken from the reaction mixture for ^{1}H NMR analysis to determine the conversion.

Other reactions were carried out under similar conditions, varying the reactant ratios, reaction time, catalyst, and temperature, as summarized in Table 7, 8 and 9.

3.1.35 Morita-Baylis-Hillman (MBH Reaction)

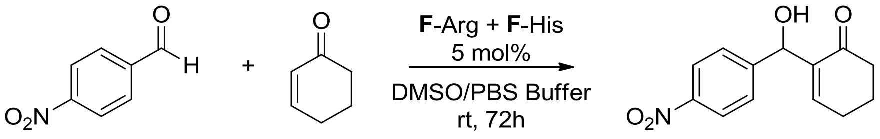

M1a **M2** **M3a**

p-Nitrobenzaldehyde (**M1**, 15 mg, 0.1 mmol) and cyclohexene-1-one (**M2**, 10 µL, 0.1 mmol) were dissolved in 0.5 mL of DMSO. To this solution, 4.5 mL of PBS containing **F**-His (10 mg) and **F**-Arg (10 mg) was added, resulting in a 5 mol% catalyst loading and a PBS:DMSO ratio of 9:1. The reaction mixture was stirred at room temperature for 72 hours. Upon completion, the mixture was diluted with 10 mL of water and extracted with EtOAc. The combined organic phase was dried over anhydrous Na_2SO_4, and the solvent was evaporated. The yield of the resulting compound was determined by ^1H NMR spectroscopy.

The same procedure was also applied using pristine histidine and arginine (5 mol% each) instead of their fullerene-functionalized forms. Additionally, a control reaction was carried out under identical conditions without any catalyst.

Column chromatography (silica gel, EtOAc:Hexane 3:1) was carried out when applied.

3.1.36 Representative 2-Amino-3-cyano-4H-chromene Synthesis Procedure

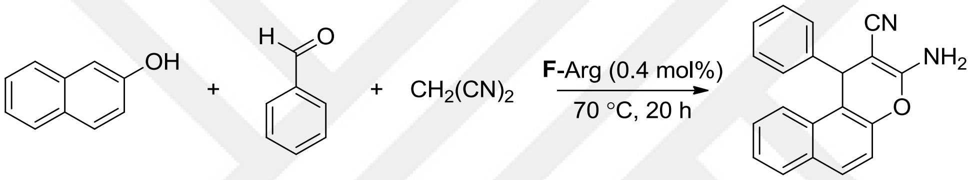

C1 **C2** **C3** **C4**

β-Naphthol (**C1**, 140 mg, 1 mmol), benzaldehyde (**C2**, 100 μL, 1 mmol), and malononitrile (**C3**, 65 mg, 1 mmol) were mixed in a test tube, followed by the addition of **F**-Arg (10 mg, 0.4 mol%). The reaction mixture was heated to 70 °C and stirred at this temperature for 20 hours. Upon completion, a solid mass formed in the test tube. The conversion yield was determined by ^1H NMR spectroscopy, as described in the Results and Discussion chapter.

Other reactions were carried out under similar conditions, with variations in the catalyst (pristine arginine or no catalyst), temperature, and solvent, as summarized in Table 10 and Table 11.

3.1.37 Prins Cyclization

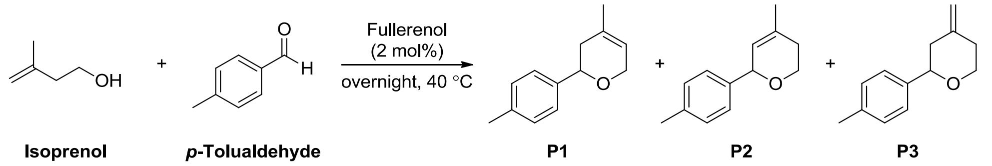

p-Tolualdehyde (120 µL, 1 mmol) and isoprenol (100 µL, 1 mmol) were mixed in a test tube, followed by the addition of fullerenol (20 mg, 0.02 mmol, 2 mol%). The reaction mixture was heated to 40 °C and then stirred overnight at room temperature. Upon completion, water was added, and the mixture was extracted with EtOAc. The combined organic phase was dried over anhydrous Na_2SO_4, and the solvent was evaporated. The yield of the resulting compound was determined by ^1H NMR spectroscopy.

The same procedure was also performed under identical conditions in the absence of any catalyst.

3.1.38 Prins-Friedel-Crafts Reaction

Benzaldehyde (40 µL, 0.4 mmol) was dissolved in 600 µL of benzene. A separate solution of 3-butene-1-ol (35 µL, 0.4 mmol) in 300 µL of benzene was then added, followed by the addition of fullerenol (25 mg, 0.02 mmol, 5 mol%). The reaction mixture was stirred overnight. Upon completion, water was added, and the mixture was extracted with EtOAc. The combined organic phase was dried over anhydrous Na_2SO_4, and the solvent was evaporated. The yield of the resulting compound was determined by ^1H NMR spectroscopy.

3.1.39 Cis-2-phenyltetrahydro-2H-pyran-4-ol (P5) Synthesis with Prins Cyclization

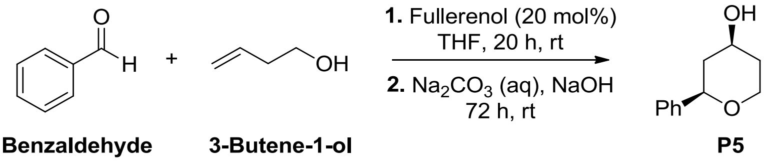

Benzaldehyde (50 µL, 0.5 mmol) and 3-butene-1-ol (65 µL, 0.75 mmol) were dissolved in 2.0 mL of THF. Fullerenol (120 mg, 0.1 mmol, 20 mol%) was then added, and the reaction mixture was stirred at room temperature for 20 hours. After this period, a saturated Na_2CO_3 solution (2 mL) and NaOH (25 mg) were added, and stirring was continued for an additional 72 hours at room temperature. Upon completion, water was added, and the mixture was extracted with DCM. The combined organic phase was dried over anhydrous Na_2SO_4, and the solvent was evaporated. The yield of the resulting compound was determined by ^{1}H NMR spectroscopy.

This reaction was also performed separately using TFA and formic acid instead of fullerenol, but each was added in 10 equivalents.

CHAPTER 4

CONCLUSION

In this study, various investigations were carried out using amino acid-functionalized fullerenol. Fullerenols functionalized with different amino acids were synthesized, and their catalytic effects in various reactions were examined.

The first part of this thesis focused on designing and developing a novel enzyme mimic inspired by the mechanism of LarE, a key component in the biosynthesis of Lactic acid racemase (LarA). To achieve this, a fullerene-based mimic (**F**-Arg) was developed to replicate catalytic function of LarE (Scheme 70). Various cysteine derivatives were then synthesized and tested under different conditions using **F**-Arg as the catalyst. Through systematic modifications and optimization studies, the most effective reaction conditions were identified. Notably, *N*-acetyl-L-cysteine-*N'*-benzylamide (compound **2d**) was found to exhibit catalytic activity at a temperature close to physiological conditions (35 °C), leading to the formation of dehydroalanine, which was successfully monitored by HPLC and further confirmed via LC-MS analysis, supporting the proposed reaction mechanism.

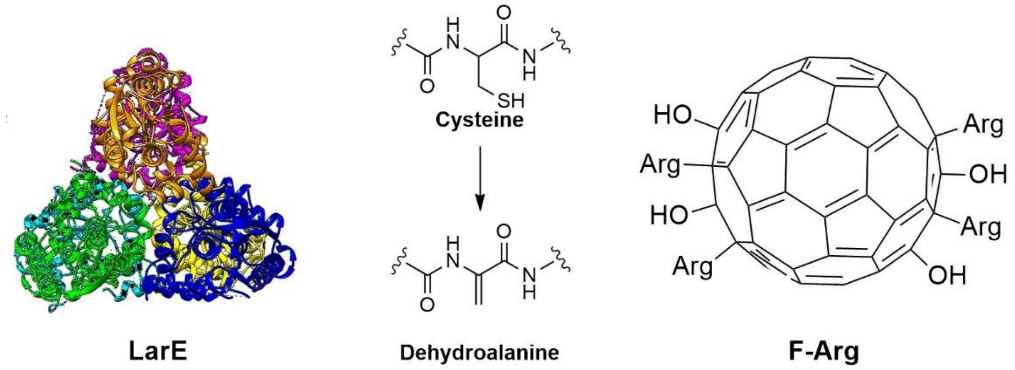

Scheme 70. LarE catalyzed the conversion of cysteine to dehydroalanine, mimicked by **F**-Arg.

Kinetic studies confirmed that the system followed Michaelis-Menten behavior, with calculated K_m and k_{cat}/K_m values suggesting efficient substrate conversion under optimized conditions. However, since LarE functions more as a reactant (a.k.a sacrificial enzyme) than a traditional enzyme, a direct comparison with literature values was not possible.

Control experiments further highlighted the catalytic role of **F**-Arg, as dehydroalanine formation did not occur in its absence. While pristine arginine required stoichiometric amounts to facilitate product formation, **F**-Arg functioned catalytically, reinforcing its role in mimicking enzymatic efficiency.

This study introduced a novel approach to biomimetic catalysis, utilizing acid functionalized fullerenols to mimic enzyme-like activity. Although the system showed promising catalytic performance, further optimization is required to improve its stability over prolonged reaction times. Additionally, future studies could explore different amino acid modifications to enhance catalytic activity and selectivity, potentially refining the efficiency of the mimic and broadening its applicability.

While this study provided valuable insights into enzyme mimicry, further investigations are required to gain a deeper understanding of the mechanistic details and to evaluate the consistency and reliability of this system under different reaction conditions. These findings contributed to biomimetic catalysis, offering new strategies for functionalized nanomaterials with enzyme-like properties.

In the second part of this thesis, an electrode based on fullerenzymes (**F**-HS) was developed as an artificial esterase-type enzyme model, demonstrating its ability to detect acetylcholine (ACh) in human serum samples. The synthesis, characterization and electrochemical evaluation of **F**-HS were described, with a focus on its potential application as a biomarker detection platform for Alzheimer’s disease diagnosis (Scheme 71).

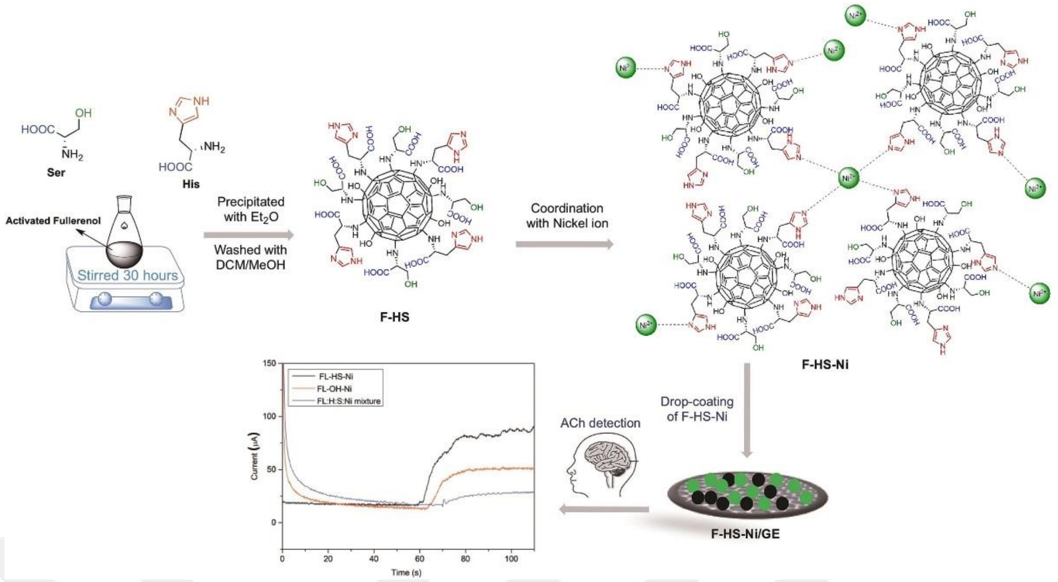

Scheme 71. The schematic representation of F-HS-Ni/GE sensor [206].

The structural and morphological properties of the synthesized conjugates were analyzed using ^{1}H NMR spectroscopy, SEM, TEM, and DLS, confirming the successful functionalization. Additionally, nickel coordination with F-HS was established to enhance its electrochemical performance. The electrochemical measurements validated the ability of the system to selectively bind and detect ACh.

The constructed **F**-HS-Ni/GE non-enzymatic sensor introduced a novel electrode design strategy, achieving high sensitivity and selectivity for ACh detection in human serum samples. This approach demonstrated high accuracy and introduced new possibilities for designing fullerenzyme-based sensor systems for point-of-care neurological disorder evaluation.

In addition to biosensing applications, amino acid-functionalized fullerenols were also employed as organocatalysts in a variety of organic transformations. Their catalytic performances were systematically evaluated under different conditions. These results offered valuable insight into the potential of fullerenes in green and metal-free catalysis (Scheme 72).

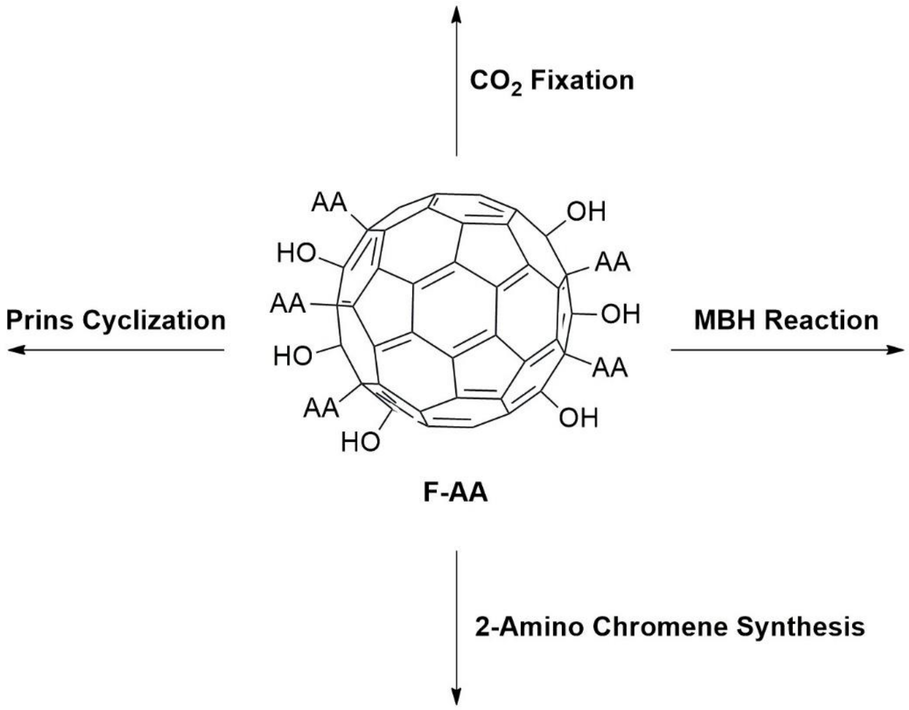

Scheme 72. Catalytic applications of **F**-AA in CO_2 fixation, MBH reaction, 2-amino chromene synthesis, and Prins cyclization.

In the third part of this thesis, versatile amino acid-conjugated fullerenols were used as H-bond donor catalysts for CO_2 fixation reactions. Different amino acid functionalized fullerenols were synthesized, and their catalytic performance was investigated at varying temperatures and reaction times. These catalysts were compared to fullerenol-based systems previously reported in the literature and their efficiency was also evaluated using different iodine sources.

While CO_2 fixation reactions using fullerenols were performed at temperatures exceeding 100 °C and under high pressure, in this study, the same transformation was achieved under significantly milder conditions. The reaction was carried out at lower temperatures and under atmospheric pressure. This approach reduced energy consumption and eliminated the need for complex pressurized setups, making the process more accessible and practical. These findings contribute to the development of milder and more sustainable catalytic strategies for CO_2 fixation. They also expand the potential applications of amino acid-functionalized fullerenols in green chemistry and carbon dioxide utilization efforts.

In the fourth part of this thesis, histidine and arginine conjugated fullerenols (**F**-His and **F**-Arg) were utilized as basic catalysts for the Morita-Baylis-Hillman (MBH) reaction between *p*-nitrobenzaldehyde and 2-cyclohexen-1-one. Control experiments showed that the reaction did not proceed in the absence of a catalyst or when pristine amino acids were used. However, with **F**-Arg and **F**-His, the reaction proceeded, leading to the formation of products, demonstrating the catalytic role of functionalized fullerenols in this transformation.

Although the obtained products could not be fully characterized within the scope of this study, the catalytic influence of fullerenol-based systems on the MBH reaction was clearly observed. Nevertheless, **F**-Arg and **F**-His conjugates still indicated an important ability to promote the reaction, despite the lack of full characterization. Future studies could focus on optimizing the reaction by exploring a wider range of aldehydes. Additionally, detailed characterization of the resulting products would help validate and expand upon these preliminary findings. Taken together, this study provided valuable insights into the potential of amino acid-functionalized fullerenols as basic organocatalysts. These findings offer a new perspective on their broader application in other carbon–carbon bond-forming reactions.

In the fifth part of this thesis, arginine-conjugated fullerenol (**F**-Arg) was utilized as basic catalysts for the synthesis of 2-amino-3-cyano-4H-chromene derivatives. The reaction was carried out under different temperatures and its efficiency was compared to reactions performed without a catalyst and with L-arginine. Additionally, the influence of protic and aprotic solvents on the reaction outcome was examined. This study also explored the effect of the degree of substitution on the fullerenol core, providing further insights into how structural modifications impact catalytic performance. These findings contributed to the ongoing development of fullerenol-based organocatalysts, offering a new approach to designing efficient catalytic systems for chromene synthesis and other related heterocyclic transformations.

In the final part of this thesis, fullerenols were employed as Brønsted-acid catalysts for the Prins cyclization reaction. Several variations of the reaction were explored to demonstrate the ability of fullerenol in this transformation. A notable comparison involved using fullerenol in a reaction typically catalyzed by trifluoroacetic acid (TFA) which is a strong acid. Despite the difference in acidity, comparable results were achieved which indicated the efficiency of fullerenol under milder conditions.

To further examine the catalytic nature of fullerenol, its performance was also compared with formic acid, which has a pK_a value close to that of fullerenol. The outcome of these experiments supported the conclusion that the acidic nature of fullerenol has a catalytic impact on the transformation. Altogether, these findings highlighted the potential of fullerenol as a milder, more sustainable alternative to traditional strong acids in Prins cyclization and opened new directions for its application in acid-catalyzed transformations.

Overall, this thesis demonstrated the versatility of amino acid-functionalized fullerenols in catalysis, highlighting their potential in biomimetic systems, organic transformations, and electrochemical applications. These results contribute to the expanding role of fullerenols in modern catalysis and inspire further research into their unexplored catalytic capabilities. While these findings represent a significant step, they also reveal how much more there is to explore, both in understanding the mechanisms and in expanding the scope of applications.

REFERENCES

1. Kroto, H. W.; Heath, J. R.; O'Brien, S. C.; Curl, R. F.; Smalley, R. E. C60: Buckminsterfullerene. *Nature*, **1985**, *318*, 162-163.
2. Haymet, A. D. Footballene: A theoretical prediction for the stable, truncated icosahedral molecule C60. *J. Am. Chem. Soc.*, **1986**, *108*, 319-321.
3. Lawton, R. G.; Barth, W. E. Synthesis of corannulene. *J. Am. Chem. Soc.*, **1971**, *93*, 1730-1745.
4. Kroto, H. Symmetry, space, stars, and C60 (Nobel lecture). *Angew. Chem. Int. Ed. Engl.*, **1997**, *36*, 1578-1593.
5. Krätschmer, W.; Lamb, L. D.; Fostiropoulos, K. H. D. R.; Huffman, D. R. Solid C60: a new form of carbon. *Nature*, **1990**, *347*, 354-358.
6. Hawkins, J. M.; Meyer, A.; Lewis, T. A.; Loren, S.; Hollander, F. J. Crystal structure of osmylated C60: confirmation of the soccer ball framework. *Science*, **1991**, *252*, 312-313.
7. Klein, D. J.; Schmalz, T. G.; Hite, G. E.; Seitz, W. A. Resonance in C60 buckminsterfullerene. *J. Am. Chem. Soc.*, **1986**, *108*, 1301-1302.
8. Sukharev, A. G. Symmetry of Icosahedron and Optical Properties of Fullerene C60. *Opt. Spectrosc.*, **2021**, *129*, 170-184.
9. Zum Bezolproblem, Q. B.; zum Problem, Q. B. Quantentheoretische beiträge zum benzolproblem. *Z. Phys. Chem.*, **1931**, *70*, 204-286.
10. Bühl, M.; Hirsch, A. Spherical aromaticity of fullerenes. *Chem. Rev.*, **2001**, *101*, 1153-1184.
11. McKee, D. W. The thermal stability of fullerene in air. *Carbon*, **1991**, *29*, 1057-1058.
12. Fagan, P. J.; Calabrese, J. C.; Malone, B. The chemical nature of buckminsterfullerene (C60) and the characterization of a platinum derivative. *Science*, **1991**, *252*, 1160-1161.

13. Bingel, C. Cyclopropanierung von fullerenen. *Chem. Ber.*, **1993**, *126*, 1957-1959.

14. Keshavarz-K, M.; Knight, B.; Srdanov, G.; Wudl, F. Cyanodihydrofullerenes and dicyanodihydrofullerene: the first polar solid based on C60. *J. Am. Chem. Soc.*, **1995**, *117*, 11371-11372.

15. Shu, L. H.; Wang, G. W.; Wu, S. H.; Wu, H. M. Reaction of [60] fullerene with 1-(4-methoxyphenyl)-1-(trimethylsilyloxy) ethylene. *J. Chem. Soc. Chem. Commun.*, **1995**, *3*, 367-368.

16. Komatsu, K.; Murata, Y.; Takimoto, N.; Mori, S.; Sugita, N.; Wan, T. S. Synthesis and properties of the first acetylene derivatives of C60. *J. Org. Chem.*, **1994**, *59*, 6101-6102.

17. Matsuo, Y.; Iwashita, A.; Abe, Y.; Li, C. Z.; Matsuo, K.; Hashiguchi, M.; Nakamura, E. Regioselective synthesis of 1,4-Di(organo)[60] fullerenes through DMF-assisted monoaddition of silylmethyl grignard reagents and subsequent alkylation reaction. *J. Am. Chem. Soc.*, **2008**, *130*, 15429-15436.

18. Echegoyen, L.; Echegoyen, L. E. Electrochemistry of fullerenes and their derivatives. *Acc. Chem. Res.*, **1998**, *31*, 593-601.

19. Bausch, J. W.; Prakash, G. S.; Olah, G. A.; Tse, D. S.; Lorents, D. C.; Bae, Y. K.; Malhotra, R. Considered novel aromatic systems. 11. Diamagnetic polyanions of the C60 and C70 fullerenes: preparation, 13C and 7Li NMR spectroscopic observation, and alkylation with methyl iodide to polymethylated fullerenes. *J. Am. Chem. Soc.*, **1991**, *113*, 3205-3206.

20. Kelty, S. P.; Chen, C. C.; Lieber, C. M. Superconductivity at 30 K in caesium-doped C60. *Nature*, **1991**, *352*, 223-225.

21. Kortan, A. R.; Kopylov, N.; Glarum, S.; Gyorgy, E. M.; Ramirez, A. P.; Fleming, R. M.; Haddon, R. C. Superconductivity in barium fulleride. *Nature*, **1992**, *360*, 566-568.

22. Boulas, P.; Subramanian, R.; Kutner, W.; Jones, M. T.; Kadish, K. M. Facile preparation of the C60 monoanion in aprotic solvents. *J. Electrochem. Soc.*, **1993**, *140*, L130.

23. Caron, C.; Subramanian, R.; D'Souza, F.; Kim, J.; Kutner, W.; Jones, M. T.; Kadish, K. M. Selective electrosynthesis of dimethylfullerene [(CH3)2C60]: a novel method for the controlled functionalization of fullerenes. *J. Am. Chem. Soc.*, **1993**, *115*, 8505-8506.

24. Zheng, M.; Li, F. F.; Ni, L.; Yang, W. W.; Gao, X. Synthesis and identification of heterocyclic derivatives of fullerene C60: Unexpected reaction of anionic C60 with benzonitrile. *J. Org. Chem.*, **2008**, *73*, 3159-3168.

25. Xiao, Y.; Zhu, S. E.; Liu, D. J.; Suzuki, M.; Lu, X.; Wang, G. W. Regioselective Electrosynthesis of Rare 1,2,3,16- Functionalized [60] Fullerene Derivatives. *Angew. Chem.*, **2014**, *126*, 3050-3054.

26. Kräutler, B.; Maynollo, J. Diels-Alder reactions of the [60] fullerene functionalizing a carbon sphere with flexibly and with rigidly bound addends. *Tetrahedron*, **1996**, *52*, 5033-5042.

27. Maggini, M.; Scorrano, G.; Prato, M. Addition of azomethine ylides to C60: Synthesis, characterization, and functionalization of fullerene pyrrolidines. *J. Am. Chem. Soc.*, **1993**, *115*, 9798-9799.

28. Hoke, S. H.; Molstad, J.; Dilettato, D.; Jay, M. J.; Carlson, D.; Kahr, B.; Cooks, R. G. Reaction of fullerenes and benzyne. *J. Org. Chem.*, **1992**, *57*, 5069-5071.

29. Wilson, S. R.; Kaprinidis, N.; Wu, Y.; Schuster, D. I. A new reaction of fullerenes: [2+2]-photocycloaddition of enones. *J. Am. Chem. Soc.*, **1993**, *115*, 8495-8496.

30. Zhang, X.; Fan, A.; Foote, C. S. [2+2] Cycloaddition of fullerenes with electron-rich alkenes and alkynes. *J. Org. Chem.*, **1996**, *61*, 5456-5461.

31. Komatsu, K.; Wang, G. W.; Murata, Y.; Tanaka, T.; Fujiwara, K.; Yamamoto, K.; Saunders, M. Mechanochemical synthesis and characterization of the fullerene dimer C120. *J. Org. Chem.*, **1998**, *63*, 9358-9366.

32. Heath, J. R.; O'Brien, S. C.; Zhang, Q.; Liu, Y.; Curl, R. F.; Tittel, F. K.; Smalley, R. E. Lanthanum complexes of spheroidal carbon shells. *J. Am. Chem. Soc.*, **1985**, *107*, 7779-7780.
33. Cioslowski, J.; Fleischmann, E. D. Endohedral complexes: Atoms and ions inside the C60 cage. *J. Chem. Phys.*, **1991**, *94*, 3730-3734.
34. Wang, L.; Alford, J. M.; Smalley, R. E. wlth Metals Inside. *J. Phys. Chem.*, **1991**, *95*, 7564-7568.
35. Kikuchi, K.; Suzuki, S.; Nakao, Y.; Nakahara, N.; Wakabayashi, T.; Shiromaru, H.; Saito, K.; Ikemoto, I.; Achiba, Y. Isolation and characterization of the metallofullerene LaC82. *Chem. Phys. Lett.*, **1993**, *216*, 67-71.
36. Weaver, J. H.; Chai, Y.; Kroll, G. H.; Jin, C.; Ohno, T. R.; Haufler, R. E.; Guo, T.; Alford, J. M.; Conceicao, J.; Chibante, L. P. F.; Jain, A.; Palmer, G.; Smalley, R. E. XPS probes of carbon-caged metals. *Chem. Phys. Lett.*, **1992**, *190*, 460-464.
37. Bethune, D. S.; Johnson, R. D.; Salem, J. R.; De Vries, M. S.; Yannoni, C. S. Atoms in carbon cages: the structure and properties of endohedral fullerenes. *Nature*, **1993**, *366*, 123-128.
38. Shinohara, H.; Sato, H.; Ohkohchi, M.; Ando, Y.; Kodama, T.; Shida, T.; Kato, T.; Saito, Y. Encapsulation of a scandium trimer in C82. *Nature*, **1992**, *357*, 52-54.
39. Stevenson, S.; Rice, G.; Glass, T.; Harich, K.; Cromer, F.; Jordan, M. R.; Craft, J.; Hadju, E.; Bible, R.; Olmstead, M. M.; Maitra, K.; Fisher, A. J.; Balch, A. L.; Dorn, H. C. Small-bandgap endohedral metallofullerenes in high yield and purity. *Nature*, **1999**, *401*, 55-57.
40. Wang, C. R.; Kai, T.; Tomiyama, T.; Yoshida, T.; Kobayashi, Y.; Nishibori, E.; Takata, M.; Sakata, M.; Shinohara, H. A scandium carbide endohedral metallofullerene: (Sc2C2)@C84. *Angew. Chem. Int. Ed.*, **2001**, *40*, 397-399.
41. Liu, F.; Gao, C.L.; Deng, Q.; Zhu, X.; Kostanyan, A.; Westerström, R.; Wang, S.; Tan, Y.Z.; Tao, J.; Xie, S.Y.; Popov, A. A.; Greber, T.; Yang, S.

Triangular monometallic cyanide cluster entrapped in a carbon cage with geometry-dependent molecular magnetism. *J. Am. Chem. Soc.*, **2016**, *138*, 14764–14771.

42. Stevenson, S.; Mackey, M. A.; Stuart, M. A.; Phillips, J. P.; Easterling, M. L.; Chancellor, C. J.; Olmstead, M. M.; Balch, A. L. A distorted tetrahedral metal oxide cluster inside an icosahedral carbon cage: Synthesis, isolation, and structural characterization of Sc4(μ3-O)2@Ih-C80. *J. Am. Chem. Soc.*, **2008**, *130*, 11844-11845.
43. Dunsch, L.; Yang, S.; Zhang, L.; Svitova, A.; Oswald, S.; Popov, A. A. Metal sulfide in a C82 fullerene cage: A new form of endohedral clusterfullerenes. *J. Am. Chem. Soc.*, **2010**, *132*, 5413-5421.
44. Krause, M.; Ziegs, F.; Popov, A. A.; Dunsch, L. Entrapped bonded hydrogen in a fullerene: The five-atom cluster Sc3CH in C80. *ChemPhysChem*, **2007**, *8*, 537-540.
45. Wang, T.S.; Feng, L.; Wu, J.Y.; Xu, W.; Xiang, J.F.; Tan, K.; Ma, Y.H.; Zheng, J.P.; Jiang, L.; Lu, X.; Shu, C.-Y.; Wang, C.-R. Triangular monometallic cyanide cluster entrapped in carbon cage with geometry-dependent molecular magnetism. *J. Am. Chem. Soc.*, **2010**, *132*, *46*, 16362–16364.
46. Fuertes-Espinosa, C.; Pujals, M.; Ribas, X. Supramolecular purification and regioselective functionalization of fullerenes and endohedral metallofullerenes. *Chem.*, **2020**, *6*, 3219-3262.
47. Saunders, M.; Jiménez-Vázquez, H. A.; Cross, R. J.; Poreda, R. J. Stable compounds of helium and neon: He@C60 and Ne@C60. *Science*, **1993**, *259*, 1428-1430.
48. Campbell, E. E. B.; Tellgmann, R.; Krawez, N.; Hertel, I. V. Production and LDMS characterization of endohedral alkalifullerene films. *J. Phys. Chem. Solids*, **1997**, *58*, 1763-1769.
49. Ruoff, R. S.; Malhotra, R.; Huestis, D. L.; Tse, D. S.; Lorents, D. C. Anomalous solubility behavior of C60. *Nature*, **1993**, *362*, 140-141.

50. Chiang, L. Y.; Swirczewski, J. W.; Hsu, C. S.; Chowdhury, S. K.; Cameron, S.; Creegan, K. Multi-hydroxy additions onto C60 fullerene molecules. *J. Chem. Soc. Chem. Commun.*, **1992**, *24*, 1791-1793.
51. Scrivens, W. A.; Tour, J. M.; Creek, K. E.; Pirisi, L. Synthesis of 14C-labeled C60, its suspension in water, and its uptake by human keratinocytes. *J. Am. Chem. Soc.*, **1994**, *116*, 4517-4518.
52. Prilutski, Y.; Durov, S.; Bulavin, L.; Pogorelov, V.; Astashkin, Y.; Yashchuk, V.; Ogul'chansky, T.; Buzaneva, E.; Andrievsky, G. Study of structure of colloidal particles of fullerenes in water solution. *Mol. Cryst. Liq. Cryst.*, **1998**, *324*, 65-70.
53. Deguchi, S.; Alargova, R. G.; Tsujii, K. Stable dispersions of fullerenes, C60 and C70, in water: Preparation and characterization. *Langmuir*, **2001**, *17*, 6013-6017.
54. Chiang, L. Y.; Swirczewski, J. W.; Hsu, C. S.; Chowdhury, S. K.; Cameron, S.; Creegan, K. Multi-hydroxy additions onto C60 fullerene molecules. *J. Chem. Soc. Chem. Commun.*, **1992**, *24*, 1791-1793.
55. Li, J.; Takeuchi, A.; Ozawa, M.; Li, X.; Saigo, K.; Kitazawa, K. C60 fullerol formation catalyzed by quaternary ammonium hydroxides. *J. Chem. Soc. Chem. Commun.*, **1993**, *23*, 1784-1785.
56. Chiang, L. Y.; Wang, L. Y.; Swirczewski, J. W.; Soled, S.; Cameron, S. Efficient synthesis of polyhydroxylated fullerene derivatives via hydrolysis of polycyclosulfated precursors. *J. Org. Chem.*, **1994**, *59*, 3960-3968.
57. Kokubo, K.; Matsubayashi, K.; Tategaki, H.; Takada, H.; Oshima, T. Facile synthesis of highly water-soluble fullerenes more than half-covered by hydroxyl groups. *ACS Nano*, **2008**, *2*, 327-333.
58. Husebo, L. O.; Sitharaman, B.; Furukawa, K.; Kato, T.; Wilson, L. J. Fullerenols revisited as stable radical anions. *J. Am. Chem. Soc.*, **2004**, *126*, 12055-12064.

59. Djordjevic, A.; Srdjenovic, B.; Seke, M.; Petrovic, D.; Injac, R.; Mrdjanovic, J. Review of synthesis and antioxidant potential of fullerenol nanoparticles. *J. Nanomater.*, **2015**, *2015*, 567073.

60. He, H.; Zheng, L.; Jin, P.; Yang, M. The structural stability of polyhydroxylated C60(OH)24: Density functional theory characterizations. *Comput. Theor. Chem.*, **2011**, *974*, 16-20.

61. Djordjevic, A.; Canadanovic-Brunet, J. M.; Vojinovic-Miloradov, M.; Bogdanovic, G. Antioxidant properties and hypothetic radical mechanism of fullerenol C60(OH)24. *Oxid. Commun.*, **2004**, *27*, 806-812.

62. Chiang, L. Y.; Lu, F. J.; Lin, J. T. Free radical scavenging activity of water-soluble fullerenols. *J. Chem. Soc. Chem. Commun.*, **1995**, *12*, 1283-1284.

63. Xiao, L.; Aoshima, H.; Saitoh, Y.; Miwa, N. Highly hydroxylated fullerene localizes at the cytoskeleton and inhibits oxidative stress in adipocytes and a subcutaneous adipose-tissue equivalent. *Free Radic. Biol. Med.*, **2011**, *51*, 1376-1389.

64. Lai, H. S.; Chen, W. J.; Chiang, L. Y. Free radical scavenging activity of fullerenol on the ischemia-reperfusion intestine in dogs. *World J. Surg.*, **2000**, *24*, 450-454.

65. Lai, H. S.; Chen, Y.; Chen, W. J.; Chang, J.; Chiang, L. Y. Free radical scavenging activity of fullerenol on grafts after small bowel transplantation in dogs. *Transplant. Proc.*, **2000**, *32*, 1272-1274.

66. Mirkov, S. M.; Djordjevic, A. N.; Andric, N. L.; Andric, S. A.; Kostic, T. S.; Bogdanovic, G. M.; Vojinovic-Miloradov, M. B.; Kovacevic, R. Z. Nitric oxide-scavenging activity of polyhydroxylated fullerenol, C60(OH)24. *Nitric Oxide*, **2004**, *11*, 201-207.

67. Grebowski, J.; Kazmierska, P.; Krokosz, A. Fullerenols as a new therapeutic approach in nanomedicine. *BioMed Res. Int.*, **2013**, *2013*, 751913.

68. Grebowski, J.; Krokosz, A.; Konarska, A.; Wolszczak, M.; Puchala, M. Rate constants of highly hydroxylated fullerene C60 interacting with hydroxyl

radicals and hydrated electrons. Pulse radiolysis study. *Radiat. Phys. Chem.*, **2014**, *103*, 146-152.

69. Li, Y.; Xu, T.; Huang, Q.; Zhu, L.; Yan, Y.; Peng, P.; Li, F. F. C60 fullerenol to stabilize and activate Ru nanoparticles for highly efficient hydrogen evolution reaction in alkaline media. *ACS Catal.*, **2023**, *13*, 7597-7605.
70. Ouyang, H.; Liang, A.; Jiang, Z. Fullerol nanocatalysis and trimodal surface plasmon resonance for the determination of isocarbophos. *Front. Chem.*, **2020**, *8*, 673.
71. Chaudhuri, P.; Paraskar, A.; Soni, S.; Mashelkar, R. A.; Sengupta, S. Fullerenol− cytotoxic conjugates for cancer chemotherapy. *ACS Nano*, **2009**, *3*, 2505-2514.
72. Xu, B.; Yuan, L.; Hu, Y.; Xu, Z.; Qin, J. J.; Cheng, X. D. Synthesis, characterization, cellular uptake, and in vitro anticancer activity of fullerenol-doxorubicin conjugates. *Front. Pharmacol.*, **2021**, *11*, 598155.
73. Nurzynska, A.; Piotrowski, P.; Klimek, K.; Król, J.; Kaim, A.; Ginalska, G. Novel C60 fullerenol-gentamicin conjugate–physicochemical characterization and evaluation of antibacterial and cytotoxic properties. *Molecules*, **2022**, *27*, 4366.
74. Tipton, K.; Boyce, S. History of the enzyme nomenclature system. *Bioinformatics*, **2000**, *16*, 34-40.
75. McGovern, P. E.; Zhang, J.; Tang, J.; Zhang, Z.; Hall, G. R.; Moreau, R. A.; Nuñez, A.; Butrym, E. D.; Richards, M. P.; Wang, C.-S.; Cheng, G.; Zhao, Z.; Wang, C.-S. Fermented beverages of pre- and proto-historic China. *Proc. Natl. Acad. Sci. U. S. A.*, **2004**, *101*, *51*, 17593-17598.
76. Payen, A.; Persoz, J. *Ann. Chim. Phys.*, **1833**, *53*, 73–92.
77. Armstrong, E. F. Enzymes: A discovery and its consequences. *Nature,* **1933**, *131*, 535-537.
78. Pasteur, L. Sur les corpuscules organisés qui existent dans l'atmosphère: Examen de la doctrine des générations spontanées. *Compt. Rendus Chim.*, **1858**, *52*, 404–418.

79. Buchner, E. Alkoholische gährung ohne hefezellen. *Ber. Dtsch. Chem. Ges.*, **1897**, *30*, 117-124.

80. Sumner, J. B. Note. The recrystallization of urease. *J. Biol. Chem.*, **1926**, *70*, 97-98.

81. Fischer, E. Einfluss der Configuration auf die Wirkung der Enzyme. II. *Ber. Dtsch. Chem. Ges.*, **1894**, *27*, 3479-3483.

82. Michaelis, L. Kinetics of invertase action. *Biochem. Z.*, **1913**, *49*, 369.

83. O'Connell, A.; Barry, A.; Burke, A. J.; Hutton, A. E.; Bell, E. L.; Green, A. P.; O'Reilly, E. Biocatalysis: Landmark discoveries and applications in chemical synthesis. *Chem. Soc. Rev.*, **2024**, *53*, 751913.

84. Kirby, A. J. Enzyme mechanisms, models, and mimics. *Angew. Chem. Int. Ed. Engl.*, **1996**, *35*, 706-724.

85. Yin, Y.; Dong, Z.; Luo, Q.; Liu, J. Biomimetic catalysts designed on macromolecular scaffolds. *Prog. Polym. Sci.*, **2012**, *37*, 1476-1509.

86. Breslow, R.; Campbell, P. Selective aromatic substitution within a cyclodextrin mixed complex. *J. Am. Chem. Soc.*, **1969**, *91*, 3085-3085.

87. Breslow, R.; Overman, L. E. "Artificial enzyme" combining a metal catalytic group and a hydrophobic binding cavity. *J. Am. Chem. Soc.*, **1970**, *92*, 1075-1077.

88. Manea, F.; Houillon, F. B.; Pasquato, L.; Scrimin, P. Nanozymes: Gold-nanoparticle-based transphosphorylation catalysts. *Angew. Chem. Int. Ed.*, **2004**, *43*, 6165-6169.

89. Gao, L.; Zhuang, J.; Nie, L.; Zhang, J.; Zhang, Y.; Gu, N.; Wang, T.; Feng, J.; Yang, D.; Perrett, S.; Yan, X. Intrinsic peroxidase-like activity of ferromagnetic nanoparticles. *Nat. Nanotechnol.*, **2007**, *2*, 577–583.

90. Huerta, E.; Stals, P. J.; Meijer, E. W.; Palmans, A. R. Consequences of folding a water-soluble polymer around an organocatalyst. *Angew. Chem. Int. Ed.*, **2013**, *52*, 2906-2910.

91. Izadyar, L.; Friboulet, A.; Remy, M. H.; Roseto, A.; Thomas, D. Monoclonal anti-idiotypic antibodies as functional internal images of enzyme active sites:

production of a catalytic antibody with a cholinesterase activity. *Proc. Natl. Acad. Sci. U. S. A.*, **1993**, *90*, 8876-8880.

92. Makam, P.; Yamijala, S. R. K. C.; Tao, K.; Shimon, L. J. W.; Eisenberg, D. S.; Sawaya, M. R.; Wong, B. M.; Gazit, E. Non-proteinaceous hydrolase comprised of a phenylalanine metallo-supramolecular amyloid-like structure. *Nat. Catal.*, **2019**, *2*, 977-985.
93. Greenwald, J.; Riek, R. On the possible amyloid origin of protein folds. *J. Mol. Biol.*, **2012**, *421*, 417-426.
94. Greenwald, J.; Kwiatkowski, W.; Riek, R. Peptide amyloids in the origin of life. *J. Mol. Biol.*, **2018**, *430*, 3735-3750.
95. Atassi, M. Z.; Manshouri, T. Design of peptide enzymes (pepzymes): Surface-simulation synthetic peptides that mimic the chymotrypsin and trypsin active sites exhibit the activity and specificity of the respective enzyme. *Proc. Natl. Acad. Sci. U. S. A.*, **1993**, *90*, 8282-8286.
96. Pagar, A. D.; Patil, M. D.; Flood, D. T.; Yoo, T. H.; Dawson, P. E.; Yun, H. Recent advances in biocatalysis with chemical modification and expanded amino acid alphabet. *Chem. Rev.*, **2021**, *121*, 6173-6245.
97. Rufo, C. M.; Moroz, Y. S.; Moroz, O. V.; Stöhr, J.; Smith, T. A.; Hu, X.; DeGrado, W. F.; Korendovych, I. V. Short peptides self-assemble to produce catalytic amyloids. *Nat. Chem.*, **2014**, *6*, 303-309.
98. Zhang, C.; Xue, X.; Luo, Q.; Li, Y.; Yang, K.; Zhuang, X.; Jiang, Y.; Zhang, J.; Liu, J.; Zou, G.; Liang, X.-J. Self-assembled peptide nanofibers designed as biological enzymes for catalyzing ester hydrolysis. *ACS Nano*, **2014**, *8*, 11715-11723.
99. Jackson, J. C.; Duffy, S. P.; Hess, K. R.; Mehl, R. A. Improving nature's enzyme active site with genetically encoded unnatural amino acids. *J. Am. Chem. Soc.*, **2006**, *128*, 11124-11127.
100. Gulseren, G.; Saylam, A.; Marion, A.; Özçubukçu, S. Fullerene-based mimics of biocatalysts show remarkable activity and modularity. *ACS Appl. Mater. Interfaces*, **2021**, *13*, 45854-45863.

101. Yeniterzi, D.; Demirsoy, Z.; Saylam, A.; Özçubukçu, S.; Gülseren, G. Nanoarchitectonics of fullerene-based enzyme mimics for osteogenic induction of stem cells. *Macromol. Biosci.*, **2022**, *22*, 2200079.

102. Scheele, C. W. Om Mjolk: *Kgl. Vetenskaps-Academiens nya Handlingar*, **1780**, *1*, 116–124.

103. Németh, Á.; Sevella, B. Role of pH-regulation in lactic acid fermentation: Second steps in a process improvement. *Chem. Eng. Process. Process Intensif.*, **2011**, *50*, 293-299.

104. Bai, D. M.; Zhao, X. M.; Li, X. G.; Xu, S. M. Strain improvement of *Rhizopus oryzae* for over-production of L (+)-lactic acid and metabolic flux analysis of mutants. *Biochem. Eng. J.*, **2004**, *18*, 41-48.

105. Mujtaba, I. M.; Edreder, E. A.; Emtir, M. Significant thermal energy reduction in lactic acid production process. *Appl. Energy*, **2012**, *89*, 74-80.

106. Dennis, D. [58] Lactic acid racemase. In *Methods in Enzymology*, Vol. 5, pp. 426-432. Academic Press, **1962**.

107. Tanner, M. E. Understanding nature's strategies for enzyme-catalyzed racemization and epimerization. *Acc. Chem. Res.*, **2002**, *35*, 237-246.

108. Gaspar, P.; Carvalho, A. L.; Vinga, S.; Santos, H.; Neves, A. R. From physiology to systems metabolic engineering for the production of biochemicals by lactic acid bacteria. *Biotechnol. Adv.*, **2013**, *31*, 764-788.

109. Gordon, G. L.; Doelle, H. W. Production of racemic lactic acid in *Pediococcus cerevisiae* cultures by two lactate dehydrogenases. *J. Bacteriol.*, **1975**, *121*, 600-607.

110. Goffin, P.; Deghorain, M.; Mainardi, J. L.; Tytgat, I.; Champomier-Verges, M. C.; Kleerebezem, M.; Hols, P. Lactate racemization as a rescue pathway for supplying D-lactate to the cell wall biosynthesis machinery in *Lactobacillus plantarum*. *J. Bacteriol.*, **2005**, *187*, 6750-6761.

111. Desguin, B.; Goffin, P.; Viaene, E.; Kleerebezem, M.; Martin-Diaconescu, V.; Maroney, M. J.; Declercq, J.-P.; Soumillion, P.; Hols, P. Lactate racemase

is a nickel-dependent enzyme activated by a widespread maturation system. *Nat. Commun.*, **2014**, *5*, 3615.

112. Desguin, B.; Soumillion, P.; Hols, P.; Hausinger, R. P. Nickel-pincer cofactor biosynthesis involves LarB-catalyzed pyridinium carboxylation and LarE-dependent sacrificial sulfur insertion. *Proc. Natl. Acad. Sci. U. S. A.*, **2016**, *113*, 5598-5603.
113. Desguin, B.; Zhang, T.; Soumillion, P.; Hols, P.; Hu, J.; Hausinger, R. P. A tethered niacin-derived pincer complex with a nickel-carbon bond in lactate racemase. *Science*, **2015**, *349*, 66-69.
114. Fellner, M.; Desguin, B.; Hausinger, R. P.; Hu, J. Structural insights into the catalytic mechanism of a sacrificial sulfur insertase of the N-type ATP pyrophosphatase family, LarE. *Proc. Natl. Acad. Sci. U. S. A.*, **2017**, *114*, 9074-9079.
115. Rostagno, A. A. Pathogenesis of Alzheimer’s disease. *Int. J. Mol. Sci.*, **2022**, *24*, 107.
116. Chandrasekaran, A. R.; Halvorsen, K. DNA-based smart reagent for detecting Alzheimer’s associated microRNAs. *ACS Sensors*, **2021**, *6*, 3176-3181.
117. Sharma, P.; Srivastava, P.; Seth, A.; Tripathi, P. N.; Banerjee, A. G.; Shrivastava, S. K. Comprehensive review of mechanisms of pathogenesis involved in Alzheimer’s disease and potential therapeutic strategies. *Prog. Neurobiol.*, **2019**, *174*, 53-89.
118. Majdi, A.; Sadigh-Eteghad, S.; Rahigh Aghsan, S.; Farajdokht, F.; Vatandoust, S. M.; Namvaran, A.; Mahmoudi, J. Amyloid-β, tau, and the cholinergic system in Alzheimer’s disease: Seeking direction in a tangle of clues. *Rev. Neurosci.*, **2020**, *31*, 391-413.
119. Picciotto, M. R.; Higley, M. J.; Mineur, Y. S. Acetylcholine as a neuromodulator: Cholinergic signaling shapes nervous system function and behavior. *Neuron*, **2012**, *76*, 116-129.

120. Emran, M. Y.; Shenashen, M. A.; El Sabagh, A.; Selim, M. M.; El-Safty, S. A. Enzymeless copper microspheres@carbon sensor design for sensitive and selective acetylcholine screening in human serum. *Colloids Surf. B Biointerfaces*, **2022**, *210*, 112228.

121. Castle, L. M.; Schuh, D. A.; Reynolds, E. E.; Furst, A. L. Electrochemical sensors to detect bacterial foodborne pathogens. *ACS Sensors*, **2021**, *6*, 1717-1730.

122. Dhull, V.; Gahlaut, A.; Dilbaghi, N.; Hooda, V. Acetylcholinesterase biosensors for electrochemical detection of organophosphorus compounds: A review. *Biochem. Res. Int.*, **2013**, *2013*, 731501.

123. Balasubramanian, P.; Balamurugan, T. S. T.; Chen, S. M.; Chen, T. W. Facile synthesis of spinel-type copper cobaltite nanoplates for enhanced electrocatalytic detection of acetylcholine. *ACS Sustainable Chem. Eng.*, **2019**, *7*, 7642-7651.

124. da Silva, W.; Brett, C. M. Novel biosensor for acetylcholine based on acetylcholinesterase/poly(neutral red)–deep eutectic solvent/Fe2O3 nanoparticle modified electrode. *J. Electroanal. Chem.*, **2020**, *872*, 114050.

125. Balasubramanian, P.; Balamurugan, T. S. T.; Chen, S. M.; Chen, T. W.; Sathesh, T. Rational design of Cu@Cu2O nanospheres anchored B, N Co-doped mesoporous carbon: A sustainable electrocatalyst to assay eminent neurotransmitters acetylcholine and dopamine. *ACS Sustainable Chem. Eng.*, **2018**, *7*, 5669-5680.

126. Poolakkandy, R. R.; Ramalakshmi, N. A.; Padmalayam, K. A.; Krishnamurthy, R. G.; Menamparambath, M. M. Braided copper cobaltite/MWCNT composites enable acetylcholine detection at sub-nanomolar levels in vitro. *Sensors Diagn.*, **2023**, *2*, 726-735.

127. Wang, L.; Chen, X.; Liu, C.; Yang, W. Non-enzymatic acetylcholine electrochemical biosensor based on flower-like NiAl layered double hydroxides decorated with carbon dots. *Sens. Actuators B Chem.*, **2016**, *233*, 199-205.

128. Chu, S. Carbon capture and sequestration. *Science*, **2009**, *325*, 1599-1599.

129. Markewitz, P.; Kuckshinrichs, W.; Leitner, W.; Linssen, J.; Zapp, P.; Bongartz, R.; Schreiber, A.; Müller, T. E. Worldwide innovations in the development of carbon capture technologies and the utilization of CO2. *Energy Environ. Sci.*, **2012**, *5*, 7281-7305.

130. Omae, I. Aspects of carbon dioxide utilization. *Catal. Today*, **2006**, *115*, 33-52.

131. Rahman, F. A.; Aziz, M. M. A.; Saidur, R.; Bakar, W. A. W. A.; Hainin, M. R.; Putrajaya, R.; Hassan, N. A. Pollution to solution: Capture and sequestration of carbon dioxide (CO2) and its utilization as a renewable energy source for a sustainable future. *Renew. Sustain. Energy Rev.*, **2017**, *71*, 112-126.

132. Correa, S. S.; Schultz, J.; Lauersen, K. J.; Rosado, A. S. Natural carbon fixation and advances in synthetic engineering for redesigning and creating new fixation pathways. *J. Adv. Res.*, **2023**, *47*, 75-92.

133. Tsutsumi, H.; Sumiyoshi, Y.; Onimura, K.; Oishi, T. Preparation of new polymer electrolytes based on poly (acrylonitrile-co-vinylimidazoline) matrix and improvement of polarization behavior of lithium electrode in the electrolyte by using cascade nitrile compound. *Solid State Ion.*, **2003**, *160*, 131-139.

134. Bayardon, J.; Holz, J.; Schaffner, B.; Andrushko, V.; Verevkin, S.; Preetz, A.; Borner, A. Propylene carbonate as a solvent for asymmetric hydrogenations. *Angew. Chem. Int. Ed. Engl.*, **2007**, *46*, 5971-5974.

135. Ochiai, B.; Endo, T. Carbon dioxide and carbon disulfide as resources for functional polymers. *Prog. Polym. Sci.*, **2005**, *30*, 183-215.

136. Nemirowsky, J. Ueber die Einwirkung von Chlorkohlenoxyd auf Aethylenglycol; vorläufige Mittheilung. *J. Prakt. Chem.*, **1883**, *28*, 439-440.

137. Shaikh, A. A. G.; Sivaram, S. Organic carbonates. *Chem. Rev.*, **1996**, *96*, 951-976.

138. Wang, J.; Jia, C. S.; Li, C. J.; Peng, X. L.; Zhang, L. H.; Liu, J. Y. Thermodynamic properties for carbon dioxide. *ACS Omega*, **2019**, *4*, 19193-19198.

139. Sakakura, T.; Choi, J. C.; Yasuda, H. Transformation of carbon dioxide. *Chem. Rev.*, **2007**, *107*, 2365-2387.

140. Pfennig, V. S.; Villella, R. C.; Nikodemus, J.; Bolm, C. Mechanochemical Grignard reactions with gaseous CO2 and sodium methyl carbonate. *Angew. Chem.*, **2022**, *134*, e202116514.

141. Natongchai, W.; Crespy, D.; D'Elia, V. CO2 fixation: Cycloaddition of CO2 to epoxides using practical metal-free recyclable catalysts. *Chem. Commun.*, **2025**, *61*, 419-440.

142. Fu, H.-Q.; Mao, H.; Wang, C.; Yin, K.; Jin, M.; Dong, Z.; Zhao, Y.; Liu, J. The Al(III)-based polydentate chelate complex catalyzed cycloaddition of carbon dioxide and epoxides: Synthetic optimization and mechanistic study. *React. Chem. Eng.*, **2022**, *7*, 2313-2321.

143. Castro-Ruiz, A.; Grefe, L.; Mejía, E.; Suman, S. G. Cobalt complexes with α-amino acid ligands catalyze the incorporation of CO2 into cyclic carbonates. *Dalton Trans.*, **2023**, *52*, 4186-4199.

144. Taniya, S.; Khanra, S.; Salam, N.; Das, D. Exploring a Bis- imine Derived Azide Containing Dinuclear Iron (III) Complex: Fluorescence Recognition of F− and Atmospheric CO2 Fixation. *ChemistrySelect*, **2023**, *8*, e202204787.

145. Deori, N.; Lahkar, S.; Paul, S.; Borah, R.; Brahma, S. Chemical Fixation of CO2 with Epoxides Catalyzed by Zinc Metalated Schiff Base Organic Polymer. *Catal. Lett.*, **2024**, *154*, 3107-3117.

146. Muthuramalingam, S.; Velusamy, M.; Singh Rajput, S.; Alam, M.; Mayilmurugan, R. Nickel (II) Complexes of Tripodal Ligands as Catalysts for Fixation of Atmospheric CO2 as Organic Carbonates. *Chem. Asian J.*, **2023**, *18*, e202201204.

147. Shen, Y. M.; Duan, W. L.; Shi, M. Phenol and organic bases co- catalyzed chemical fixation of carbon dioxide with terminal epoxides to form cyclic carbonates. *Adv. Synth. Catal.*, **2003**, *345*, 337-340.

148. Yue, S.; Qu, H. L.; Song, X. X.; Feng, X. N. Novel hydroxyl-functionalized ionic liquids as efficient catalysts for the conversion of CO2 into cyclic carbonates under metal/halogen/cocatalyst/solvent-free conditions. *New J. Chem.*, **2022**, *46*, 5881-5888.

149. Yang, Z.; Sun, J.; Cheng, W.; Wang, J.; Li, Q.; Zhang, S. Biocompatible and recyclable amino acid binary catalyst for efficient chemical fixation of CO2. *Catal. Commun.*, **2014**, *44*, 6-9.

150. Sun, Y. B.; Cao, C. Y.; Yang, S. L.; Huang, P. P.; Wang, C. R.; Song, W. G. C60 fullerenol as an active and stable catalyst for the synthesis of cyclic carbonates from CO2 and epoxides. *Chem. Commun.*, **2014**, *50*, 10307-10310.

151. Hardman- Baldwin, A. M.; Mattson, A. E. Silanediol- catalyzed carbon dioxide fixation. *ChemSusChem*, **2014**, *7*, 3275-3278.

152. Morita, K. I.; Suzuki, Z.; Hirose, H. A tertiary phosphine-catalyzed reaction of acrylic compounds with aldehydes. *Bull. Chem. Soc. Jpn.*, **1968**, *41*, 2815-2815.

153. Baylis, A. B.; Hillman, M. E. D. German Patent, 2155113, **1972**. *Chem. Abstr.*, **1972**, *trans*.

154. Drewes, S. E.; Emslie, N. D. Necic acid synthons. Part 1. Total synthesis of integerrinecic acid. *J. Chem. Soc. Perkin Trans. 1*, **1982**, 2079-2083.

155. Reddy, L. R.; Saravanan, P.; Corey, E. J. A simple stereocontrolled synthesis of salinosporamide A. *J. Am. Chem. Soc.*, **2004**, *126*, 6230-6231.

156. McCauley, J. A.; Nagasawa, K.; Lander, P. A.; Mischke, S. G.; Semones, M. A.; Kishi, Y. Total synthesis of pinnatoxin A. *J. Am. Chem. Soc.*, **1998**, *120*, 7647-7648.

157. Reddy, Y. S.; Kadigachalam, P.; Basak, R. K.; Pal, A. J.; Vankar, Y. D. Total synthesis of (+)-pericosine B and (+)-pericosine C and their enantiomers by

using the Baylis–Hillman reaction and ring-closing metathesis as key steps. *Tetrahedron Lett.*, **2012**, *53*, 132-136.

158. Zhong, W.; Liu, Y.; Wang, G.; Hong, L.; Chen, Y.; Chen, X.; Zheng, Y.; Zhang, W.; Ma, W.; Shen, Y.; Yao, Y. Recent advances in construction of nitrogen-containing heterocycles from Baylis-Hillman adducts. *Org. Prep. Proced. Int.*, **2011**, *43*, 1-66.

159. Gowrisankar, S.; Lee, H. S.; Kim, S. H.; Lee, K. Y.; Kim, J. N. Recent advances in the Pd-catalyzed chemical transformations of Baylis–Hillman adducts. *Tetrahedron*, **2009**, *65*, 8769-8780.

160. Amarante, G. W.; Benassi, M.; Pascoal, R. N.; Eberlin, M. N.; Coelho, F. Mechanism and synthesis of pharmacologically active quinolones from Morita–Baylis–Hillman adducts. *Tetrahedron*, **2010**, *66*, 4370-4376.

161. Kohn, L. K.; Pavam, C. H.; Veronese, D.; Coelho, F.; De Carvalho, J. E.; Almeida, W. P. Antiproliferative effect of Baylis–Hillman adducts and a new phthalide derivative on human tumor cell lines. *Eur. J. Med. Chem.*, **2006**, *41*, 738-744.

162. Feltrin, M. P.; Almeida, W. P. A synthesis of Captopril through a Baylis–Hillman reaction. *Synth. Commun.*, **2003**, *33*, 1141-1146.

163. Basavaiah, D.; Rao, A. J.; Satyanarayana, T. Recent advances in the Baylis−Hillman reaction and applications. *Chem. Rev.*, **2003**, *103*, 811-892.

164. Bugaenko, D. I.; Karchava, A. V.; Yurovskaya, M. A. The versatility of DABCO: Synthetic applications of its basic, nucleophilic, and catalytic properties. Part 1. Catalysis of Morita–Baylis–Hillman and Knoevenagel reactions. *Chem. Heterocycl. Compd.*, **2020**, *56*, 128-144.

165. Aggarwal, V. Superior amine catalysts for the Baylis–Hillman reaction: The use of DBU and its implications. *Chem. Commun.*, **1999**, *22,* 2311-2312.

166. Luo, S.; Zhang, B.; He, J.; Janczuk, A.; Wang, P. G.; Cheng, J. P. Aqueous Baylis–Hillman reactions of cyclopent-2-enone using imidazole as catalyst. *Tetrahedron Lett.*, **2002**, *43*, 7369-7371.

167. Chang, L.; Thorimbert, S.; Dechoux, L. The bio-based methyl coumalate involved Morita–Baylis–Hillman reaction. *Org. Biomol. Chem.*, **2019**, *17*, 2784-2791.

168. Tietze, L. F.; Hölsken, S.; Adrio, J.; Kinzel, T.; Wegner, C. Facial-selective allylation of methyl ketones for the asymmetric synthesis of tertiary homoallylic ethers. *Synthesis*, **2004**, *13*, 2236-2239.

169. Vazquez-Chavez, J.; Luna-Morales, S.; Cruz-Aguilar, D. A.; Díaz-Salazar, H.; Vallejo Narváez, W. E.; Silva-Gutiérrez, R. S.; Hernández-Ortega, S.; Rocha-Rinza, T.; Hernández-Rodríguez, M. The effect of chiral N-substituents with methyl or trifluoromethyl groups on the catalytic performance of mono- and bifunctional thioureas. *Org. Biomol. Chem.*, **2019**, *17*, 10045-10051.

170. Aggarwal, V. K.; Mereu, A.; Tarver, G. J.; McCague, R. Metal-and ligand-accelerated catalysis of the Baylis−Hillman reaction. *J. Org. Chem.*, **1998**, *63*, 7183-7189.

171. Li, G.; Wei, H. X.; Gao, J. J.; Caputo, T. D. TiCl4-Mediated Baylis–Hillman and aldol reactions without the direct use of a Lewis base. *Tetrahedron Lett.*, **2000**, *41*, 1-5.

172. Patel, C.; Sunoj, R. B. TiCl4-Promoted Baylis−Hillman Reaction: Mechanistic rationale toward product distribution and stereoselectivity. *J. Org. Chem.*, **2010**, *75*, 359-367.

173. Joshi, P. N.; Purushottam, L.; Das, N. K.; Mukherjee, S.; Rai, V. Protein self-assembly induces promiscuous nucleophilic biocatalysis in Morita–Baylis–Hillman (MBH) reaction. *RSC Adv.*, **2016**, *6*, 208-211.

174. Jankun, J.; Selman, S. H.; Swiercz, R.; Skrzypczak-Jankun, E. Why drinking green tea could prevent cancer. *Nature*, **1997**, *387*, 561-561.

175. van Rensburg, H.; van Heerden, P. S.; Bezuidenhoudt, B. C.; Ferreira, D. Enantioselective synthesis of the four catechin diastereomer derivatives. *Tetrahedron Lett.*, **1997**, *38*, 3089-3092.

176. Reynolds, G. A.; Drexhage, K. H. New coumarin dyes with rigidized structure for flashlamp-pumped dye lasers. *Opt. Commun.*, **1975**, *13*, 222-225.

177. Bissell, E. R.; Mitchell, A. R.; Smith, R. E. Synthesis and chemistry of 7-amino-4-(trifluoromethyl) coumarin and its amino acid and peptide derivatives. *J. Org. Chem.*, **1980**, *45*, 2283-2287.

178. Delbaere, S.; Micheau, J. C.; Vermeersch, G. NMR kinetic investigations of the photochemical and thermal reactions of a photochromic chromene. *J. Org. Chem.*, **2003**, *68*, 8968-8973.

179. Kemnitzer, W.; Kasibhatla, S.; Jiang, S.; Zhang, H.; Zhao, J.; Jia, S.; Xu, L.; Crogan-Grundy, C.; Denis, R.; Barriault, N.; Vaillancourt, L.; Charron, S.; Dodd, J.; Attardo, G.; Labrecque, D.; Lamothe, S.; Gourdeau, H.; Tseng, B.; Drewe, J.; Cai, S. X. Discovery of 4-aryl-4H-chromenes as a new series of apoptosis inducers using a cell- and caspase-based high-throughput screening assay. 2. Structure–activity relationships of the 7- and 5-, 6-, 8-positions. *Bioorg. Med. Chem. Lett.*, **2005**, *15*, 4745-4751.

180. Patil, S. A.; Wang, J.; Li, X. S.; Chen, J.; Jones, T. S.; Hosni-Ahmed, A.; Patil, R.; Seibel, W. L.; Li, W.; Miller, D. D. New substituted 4H-chromenes as anticancer agents. *Bioorg. Med. Chem. Lett.*, **2012**, *22*, 4458-4461.

181. Kumar, D.; Reddy, V. B.; Sharad, S.; Dube, U.; Kapur, S. A facile one-pot green synthesis and antibacterial activity of 2-amino-4H-pyrans and 2-amino-5-oxo-5,6,7,8-tetrahydro-4H-chromenes. *Eur. J. Med. Chem.*, **2009**, *44*, 3805-3809.

182. Kafi- Ahmadi, L.; Poursattar Marjani, A.; Nozad, E. Ultrasonic- assisted preparation of Co3O4 and Eu- doped Co3O4 nanocatalysts and their application for solvent- free synthesis of 2- amino- 4H- benzochromenes under microwave irradiation. *Appl. Organometal. Chem.*, **2021**, *35*, e6271.

183. Paplal, B.; Nagaraju, S.; Veerabhadraiah, P.; Sujatha, K.; Kanvah, S.; Kumar, B. V.; Kashinath, D. Recyclable Bi2WO6-nanoparticle mediated one-pot

multicomponent reactions in aqueous medium at room temperature. *RSC Adv.*, **2014**, *4*, 54168-54174.

184. Akrami, H.; Mirjalili, B. F.; Firuzi, O.; Hekmat, A.; Saboury, A. A.; Miri, R.; Sabzevari, O.; Pirali-Hamedani, M.; Jeivad, F.; Moghimi, S.; Emami, S.; Foroumadi, A.; Khoobi, M. Cytotoxic activity and DNA binding property of new aminopyrimidine derivatives. *Lett. Drug Des. Discov.*, **2020**, *17*, 640-654.

185. Han, G. F.; Wang, M.; Jin, Y.; Chen, L. Z. Synthesis and characterization of benzochromeno [2,3- b] tetrahydroquinolinone derivatives. *J. Heterocycl. Chem.*, **2014**, *51*, 648-655.

186. Ben Said, A.; Romdhane, A.; Elie, N.; Touboul, D.; Ben Jannet, H. Synthesis of novel fused coumarine and naphtho [2,1-b] pyrano [3,2-e][1,2,4] triazolo [1,5-c] pyrimidine derivatives. *Lett. Org. Chem.*, **2013**, *10*, 185-190.

187. Kaur, R.; Naaz, F.; Sharma, S.; Mehndiratta, S.; Gupta, M. K.; Bedi, P. M. S.; Nepali, K. Screening of a library of 4-aryl/heteroaryl-4H-fused pyrans for xanthine oxidase inhibition: Synthesis, biological evaluation and docking studies. *Med. Chem. Res.*, **2015**, *24*, 3334-3349.

188. Kaur, M.; Kaur, A.; Mankotia, S.; Singh, H.; Singh, A.; Singh, J. V.; Gupta, M. K.; Sharma, S.; Nepali, K.; Bedi, P. M. S. Synthesis, screening and docking of fused pyrano[3,2-d]pyrimidine derivatives as xanthine oxidase inhibitor. *Eur. J. Med. Chem.*, **2017**, *131*, 14-28.

189. Dekamin, M. G.; Eslami, M. Highly efficient organocatalytic synthesis of diverse and densely functionalized 2-amino-3-cyano-4H-pyrans under mechanochemical ball milling. *Green Chem.*, **2014**, *16*, 4914-4921.

190. Azizi, K.; Karimi, M.; Shaterian, H. R.; Heydari, A. Ultrasound irradiation for the green synthesis of chromenes using L-arginine-functionalized magnetic nanoparticles as a recyclable organocatalyst. *RSC Adv.*, **2014**, *4*, 42220-42225.

191. Prins, H. J. On the condensation of formaldehyde with some unsaturated compounds. In *KNAW, Proceedings*, **1919**, *22*, 1919-1920.

192. Kriewitz, O. Ueber Addition von Formaldehyd an einige Terpene. *Ber. Dtsch. Chem. Ges.*, **1899**, *32*, 57–60.

193. Nasir, N. M.; Ermanis, K.; Clarke, P. A. Strategies for the construction of tetrahydropyran rings in the synthesis of natural products. *Org. Biomol. Chem.*, **2014**, *12*, 3323-3335.

194. Liu, L.; Floreancig, P. E. Structurally and stereochemically diverse tetrahydropyran synthesis through oxidative C–H bond activation. *Angew. Chem. Int. Ed.*, **2010**, *49*, 3069-3072.

195. Fuwa, H. Total synthesis of tetrahydropyran-containing natural products exploiting intramolecular oxa-conjugate cyclization. *Heterocycles*, **2012**, *85*, 1255-1298.

196. Grese, T. A.; Hutchinson, K. D.; Overman, L. E. General approach to halogenated tetrahydrofuran natural products from red algae of the genus Laurencia. Total synthesis of (+/-)-kumausallene and (+/-)-1-epi-kumausallene. *J. Org. Chem.*, **1993**, *58*, 2468-2477.

197. Wipf, P. Synthetic studies of biologically active marine cyclopeptides. *Chem. Rev.*, **1995**, *95*, 2115-2134.

198. Tamura, Y.; Omori, N.; Kouyama, N.; Nishiura, Y.; Hayashi, K.; Watanabe, K.; Tanaka, Y.; Chiba, T.; Yukioka, H.; Sato, H.; Okuno, T. Identification of a novel and orally available benzimidazole derivative as an NPY Y5 receptor antagonist with in vivo efficacy. *Bioorg. Med. Chem. Lett.*, **2012**, *22*, 6554-6558.

199. Winge, T.; Schepmann, D.; Schmidt, J.; Daniliuc, C.; Würthwein, E. U.; Wünsch, B. Diastereoselective synthesis and structure–affinity relationships of σ1 receptor ligands with spirocyclic scaffold. *Org. Biomol. Chem.*, **2023**, *21*, 7730-7752.

200. Borah, K. J.; Borah, R. Investigation of Prins reaction for the synthesis of 2,4-disubstituted tetrahydropyran derivatives and 1,3-dioxanes using polyaniline supported acid as reusable catalyst. *J. Chem. Sci.*, **2011**, *123*, 623-630.

201. Miranda, P. O.; Díaz, D. D.; Padrón, J. I.; Bermejo, J.; Martín, V. S. Iron (III)-catalyzed Prins-type cyclization using homopropargylic alcohol: A method for the synthesis of 2-alkyl-4-halo-5,6-dihydro-2H-pyrans. *Org. Lett.*, **2003**, *5*, 1979-1982.

202. Cheung, C. W.; Ren, P.; Hu, X. Mild and phosphine-free iron-catalyzed cross-coupling of nonactivated secondary alkyl halides with alkynyl Grignard reagents. *Org. Lett.*, **2014**, *16*, 2566-2569.

203. Zhao, H.; McMillan, A. J.; Constantin, T.; Mykura, R. C.; Julia, F.; Leonori, D. Merging halogen-atom transfer (XAT) and cobalt catalysis to override E2-selectivity in the elimination of alkyl halides: A mild route toward contra-thermodynamic olefins. *J. Am. Chem. Soc.*, **2021**, *143*, 14806-14813.

204. Reddy, U. C.; Bondalapati, S.; Saikia, A. K. Stereoselective one-pot, three-component synthesis of 4-aryltetrahydropyran via Prins−Friedel−Crafts reaction. *J. Org. Chem.*, **2009**, *74*, 2605-2608.

205. Winge, T.; Schepmann, D.; Schmidt, J.; Daniliuc, C.; Würthwein, E. U.; Wünsch, B. Diastereoselective synthesis and structure–affinity relationships of σ1 receptor ligands with spirocyclic scaffold. *Org. Biomol. Chem.*, **2023**, *21*, 7730-7752.

206. Soylemez, S.; Dolgun, V.; Özçubukçu, S. Fullerene-Based Mimics for Enhanced Acetylcholine Detection in the Diagnosis of Alzheimer’s Disease. *Microchem. J.* **2023**, *193*, 109099.

207. Brant, J. A.; Labille, J.; Robichaud, C. O.; Wiesner, M. Fullerol cluster formation in aqueous solutions: Implications for environmental release. *J. Colloid Interface Sci.*, **2007**, *314*, 281-288.

208. Wang, D.; Feng, H.; Li, L.; Liu, Z.; Yan, Z.; Yu, P. Access to 8-Azachromones via Activation of C–H in N-Oxides. *J. Org. Chem.* **2017**, *82* (20), 11275–11287.

209. Zhejiang University of Technology. Acylation of Amino Acids and Derivatives. **2016**, CN105777611.

210. Nicolaou, K. C.; Safina, B. S.; Funke, C.; Zak, M.; Zécri, F. J. Stereocontrolled Synthesis of the Quinaldic Acid Macrocyclic System of Thiostrepton. *Angew. Chem.* **2002**, *114*, 2017–2020.

211. Palmer, D. E.; Pattaroni, C.; Nunami, K.; Chadha, R. K.; Goodman, M.; Wakamiya, T.; Fukase, K.; Horimoto, S.; Kitazawa, M. Effects of Dehydroalanine on Peptide Conformations. *J. Am. Chem. Soc.* **1992**, *114*, 5634–5642.

212. Yano de Albuquerque, D.; Teixeira, W. K.; Sacramento, M. D.; Alves, D.; Santi, C.; Schwab, R. S. Palladium-Catalyzed Carbonylative Synthesis of Aryl Selenoesters Using Formic Acid as an Ex Situ CO Source. *J. Org. Chem.* **2021**, *87*, 595–605.

213. Levy, A. L.; Chung, D. Preparation and Properties of 3-Phenyl-2-Thiohydantoins of Serine, Threonine, and Cystine. *Biochim. Biophys. Acta* **1955**, *17*, 454–456.

214. Novotortsev, V. K.; Kuandykov, D. M.; Kukushkin, M. E.; Zyk, N. V.; Beloglazkina, E. K. Synthesis of 5-Methylidene-2-Thio- and 2-Selenohydantoins from Isothiocyanates or Isoselenocyanates and L-Serine. *Mendeleev Commun.* **2022**, *32*, 769–770.

215. Loukou, C.; Changenet-Barret, P.; Rager, M. N.; Plaza, P.; Martin, M. M.; Mallet, J. M. The Design, Synthesis, and Photochemical Study of a Biomimetic Cyclodextrin Model of Photoactive Yellow Protein (PYP). *Org. Biomol. Chem.* **2011**, *9*, 2209–2218.

216. Oiry, J.; Puy, J.-Y.; Imbach, J.-L.; Clayette, P.; Fretier, P. Novel Antioxidants, Preparation Processes, and Their Uses. U.S. Patent **2004**, US 2004/0158092 A1.

217. Yalamati, D.; Baradi, P.; Koganty, R. R. Synthetic Innate Immune Receptor Ligands and Uses Thereof. WO Patent **2020,** WO 2020/082162 A1.

218. Kapoor, M.; Majumder, A. B.; Gupta, M. N. Promiscuous Lipase-Catalyzed C–C Bond Formation Reactions Between 4-Nitrobenzaldehyde and 2-

Cyclohexen-1-one in Biphasic Medium: Aldol and Morita–Baylis–Hillman Adduct Formations. *Catal. Lett.* **2015**, *145*, 527–532.

219. Price, K. E.; Broadwater, S. J.; Walker, B. J.; McQuade, D. T. A New Interpretation of the Baylis–Hillman Mechanism. *J. Org. Chem.* **2005**, *70*, 3980–3987.

APPENDICES

A. NMR SPECTRA

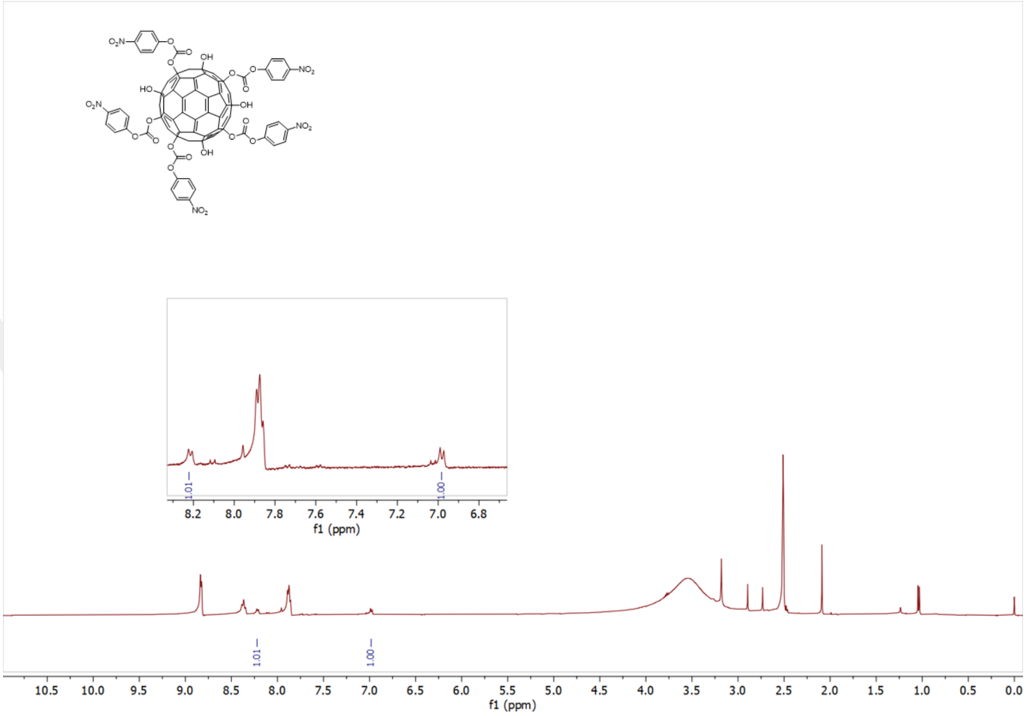

Figure A. 1. ^{1}H NMR spectrum of **activated fullerenol** in DMSO-d_6.

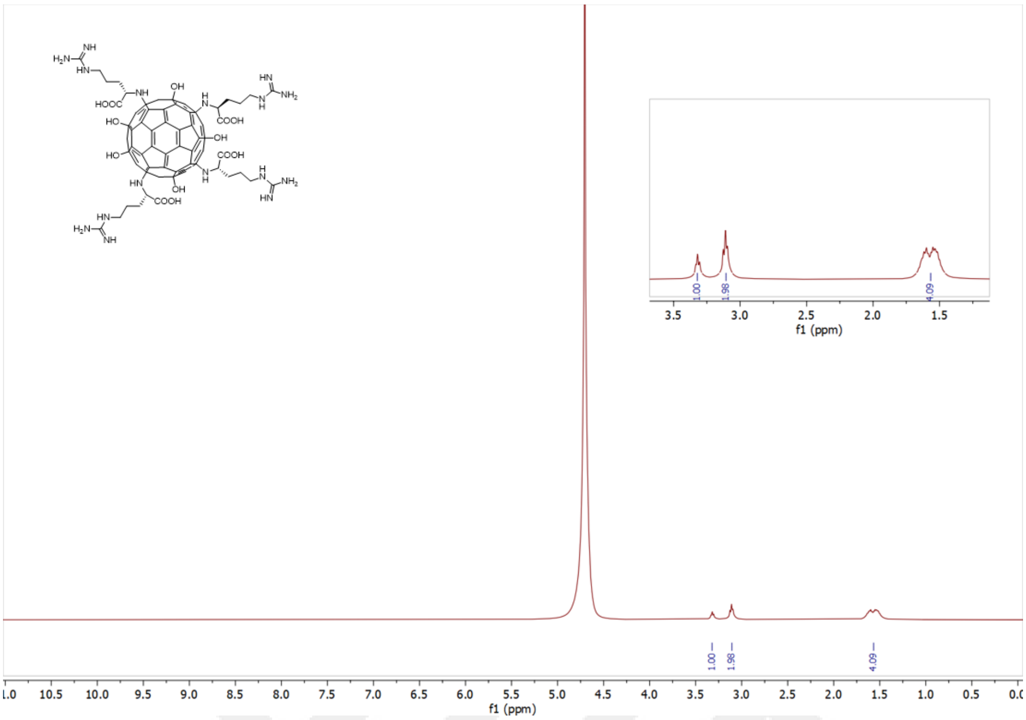

Figure A. 2. ^{1}H NMR spectrum of compound **F-**Arg in D_2O.

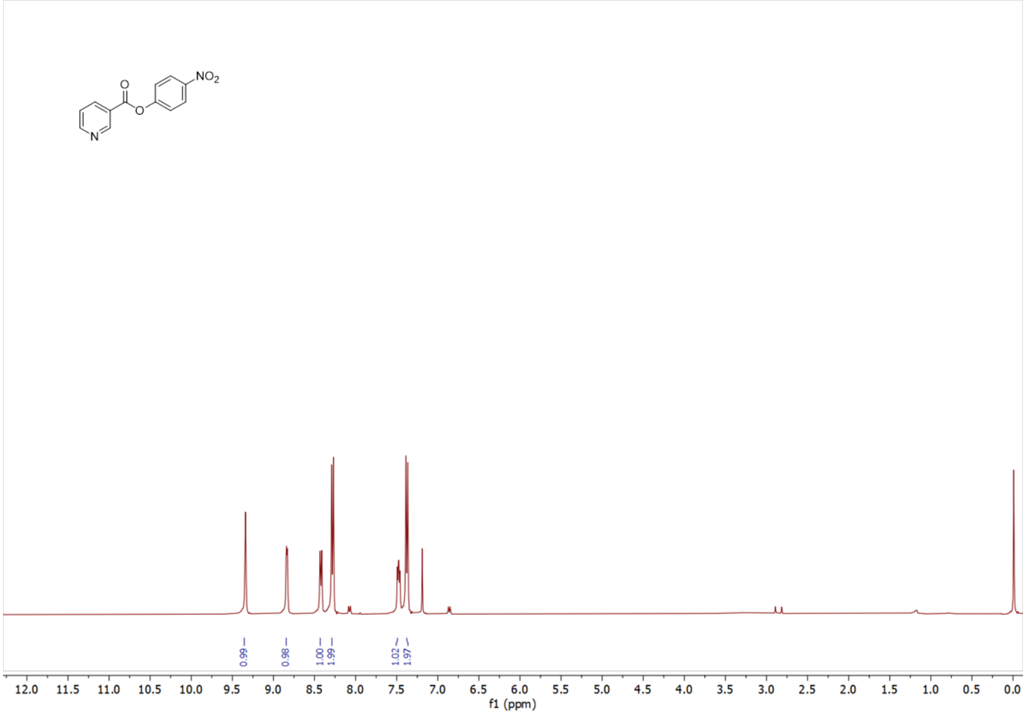

Figure A. 3. ^{1}H NMR spectrum of compound **1** in $CDCl_3$.

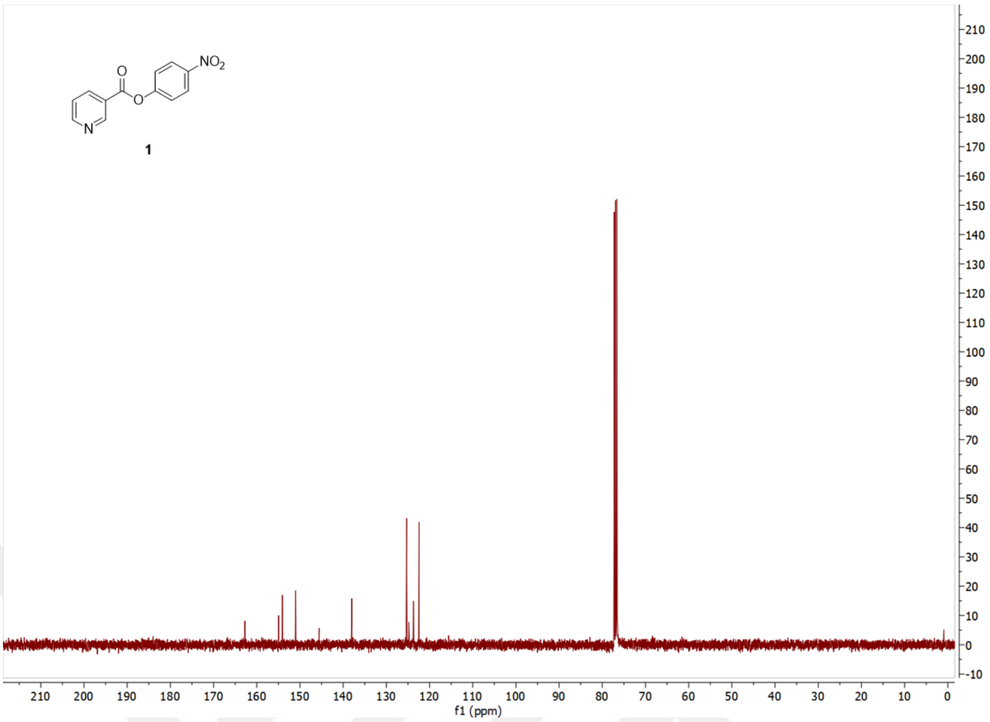

Figure A. 4. ^{13}C NMR spectrum of compound **1** in $CDCl_3$.

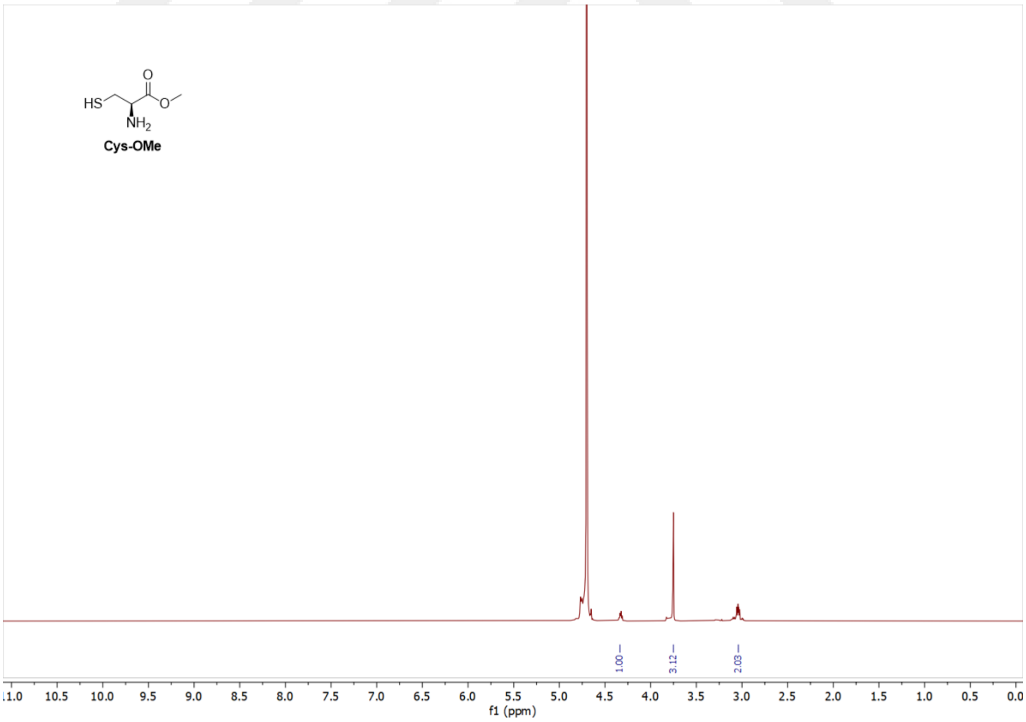

Figure A. 5. ^{1}H NMR spectrum of **Cys-OMe** in D_2O.

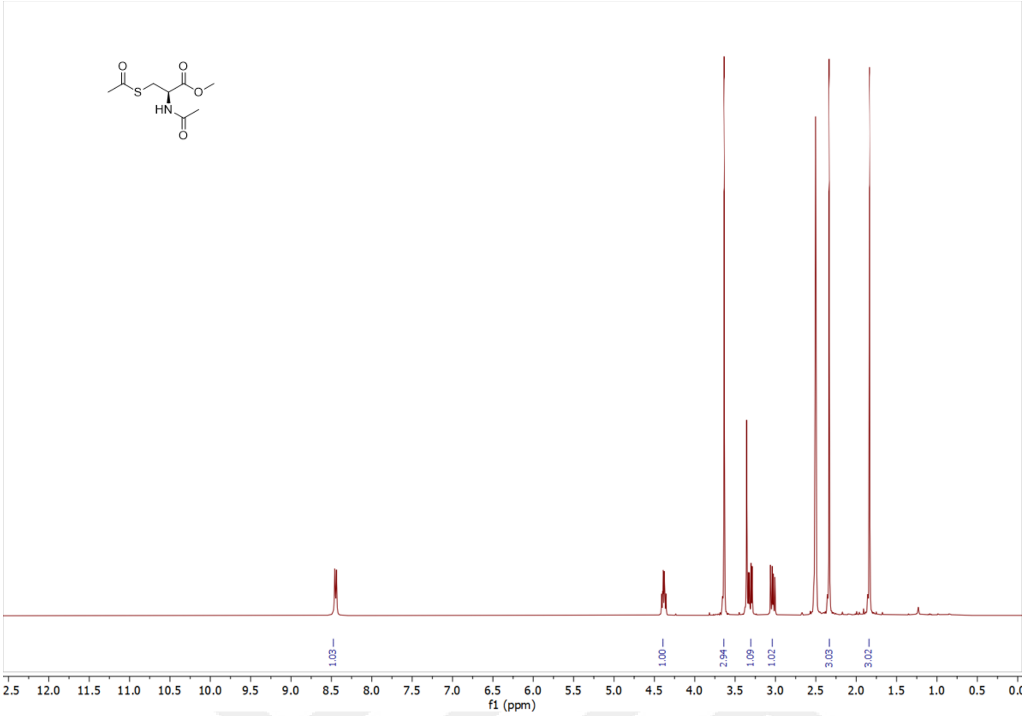

Figure A. 6. ^{1}H NMR spectrum of **Cys-Diac** in DMSO-d_6.

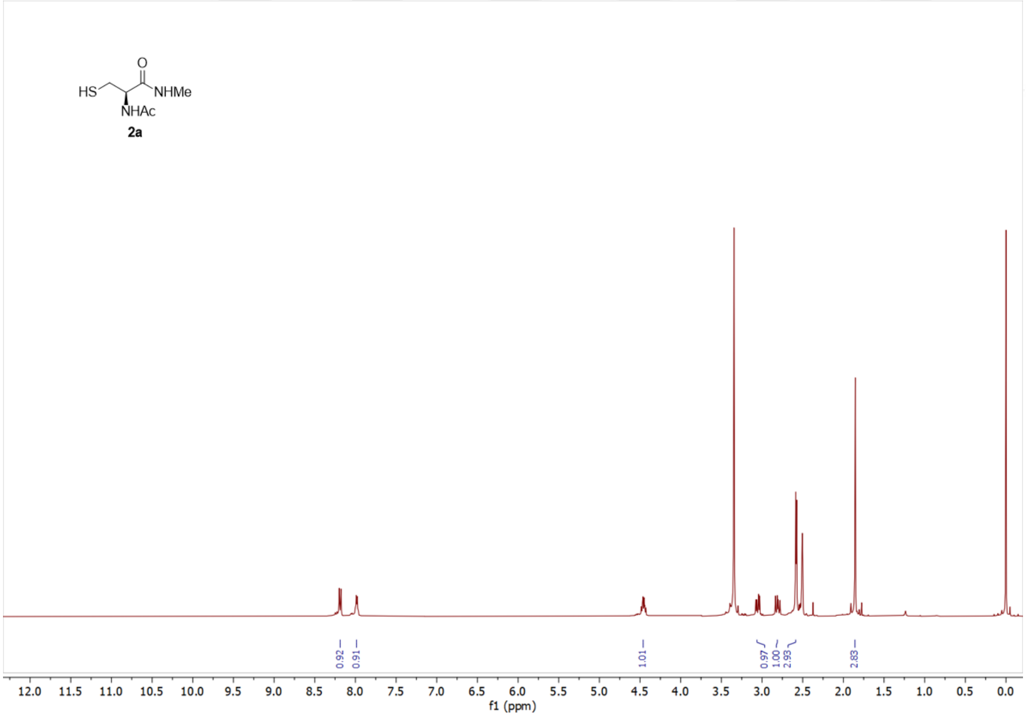

Figure A. 7. ^{1}H NMR spectrum of **2a** in DMSO-d_6.

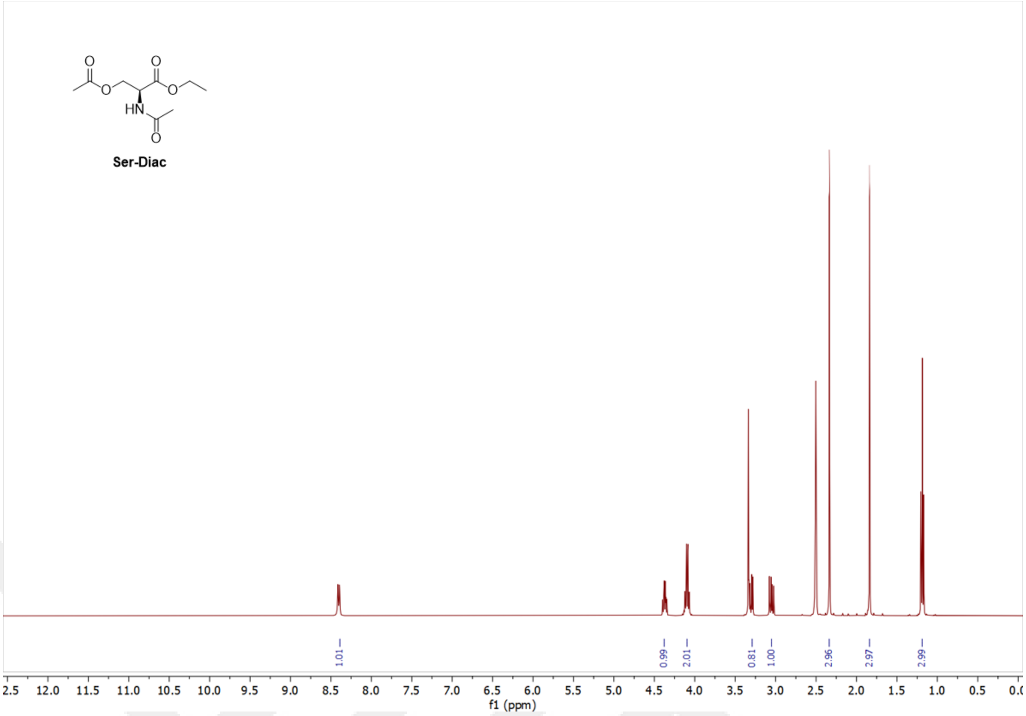

Figure A. 8. ^{1}H NMR spectrum of **Ser-Diac** in DMSO-d_6.

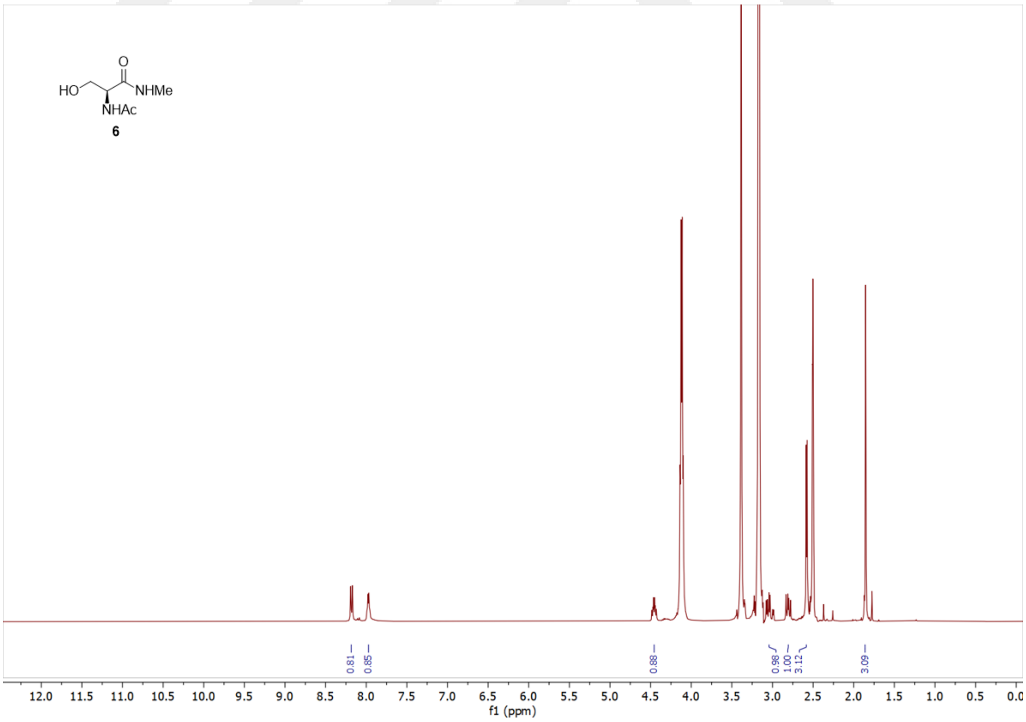

Figure A. 9. ^{1}H NMR spectrum of **6** in DMSO-d_6.

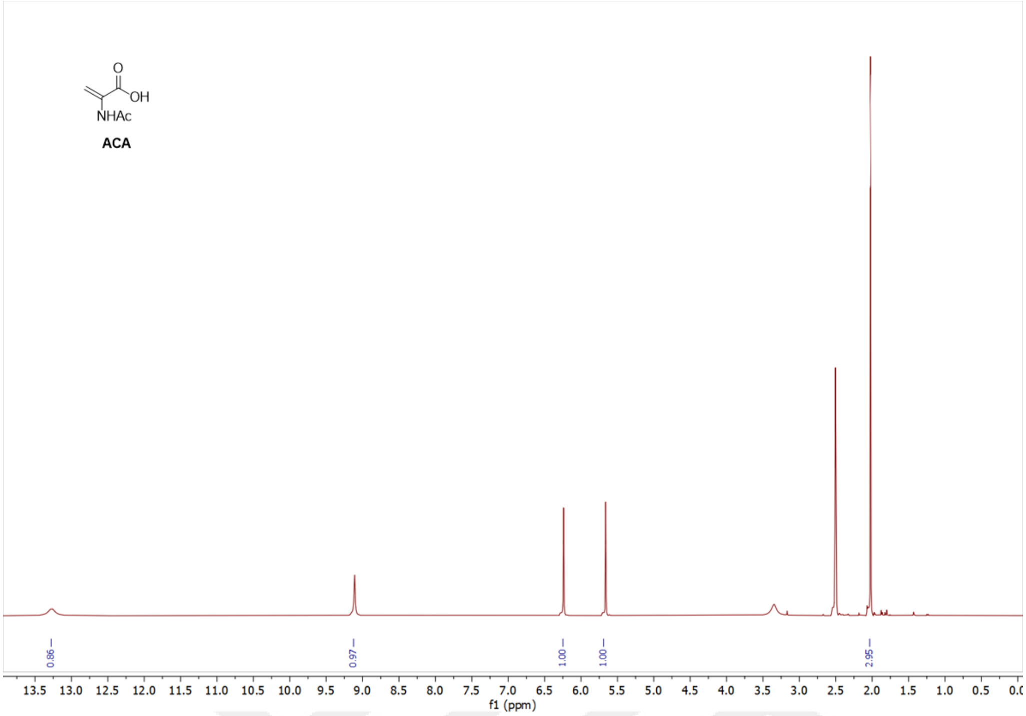

Figure A. 10. ^{1}H NMR spectrum of **ACA** in DMSO-d_6.

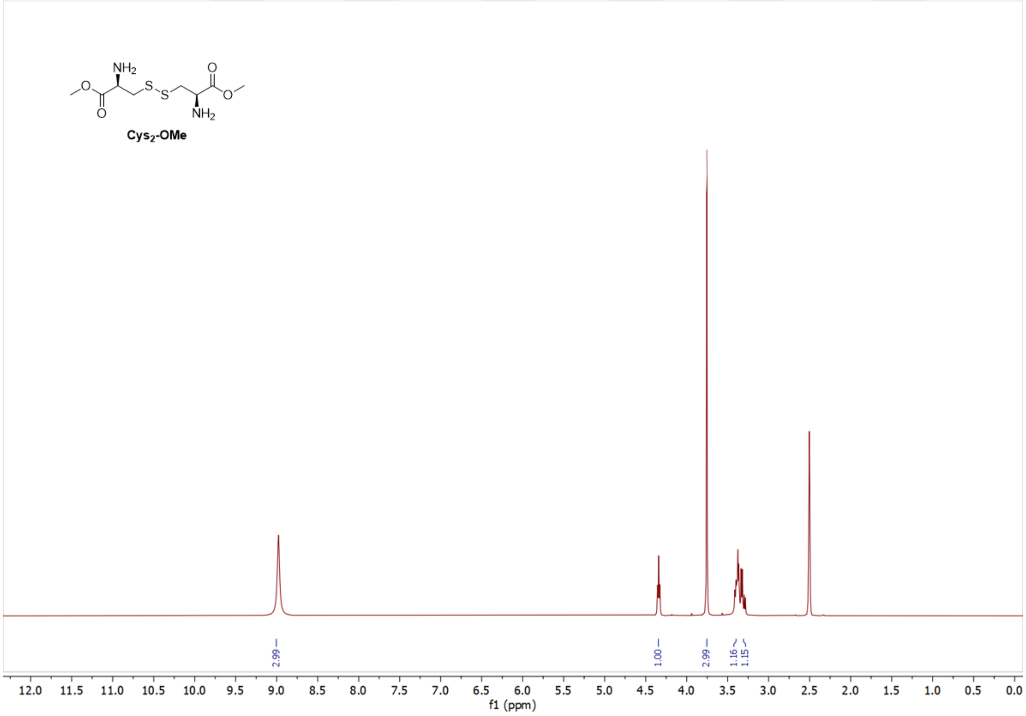

Figure A. 11. ^{1}H NMR spectrum of **Cys_2-OMe** in DMSO-d_6.

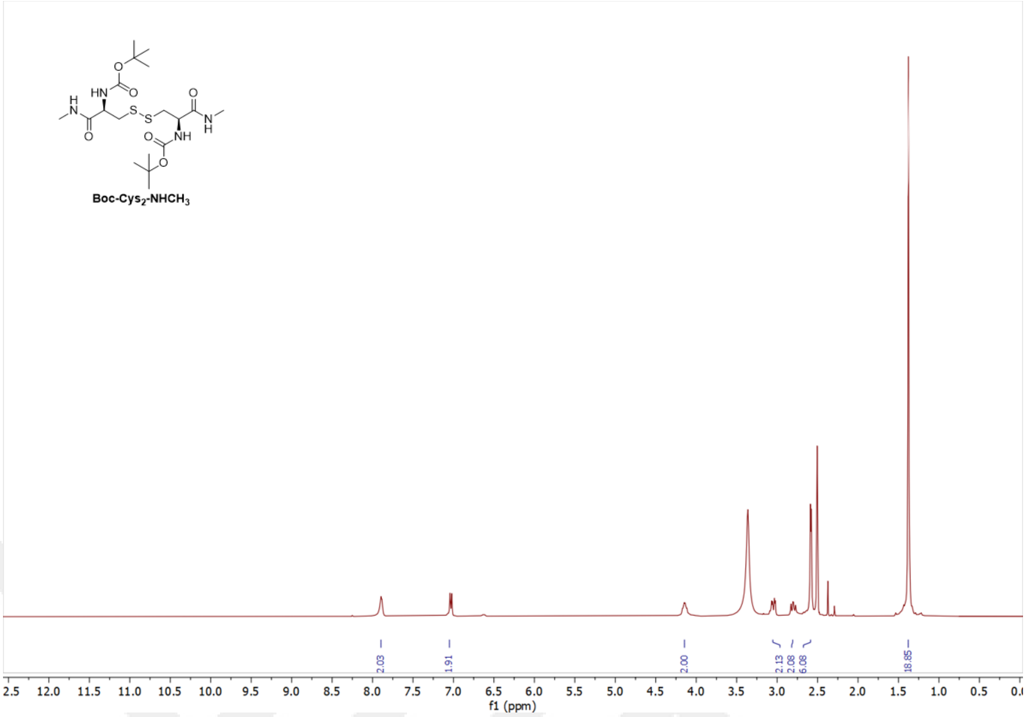

Figure A. 12. ^{1}H NMR spectrum of **Boc-Cys$_2$-NHCH$_3$** in DMSO-d_6.

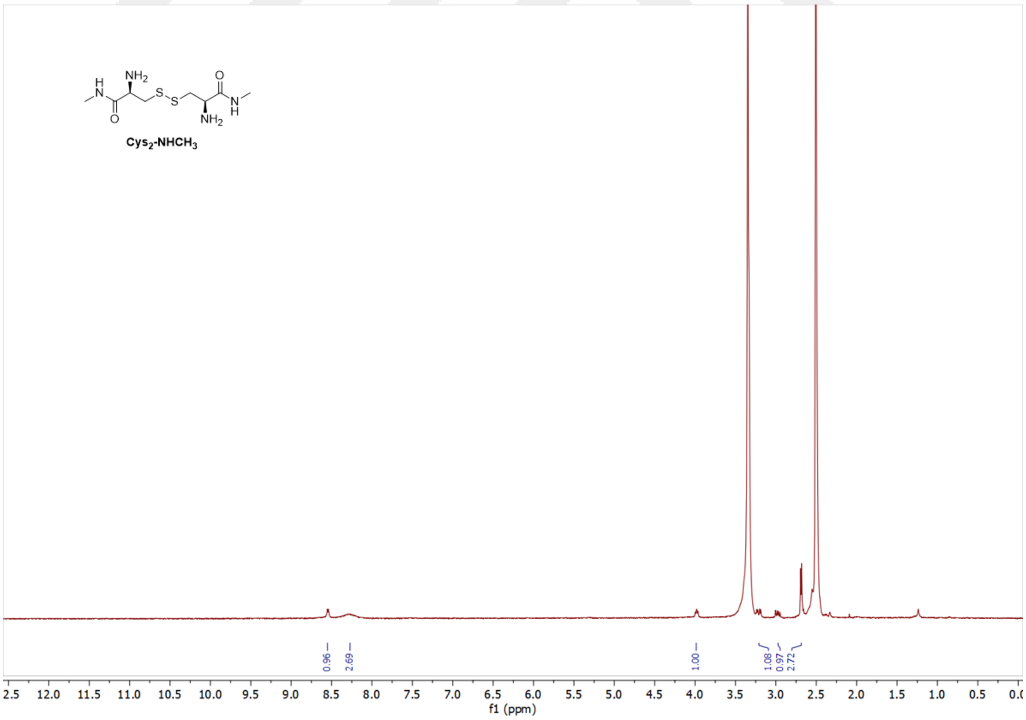

Figure A. 13. ^{1}H NMR spectrum of **Cys$_2$-NHCH$_3$** in DMSO-d_6.

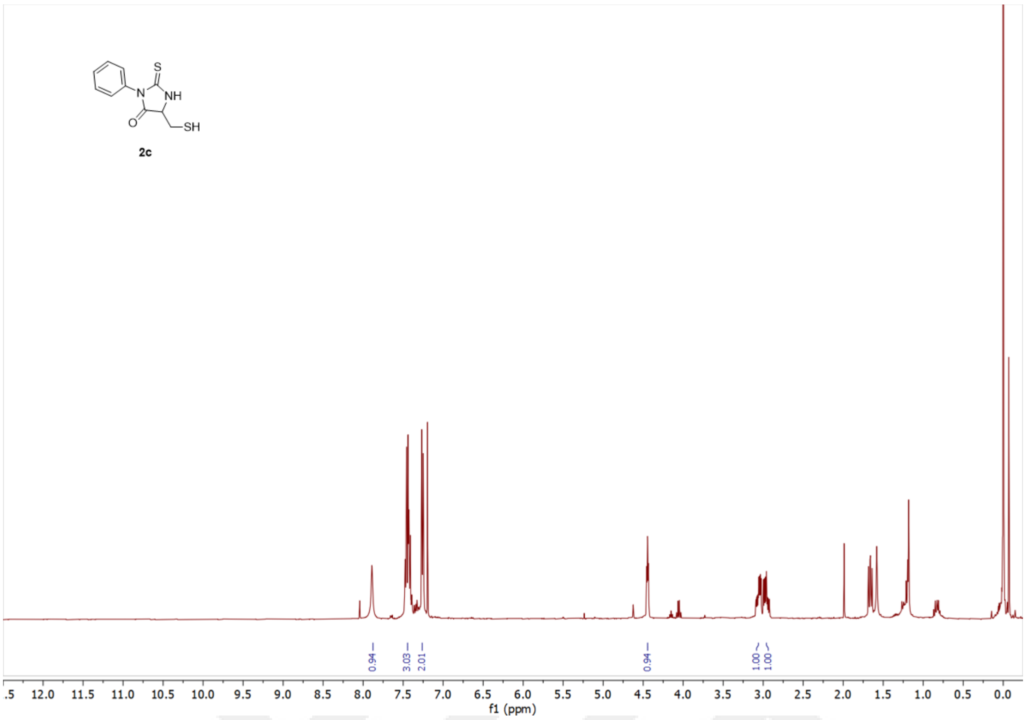

Figure A. 14. ^{1}H NMR spectrum of **2c** in $CDCl_3$.

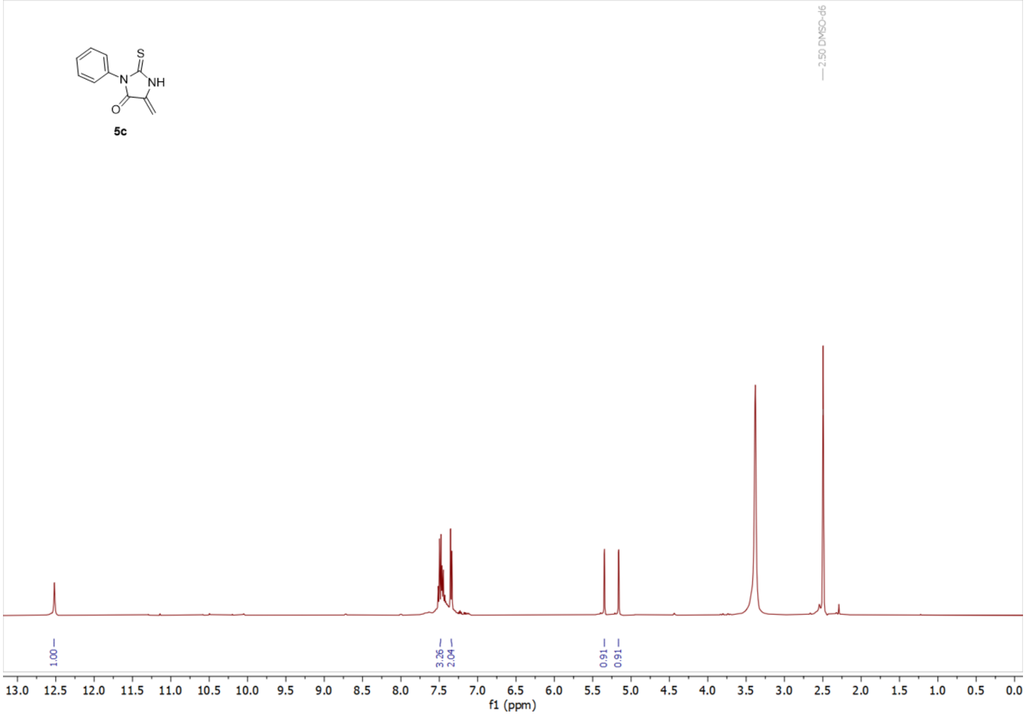

Figure A. 15. ^{1}H NMR spectrum of **5c** in DMSO-d_6.

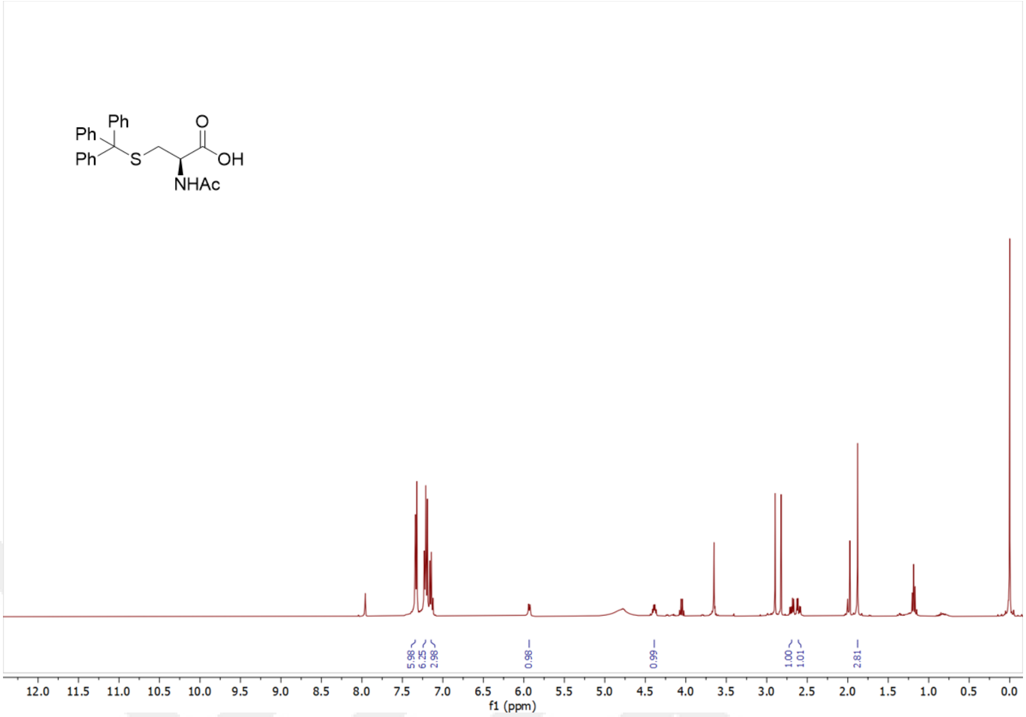

Figure A. 16. ^{1}H NMR spectrum of **Trt-NAC** in $CDCl_3$.

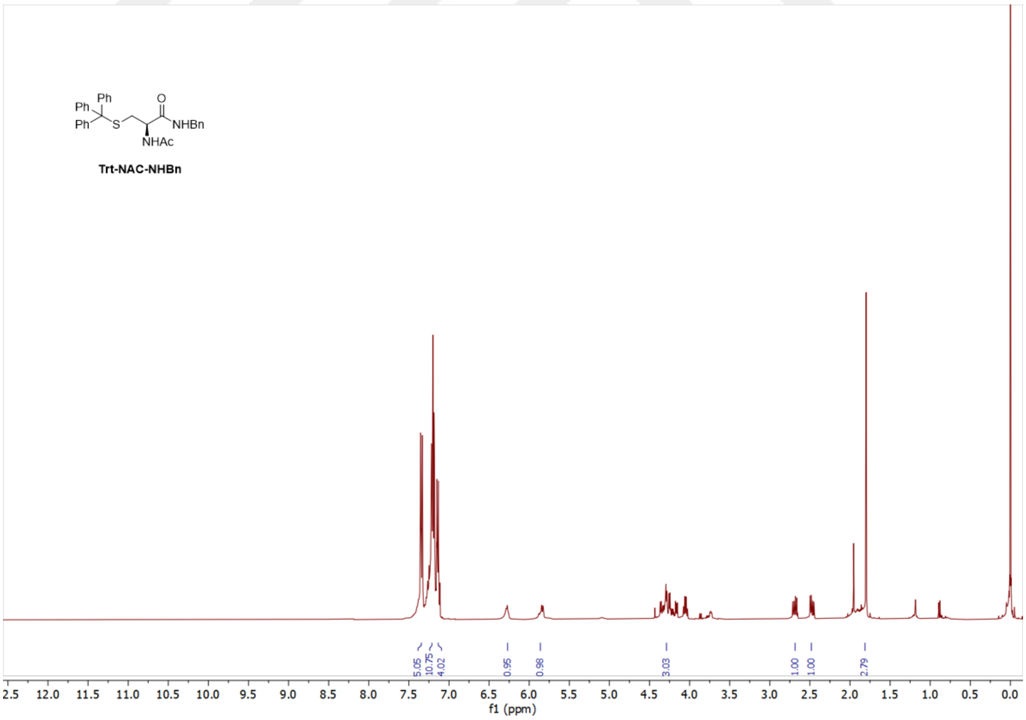

Figure A. 17. ^{1}H NMR spectrum of **Trt-NAC-NHBn** in $CDCl_3$.

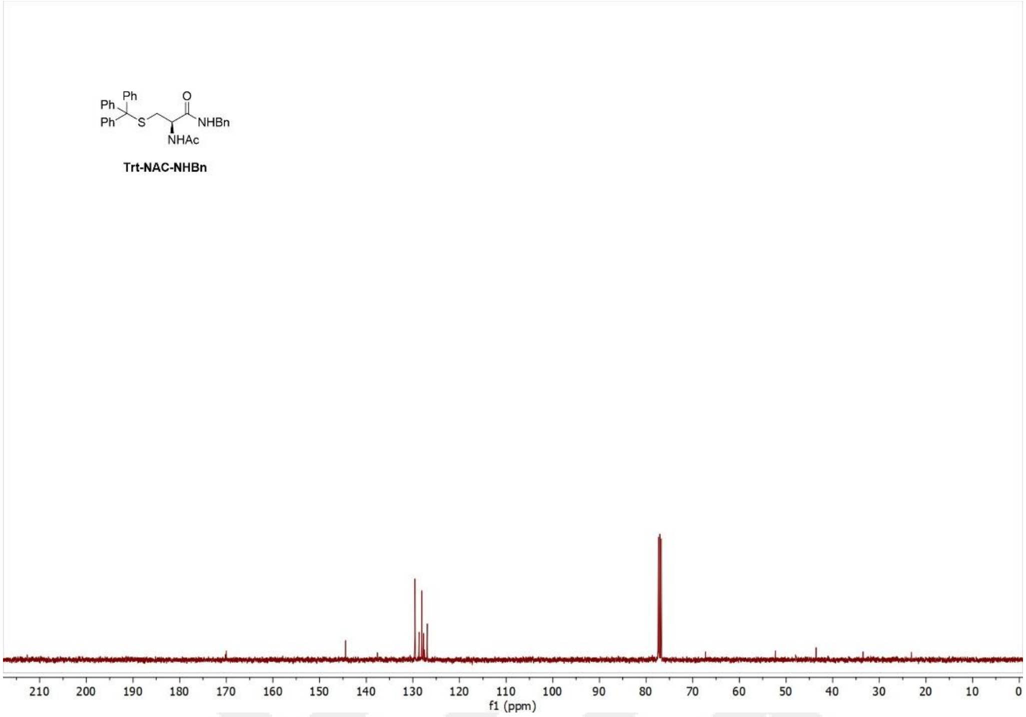

Figure A. 18. ^{13}C NMR spectrum of **Trt-NAC-NHBn** in $CDCl_3$.

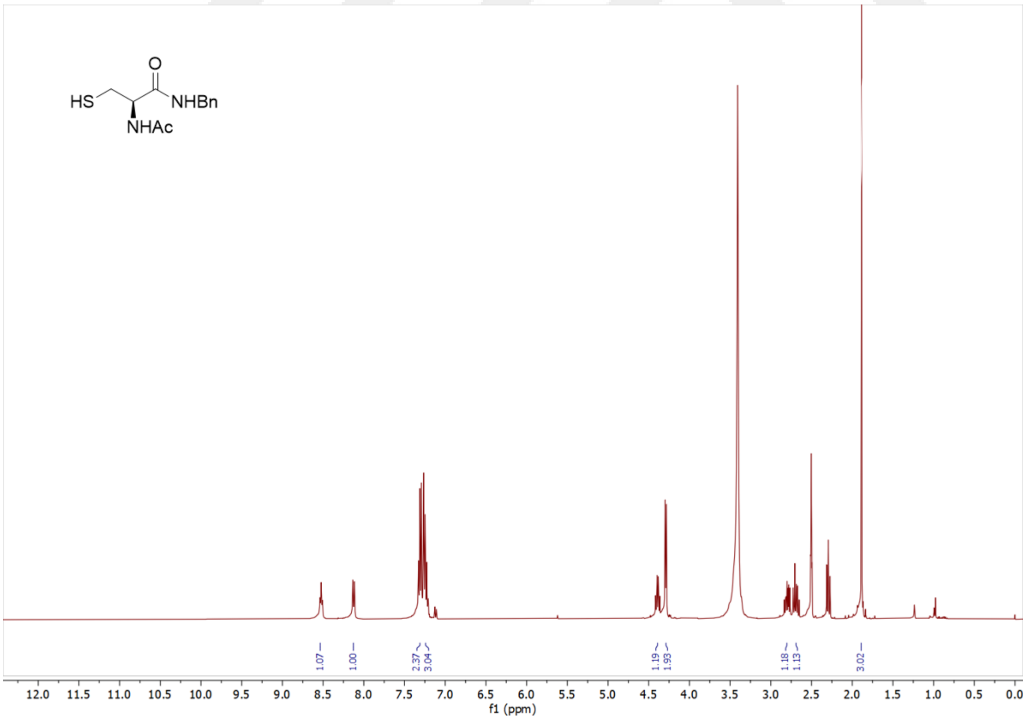

Figure A. 19. ^{1}H NMR spectrum of compound **2d** in DMSO-d_6.

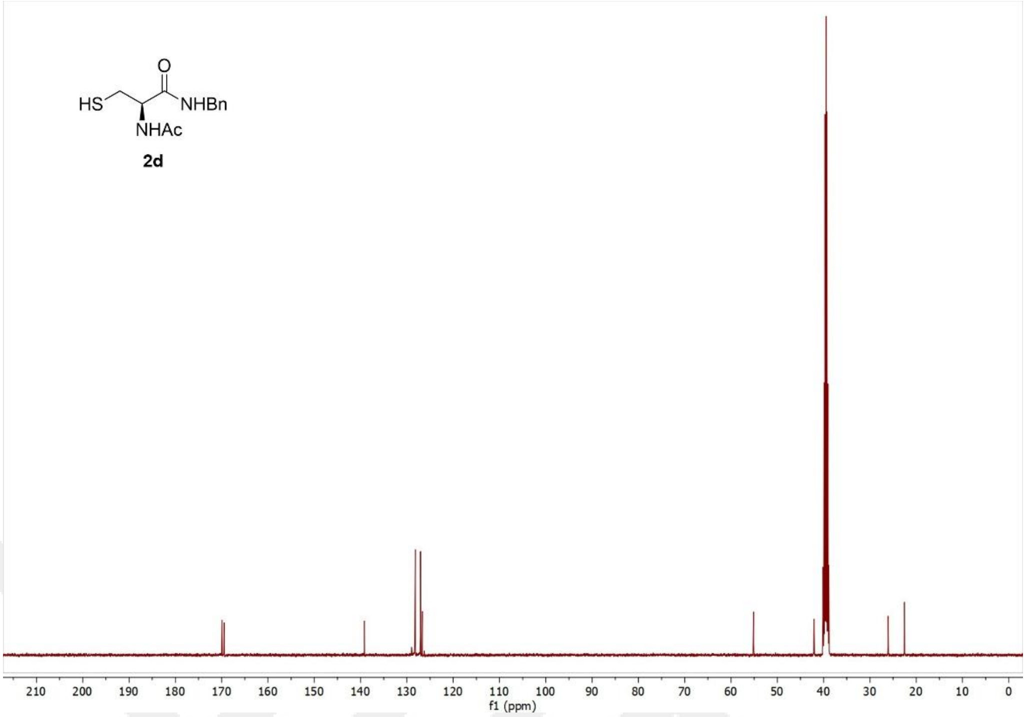

Figure A. 20. ^{13}C NMR spectrum of compound **2d** in DMSO-d_6.

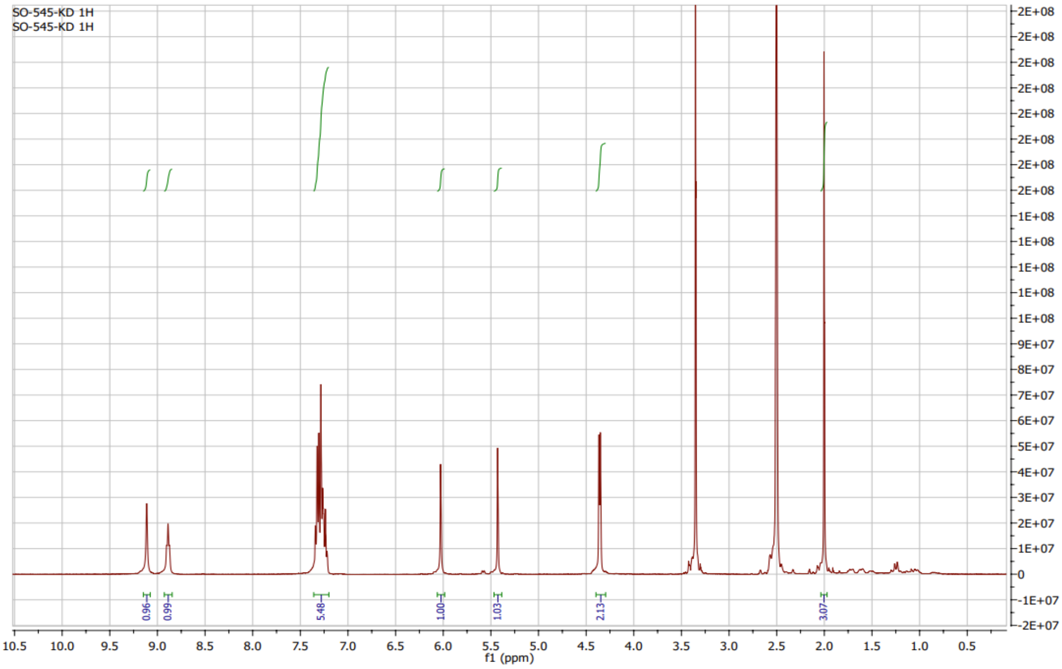

Figure A. 21. ^{1}H NMR spectrum of compound **5d** in DMSO-d_6.

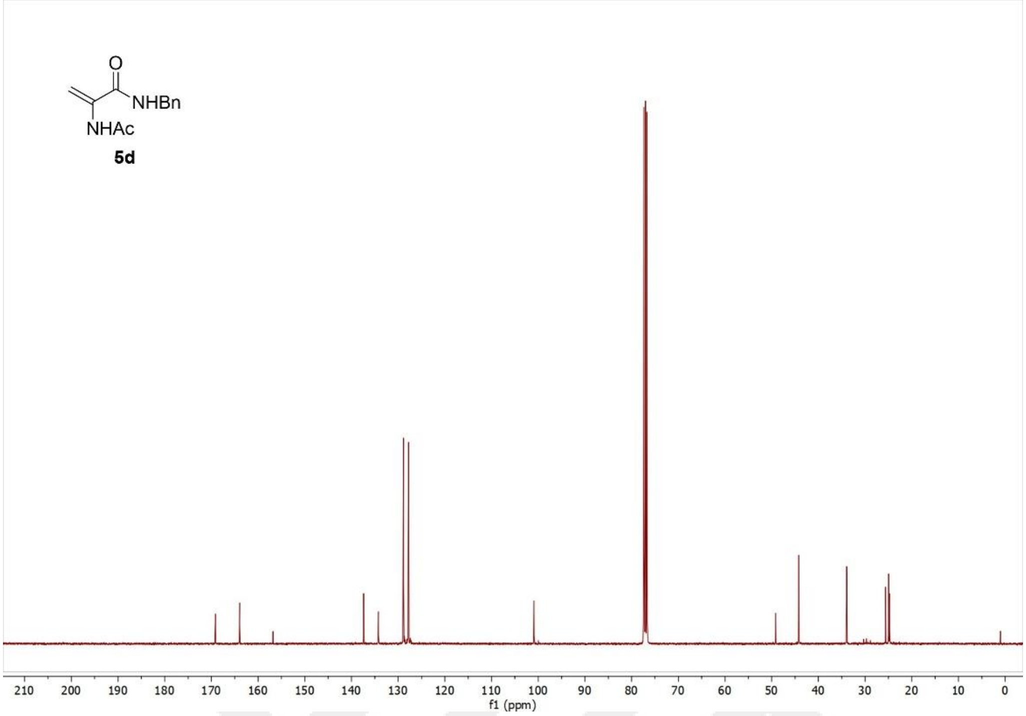

Figure A. 22. ^{13}C NMR spectrum of compound **5d** in $CDCl_3$.

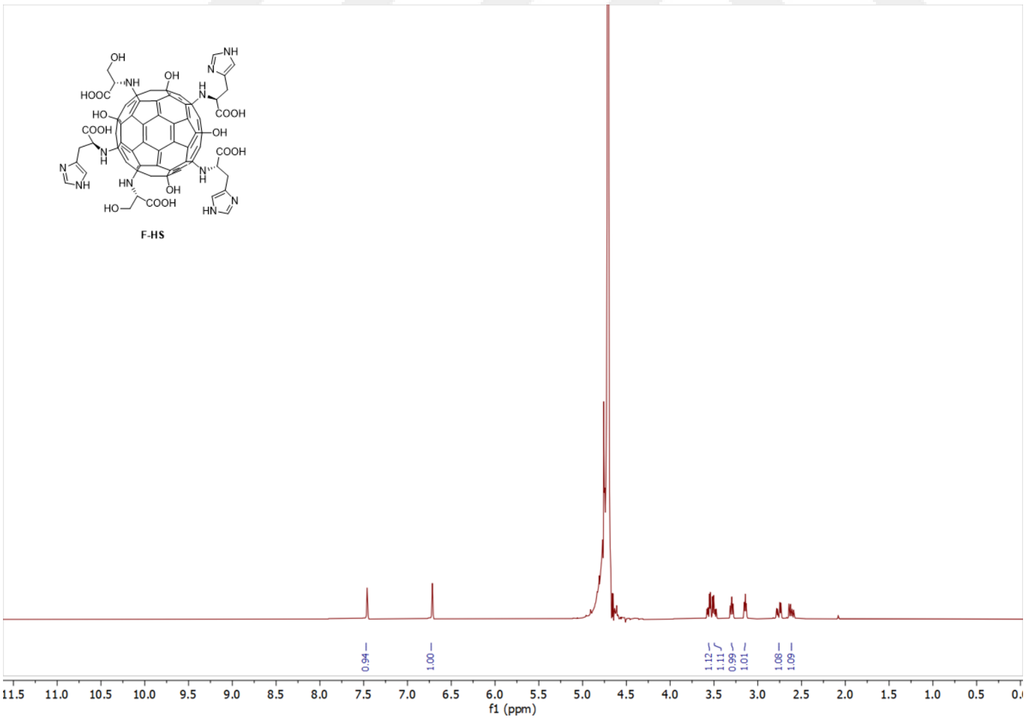

Figure A. 23. ^{1}H NMR spectrum of compound **F-**HS in D_2O.

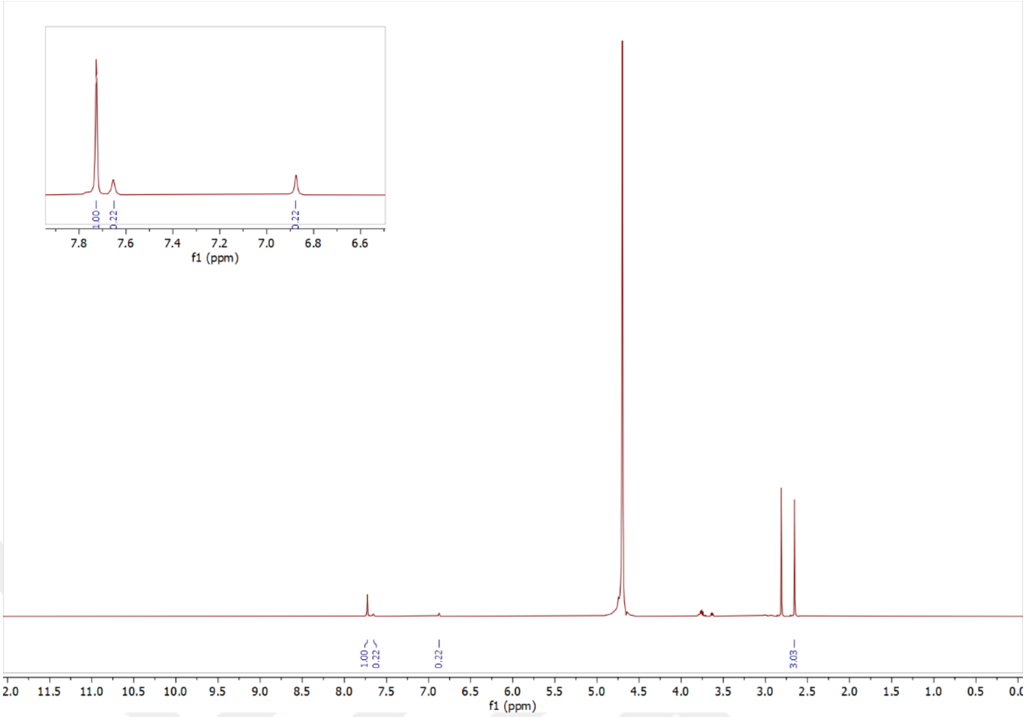

Figure A. 24. ^{1}H NMR spectrum of compound **F-**HS in D_2O with DMF as an internal standard.

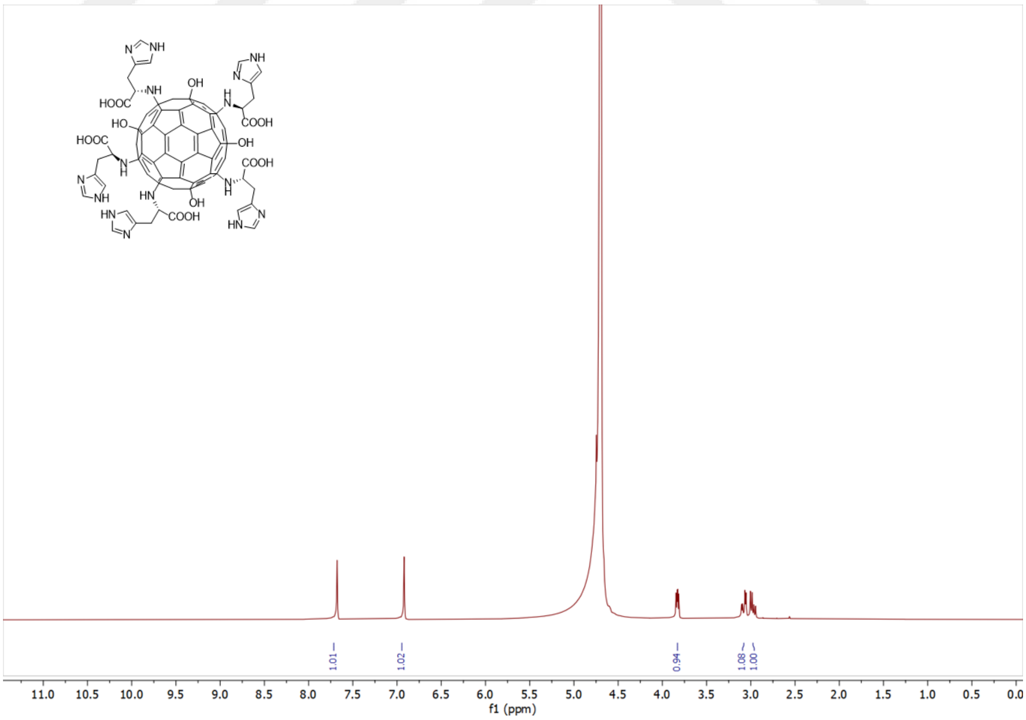

Figure A. 25. ^{1}H NMR spectrum of compound **F-**His in D_2O.

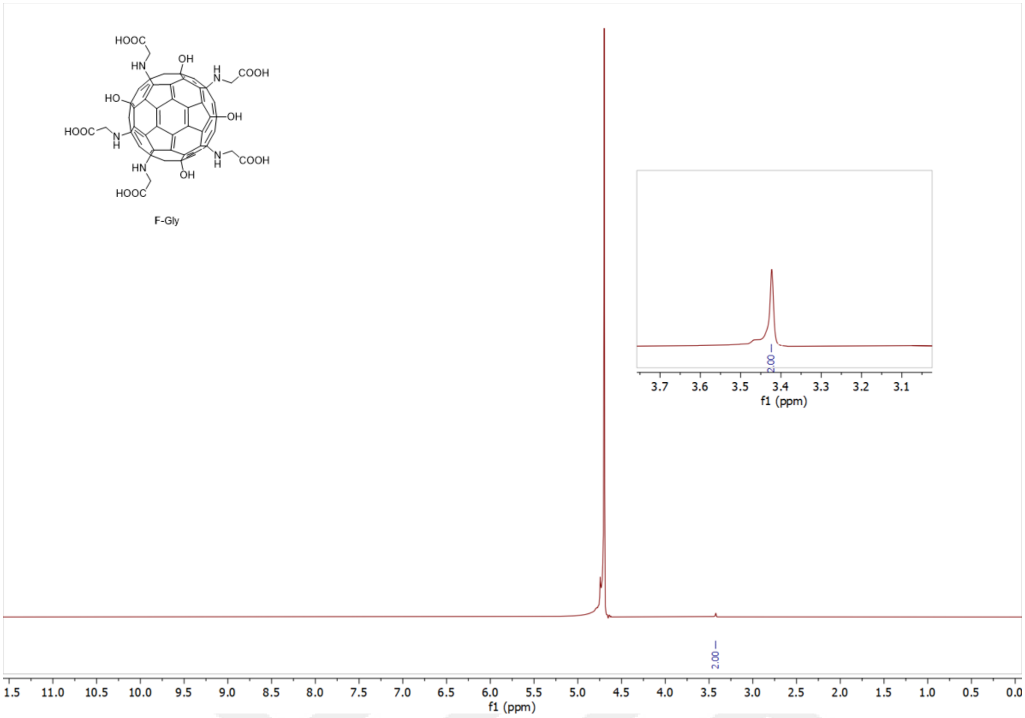

Figure A. 26. ^{1}H NMR spectrum of compound **F-**Gly in D_2O.

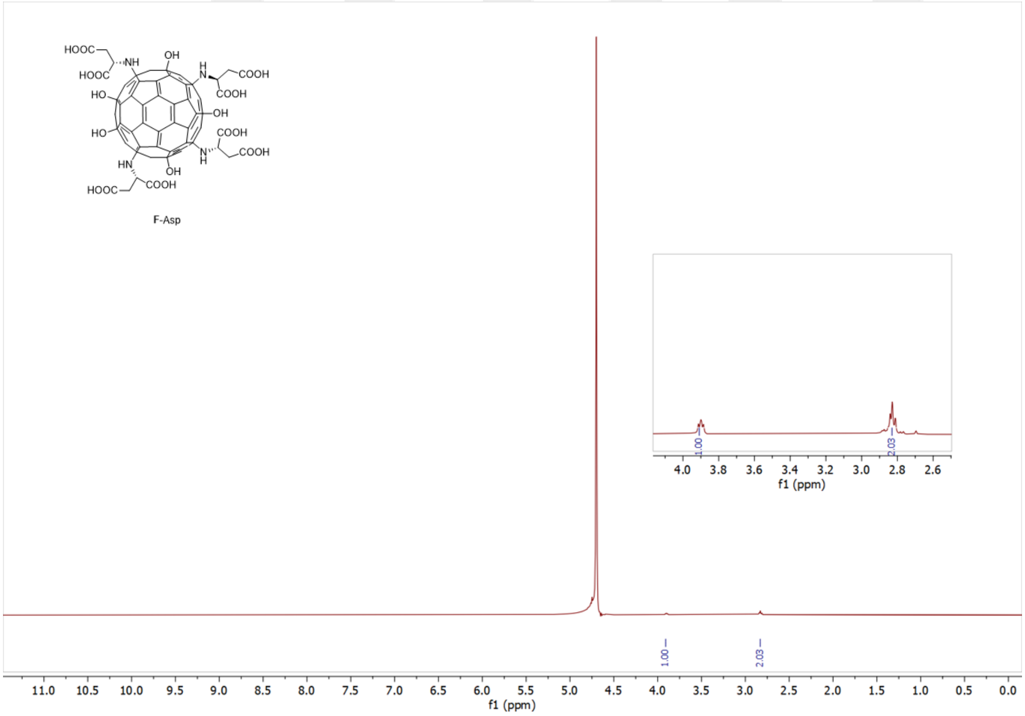

Figure A. 27. ^{1}H NMR spectrum of compound **F-**Asp in D_2O.

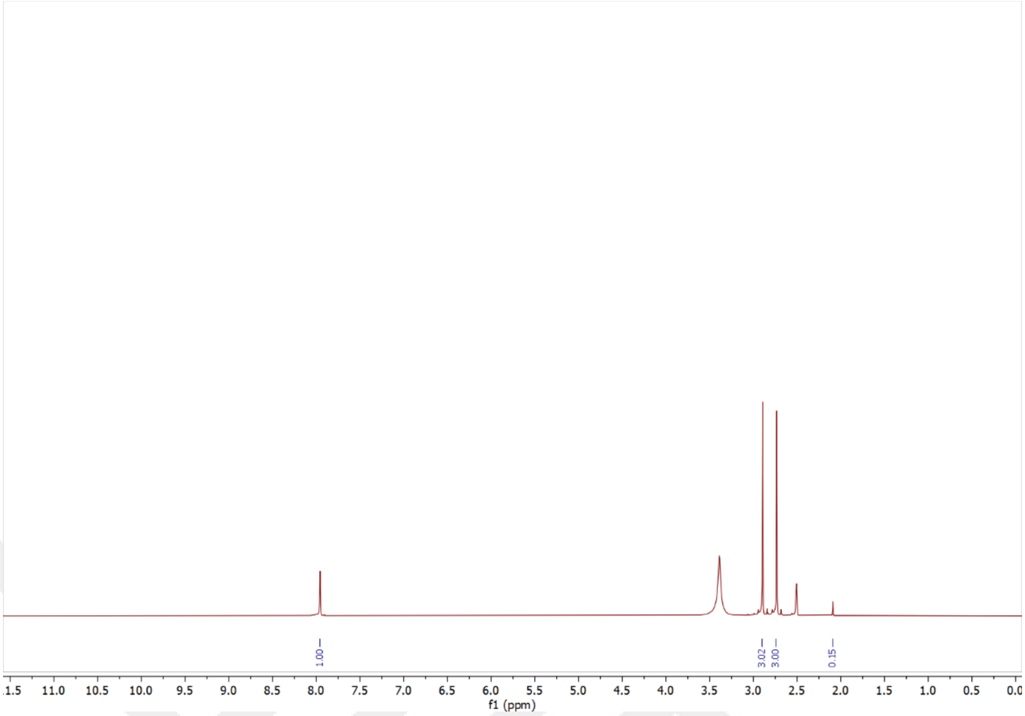

Figure A. 28. ^{1}H NMR spectrum of compound **F**-Asp in DMSO-d_6 with DMF as an internal standard.

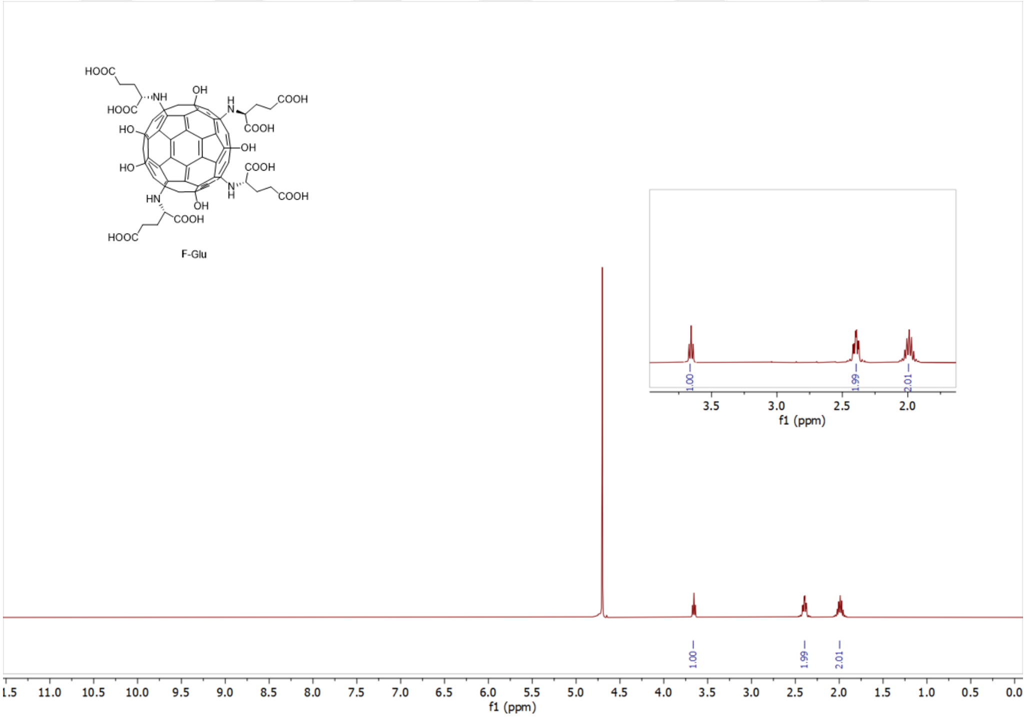

Figure A. 29. ^{1}H NMR spectrum of compound **F**-Glu in D_2O.

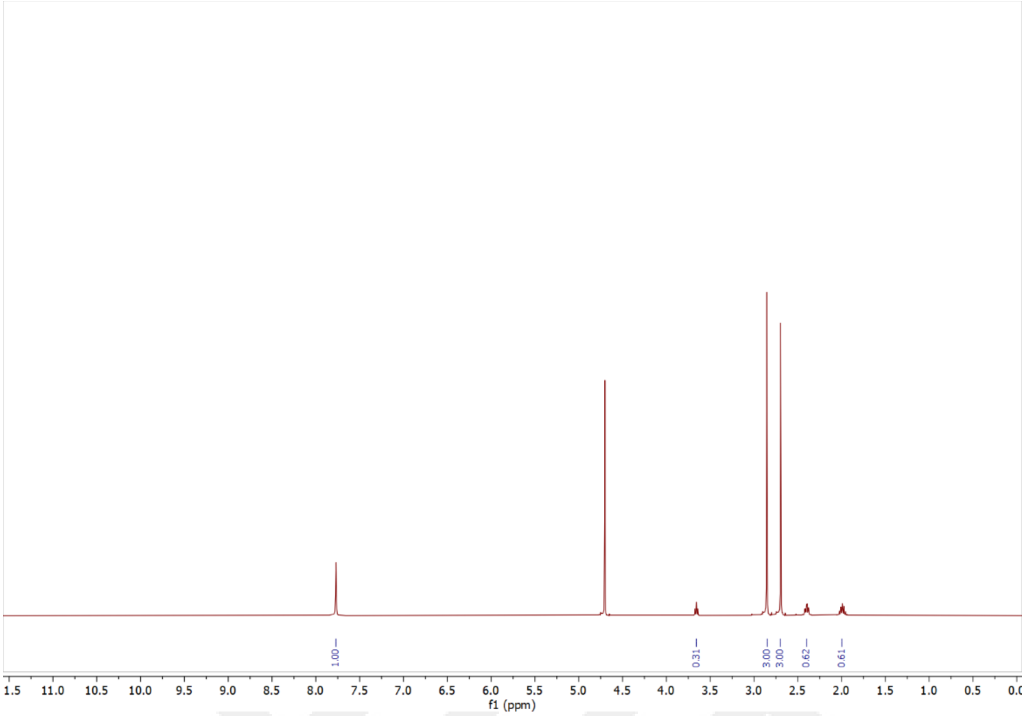

Figure A. 30. ^{1}H NMR spectrum of compound **F-**Glu in D_2O with DMF as an internal standard.

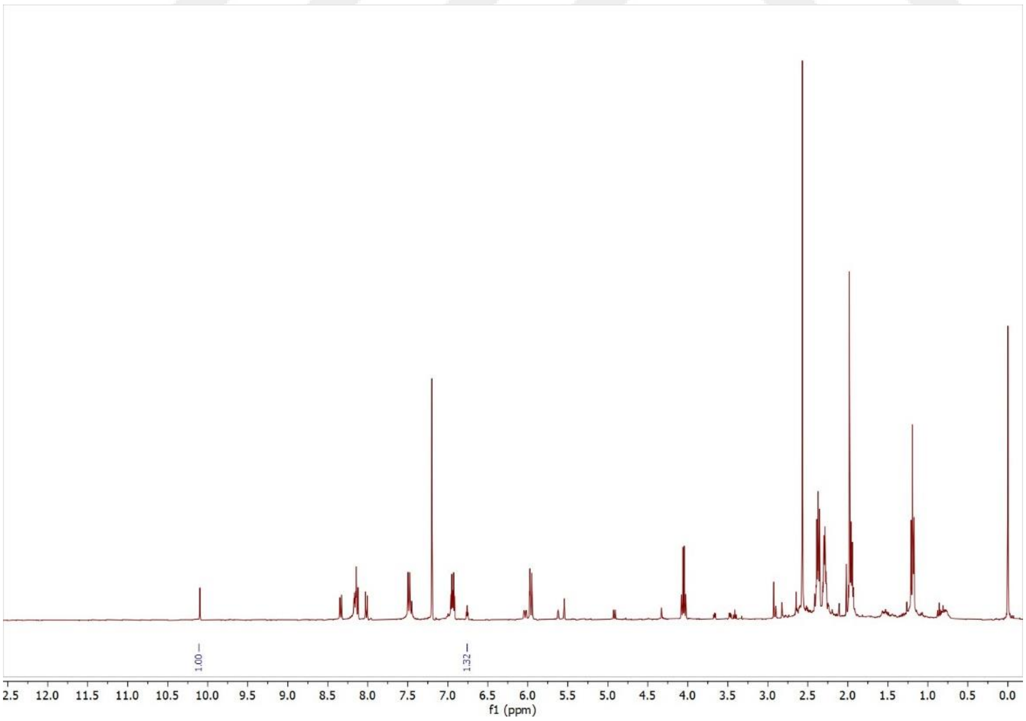

Figure A. 31. ^{1}H NMR spectrum of MBH reaction catalyzed by **F-**Arg in $CDCl_3$.

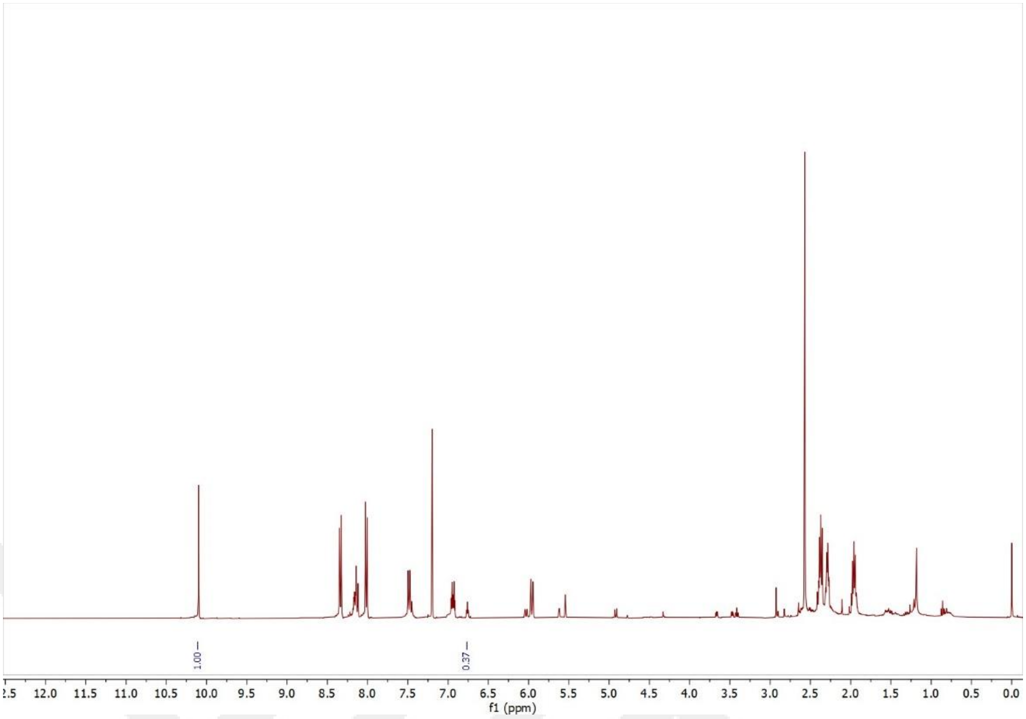

Figure A. 32. ^{1}H NMR spectrum of MBH reaction catalyzed by **F**-His in CDCl$_3$.

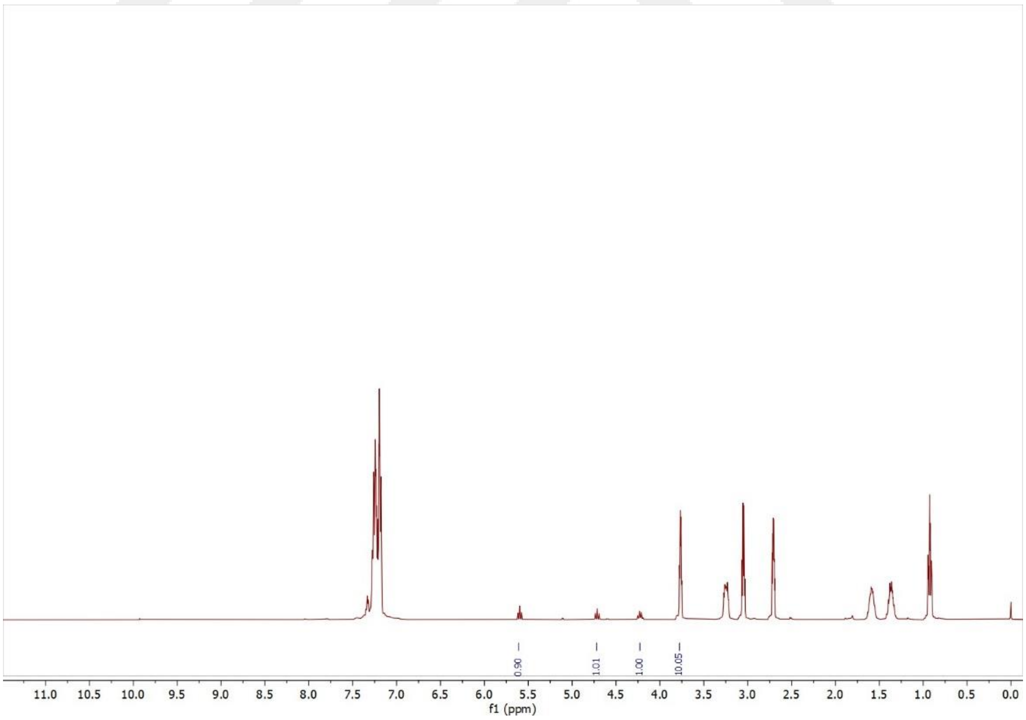

Figure A. 33. ^{1}H NMR spectrum of fullerenol catalyzed CO$_2$ fixation reaction after 2 hours at room temperature in CDCl$_3$.

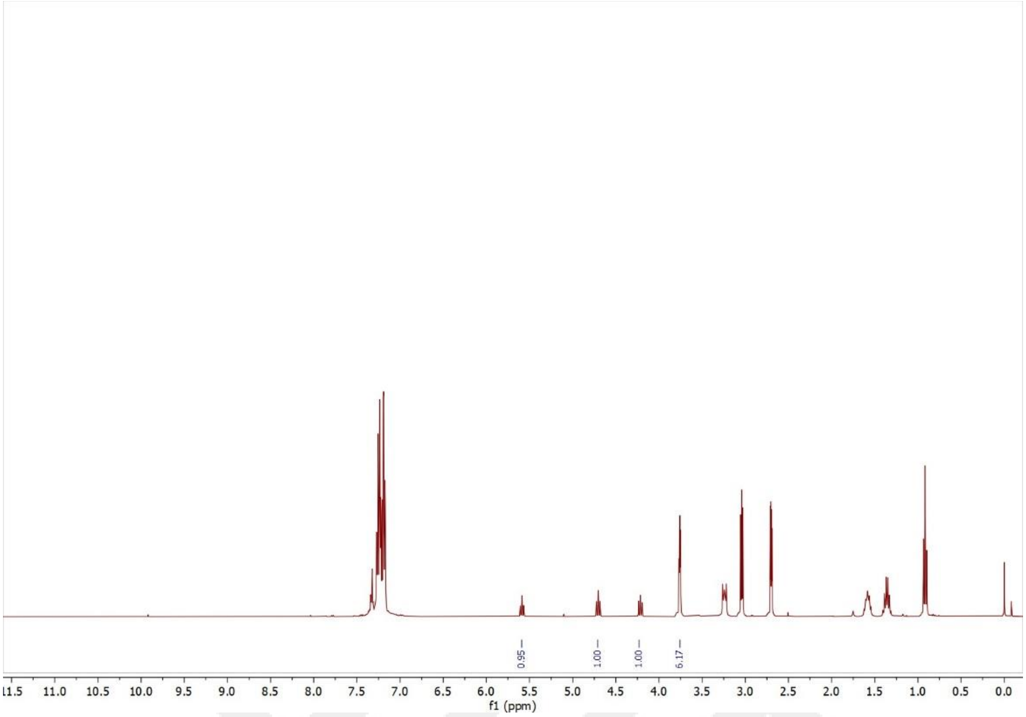

Figure A. 34. ^{1}H NMR spectrum of fullerenol catalyzed CO_2 fixation reaction after 5 hours at room temperature in $CDCl_3$.

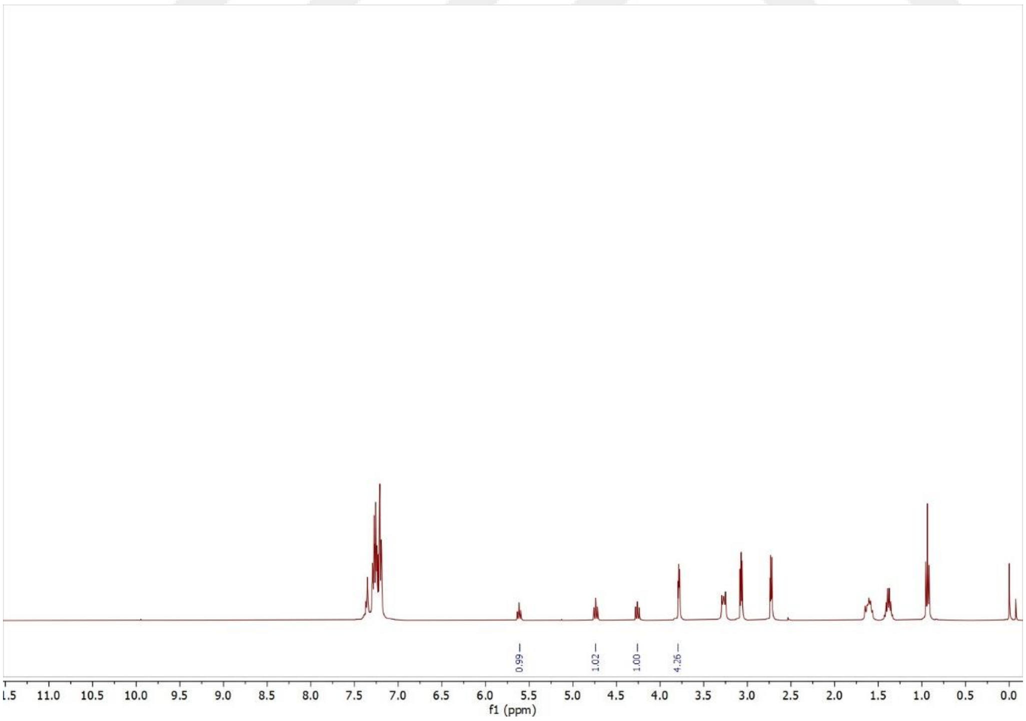

Figure A. 35. ^{1}H NMR spectrum of fullerenol catalyzed CO_2 fixation reaction after 5 hours at room temperature in $CDCl_3$.

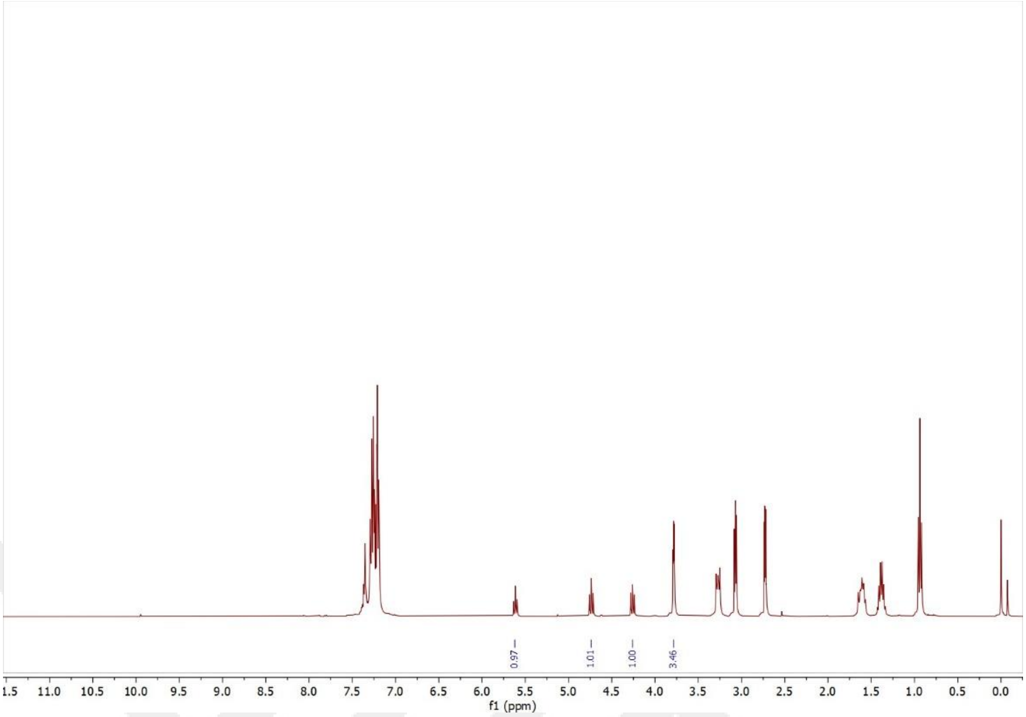

Figure A. 36. ^{1}H NMR spectrum of fullerenol catalyzed CO_2 fixation reaction after 24 hours at room temperature in $CDCl_3$.

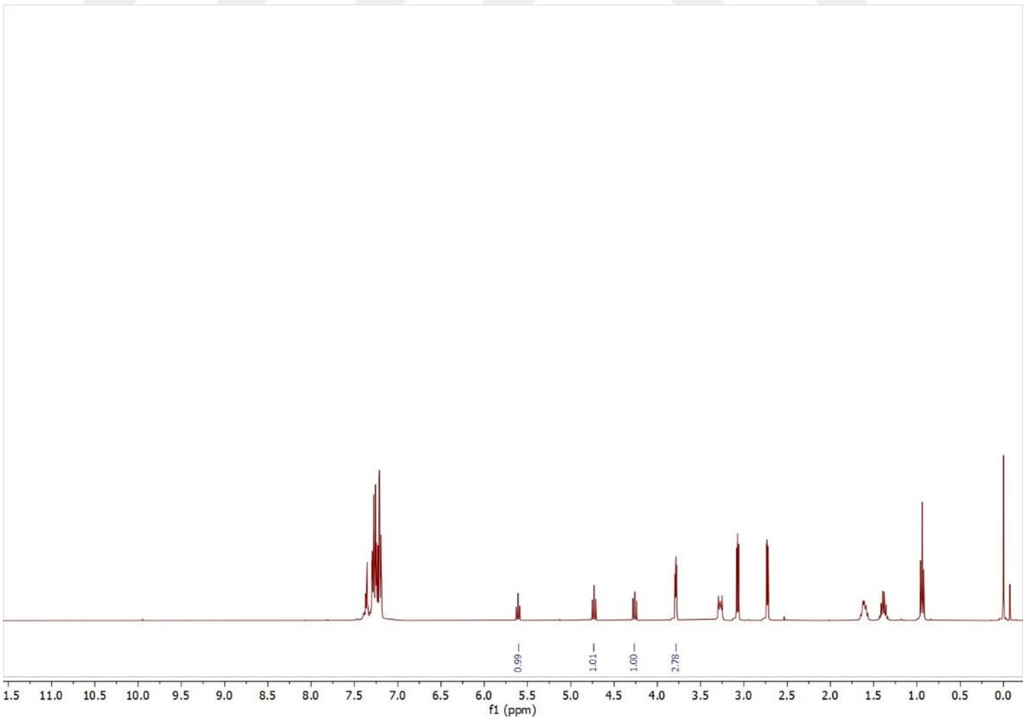

Figure A. 37. ^{1}H NMR spectrum of **F**-His catalyzed CO_2 fixation reaction after 24 hours at room temperature in $CDCl_3$.

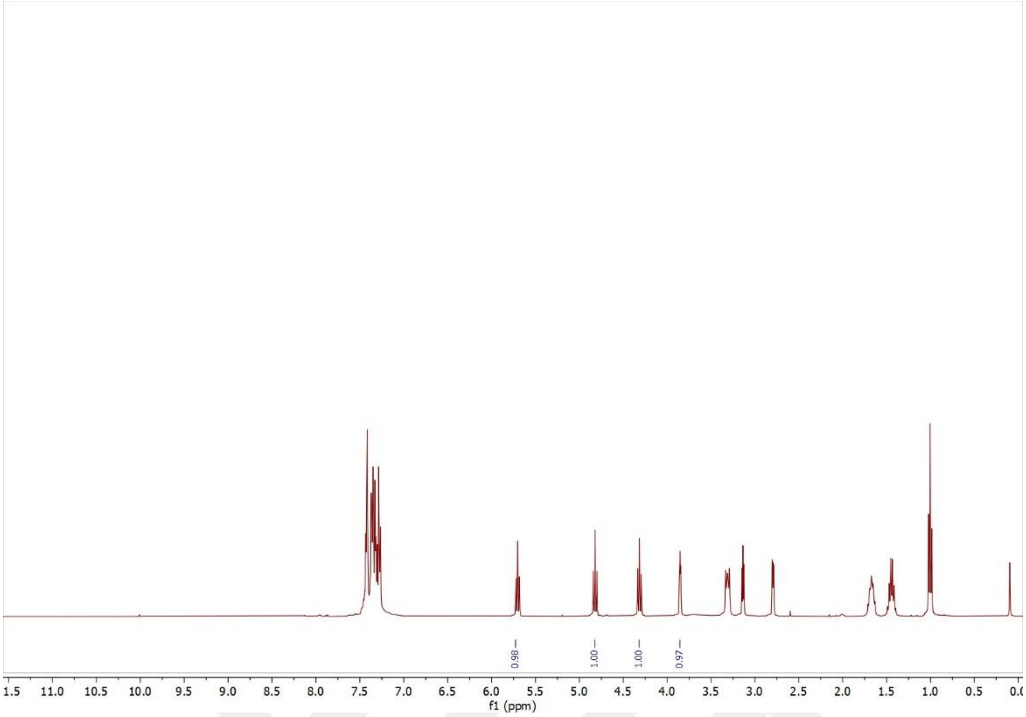

Figure A. 38. ^{1}H NMR spectrum of fullerenol catalyzed CO_2 fixation reaction after 24 hours at 50 °C in $CDCl_3$.

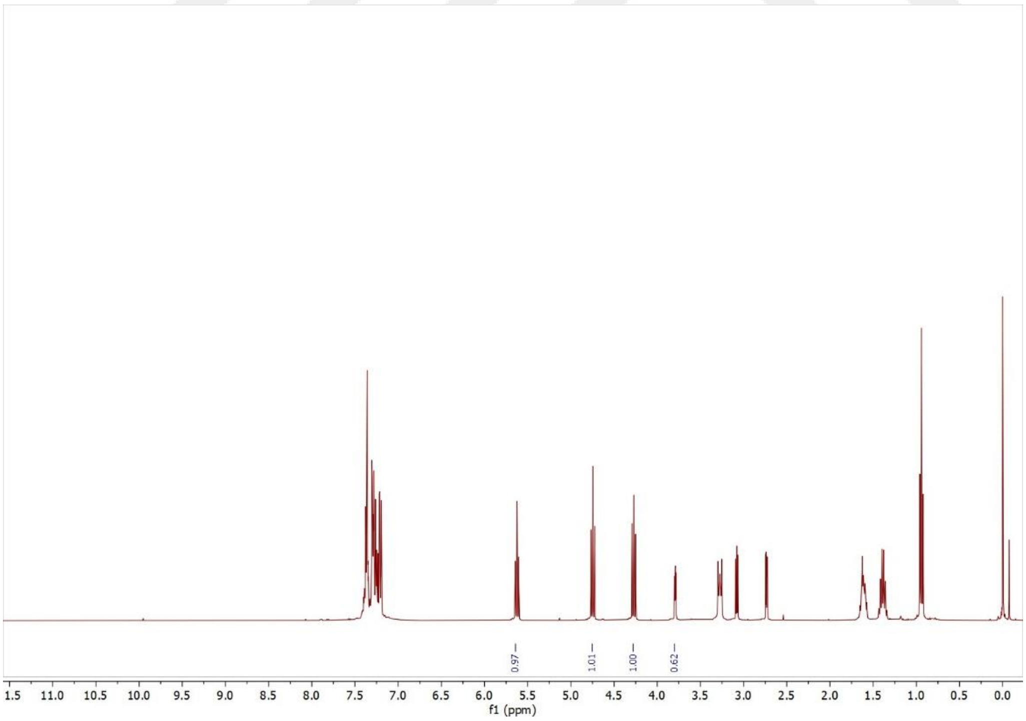

Figure A. 39. ^{1}H NMR spectrum of **F**-Gly catalyzed CO_2 fixation reaction after 24 hours at 50 °C in $CDCl_3$.

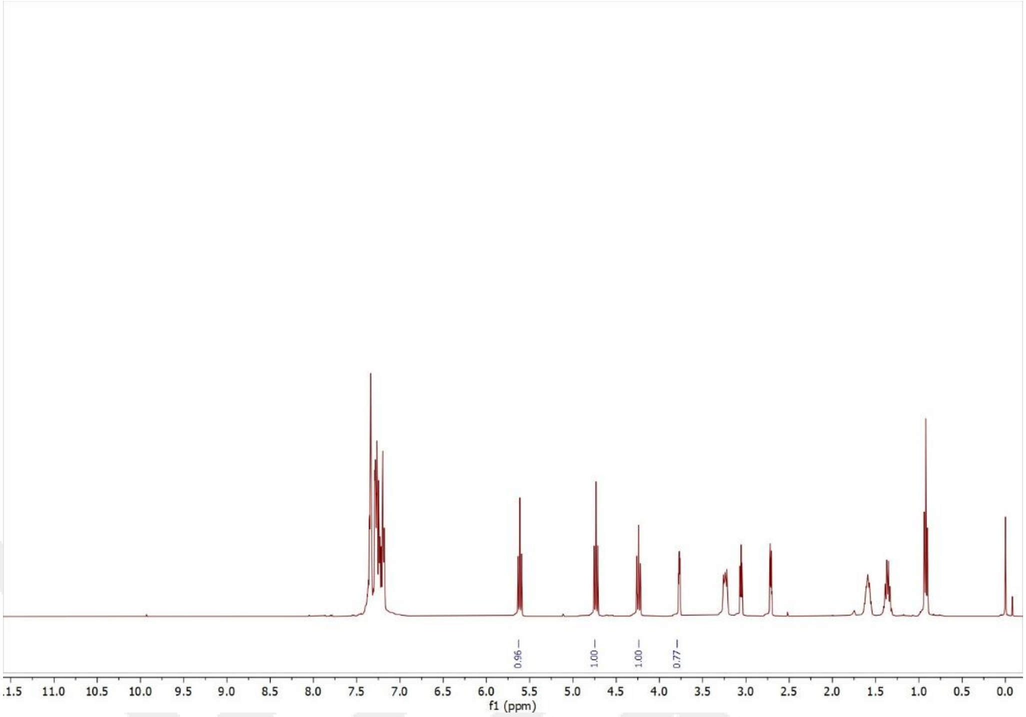

Figure A. 40. ^{1}H NMR spectrum of **F**-Arg catalyzed CO_2 fixation reaction after 24 hours at 50 °C in $CDCl_3$.

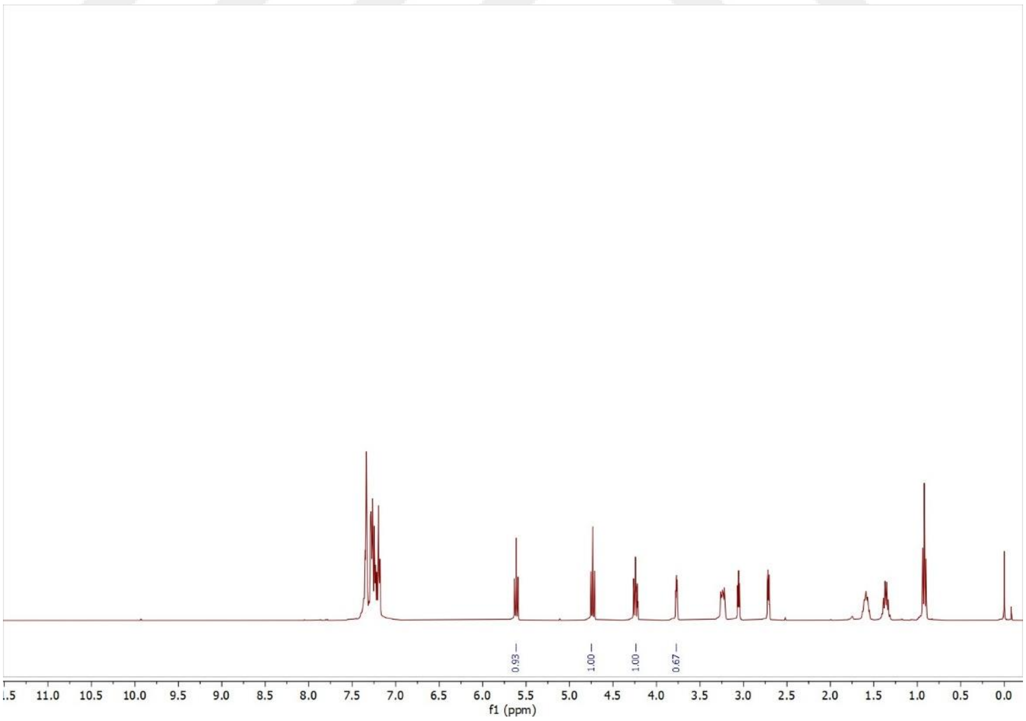

Figure A. 41. ^{1}H NMR spectrum of **F**-Asp catalyzed CO_2 fixation reaction after 24 hours at 50 °C in $CDCl_3$.

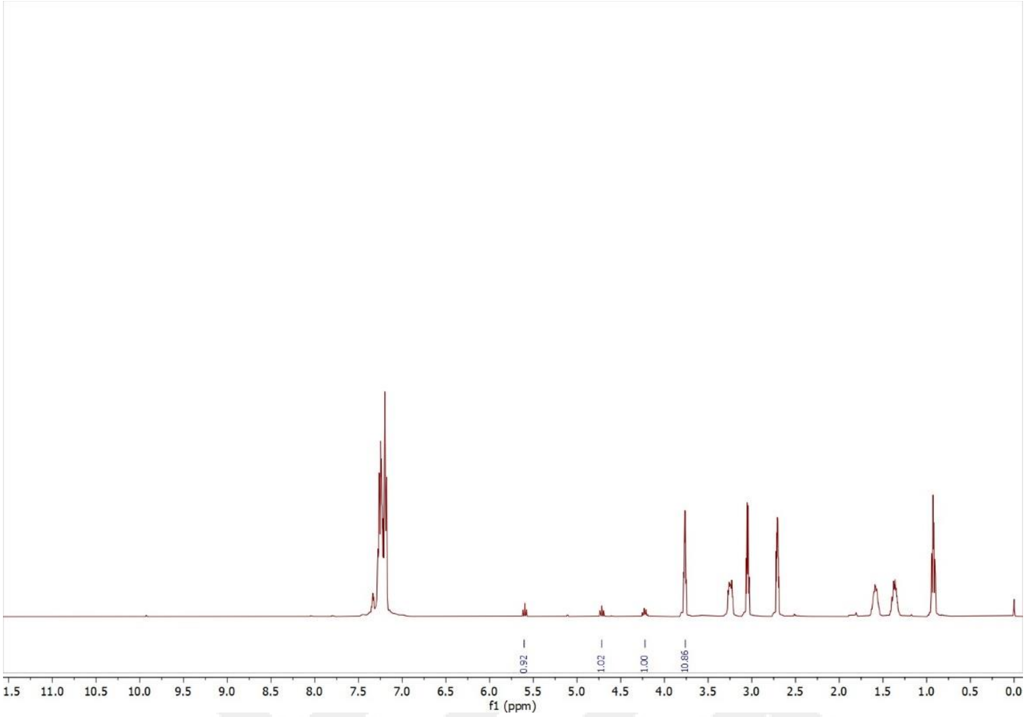

Figure A. 42. ^{1}H NMR spectrum of L-His catalyzed CO_2 fixation reaction after 24 hours at 50 °C in $CDCl_3$.

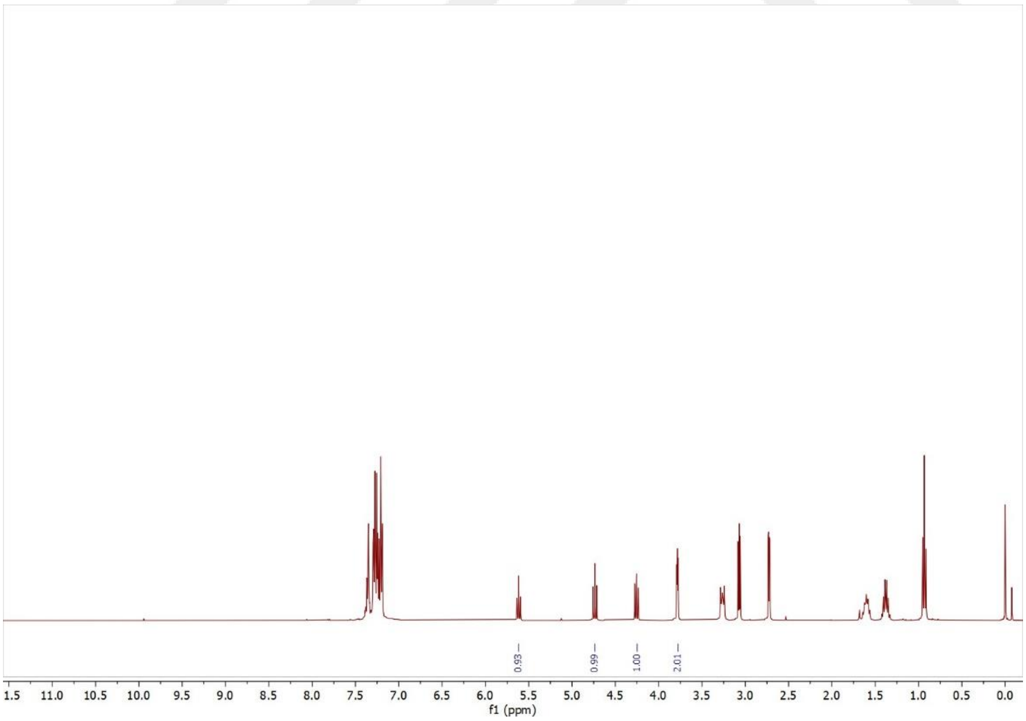

Figure A. 43. ^{1}H NMR spectrum of fullerenol and KI co-catalyzed CO_2 fixation reaction after 24 hours at 50 °C in $CDCl_3$.

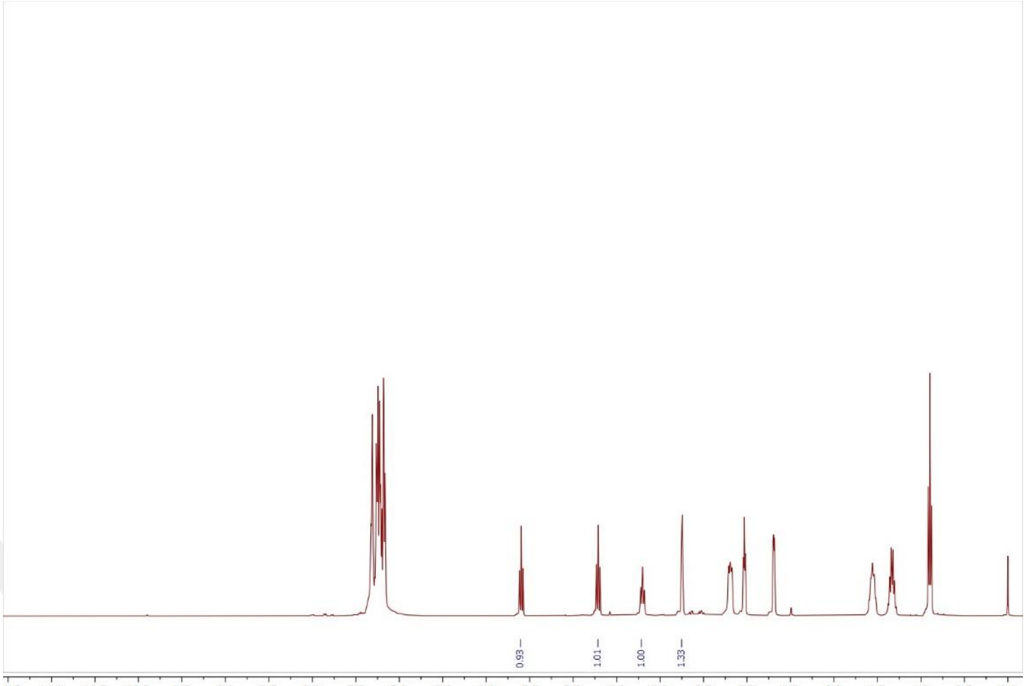

Figure A. 44. ^{1}H NMR spectrum of **F**-His and KI co-catalyzed CO_2 fixation reaction after 24 hours at 50 °C in $CDCl_3$.

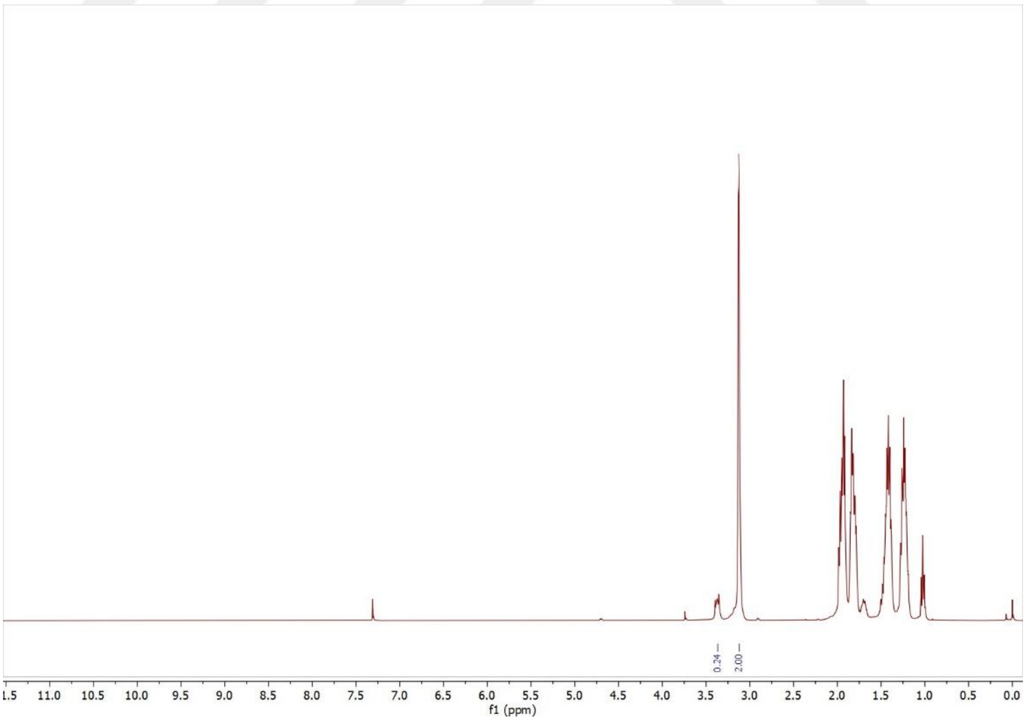

Figure A. 45. ^{1}H NMR spectrum of **F**-His catalyzed CO_2 fixation reaction with cyclohexene oxide as the epoxide after 24 hours at 50 °C in $CDCl_3$.

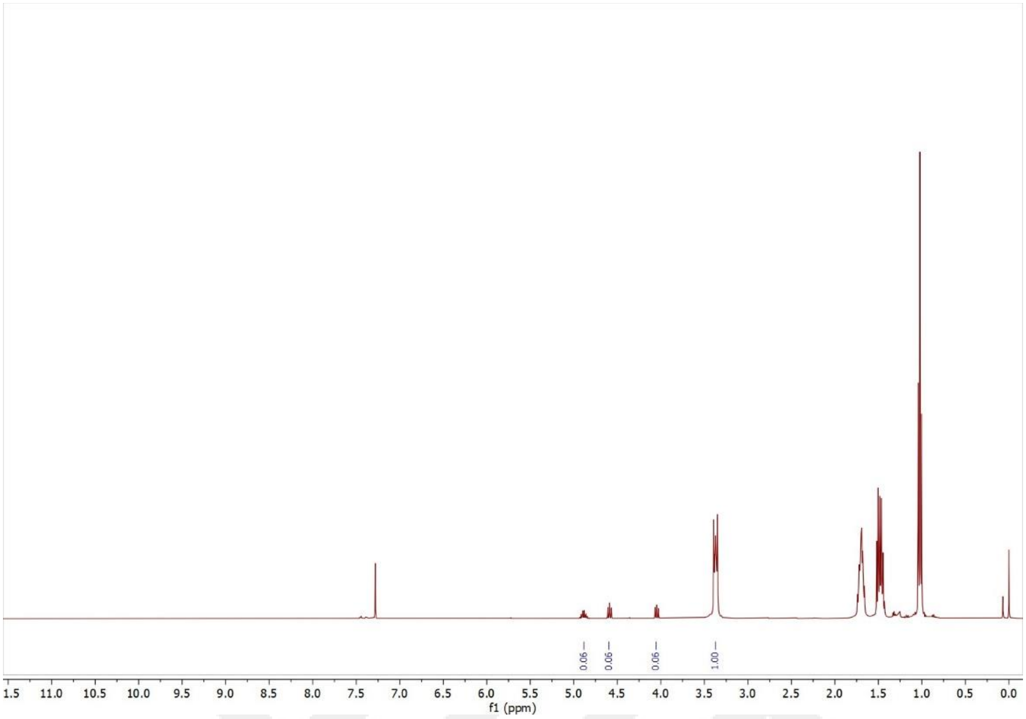

Figure A. 46. ^{1}H NMR spectrum of **F**-His catalyzed CO_2 fixation reaction with propylene oxide as the epoxide after 24 hours at 50 °C in $CDCl_3$.

B. HPLC SPECTRA

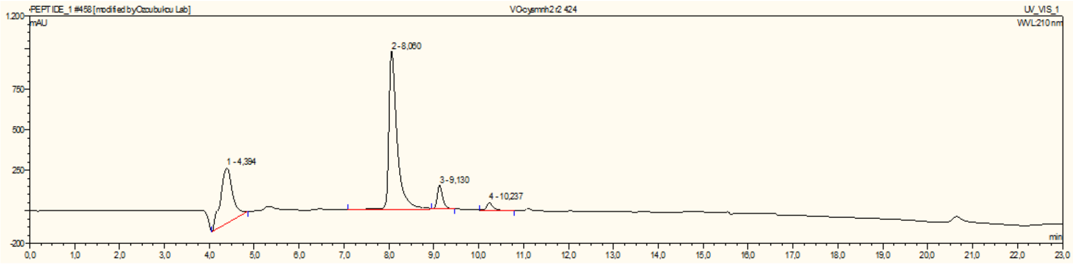

Figure B. 1. HPLC chromatogram of compound **2a** at 210 nm (C18, 20 min, gradient).

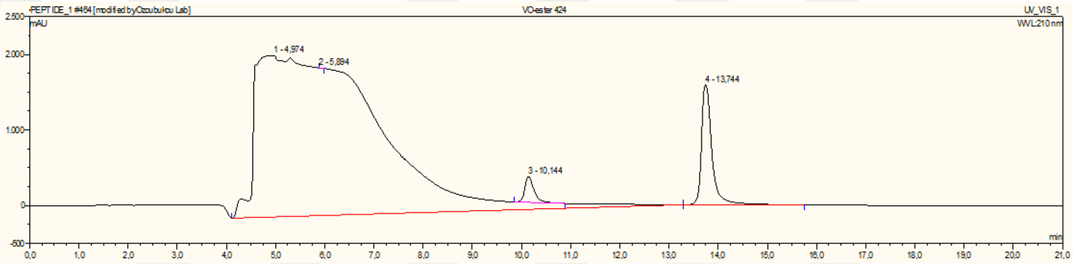

Figure B. 2. HPLC chromatogram of compound **1** and compound **4** at 210 nm (C18, 20 min, gradient).

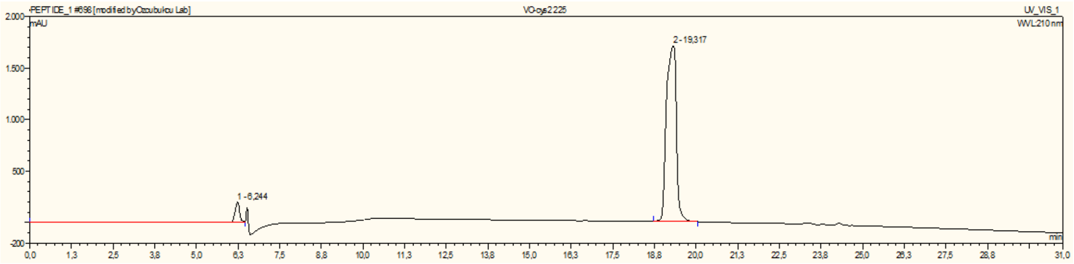

Figure B. 3. HPLC chromatogram of compound **2d** at 210 nm (PS-C18, 30 min, gradient).

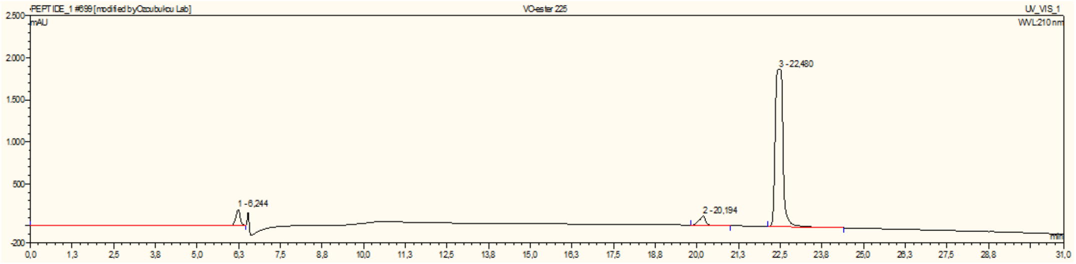

Figure B. 4. HPLC chromatogram of compound **1** at 210 nm (PS-C18, 30 min, gradient).

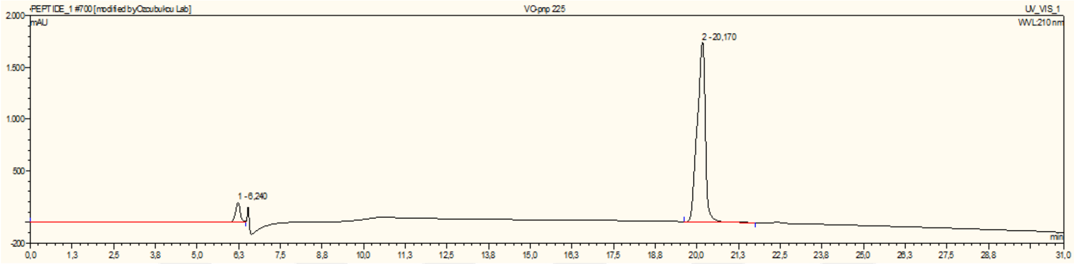

Figure B. 5. HPLC chromatogram of compound **4** at 210 nm (PS-C18, 30 min, gradient).

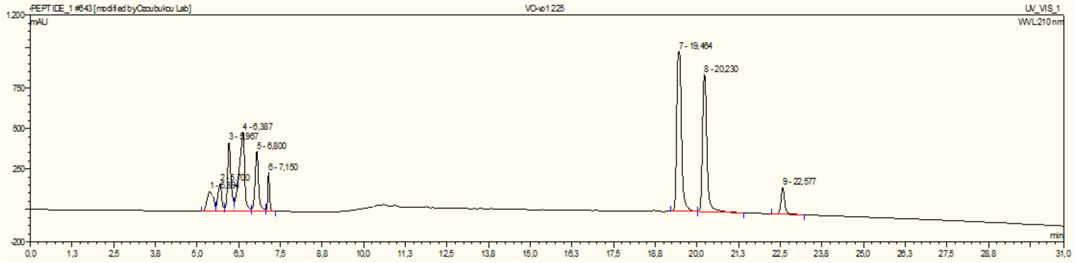

Figure B. 6. HPLC chromatogram of the enzymatic reaction with compound **2d** (Set 1, t = 5 min) at 210 nm (PS-C18, 30 min, gradient).

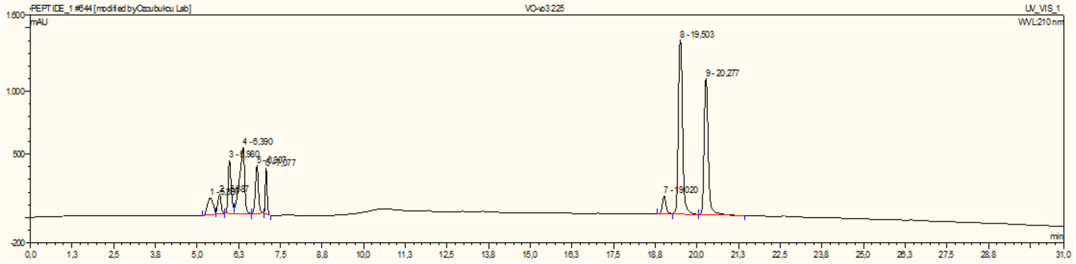

Figure B. 7. HPLC chromatogram of the enzymatic reaction with compound **2d** (Set 1, t = 45 min) at 210 nm (PS-C18, 30 min, gradient).

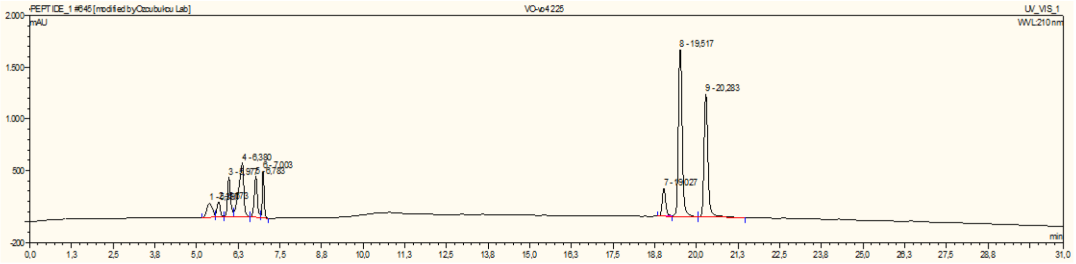

Figure B. 8. HPLC chromatogram of the enzymatic reaction with compound **2d** (Set 1, t = 75 min) at 210 nm (PS-C18, 30 min, gradient).

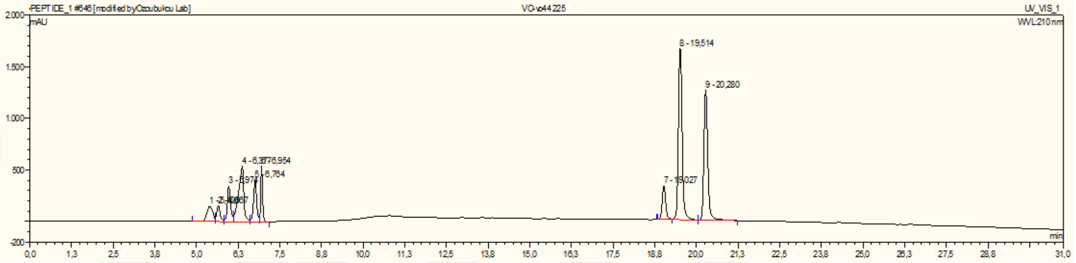

Figure B. 9. HPLC chromatogram of the enzymatic reaction with compound **2d** (Set 1, t = 110 min) at 210 nm (PS-C18, 30 min, gradient).

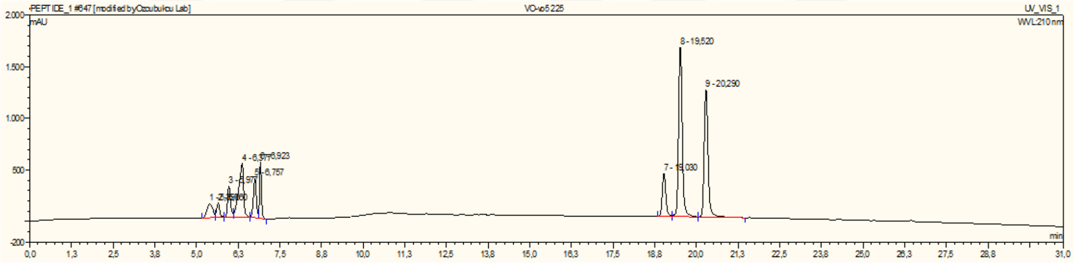

Figure B. 10. HPLC chromatogram of the enzymatic reaction with compound **2d** (Set 1, t = 150 min) at 210 nm (PS-C18, 30 min, gradient).

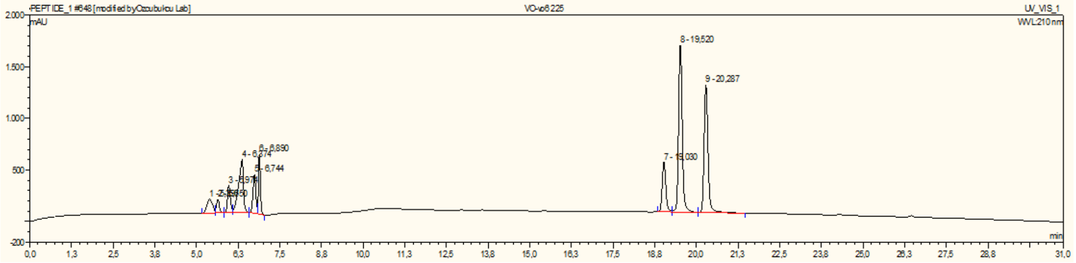

Figure B. 11. HPLC chromatogram of the enzymatic reaction with compound **2d** (Set 1, t = 200 min) at 210 nm (PS-C18, 30 min, gradient).

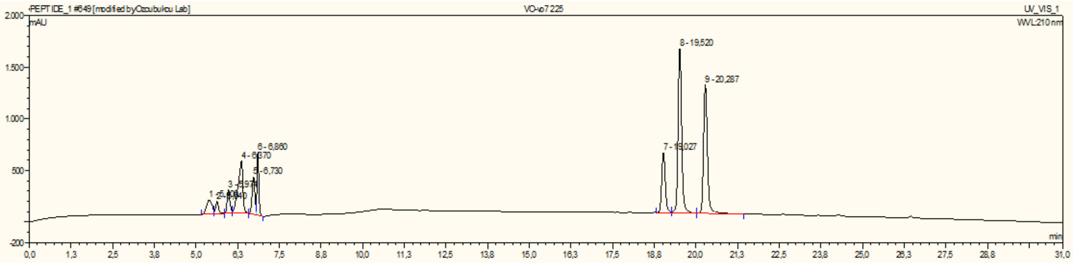

Figure B. 12. HPLC chromatogram of the enzymatic reaction with compound **2d** (Set 1, t = 300 min) at 210 nm (PS-C18, 30 min, gradient).

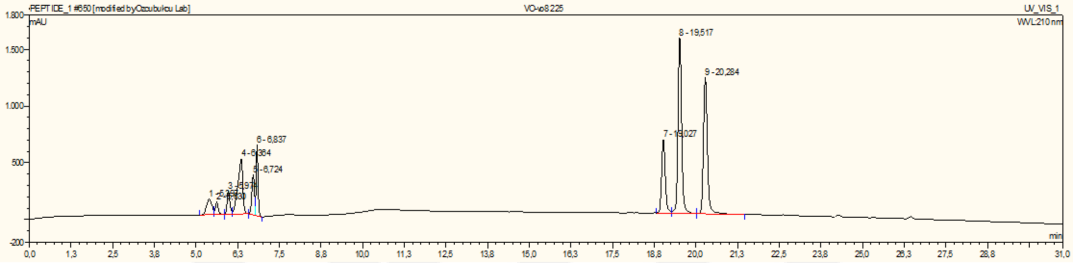

Figure B. 13. HPLC chromatogram of the enzymatic reaction with compound **2d** (Set 1, t = 420 min) at 210 nm (PS-C18, 30 min, gradient).

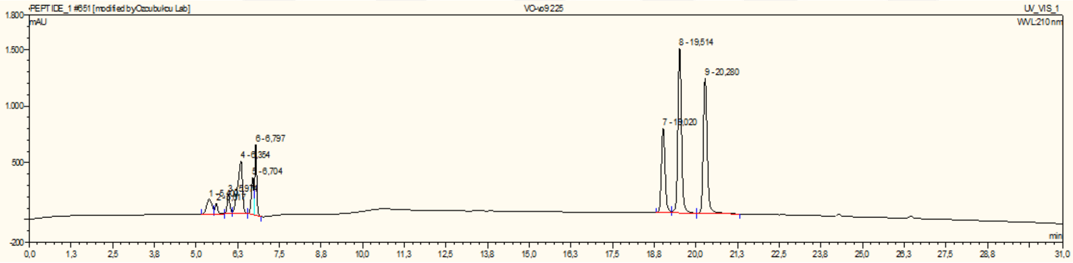

Figure B. 14. HPLC chromatogram of the enzymatic reaction with compound **2d** (Set 1, t = 1440 min) at 210 nm (PS-C18, 30 min, gradient).

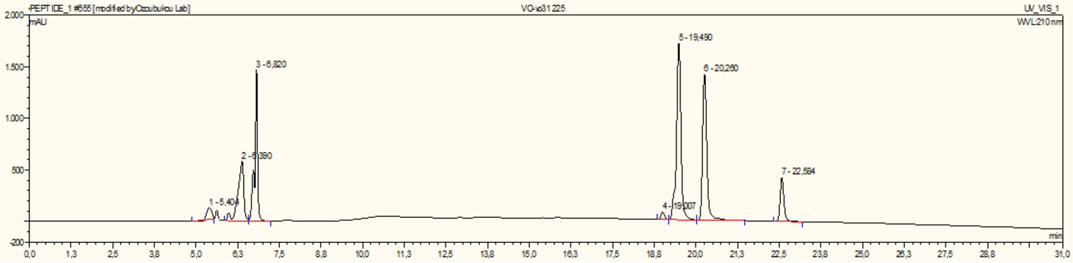

Figure B. 15. HPLC chromatogram of the enzymatic reaction with compound **2d** (Set 2, t = 45 min) at 210 nm (PS-C18, 30 min, gradient).

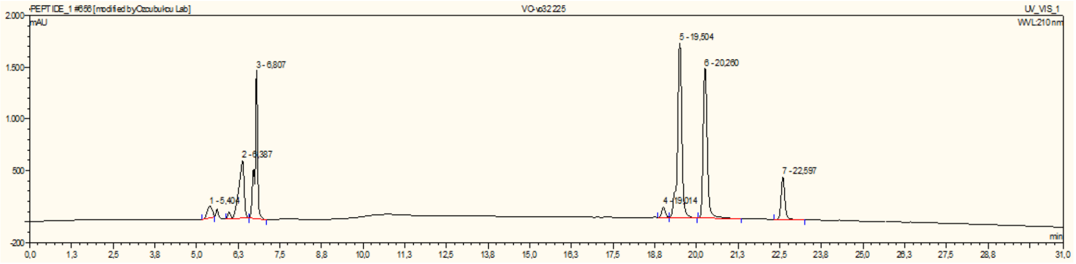

Figure B. 16. HPLC chromatogram of the enzymatic reaction with compound **2d** (Set 2, t = 75 min) at 210 nm (PS-C18, 30 min, gradient).

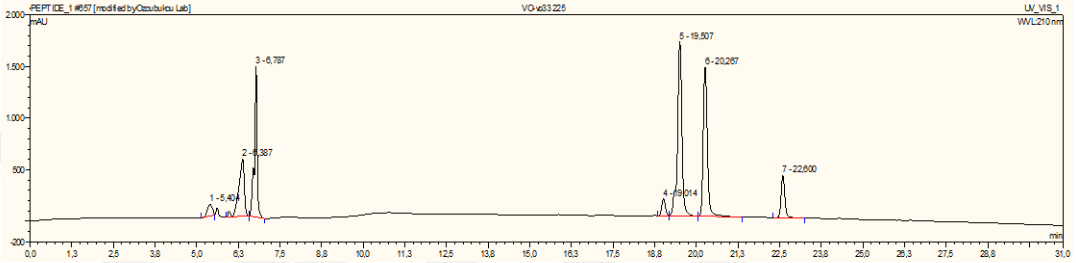

Figure B. 17. HPLC chromatogram of the enzymatic reaction with compound **2d** (Set 2, t = 110 min) at 210 nm (PS-C18, 30 min, gradient).

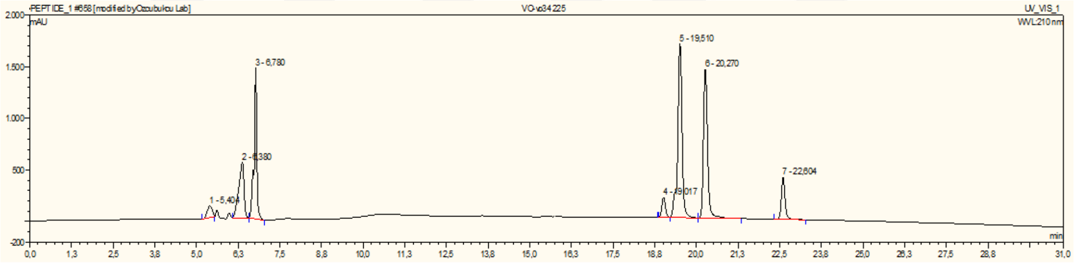

Figure B. 18. HPLC chromatogram of the enzymatic reaction with compound **2d** (Set 2, t = 150 min) at 210 nm (PS-C18, 30 min, gradient).

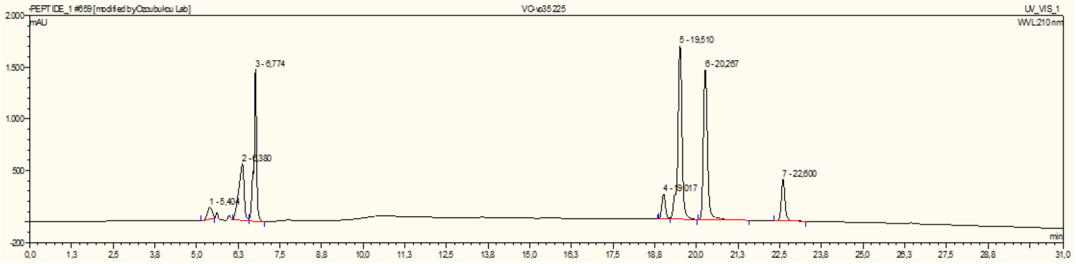

Figure B. 19. HPLC chromatogram of the enzymatic reaction with compound **2d** (Set 2, t = 200 min) at 210 nm (PS-C18, 30 min, gradient).

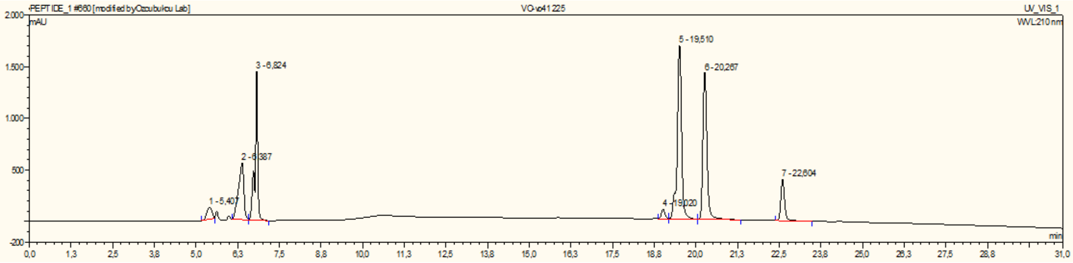

Figure B. 20. HPLC chromatogram of the enzymatic reaction with compound **2d** (Set 3, t = 45 min) at 210 nm (PS-C18, 30 min, gradient).

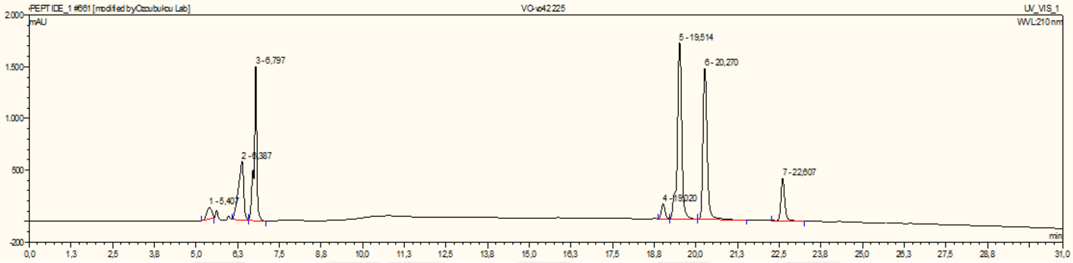

Figure B. 21. HPLC chromatogram of the enzymatic reaction with compound **2d** (Set 3, t = 75 min) at 210 nm (PS-C18, 30 min, gradient).

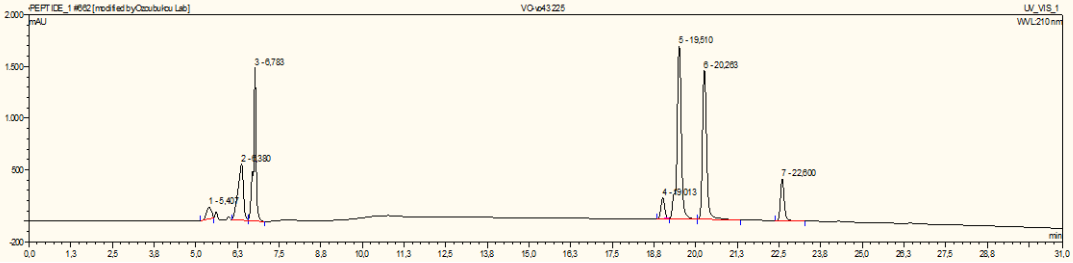

Figure B. 22. HPLC chromatogram of the enzymatic reaction with compound **2d** (Set 3, t = 110 min) at 210 nm (PS-C18, 30 min, gradient).

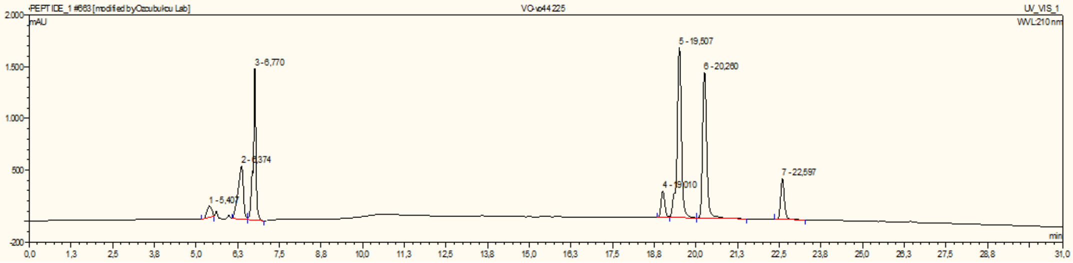

Figure B. 23. HPLC chromatogram of the enzymatic reaction with compound **2d** (Set 3, t = 150 min) at 210 nm (PS-C18, 30 min, gradient).

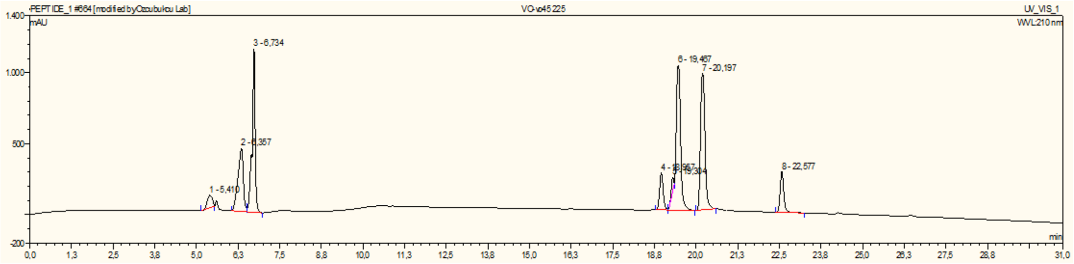

Figure B. 24. HPLC chromatogram of the enzymatic reaction with compound **2d** (Set 3, t = 200 min) at 210 nm (PS-C18, 30 min, gradient).

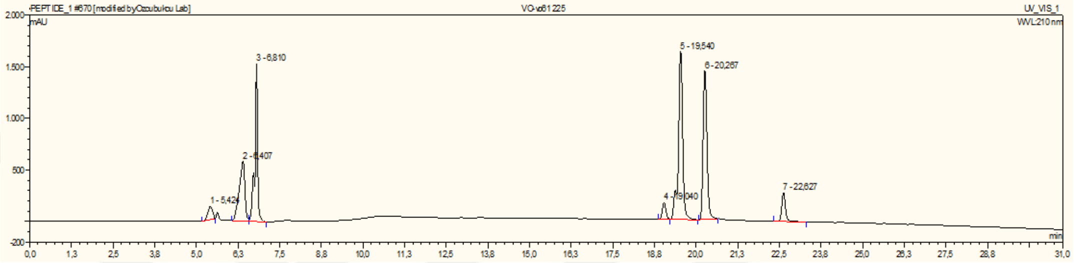

Figure B. 25. HPLC chromatogram of the enzymatic reaction with compound **2d** (Set 4, t = 45 min) at 210 nm (PS-C18, 30 min, gradient).

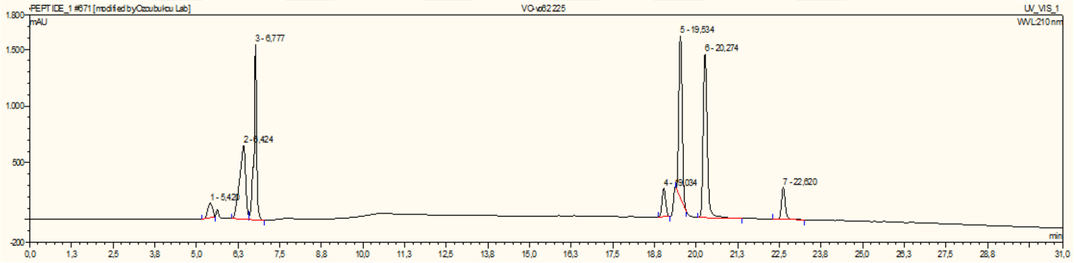

Figure B. 26. HPLC chromatogram of the enzymatic reaction with compound **2d** (Set 4, t = 75 min) at 210 nm (PS-C18, 30 min, gradient).

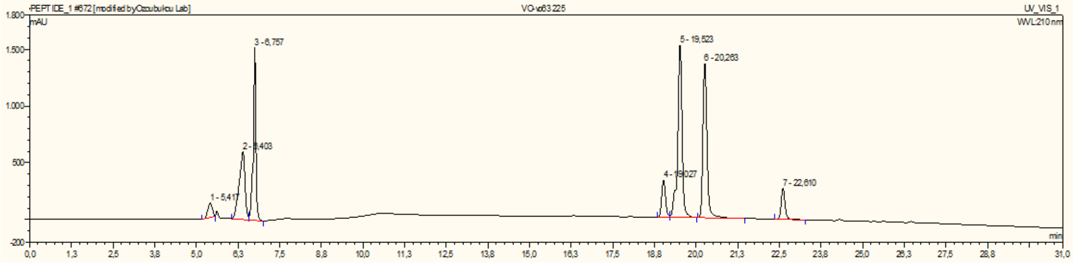

Figure B. 27. HPLC chromatogram of the enzymatic reaction with compound **2d** (Set 4, t = 110 min) at 210 nm (PS-C18, 30 min, gradient).

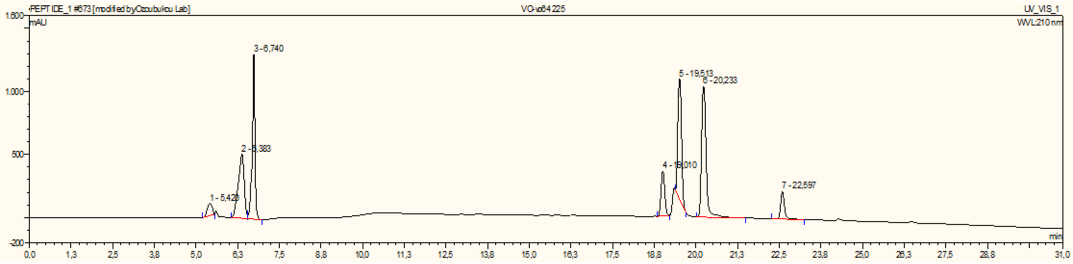

Figure B. 28. HPLC chromatogram of the enzymatic reaction with compound **2d** (Set 3, t = 150 min) at 210 nm (PS-C18, 30 min, gradient).

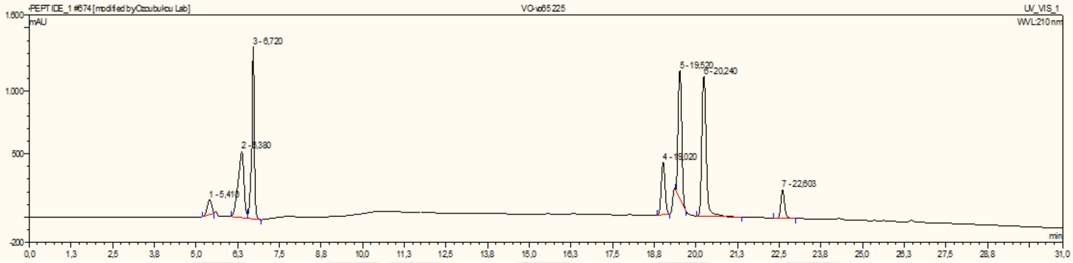

Figure B. 29. HPLC chromatogram of the enzymatic reaction with compound **2d** (Set 4, t = 200 min) at 210 nm (PS-C18, 30 min, gradient).

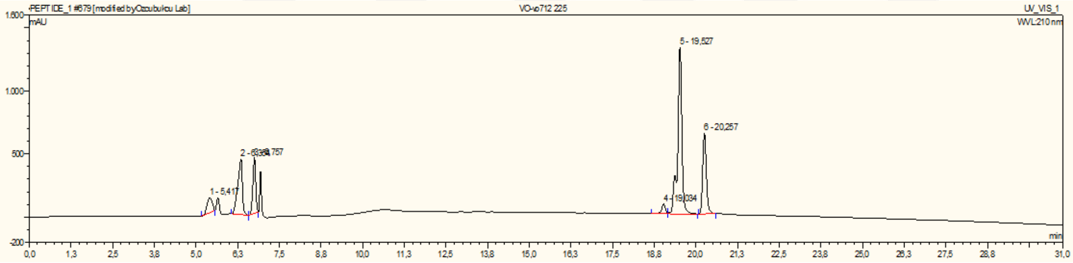

Figure B. 30. HPLC chromatogram of the enzymatic reaction with compound **2d** (Set 5, t = 45 min) at 210 nm (PS-C18, 30 min, gradient).

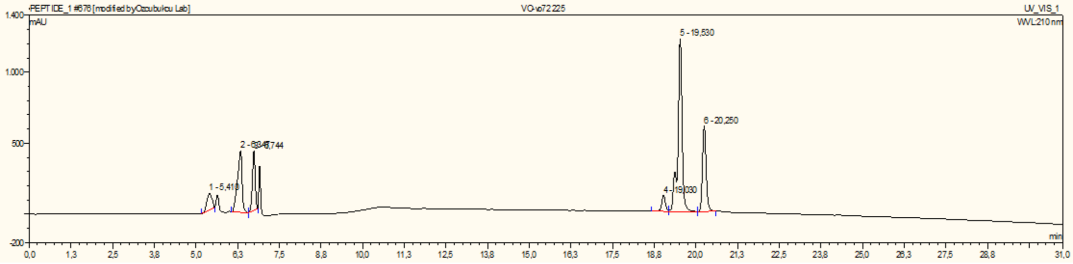

Figure B. 31. HPLC chromatogram of the enzymatic reaction with compound **2d** (Set 5, t = 75 min) at 210 nm (PS-C18, 30 min, gradient).

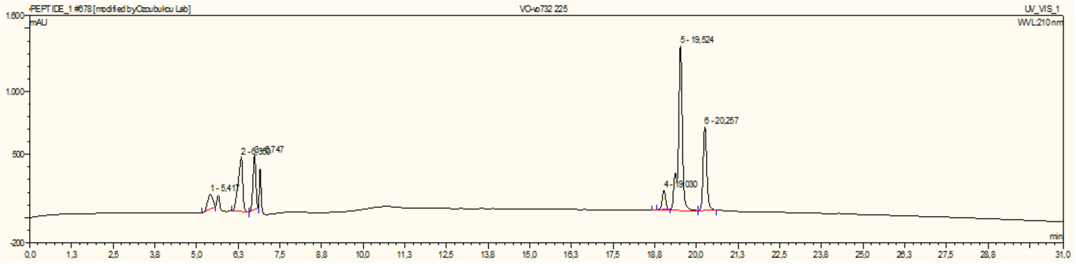

Figure B. 32. HPLC chromatogram of the enzymatic reaction with compound **2d** (Set 5, t = 110 min) at 210 nm (PS-C18, 30 min, gradient).

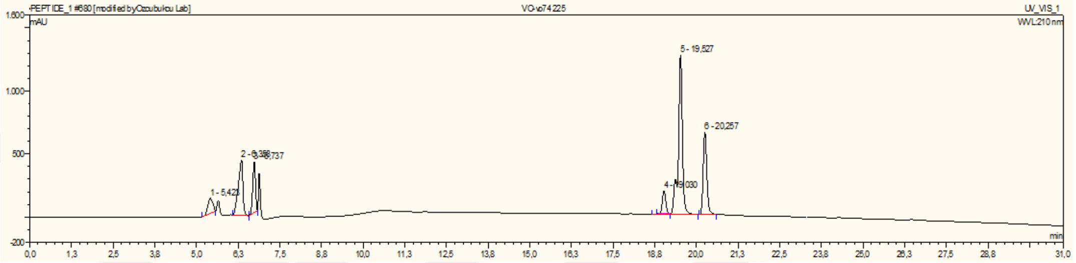

Figure B. 33. HPLC chromatogram of the enzymatic reaction with compound **2d** (Set 5, t = 150 min) at 210 nm (PS-C18, 30 min, gradient).

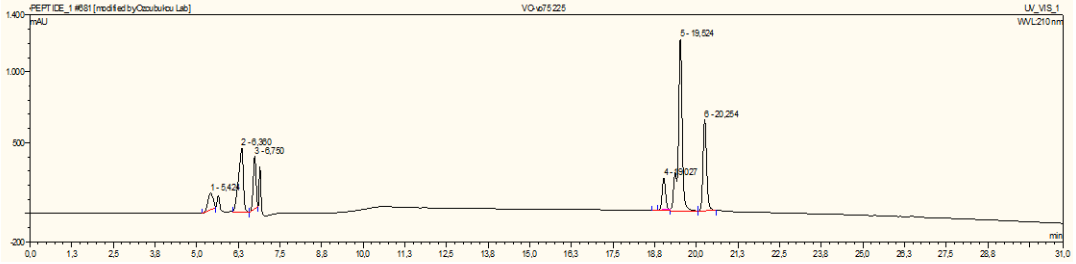

Figure B. 34. HPLC chromatogram of the enzymatic reaction with compound **2d** (Set 5, t = 200 min) at 210 nm (PS-C18, 30 min, gradient).

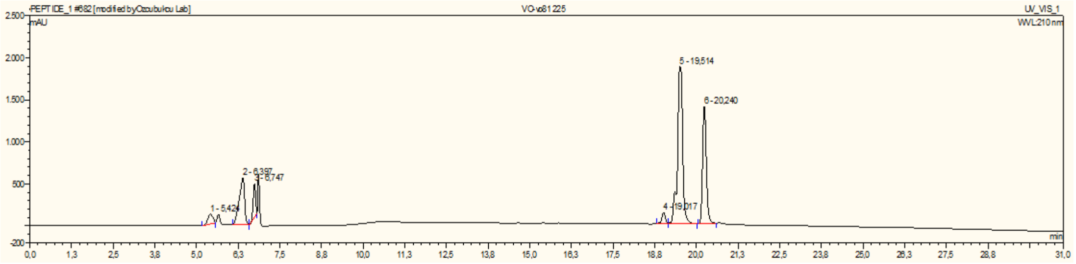

Figure B. 35. HPLC chromatogram of the enzymatic reaction with compound **2d** (Set 6, t = 45 min) at 210 nm (PS-C18, 30 min, gradient).

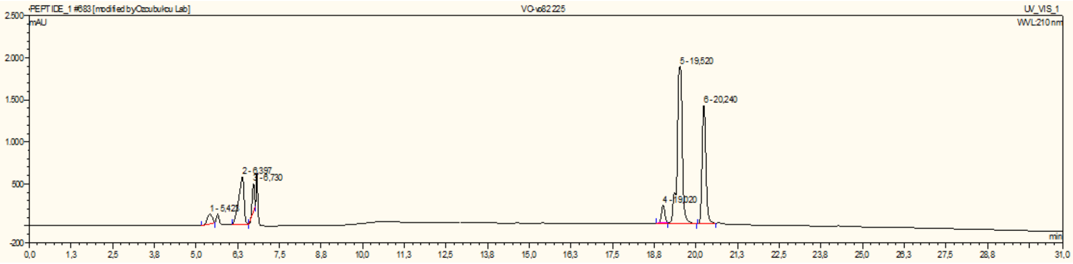

Figure B. 36. HPLC chromatogram of the enzymatic reaction with compound **2d** (Set 6, t = 75 min) at 210 nm (PS-C18, 30 min, gradient).

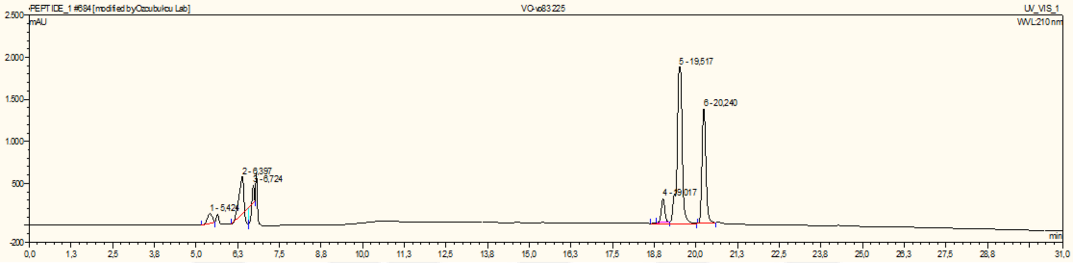

Figure B. 37. HPLC chromatogram of the enzymatic reaction with compound **2d** (Set 6, t = 110 min) at 210 nm (PS-C18, 30 min, gradient).

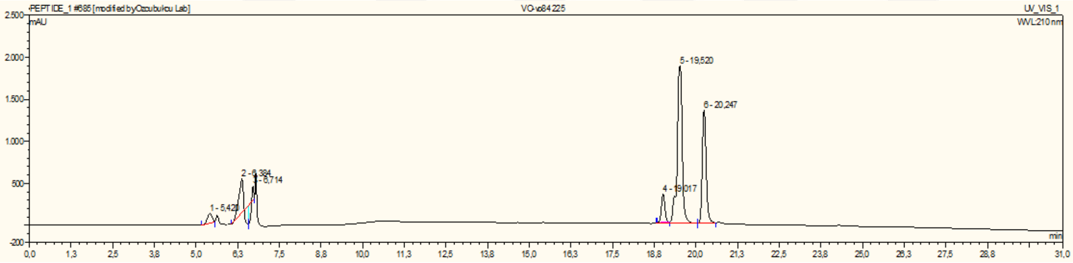

Figure B. 38. HPLC chromatogram of the enzymatic reaction with compound **2d** (Set 6, t = 150 min).

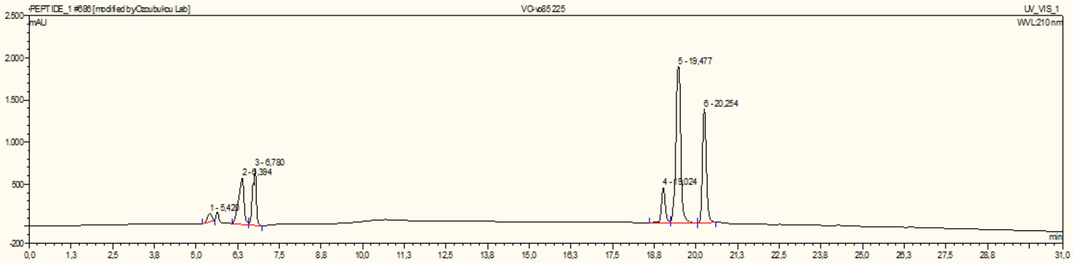

Figure B. 39. HPLC chromatogram of the enzymatic reaction with compound **2d** (Set 6, t = 200 min) at 210 nm (PS-C18, 30 min, gradient).

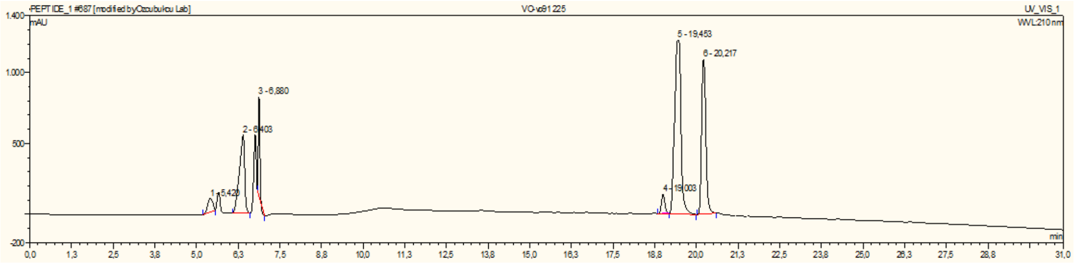

Figure B. 40. HPLC chromatogram of the enzymatic reaction with compound **2d** (Set 7, t = 45 min) at 210 nm (PS-C18, 30 min, gradient).

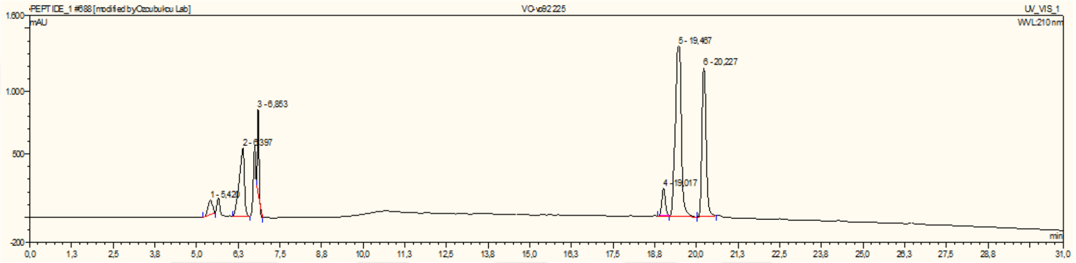

Figure B. 41. HPLC chromatogram of the enzymatic reaction with compound **2d** (Set 7, t = 75 min) at 210 nm (PS-C18, 30 min, gradient).

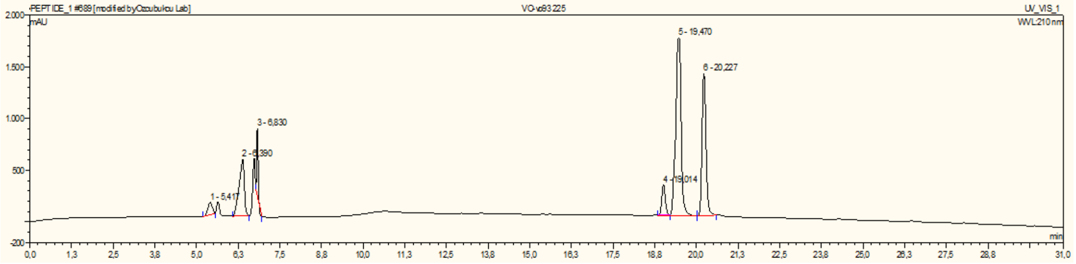

Figure B. 42. HPLC chromatogram of the enzymatic reaction with compound **2d** (Set 7, t = 110 min) at 210 nm (PS-C18, 30 min, gradient).

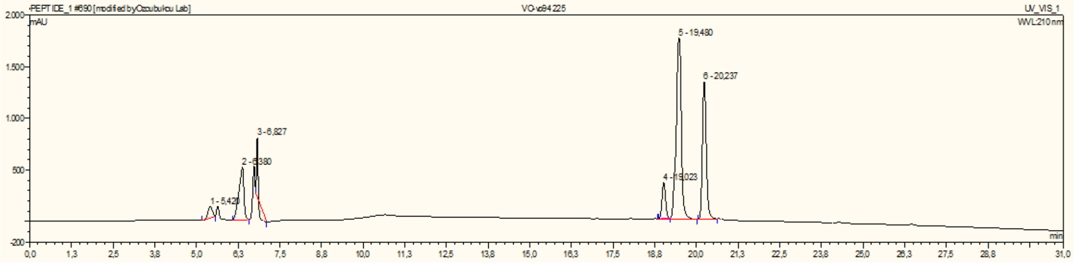

Figure B. 43. HPLC chromatogram of the enzymatic reaction with compound **2d** (Set 7, t = 150 min) at 210 nm (PS-C18, 30 min, gradient).

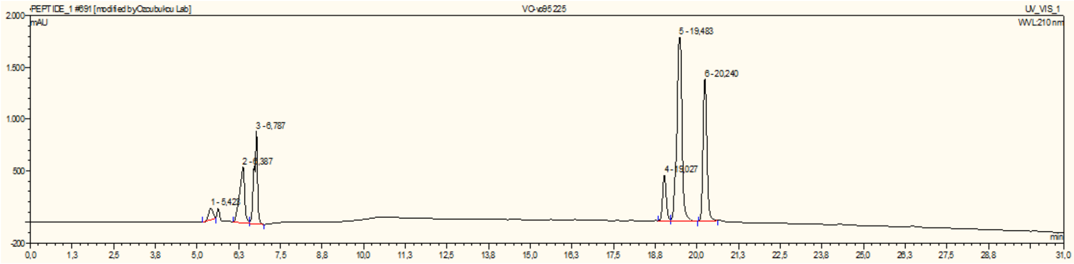

Figure B. 44. HPLC chromatogram of the enzymatic reaction with compound **2d** (Set 7, t = 200 min) at 210 nm (PS-C18, 30 min, gradient).

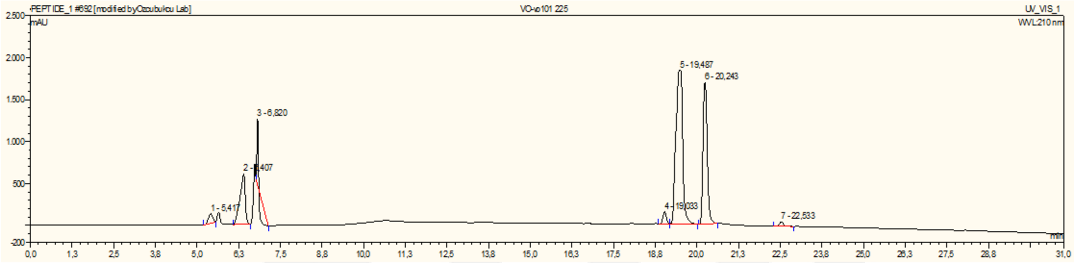

Figure B. 45. HPLC chromatogram of the enzymatic reaction with compound **2d** (Set 8, t = 45 min) at 210 nm (PS-C18, 30 min, gradient).

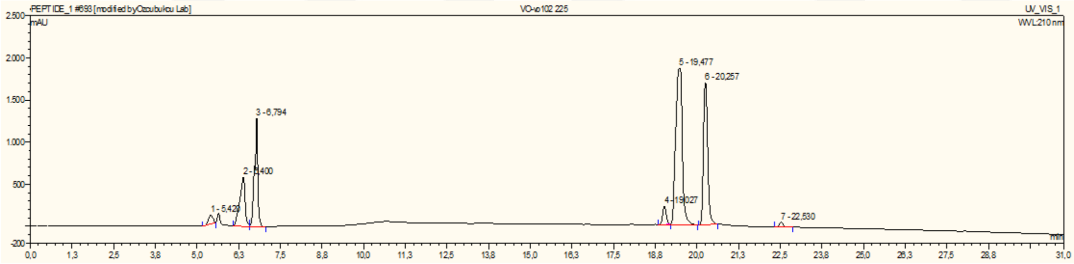

Figure B. 46. HPLC chromatogram of the enzymatic reaction with compound **2d** (Set 8, t = 75 min) at 210 nm (PS-C18, 30 min, gradient).

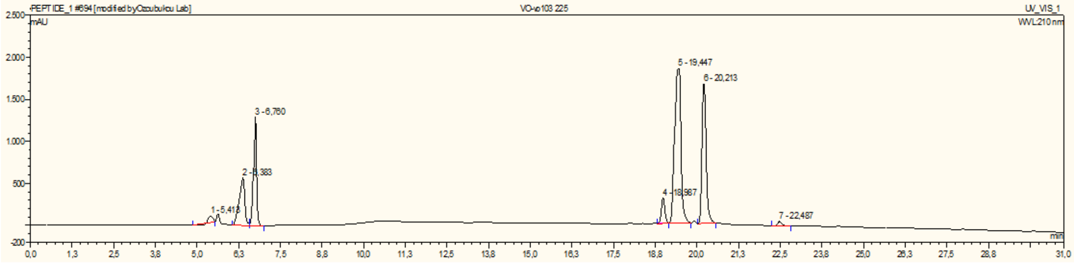

Figure B. 47. HPLC chromatogram of the enzymatic reaction with compound **2d** (Set 8, t = 110 min) at 210 nm (PS-C18, 30 min, gradient).

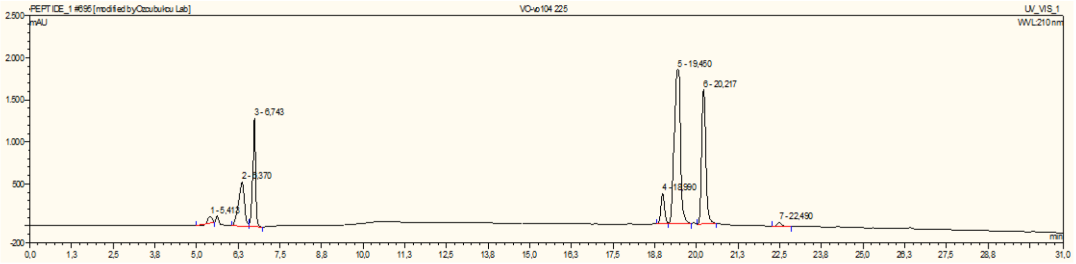

Figure B. 48. HPLC chromatogram of the enzymatic reaction with compound **2d** (Set 8, t = 150 min) at 210 nm (PS-C18, 30 min, gradient).

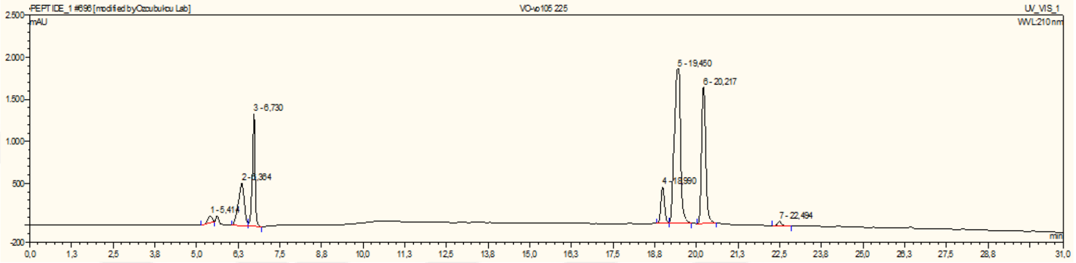

Figure B. 49. HPLC chromatogram of the enzymatic reaction with compound **2d** (Set 8, t = 200 min) at 210 nm (PS-C18, 30 min, gradient) at 210 nm (PS-C18, 30 min, gradient).

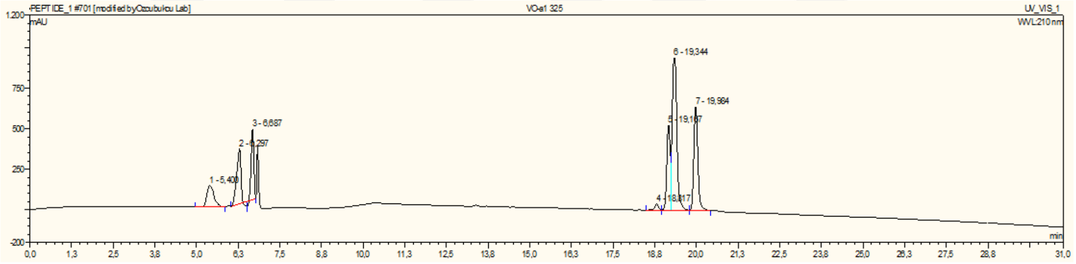

Figure B. 50. HPLC chromatogram of the second set of enzymatic reaction with compound **2d** (1 mol% of **F**-Arg, t = 30 min) at 210 nm (PS-C18, 30 min, gradient).

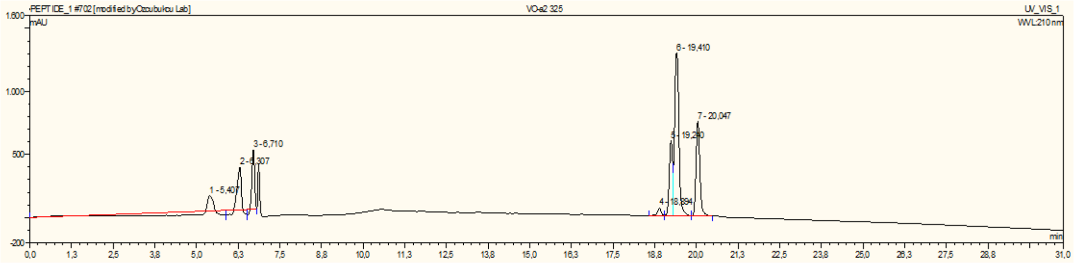

Figure B. 51. HPLC chromatogram of the second set of enzymatic reaction with compound **2d** (1 mol% of **F**-Arg, t = 50 min) at 210 nm (PS-C18, 30 min, gradient).

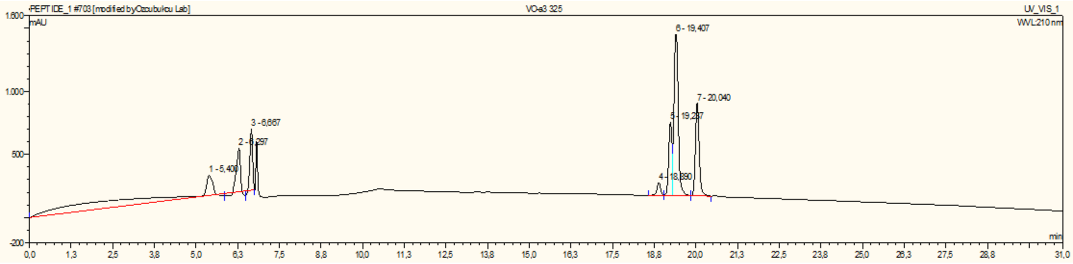

Figure B. 52. HPLC chromatogram of the second set of enzymatic reaction with compound **2d** (1 mol% of **F**-Arg, t = 70 min) at 210 nm (PS-C18, 30 min, gradient).

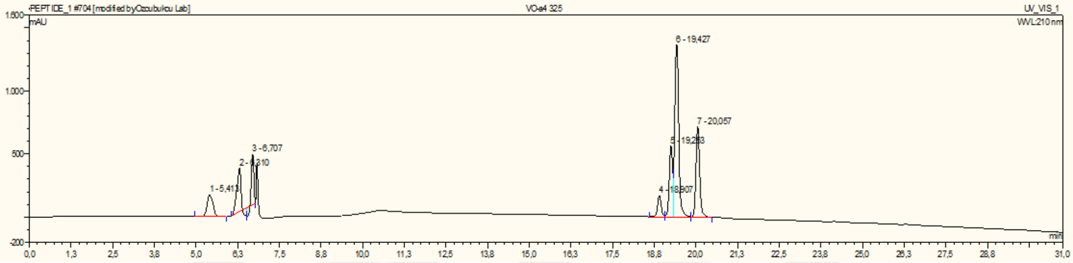

Figure B. 53. HPLC chromatogram of the second set of enzymatic reaction with compound **2d** (1 mol% of **F**-Arg, t = 90 min) at 210 nm (PS-C18, 30 min, gradient).

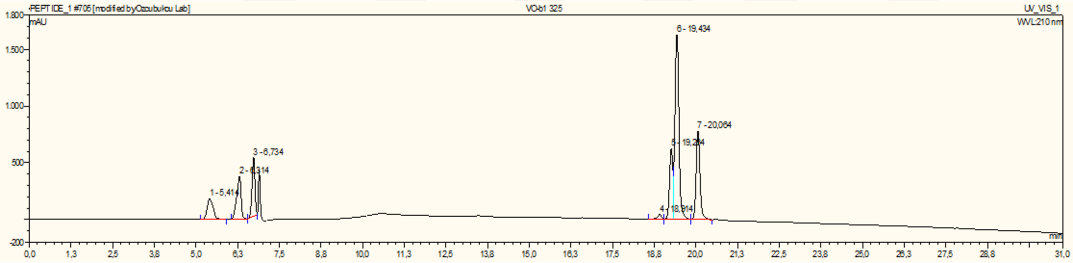

Figure B. 54. HPLC chromatogram of the second set of enzymatic reaction with compound **2d** (1.3 mol% of **F**-Arg, t = 30 min) at 210 nm (PS-C18, 30 min, gradient).

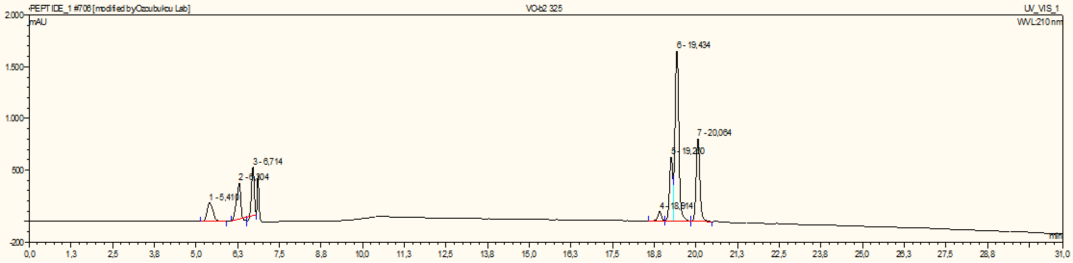

Figure B. 55. HPLC chromatogram of the second set of enzymatic reaction with compound **2d** (1.3 mol% of **F**-Arg, t = 50 min) at 210 nm (PS-C18, 30 min, gradient).

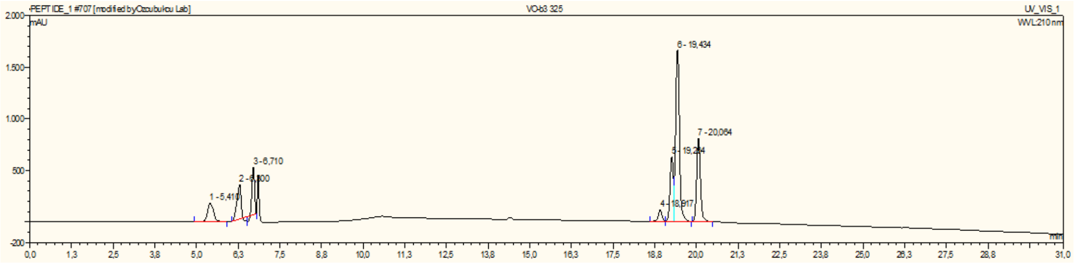

Figure B. 56. HPLC chromatogram of the second set of enzymatic reaction with compound **2d** (1.3 mol% of **F**-Arg, t = 70 min) at 210 nm (PS-C18, 30 min, gradient).

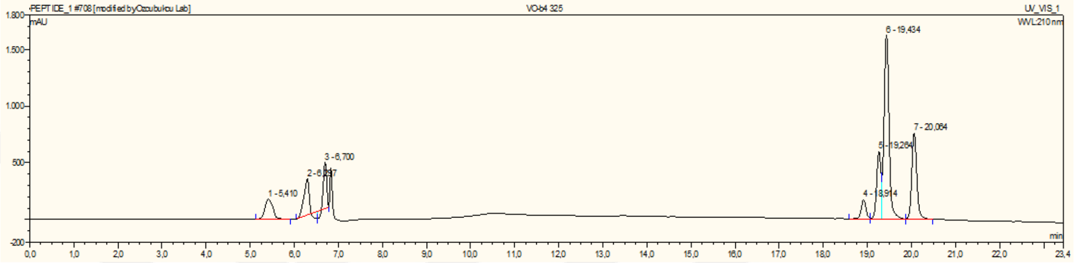

Figure B. 57. HPLC chromatogram of the second set of enzymatic reaction with compound **2d** (1.3 mol% of **F**-Arg, t = 90 min) at 210 nm (PS-C18, 30 min, gradient).

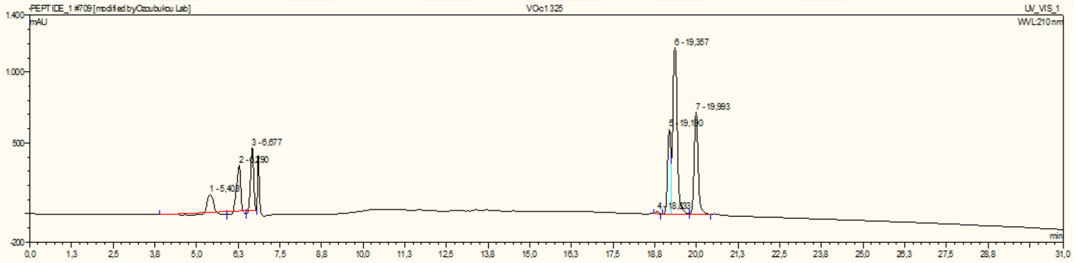

Figure B. 58. HPLC chromatogram of the second set of enzymatic reaction with compound **2d** (2.0 mol% of **F**-Arg, t = 30 min) at 210 nm (PS-C18, 30 min, gradient).

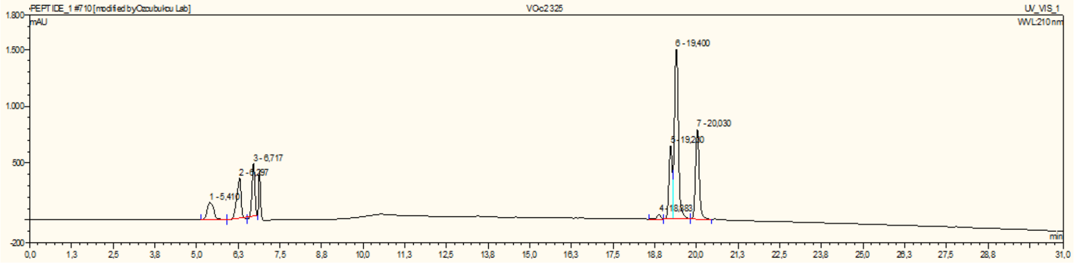

Figure B. 59. HPLC chromatogram of the second set of enzymatic reaction with compound **2d** (2.0 mol% of **F**-Arg, t = 50 min) at 210 nm (PS-C18, 30 min, gradient).

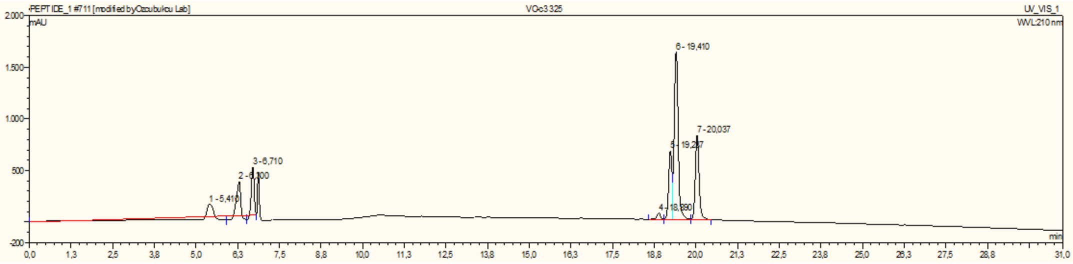

Figure B. 60. HPLC chromatogram of the second set of enzymatic reaction with compound **2d** (2.0 mol% of **F**-Arg, t = 70 min) at 210 nm (PS-C18, 30 min, gradient).

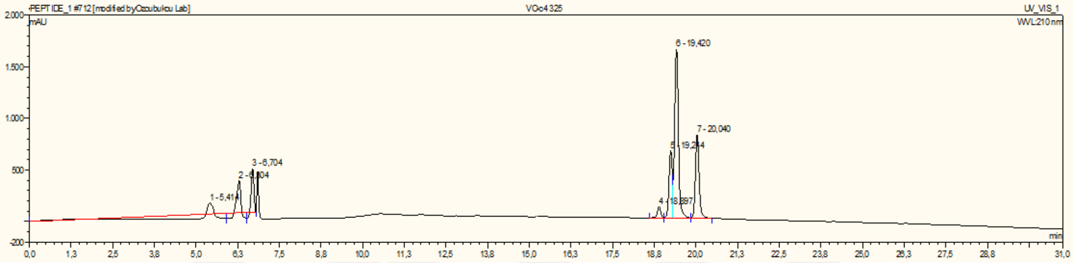

Figure B. 61. HPLC chromatogram of the second set of enzymatic reaction with compound **2d** (2.0 mol% of **F**-Arg, t = 90 min) at 210 nm (PS-C18, 30 min, gradient).

C. FT-IR SPECTRA

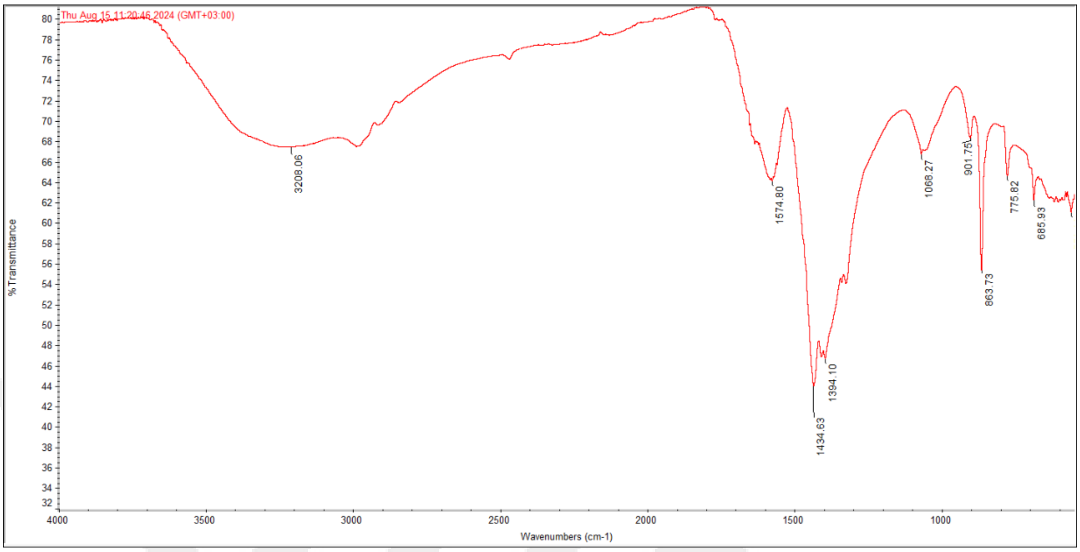

Figure C. 1. FT-IR spectrum of fullerenol.

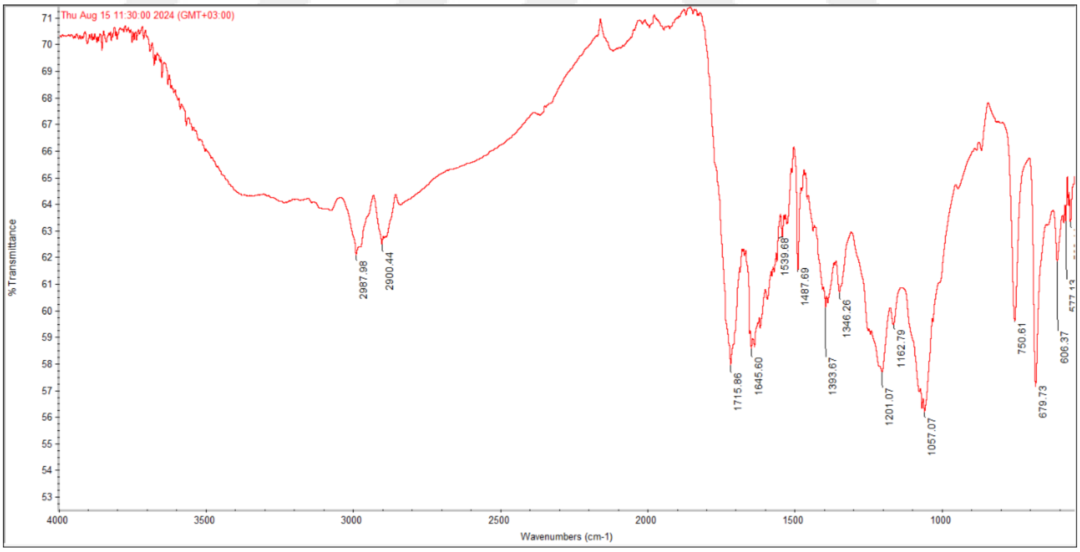

Figure C. 2. FT-IR spectrum of activated fullerenol.

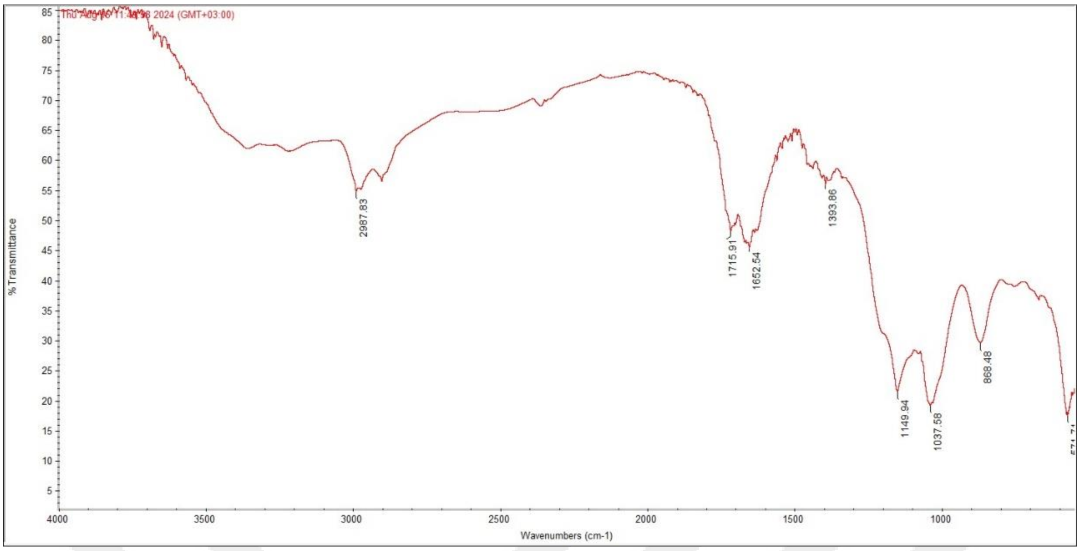

Figure C. 3. FT-IR spectrum of **F**-Arg.

CURRICULUM VITAE

Surname, Name: Dolgun, Volkan

EDUCATION

Degree	**Institution**	**Year of Graduation**
MS	METU Chemistry	2017
BS	METU Chemistry	2014
High School	İçel Anatolian High School, Mersin	2008

FOREIGN LANGUAGES

Advanced English

PUBLICATIONS

1. Soylemez, S.; Dolgun, V.; Özçubukçu, S. Fullerene-Based Mimics for Enhanced Acetylcholine Detection in the Diagnosis of Alzheimer’s Disease. *Microchem. J.* **2023**, *193*, 109099.